Optical Fibre Communication Systems in the Nonlinear Regime

Gabriel Saavedra Mondaca

A thesis submitted to the University College London (UCL) for the degree of Doctor of Philosophy

Optical Networks Group
Department of Electronic and Electrical Engineering
University College London (UCL)

October 2018

I, Gabriel Saavedra Mondaca, confirm that the work presented in this thesis is my own. Where information has been derived from other sources, I confirm that this has been indicated.

Abstract

THIS thesis studies solutions to increase the capacity of optical communication systems in the presence of nonlinear effects. Extending the optical bandwidth and mitigating nonlinear distortions were identified as promising ways to increase the throughput in transmission system.

Raman amplification was investigated as a potential replacement of the conventional erbium-doped fibre amplifier (EDFA). In this context, the performance of discrete and distributed Raman amplifiers was studied in the linear and nonlinear regimes. Despite the bandwidth benefits, discrete Raman amplifiers were shown to exhibit an increased noise figure and nonlinear distortions, compared to EDFA. Additionally, for the first time, a thorough study of digital back-propagation for distributed Raman amplified links was performed, allowing for higher transmission rates at the expense of an increase of 25% in the algorithm complexity.

A major focus of this work was to investigate the growth of nonlinear distortions in optical communication systems as the bandwidth is expanded. This work was the first to experimentally validate the Gaussian noise model (and variations accounting for inter-channel Raman scattering) in a wideband transmission regime up to 9 THz. Using these models, the merit of increasing the optical bandwidth was addressed, showing a beneficial sublinear increase in throughput despite the growth of nonlinear effects.

An alternative nonlinear compensation method is optical phase conjugation (OPC). The performance of OPC was experimentally evaluated over an installed fibre link, showing limited improvements when OPC is used with practical transmission constraints. To overcome this limitation, a new method combining OPC and Volterra equalisation was developed. This method was shown to enhance the performance of two limited nonlinear compensation techniques, offering an attractive trade-off between performance and complexity.

The results obtained in this research allow for higher information throughput to be transmitted, and can be used to plan and design future communication system and networks around the world.

Impact Statement

OPTICAL fibres form the backbone of the global telecommunications infrastructure. They will need to provide higher transmission rates to satisfy the ever increasing consumer demand for data. To do so, it is important to understand the physical phenomena that restrict the capacity of optical fibre as a communication channel, and propose methods to overcome these limitations. Optical fibres are a nonlinear medium, and therefore, signals propagated through them experience distortions depending on their optical power and bandwidth. The use of higher optical powers or large bandwidths, or both, increases these distortions, which bound the capacity of optical fibre communication systems.

In this thesis, experiments were performed to quantify the growth of nonlinear distortions in optical communication systems as the optical bandwidth is expanded up to 9 THz. This work is the first to validate the Gaussian noise model (and the variations thereof that account for inter-channel Raman scattering), a tool ubiquitously used in the design of transmission links, in a wideband transmission regime. These experiments led to a greater understanding of nonlinear interactions for wideband signals: the first step in increasing the usable fibre bandwidth to maximise the capacity of optical communications systems.

Moreover, the mitigation of nonlinear distortions using digital, optical, and a novel combination of both techniques, was addressed. Nonlinear compensation techniques are of tremendous commercial interest, as they can provide an increase in the throughput of a transmission system, and their future deployment only depends on the computational complexity of the selected algorithms. Therefore, the higher gains shown in combination with Raman amplification, and the potential of simplifying the complexity of the nonlinear compensation scheme by moving part, or the complete, signal processing towards the optical domain could be an attractive solution that can be implemented in the near future.

Overall, the solutions proposed in this work have the potential to result in revolutionary increases in the transmission capacity for future optical communication systems.

Acknowledgements

STARTING the pursuit of a PhD is a massive challenge. I could not have done it without the trust and encouragement of my supervisor, Professor Polina Bayvel. She gave me the confidence and opportunity to chase one of my dreams within the Optical Networks Group at UCL, and I will always be grateful for it.

The last 4 years have been a magnificent experience. I would like to thank the entirety of the ONG, lecturers, post-docs and fellow PhD students. My second supervisor, Dr. Robert Killey, for the advice and conversations about large bandwidth transmission and nonlinear effects. The famous 808 became a home away from home, with somebody always willing to have a cup of coffee and discuss the future of optical communications. Special thanks go to my good friends Dr. Gabriele Liga, Dr. Sezer Erkilinc and (hopefully!) soon to be doctors Paris Andreades and Boris Karanov. Also, Dr. Domaniç Lavery for giving me every possible advice, and Dr. Daniel Elson and Mr. Daniel Semrau for help in my experiments and with the GN model. I would also like to thank Dr. Lidia Galdino, Dr. Kai Shi and Dr. Robert Maher for introducing me the laboratory and helping me design and perform my experiments.

Collaborative experiments are always a challenge. I owe a great debt to my colleagues at Aston university Dr. Md.A.Iqbal, Dr. M. Tan and Dr. P. Harper, and at the Optoelectronics Research Centre in Southampton university Y. Sun, Dr. F. Parmigiani, Dr. K. Bottril and Dr. P. Petropoulos. All of them collaborated with their expertise and experience to perform the experiments described in this thesis.

Of course, I made many friends over the last few years. Among them, I would like to name Dr. Sebastian Bahamonde, Dr. Victor Montenegro and Dr. Pietro Servini, all part of the Tuesday football group.

Additionally, I acknowledge the financial support from CONICYT Chile under the Becas Chile programme and the UK EPSRC UNLOC project.

Finally, I would like to my friends and family back home for always believing in me. Special thanks to my wife, Catalina, for her continuous support and company. She decided to join me in this adventure and was always by my side when I needed her. She also gave the happiest moment of my life when our daughter Camelia was born in April 2018. I will always love my beautiful women. To all of you, thank you very much!

Contents

List of Figures

List of Tables

1 Introduction

THE exchange of information has never been higher. Driven mainly by the widespread use of smartphones, music and/or video on demand, and new applications such as augmented reality and cloud computing, the amount of data transmitted across the globe keeps increasing year after year. Moreover, the imminent deployment of the fifth generation (5G) mobile networks, with the promise of faster mobile transmission rates, will further add to this trend. As the number of devices connected to the internet keeps increasing, the anual data traffic will continue to grow, and it is expected to reach up to 3.3 Zbytes per year by 2021 with a 24% coumpound annual growth rate as forecast by Cisco [3]. In order to sustain the ever-increasing data demand a global communication infrastructure capable of providing enough capacity is required.

Optical fibres are the foundation of modern communication systems with an ubiquitous presence in today's interconnected society, from the modem in our homes to submarine cables linking different continents. In 1966, the use of the optical fibre cable as a communication medium was proposed by Kao and Hockham [4], who highlighted their capability of guiding light. In the following years the improvement in manufacturing processes allowed a dramatic reduction in the losses present in optical fibres. Starting from over 1000 dB/km in the 1960s and reaching numbers as low as 0.2 dB/km at a wavelength of 1550 nm in 1979 [5]. These improvements enabled optical fibre to become the dominant medium for communications.

1.1 Evolution of optical communication systems

With an extremely low attenuation region that spans tens of terahertz, and, the possibility to use carrier frequencies of hundreds of terahertz, optical fibres have been identified as the preferred communication channel to support the global communication infrastructure. They remain the main medium to transmit information at high speeds and have been successfully deployed all over the world in the last 40 years. Historically, different transmission windows within the low attenuation region of the optical fibre have been used. Among them we can find: the original (O-) band from 1260 to 1360 nm, the region where the minimum chromatic dispersion is found; the conventional (C-) band from 1530 to 1565 nm, the region where the minimum attenuation is found; and the long-wavelength (L-) band from 1565 to 1625 nm, the region where the second lowest attenuation is found. Several developments have allowed the capacity of optical communication systems to increase over the years: the carrier frequency was decreased towards transmission windows with lower losses to increase regenerator spacing; opto-electronic signal regenerators were replaced by optical amplifiers allowing the amplification of multiple, or multiplexed, signals with a single device independent of the modulation format and the symbol rate of the optical signal; coherent detection enabled the use of different degrees of freedom of the optical field to encode information; and information theory has delivered coding schemes that allow an increase in the information carried per symbol and the correction of errors.

Modern optical transmission systems seek to increase their capacity by transmitting more channels using the wavelength division multiplexing (WDM) technique. To do so, new amplification schemes were introduced to overcome the bandwidth limitations of the erbium-doped fibre amplifier (EDFA). Firstly, the amplification window of the EDFA was shifted towards the L-band, enabling the amplification of C- and L-bands simultaneously using a parallel configuration [6]. Moreover, Raman amplification was combined with EDFA in a hybrid configuration [7], and the use of multiplexed Raman pumps was proposed [8] with the same objective. Additionally, thanks to the re-established interest in coherent receivers [9–11], the use of amplitude, phase and polarisation to encode information has led to a greater number of bits being transmitted within a single symbol slot, thus increasing the bits transmitted over a fixed spectral range (also known as spectral efficiency and measured in bits/s/Hz) of the system. Information theory has provided forward error correction (FEC) codes to use in combination with high order modulation formats, as seen in [12] for example, which, in recent years, has been combined with constellation shaping schemes [13] to further approach the capacity limits of the fibre channel.

State-of-the-art transmission systems are starting to include all the aforementioned technologies, pushing the optical fibre capacity limits further year after year. To illustrate

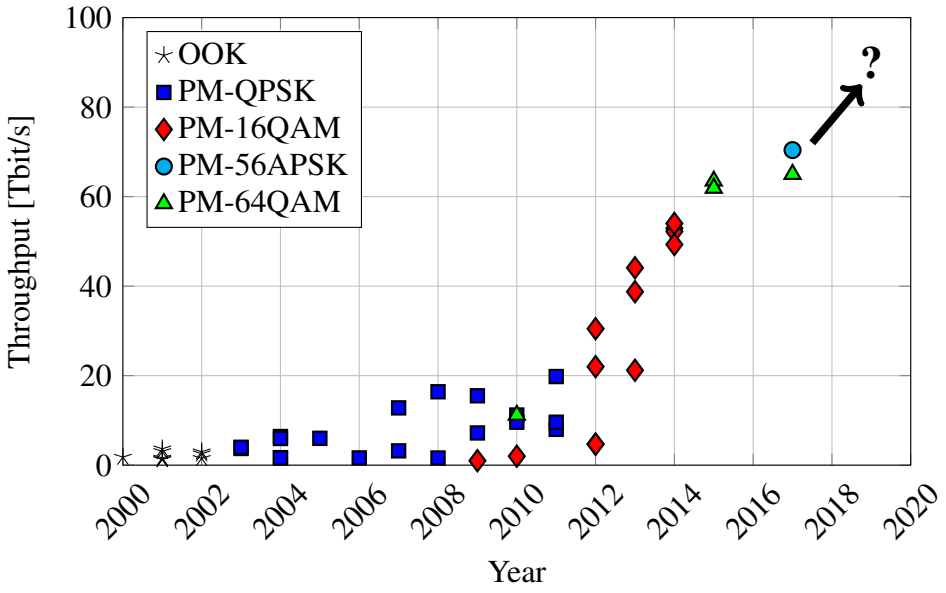

Figure 1.1: Evolution of record throughput in long-haul communication systems based on single mode fibre since the year 2000. Different markers represent the used modulation format: on-off keying (OOK), polarisation multiplexed quadrature phase shift keying (PM-QPSK), 16 quadrature amplitude keying (16-QAM), 64 quadrature amplitude keying (64-QAM), 56 amplitude phase shift keying (56-APSK).

this trend, a summary of the evolution of the record throughput demonstrations for long-haul transmission systems, using single mode fibre, is shown in Fig. 1.1. The data from Fig. 1.1 was compiled from the work in references [14–49]. The overall trend is one of growth, with more complex modulation formats and coding schemes being used as time passes. The latest record corresponds to [49], where a total throughput of 70.46 Tb/s was transmitted over 7600 km. Noticeably, in the last few years the trend seems to be slowing down, and, to date, no new record for long haul systems employing single mode fibre has been reported during 2018. However, for distances below 1000 km, new amplification solution such as wide-band semiconductor optical amplifier (SOA) and a renewed interest in hybrid EDFA-Raman amplification have lead to the transmission of throughputs in excess of 100 Tb/s [50, 51]

Considering the future demand for data, the question is then: how much further can the capacity of single mode optical fibre be increased, and what technologies will be responsible for driving a new generation of communication systems?

1.2 Capacity limits of optical communication systems

To understand the capacity limits of optical fibre systems, two clarifications, which will be formally discussed later in Chapter 2, are required. Firstly, the capacity of a communication channel is defined as the maximum rate at which reliable communication can be achieved [52]. Of practical importance is the case of an additive white Gaussian

noise (AWGN) channel, which is used to model the effect of various noise sources present in nature such as thermal and shot noise. It was shown in [52] that the capacity of an AWGN channel is determined by:

$$C = W \log_2 \left(1 + \frac{P}{N_0} \right), \tag{1.1}$$

where W, P and $N_0/2$ correspond to the signal bandwidth, signal power and noise power, respectively. The quantity $\frac{P}{N_0}$ is referred to as signal-to-noise ratio (SNR).

Secondly, optical fibre is a nonlinear channel, and, thus, determining the exact capacity of the channel is a complex problem. However, assuming that the noise contributions to the system are additive and approximately Gaussian, Eq. (1.1) can be used to obtain insight into the factors that limit the capacity of an optical communication system. They are: (i) the SNR and (ii) the optical bandwidth available to transmit signals. Therefore, it is possible to conclude that in order to increase the capacity of the optical fibre channel two courses of action can be taken: (i) maximise the received SNR, and/or (ii) increase the bandwidth of the transmitted signal. Increasing the SNR can be achieved in two ways, either by reducing the noise added to the signal during transmission or increasing the power of the signal. However, limitations are found in both proposed solutions. The use of amplifiers leads to the addition of a minimum amount of noise to the signal [53], and an increase in used optical power will, in turn, lead to the generation of nonlinear effects.

Bandwidth is directly proportional to the rate of the information transmitted and corresponds to the range of frequencies covered by a modulated signal. In a communication system, the bandwidth available to transmit information is limited by the frequency response of the channel or its subsystems. Fortunately, single-mode optical fibres present a low-loss region, with losses below 0.4 dB/km, which potentially enables transmission of signals over a bandwidth of approximately 50 THz (from 1260 to 1700 nm). In this region, multiplexing techniques, such as WDM, can be employed to use the available bandwidth to its full potential. To date, commercially available EDFAs solutions are only able to support transmission over approximately 9 THz (from 1530 to 1600 nm), corresponding to 20% of the low-loss region of single-mode fibres. Alternative optical amplification solutions have been demonstrated to operate for bandwidths up to approximately 12.5 THz (100 nm) using semiconductor optical amplifiers [50], and up to 17 THz (136 nm) using amplification based on the stimulated Raman scattering effect [54]. However, both proposed solutions have not been demonstrated to work in a long-haul communication system.

1.3 Research problem

The capacity of an optical communication system is related to the physical processes occurring in the communication channel. Key components of the communication channel are optical fibres and optical amplifiers, and, therefore, their properties, namely noise performance, bandwidth and nonlinear effects, determine the capacity of the system. The research described in this thesis focuses on the investigation of ways to increase the capacity of optical communication systems. Three main problems were addressed, which are: (i) the performance in transmission systems of wideband amplification solutions, namely Raman amplification, in terms of the generation of noise and nonlinearites; (ii) the accumulation of nonlinear effects due to the Kerr effect and stimulated Raman scattering, and their detrimental effects as the optical fibre bandwidth is increased; and (iii) the mitigation of fibre nonlinearities experienced in the optical channel using receiver based digital signal processing (DSP) techniques or optical nonlinearity compensation schemes, or both, as a way to increase the received SNR.

Firstly, extending the transmission bandwidth requires new optical amplification solutions. Raman amplification was studied as an alternative to the conventional EDFA to extend the transmission window. The stimulated Raman scattering effect, where energy is transferred from high to low frequencies, can be used to amplify signals in an optical fibre. Raman amplifiers have been shown to provide up to 100 nm amplification bandwidth by using multiple pump wavelengths [8, 55]. Amplification beyond this bandwidth has been shown to be possible by multiplexing the optical signals in the same spectral region as the Raman pump [54]. Additionally, Raman amplifiers can be used to amplify a signal in a *distributed* manner along the transmission fibre with reduced generation of amplified spontaneous emission (ASE) noise compared to EDFAs [56]. In this work, the performance of Raman amplifiers was studied in optical fibre transmission systems. The generation of ASE noise for different Raman amplifier configurations, namely *discrete* and *distributed*, was analysed. Further, the nonlinear distortions induced in the gain fibre of *discrete* Raman amplifiers, and due to modified signal power evolution in *distributed* Raman amplifiers were quantified.

Secondly, the question of how much the optical bandwidth, and thus the system throughput, can potentially be increased, was assessed. The use of larger optical bandwidths has the drawback of increasing the nonlinear effects generated in the transmission fibre. These are hard to quantify using numerical simulation tools, due to the high computation resources needed to numerically solve the Manakov equation, which describes signal propagation in optical fibres. A simpler way to model fibre nonlinearites to predict the performance of a transmission is system, is using the Gaussian noise (GN) model [57]. The GN model describes nonlinear propagation in dispersion uncompensated coherent transmission systems, and it is used to calculate a

noise power spectral density for the fibre nonlinearities. It assumes that the transmitted signal behaves as a Gaussian process, and that nonlinearities can be modelled as additive noise. The validity of this assumptions, and the accuracy of the GN model have been numerically [57] and experimentally [58, 59] confirmed, however, they had not been verified for optical bandwidths larger than 3.5 THz. Another effect that limits the throughput as the optical bandwidth is increased, is the power transfer between co-propagating channels due to stimulated Raman scattering (inter-channel stimulated Raman scattering (ISRS)). ISRS modifies the power profiles of channels transmitted along the fibre, changing this way the strength of the nonlinear distortions experienced by them. To date, the detrimal effect of ISRS in transmisison systems had only been addressed theoretically, using a modified GN model in [60]. This thesis focuses on experimentally studying the growth of nonlinear distortions as the optical bandwidth is increased. These results were used validate the predictions from the GN model in a wideband transmission regime up to 7.3 THz. In additional, the influence of ISRS on the evolution of the signal power, and thus the enhancement of nonlinear distortions, was experimentally evaluated, confirming the validity of the model from [60] for optical bandwidths up to 9 THz.

Finally, different nonlinearity compensation schemes were studied as a way to increase the received SNR. Digital back-propagation (DBP) [61, 62] is a technique where the the fibre propagation effects are digitally reversed. Previously, it had received modest attention in Raman amplified systems, with demonstrations showing limited performance improvementd [63–66]. In the research described in this thesis, DBP was investigated as tool to mitigate the generation of nonlinearities for Raman amplified links, and, additionally, as a way to reduce the impact of ISRS on transmission systems. DBP achieves perfect compensation of the fibre nonlinearities, however, it requires a large computational complexity to process wide optical bandwidths. An alternative to DBP is the use optical phase conjugation (OPC) [67, 68], which is a method to compensate for propagation impairments within the transmission link itself. OPC imposes a set of symmetry conditions on the transmission link to fully compensate for fibre nonlinearities [69], requiring a symmetric signal power profile relative to the conjugation point. This condition is not fulfilled using EDFA in transmission links. For this reason, the effectiveness of this technique has usually been assessed in laboratory enviroments where, for example, complex distributed optical amplification solutions could be used [70]. The benefits from OPC were previously studied in an installed fibre link using dispersion compensating modules [1, 2]. In this work, the performance of OPC in modern dispersion uncompensated links was evaluated using the *National Dark Fibre Infrastructure Service* (NDFIS) installed optical network. Additionally, due to the reduced performance improvement found using OPC in practical systems, a novel method to overcome the OPC symmetry constraints was proposed and studied, which

consists in the use of a Volterra series frequency equaliser (the Volterra-assisted OPC (VAO) method) to compensate for the residual nonlinearity present after transmission. The Volterra series expansion is a tool used to model the behaviour of nonlinear systems, in particular for optical communication systems, the first- and third- order terms represent the linear and nonlinear transfer functions of the system, respectively [71], and can be used to compensate for fibre nonlinearities.

1.4 Thesis outline

The remainder of this thesis is organised as follows. Chapter 2 introduces the theory of optical communication systems together with the physical phenomena impairing signal propagation in optical fibres. Additionally, the theory of Raman amplification and approaches to nonlinearity compensation are presented.

Chapter 3 addresses the advantages of Raman amplification as an alternative to the conventional EDFA. The transmission properties of *discrete* Raman amplifiers are characterised experimentally, and the properties of the *distributed* Raman amplifiers are studied though numerical simulations.

Chapter 4 studies the behaviour of nonlinear effects in transmission systems as the optical bandwidth is increased. The accumulation of nonlinear effects, and the influence of inter-channel stimulated Raman scattering are studied experimentally. Additionally, the merit of increasing the optical bandwidth to obtain higher capacities is theoretically analysed.

Chapter 5 focuses on an alternative approach to nonlinear compensation, namely the use of optical phase conjugation (OPC). The performance of OPC in an installed systems is assessed, and a novel nonlinear compensation method is proposed combining OPC with Volterra equalisation.

A summary of the thesis is given in chapter 6, highlighting the most important findings, and suggestions for future work are proposed.

1.5 Key contributions

The key contributions of the work described in this thesis are listed below:

- In section 3.2, the performance of Raman amplifiers as an alternative for conventional EDFAs was experimentally and numerically studied. Highly nonlinear fibre (HNLF) and dispersion compensating fibre (DCF) were studied as gain media to build *discrete* Raman amplifiers with 70 nm bandwidth. HNFL was shown to result in an improved transmission performance due to the reduced amount of nonlinear distortions generated, compared to DCF.

- For the first time, the benefits of using *distributed* Raman amplifiers together with digital back-propagation (DBP) in long haul transmission systems occupying the full C-band was studied. Using *distributed* Raman amplification and full-field DBP, a 1.3 dB higher gain was found, compared to EDFA. Finally, an increase in the transmission rates of 2 bit per symbol, compared to EDFA, was found using DBP together with *distributed* Raman amplification for the studied back-propagated bandwidths using 256-QAM as modulation format. These results are reported in section 3.3 and published in item **3** from the list of publications.

- Experiments were performed to quantify the growth of nonlinear distortions as a function of the transmitted optical bandwidth. This work corroborated the validity of the Gaussian noise model in a wideband regime up to 7.3 THz. Additionally, the trade-off between an increase in the transmission bandwidth and the growth of nonlinear effects was studied. It was concluded that, to increase the transmission system capacity, using a larger transmission bandwidth overwhelmingly outweighs the benefits of nonlinearity compensation. These results are reported in section 4.1 and published in items **6** and **11** from the list of publications.

- In section 4.2, an experimental study to quantify the interplay between inter-channel Raman scattering and nonlinear distortions was performed using an optical bandwidth of 9 THz. The predictions from the model presented in [60] were validated within the studied transmission bandwidth. These results were published in **13** from the list of publications.

- The merit of increasing the optical bandwidth as a solution to increase the capacity of single mode optical communication system was theoretically studied in section 4.3. The use of a transmission bandwidth of 35 THz was shown to increase the system throughput by a factor of 3.3, compared to state-of-the-art 9 THz bandwidth. For all studied cases increasing the transmission bandwidth resulted in higher throughputs.

- The performance of optical phase conjugation (OPC) as a nonlinearity compensation scheme was studied in section 5.1 using the *National Dark Fibre Infrastructure Service* (NDFIS) optical network, high order modulation formats and large number of channels. A limited nonlinearity compensation gain was found due to the lack of link symmetry properties in dispersion uncompensated EDFA-based links. For the studied link no improvement in the maximum SNR of the system was found when using OPC, results published in **14** from the list of publications.

- In section 5.2, a new nonlinearity compensation scheme that combines OPC and Volterra equalisation was proposed and evaluated. Volterra-assisted OPC was

demonstrated to effectively enhance the nonlinearity compensating capabilities of OPC in EDFA-based links, and SNR gains up to 4.2 dB, compared to either OPC or Volterra equalisation, were found using this scheme for a 1000 km transmission link, results published in **17** and **18** from the list of publications.

1.6 List of publications

The following publications were generated from the research described in this thesis:

Journal papers

1. A.D. Ellis, M. Tan, M.A. Iqbal, M.A.Z. Al-Khateeb, V. Gordienko, **G. Saavedra Mondaca**, S. Fabbri, M.F.C. Stephens, M.E. McCarthy, A. Perentos, I.D. Phillips, D. Lavery, G. Liga, R. Maher, P. Harper, N. Doran, S.K. Turitsyn, S. Sygletos, and P. Bayvel, "4 Tb/s Transmission Reach Enhancement Using 10 $\times$ 400 Gb/s Super-Channels and Polarization Insensitive Dual Band Optical Phase Conjugation," in Journal of Lightwave Technology, vol. 34, no. 8, pp. 1717-1723, April, 15 2016.

2. L. Galdino, D. Semrau, D. Lavery, **G. Saavedra**, C.B. Czegledi, E. Agrell, R.I. Killey, and P. Bayvel, "On the limits of digital back-propagation in the presence of transceiver noise," Opt. Express 25, 4564-4578 (2017)

3. **G. Saavedra**, D. Semrau, L. Galdino, R.I. Killey, and P. Bayvel, "Digital back-propagation for nonlinearity mitigation in distributed Raman amplified links," Opt. Express 25, 5431-5439 (2017)

4. D.J. Elson, **G. Saavedra**, K. Shi, D. Semrau, L. Galdino, R. Killey, B.C. Thomsen, and P. Bayvel, "Investigation of bandwidth loading in optical fibre transmission using amplified spontaneous emission noise," Opt. Express 25, 19529-19537 (2017)

5. D. Semrau, **G. Saavedra**, D. Lavery, R. I. Killey and P. Bayvel, "A Closed-Form Expression to Evaluate Nonlinear Interference in Raman-Amplified Links," in Journal of Lightwave Technology, vol. 35, no. 19, pp. 4316-4328, Oct.1, 1 2017.

6. **G. Saavedra**, M. Tan, D.J. Elson, L. Galdino, D. Semrau, M. A. Iqbal, I.D. Phillips, P. Harper, A.D. Ellis, B.C. Thomsen, D. Lavery, R.I. Killey, and P. Bayvel, "Experimental Analysis of Nonlinear Impairments in Fibre Optic Transmission Systems up to 7.3 THz," in Journal of Lightwave Technology, vol. 35, no. 21, pp. 4809-4816, Nov.1, 1 2017.

Conference proceedings

7. A.D. Ellis, I.D. Phillips, M. Tan, M.F.C. Stephens, M.E. McCarthy, M.A.Z. Al-Kahteeb, M.A. Iqbal, A. Perentos, S. Fabbri, V. Gordienko, D. Lavery, G. Liga, **G. Saavedra**, R. Maher, S. Sygletos, P. Harper, N.J. Doran, P. Bayvel, and S.K. Turitsyn, "Enhanced superchannel transmission using phase conjugation," 2015 European Conference on Optical Communication (ECOC), Valencia, 2015, pp. 1-3.

8. L. Galdino, G. Liga, **G. Saavedra**, D. Ives, R. Maher, A. Alvarado, S. Savory, R. Killey, and P. Bayvel, "Experimental Demonstration of Modulation-Dependent Nonlinear Interference in Optical Fibre Communication," ECOC 2016; 42nd European Conference on Optical Communication, Dusseldorf, Germany, 2016, pp. 950-952.

9. N.A. Shevchenko, T. Xu, D. Semrau, **G. Saavedra**, G. Liga, M. Paskov, L. Galdino, A. Alvarado, R.I. Killey, and P. Bayvel, "Achievable Information Rates Estimation for 100-nm Raman-Amplified Optical Transmission System," ECOC 2016; 42nd European Conference on Optical Communication, Dusseldorf, Germany, 2016, pp. 878-891.

10. D.S. Millar, L. Galdino, R. Maher, M. Pajovic, T. Koike-Akino, **G. Saavedra**, D.J. Elson, D. Lavery, K. Shi, M.S. Erkilinc, E. Sillekens, R.I. Killey, B.C. Thomsen, K. Kojima, K. Parsons, and P. Bayvel, "A simplified dual-carrier DP-64QAM 1 Tb/s transceiver," 2017 Optical Fiber Communications Conference and Exhibition (OFC), Los Angeles, CA, 2017, paper M3D.2.

11. **G. Saavedra**, M. Tan, D.J. Elson, L. Galdino, D. Semrau, M.A. Iqbal, I.D. Phillips, P. Harper, N. Mac Suibhne, A.D. Ellis, D. Lavery, B.C. Thomsen, R.I. Killey, and P. Bayvel, "Experimental investigation of nonlinear signal distortions in ultra-wideband transmission systems," 2017 Optical Fiber Communications Conference and Exhibition (OFC), Los Angeles, CA, 2017, paper W1G.1.

12. L. Galdino, **G. Saavedra**, D. Semrau, D. J. Elson, D. Lavery, M. Tan, M. A. Iqbal, P. Harper, R. I. Killey, and P. Bayvel, "Digital Back-Propagation Performance in Wideband Optical Fibre Transmission Systems," ECOC 2017; 43rd European Conference on Optical Communication, Gothenburg, Sweden, 2017, paper Th.2.E.

13. **G. Saavedra**, D. Semrau, M. Tan, Md. A. Iqbal, D. J. Elson, L. Galdino, P. Harper, R. I. Killey, and P. Bayvel, "Inter-channel Stimulated Raman Scattering and its Impact in Wideband Transmission Systems," 2018 Optical Fiber Communications Conference and Exhibition (OFC), San Diego, CA, 2018, paper Th1C.3

14. **G. Saavedra**,Y. Sun, K. R. H. Bottrill, L. Galdino, F. Parmigiani, Z. Liu, D.J. Richardson, P. Petropoulos, R. I. Killey, and P. Bayvel, "Optical Phase Conjugation in Installed Optical Networks," 2018 Optical Fiber Communications Conference and Exhibition (OFC), San Diego, CA, 2018, paper W3E.2.

15. L. Galdino, D. Lavery, Z. Liu, K. Balakier, E. Sillekens, D. Elson, **G. Saavedra**, R. Killey, and P. Bayvel, "The Trade-Off between Tranceiver Capacity and Symbol Rate," 2018 Optical Fiber Communications Conference and Exhibition (OFC), San Diego, CA, 2018, paper W1B.4.

16. Z. Liu, T. Xu, **G. Saavedra**, and P. Bayvel "448-Gb/s PAM4 Transmission Over 300-km SMF-28 Without Dispersion Compensation Fiber ," 2018 Optical Fiber Communications Conference and Exhibition (OFC), San Diego, CA, 2018, paper W1J.6.

17. G. Liga, **G. Saavedra**, and P. Bayvel , "Combining Optical Phase Conjugation and Volterra Equalisation: a Novel Nonlinearity Compensation Scheme," ECOC 2018; 44th European Conference on Optical Communication, Rome, Italy, 2018, paper Tu1F.4.

Submitted papers

18. **G. Saavedra**, G. Liga , and P. Bayvel , "Volterra-assisted Optical Phase Conjugation: a Hybrid Optical-Digital Scheme For Fibre Nonlinearity Compensation," submitted to Journal of Lightwave Technology.

2

Theory and literature review

OPTICAL FIBRES currently form the underlying structure of our communications networks. They act as the communication channel and can be found in networks connecting servers inside a data centre to cities separated by thousands of kilometres. To utilise them to their full potential, it is essential to understand their working principles and the physical phenomena that govern the propagation of signals through them. This chapter reviews the concepts introduced in chapter 1 in addition to the linear and nonlinear impairments induced during propagation in optical fibres, and different techniques that allow for their mitigation.

2.1 Information theory

Since the revolutionary work presented by Shannon in [52], information theory has been used to understand and design communication systems. Several new concepts were introduced in the aforementioned publication, some of which have high relevance for the work presented in this thesis.

2.1.1 Mutual information

Mutual information (MI) is a measurement of how much information from a message generated by the transmitter can be obtained by the receiver in a communication system. Consider that the transmitted and received signals are represented by the random

variables X and Y, respectively. Then, the mutual information is given by [52]:

$$I(X;Y) = \iint p_{X,Y}(x,y) \log_2 \left(\frac{p_{X,Y}(x,y)}{p_X(x) p_Y(y)} \right), \tag{2.1}$$

where $p_{X,Y}(x,y)$ is the joint probability density function of X and Y, and $p_X(x)$ and $p_Y(y)$ are the marginal probability density functions of X and Y respectively. MI represents the maximum rate at which a communication system can reliably transmit information using an optimal coded modulation scheme, and is measured in bits per symbol. MI has recently been proposed to characterise optical communication systems and their achievable rates [72–74], and is used as a system performance metric in sections 3.3 and 4.1 of this thesis.

2.1.2 Channel capacity

As mentioned in chapter 1, the capacity of a communication channel is defined as the maximum rate at which reliable communication can be achieved. The channel capacity corresponds, therefore, to the maximum MI, maximised over all possible inputs [52].

$$C = \max_{p(x)} I(X;Y). \tag{2.2}$$

The capacity of a communication channel is measured in bits per symbol. In a channel affected by noise, the capacity is determined by the previously defined Eq. (1.1).

2.1.3 Throughput

The throughput of a communication system is the rate at which information is successfully transmitted over the communication channel. The system throughput is measured in bits per second and is defined as:

$$T = R_s R_c \log_2 M, \tag{2.3}$$

where R_s is the symbol rate, R_c is the code rate defined as $R_c \triangleq k/n$, with message length k and coded block length n. $\log_2 M$ represents the nominal spectral efficiency, or the amount of information per bandwidth unit in bit/s/Hz, of the system. The symbol rate corresponds to the rate at which the transmitter is able to generate and transmit symbols and is measured in Baud. The code rate is the proportion of useful information in a coded message using a FEC code.

In the same way that the channel capacity is an upper bound for the MI, the product of the symbol rate and the MI corresponds to an upper bound for the system throughput. The throughput of optical fibre communication systems in the presence of nonlinear

effects is studied in sections 4.1 and 4.3.

2.2 Advanced optical communication systems

Optical fibres potentially offer a large bandwidth with low attenuation losses. To date, researchers are focused on developing transceivers capable of operating at rates in excess of 100 GBd [75–78], which corresponds to only 2% of the bandwidth available in C-band. For this reason, different techniques are used to benefit from the available bandwidth and allow for high capacity transmission systems. The use of individual channels with a different optical carrier frequency results in an increase of the used optical bandwidth, while advanced modulation formats increase the amount of information carried per unit bandwidth.

2.2.1 Multichannel system

Optical fibres offer the possibility of transmitting multiple channels at the same time by multiplexing them. This can be done either in the time or frequency domain. The technique that employs different optical carrier frequencies, or wavelengths, to allocate separate channels is called wavelength division multiplexing (WDM). Each carrier is modulated using an individual and independent bit stream and later combined into the same fibre for transmission. At the receiver the channels are either demultiplexed or filtered out and detected individually. The WDM technique allows one to take advantage of the large bandwidth available in the previously mentioned transmission windows. The total number of carrier frequencies is determined by the frequency spacing between the channels and the available optical amplifier bandwidth. Standard erbium doped fibre amplifiers can be used in the optical C-band and, with some modifications, in the L-band, with a total combined bandwidth of approximately 9 THz. Currently, the international telecommunication union (ITU) standard G.649 defines a frequency grid as "*a reference set of frequencies used to denote allowed nominal central frequencies that may be used to for defining applications*" [79]. The frequency grids are anchored to 193.1 THz and current steps in channel spacing for fixed grids have historically evolved by sub-dividing the 100 GHz grid by factors of two. This way, frequency grids ranging from 12.5 GHz to 100 GHz are employed.

2.2.1.1 Nyquist spaced WDM

To increase a systems' spectral efficiency, or the information transmitted within a given bandwidth, one can reduce the frequency spacing between the transmitted WDM channels. In order to do this, and, avoid interference between adjacent channels in frequency, and transmitted symbols in time, spectral and temporal orthogonality needs

to be fulfilled. The use of *sinc* shaped pulses satisfies the Nyquist criteria of inter-symbol interference creating orthogonal signals in the time domain. Additionally, the spectrum of a *sinc* pulse is a square which allows one to reduce the spacing between adjacent channels in the frequency domain. In practical cases it is only possible to approximate a perfectly rectangular filter in the frequency domain, and studies have been performed evaluating the performance of optical, electrical and digital filters to perform this action: these concluded that filtering in the digital domain provides the optimal performance [80]. Typically, root raised cosine is used at the transmitter and receiver to perform the digital filtering. The number of channels used in optical systems is determined by the symbol rate and the spacing between them. Up to date experimental demonstrations using 295 channels have been performed using a symbol rate of 32.6 GBd and a spacing of 33 GHz [49] using a bandwidth of 9.74 THz. The total throughput for the experiment reported in [49] was 70.46 Tb/s over a distance of 6,970 km.

2.2.1.2 Polarisation Multiplexing

Single mode optical fibres support the propagation of two signals at the same frequency on orthogonal polarisations. When this technique is used to transmit two independent signals it is known as polarisation multiplexing (PM) and allows one to double the amount of information being transmitted through an optical fibre. Additionally, different polarisation states of the optical signal can be used to encode information. This modulation format is known as polarisation shift keying (Pol-SK); however, due to the need for active polarisation management at the receiver, Pol-SK has received little attention over the years [81].

Due to random polarisations drifts during transmission, PM is typically used in coherent system that allow the tracking of the polarisation rotations using DSP [82]. Equalisation algorithms such as the constant modulus algorithm (CMA) allow one to approximate the inverse of the channel response to recover the original polarisation state of the signal [83]. PM is used in the work described in this thesis to maximise the amount of information transmitted by the systems under study. Simulations neglected effect of polarisation mode dispersion (PMD) to focus on different transmission effects; and experimental work used the CMA algorithm to recover the polarisation states.

2.2.2 Advanced modulation formats

Aided by the use of coherent receivers and DSP, the implementation of more efficient modulation schemes was performed. The electrical field of an optical carrier is defined as follows [82]:

$$E(t) = Re\left[Ae^{(i\phi - i\omega_0 t)}\right], \tag{2.4}$$

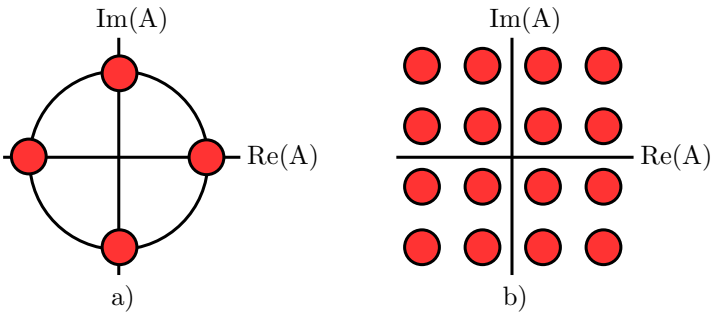

Figure 2.1: Example of advanced modulation formats used in optical fibre communication systems, a) QPSK and b) 16-QAM.

where A is the amplitude, ϕ is the phase and ω_0 is the carrier frequency. By using both the amplitude and the phase of an optical carrier to encode information it is possible to increase the spectral efficiency of transmission systems, compared to amplitude modulated systems.

Of particular interest for coherent optical communication systems are quadrature amplitude modulation (QAM) formats. To generate QAM formats, an optical carrier is split into two waves, out of phase from each other by 90°, and modulated in amplitude before being recombined. A constellation diagram is used to represent modulated QAM waveforms, and it displays the signal as a XY-plane diagram in the complex plane at symbol sampling instants. The X and Y axis of the diagram represents the in-phase and in-quadrature carriers, respectively, that form the QAM waveform. Fig. 2.1 shows examples of two frequently used modulation formats in optical communication system, QPSK and 16-QAM.

A QAM constellation formed by a total of M symbols, carries $\log_2(M)$ bits of information per symbol, thereby increasing the number of symbols contained in the modulation format leads to improvements in spectral efficiency.

In experiments and simulations performed during the research reported in this thesis different modulation formats were used. Experimental demonstrations in chapters 4 and 5 employed higher order modulation formats such as 64- and 256-QAM to maximise the throughput of the transmission system. On the other hand, simulation work from chapters 3 and 5 focused on physical phenomena experienced during fibre propagation, therefore 16-QAM was used for this purpose.

2.3 Impairments of the optical fibre channel

2.3.1 Chromatic dispersion

In an optical fibre different frequency components travel at different group velocities. This effect is known as group velocity dispersion (GVD), and it affects a pulse being

propagated in an optical fibre by temporally spreading it, since different spectral components reach the destination at different times. If $\Delta\omega$ is the spectral width of an optical pulse, after travelling along a fibre length of L_s, the total pulse broadening is given by [82]:

$$\Delta T = \frac{d}{d\omega}\left(\frac{L_s}{v_g}\right)\Delta\omega = L_s\frac{d^2\beta}{d\omega^2}\Delta\omega = L_S\beta_2\Delta\omega, \tag{2.5}$$

where v_g is the group velocity, and the parameter β_2 is known as the GVD parameter. Usually, optical fibre manufacturers use a different parameter, called the *dispersion parameter D* whose physical units are ps·km^{-1}·nm^{-1}, and is related to β_2 as follows:

$$D = -\frac{2\pi c}{\lambda^2}\beta_2, \tag{2.6}$$

where λ is the wavelength of the optical wave and c is speed of light in vacuum. This way, the evolution of a signal travelling through an optical fibre with complex amplitude $A(z,t)$ in the presence of chromatic dispersion is given by

$$\frac{dA(z,t)}{dz} = -i\frac{\beta_2}{2}\frac{\partial^2 A(z,t)}{\partial t^2}. \tag{2.7}$$

This equation can be solved analytically using a Fourier transform, and the frequency domain transfer function is then given by:

$$\tilde{A}(z,\omega) = \tilde{A}(0,\omega)e^{i\frac{\beta_2}{2}\omega^2 z}, \tag{2.8}$$

where $\tilde{A}(z,\omega)$ is the Fourier transform of $A(z,t)$. Dispersion can cause inter-symbol interference if the broadening of the pulse is larger than the assigned time slot for it, and eventually limit the propagation distance or the data rate. For standard single-mode fibre used in telecommunication, the dispersion parameter D has a value of about 16 ps·km^{-1}·nm^{-1} at $\lambda = 1550$ nm. To minimise the effects of chromatic dispersion, different fibre types have been developed. The development of dispersion shifted fibre (DSF) was realised by tailoring the core-cladding profile to shift the zero dispersion wavelength from the 1300 nm region to 1550 nm. However DSF was not suitable for use in multichannel systems, due to the enhancement of nonlinear effects such as four-wave mixing. A different approach to manage dispersion in optical fibres is to compensate for the accumulated dispersion after the signal has propagated. For this purpose fibres with negative dispersion values were developed. This way, a fibre based optical solution to the dispersion problem emerged. The use of dispersion maps was introduced, where the accumulated dispersion of a fibre span was compensated by a dispersion compensating fibre (DCF) module. DCF, however, showed a high attenuation due to its long length of several kilometres. The introduction of the coherent receiver and DSP techniques allowed one to compensate for the total link dispersion at the receiver. By using the

inverse of Eq. (2.8), a digital filter can be realised to compensate for the effects of dispersion on the received signal [83].

Compensation of chromatic dispersion impairments is necessary in every optical communication system. It allows for the detection of signals without inter-symbol interference, which is critical to successfully demodulate and decode the transmitted data. The use of uncompensated transmission links, where dispersion is compensated digitally at the receiver, has offered several benefits over dispersion managed systems. The amplifier design has become simpler and cheaper without the need to support additional losses from the DCF modules. Additionally, dispersion uncompensated systems are less affected by nonlinear distortions due to the temporal spreading of the transmitted pulses.

2.3.2 Attenuation

When light is propagated through a medium, the intensity of the optical field is attenuated. The power of the optical signal is related to the attenuation of the medium as follows [82]:

$$\frac{dP}{dz} = -\alpha P, \tag{2.9}$$

where α is known as the attenuation coefficient of the medium. It is possible to solve this differential equation to find the optical power after propagation over a fibre of length L_s, and is given by:

$$P_{\text{out}} = P_{\text{in}} e^{-\alpha L_s}, \tag{2.10}$$

where P_{out} and P_{in} represent optical power after and before propagation. In optical fibres, the attenuation coefficient depends on the wavelength of the signal and the main physical processes responsible for it are Rayleigh scattering and infra-red absorption. A lower limit on attenuation (α_T) can be calculated from [84]:

$$\alpha_T = \alpha_R + \alpha_{IR}, \tag{2.11}$$

where α_R and α_{IR} are the contributions from Rayleigh scattering and infra-red absorption respectively and are defined as:

$$\alpha_R = \frac{A}{\lambda^4}, \tag{2.12}$$

$$\alpha_{IR} = B exp\left(J\lambda\right), \tag{2.13}$$

where A, B and J are different constants that depend on the fibre type. For standard Single Mode Fibre (SMF) they are: $A = 8.5 \times 10^{-25}$, $B = 4.6 \times 10^{-14}$ and $J = 1.72 \times 10^7$ [85].

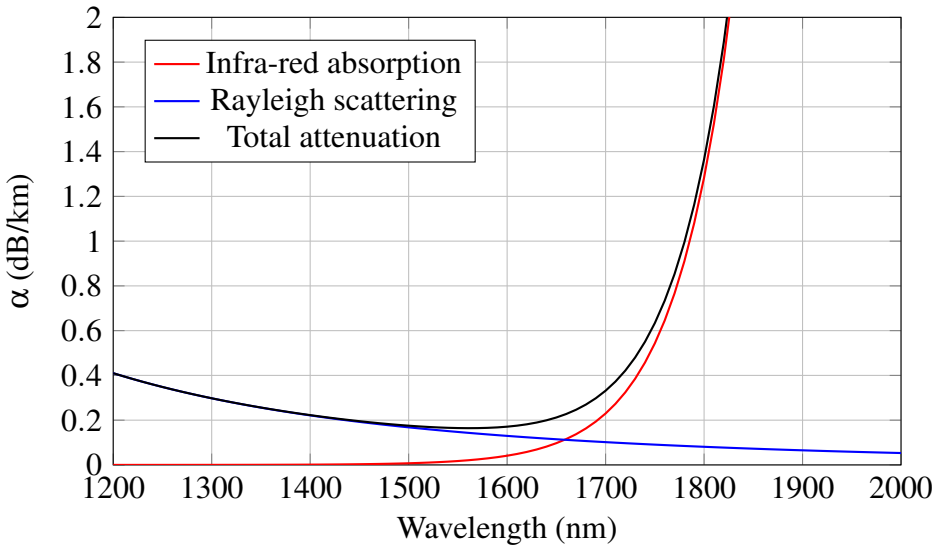

Figure 2.2: Fibre attenuation coefficient (α) as a function of optical wavelength.

In Fig. 2.2, the attenuation coefficient as a function of wavelength is illustrated for an optical fibre according to Eq. (2.11). Of special interest is the region between 1300 and 1700 nm, that shows the lowest loss for single mode transmission, and corresponds to a total bandwidth of approximately 50 THz.

Recent advances in fibre fabrication made possible to reduce the attenuation coefficient of single mode fibres. The use of pure silica core together with fluorine as a cladding dopant ensured the reduction of compositional Rayleigh scattering. To date, the lowest attenuation coefficient reported is of 0.1419 dB/km at 1560 nm [86]. Reduction of the attenuation coefficient is critical for long haul and submarine systems, it allows to increase the repeater spacing or reduce the output power requirements of the optical amplifiers.

To overcome attenuation in optical fibres transmission, optical amplifiers are employed. They are optical devices capable of amplifying the amplitude of an optical signal. The amplification process, however, generates amplified spontaneous emission (ASE) that corresponds to incoherent amplified light produced by the spontaneous emission process and is added to the optical signal as noise during amplification.

2.3.3 Nonlinear effects

The core of an optical fibre, the section through which the light is guided, has a diameter of 8 μm for standard single mode fibres. Due to this small size and the low attenuation of optical fibres, the light confined in it has high intensity, leading to nonlinear effects that can be divided into three categories:

- **Stimulated light scattering:** is the process where light is scattered generating a new lower energy frequency component. Two different scattering processes can be

distinguished as *Brillouin* and *Raman*, the main difference between them being the frequency shift experienced by the newly generated photons. Brillouin scattering has a frequency shift of approximately 10 GHz, while Raman scattered photons experience a shift of approximately 13 THz. The fundamental difference between both nonlinear scattering phenomena is the nature of the phonons that participate in the process: while acoustic phonons participate in Brillouin scattering, optical phonons are responsible for Raman scattering. This also determines the frequency shift experienced in both processes. When the intensity of the incident light field exceeds a threshold value, both processes become stimulated. Both scattering processes can be detrimental for communication systems as they result in a loss of optical power for signals propagating through optical fibres.

- **Nonlinear phase modulation:** when the intensity of an optical field confined in an optical fibre is high, the refractive index of the medium is modified due to the Kerr effect. This effect causes an intensity dependence in the propagation constant as follows [82]

$$\beta' = \beta + \gamma P, \tag{2.14}$$

where $\gamma = 2\pi n_2/(A_{\text{eff}}\lambda)$ is known as the nonlinear coefficient, n_2 and A_{eff} correspond to the nonlinear refractive index and effective area of the optical fibre respectively. Effective area is defined as $A_{\text{eff}} = \pi w$, where w is the radius of the optical field, also known as the *spot size*. Usually for SMF, $\gamma \approx 1$ W^{-1}km^{-1}. When an optical wave is propagated through an optical fibre β' will cause a nonlinear phase shift. If the phase shift occurs due to the power of the channel on itself the effect is known as self phase modulation (SPM); on the other hand, if the effect is caused due the intensity of adjacent channels it is known a cross-phase modulation (XPM). Nonlinear phase modulation will induce phase distortions into signals being transmitted through the fibre channel as the power is increased. Nonlinear phase modulation is translated into amplitude noise due to the interplay between Kerr nonlinearity and chromatic dispersion, thus limiting the performance of transmission systems.

- **Parametric processes:** Third order parametric processes can be observed in optical fibres, involving nonlinear interactions between four optical waves. Phenomena such as third-harmonic generation, four wave mixing (FWM) and parametric amplification fall into this category. FWM has been extensively studied in optical fibres due to its efficiency to generate new wavelengths. When 3 optical waves of frequencies ω_1, ω_2 and ω_3 propagate through an optical fibre, a new wave of frequency ω_4 given by:

$$\omega_4 = \omega_1 \pm \omega_2 \pm \omega_3 \tag{2.15}$$

is generated. In practice, most of the combinations of frequencies are not generated due to phase matching conditions; however the combination $\omega_4 = \omega_1 + \omega_2 - \omega_3$ becomes nearly phase matched at wavelengths close to the zero dispersion point. FWM impacts communication systems by transferring power from signal waves to new frequency components, and increasing crosstalk between channels. Nonetheless FWM has several applications in optical communications systems, such as wavelength conversion or the generation of optical phase-conjugated signals.

The increase of the effective area of optical fibres has allowed the reduction of nonlinear effects and the use of higher signal powers. Commercially available optical fibres such as Corning® Vascade® offer different effective areas for different applications, from 27 μm^2 for negative dispersion fibres up to 150 μm^2 for long-haul systems.

2.3.4 Propagation of pulses through optical fibres

2.3.4.1 Nonlinear Schrödinger equation

The mathematical description of the propagation effects in an optical fibre is usually performed by including the different effects into one single equation known as the nonlinear Schrödinger equation (NLSE) [82]. The NLSE for fibre propagation is given by:

$$\frac{dA}{dz} = -\frac{\alpha}{2}A - i\frac{\beta_2}{2}\frac{\partial^2 A}{\partial t^2} + i\gamma|A|^2 A, \tag{2.16}$$

where the slowly-varying complex envelope of the optical field $A(z,t)$ is notated as A. This equation includes all the previously mentioned propagation impairments and needs to be solved numerically in order to design or evaluate system performance. Some simplifying assumptions are required for the derivation of Eq. (2.16). In particular, one uses the slowly varying envelope assumption [82], where the central frequency of the carrier (ω_0) is assumed to be much greater than the signal bandwidth ($\Delta\omega$), such that $\Delta\omega/\omega_0 << 1$. The use of carrier frequencies of hundreds of THz makes this assumption valid for pulses as short as 0.1 ps. The NLSE describes the evolution of a single polarisation signal; however it does not account for the effects of fibre birefringence. Birefringence is the property of a material whose refractive index presents a dependence on polarisation and propagation direction of light. The use of the NLSE for optical fibre communication systems therefore leads to a description of the signal propagation where the polarisation-dependent effects, such as PMD, are ignored. In order to study the polarisation-dependent effects, a vectorial form of Eq. (2.16) is needed, known as

the coupled NLSE [87] given by:

$$\begin{aligned}\frac{dA_X}{dz} &= -\frac{\alpha}{2}A_X - i\frac{\beta_2}{2}\frac{\partial^2 A_X}{\partial t^2} + i\gamma\left(|A_X|^2 + \frac{2}{3}|A_Y|^2\right)A_X + \frac{i\gamma}{3}A_X^* A_Y^2 \exp(-2i\Delta\beta z)\\ \frac{dA_Y}{dz} &= -\frac{\alpha}{2}A_Y - i\frac{\beta_2}{2}\frac{\partial^2 A_Y}{\partial t^2} + i\gamma\left(|A_Y|^2 + \frac{2}{3}|A_X|^2\right)A_Y + \frac{i\gamma}{3}A_Y^* A_X^2 \exp(-2i\Delta\beta z),\end{aligned} \tag{2.17}$$

where A_X and A_Y are the complex amplitudes of the X and Y polarisations, and $\Delta\beta$ corresponds to the phase mismatch between both polarisations.

2.3.4.2 Manakov equation

Where the effect of birefringence cannot be ignored, as in transmission system using more than a single polarisation state to transmit information, the Manakov equation should be used. Optical fibre communication systems typically present birefringence beat lengths, transmission distance after which a 2π phase delay between polarisation is found, in the range of 10–100 m, and rapid changes in the orientation of the birefringence of 0.3–300 m [88]. Due to the rapidly varying nature of fibre birefringence, the Manakov equation is obtained from the coupled NLSE [89] by averaging the nonlinear mixing between states of polarisation over the Poincaré sphere. From [89], the Manakov equation is given by :

$$\begin{aligned}\frac{dA_X}{dz} &= -\frac{\alpha}{2}A_X - i\frac{\beta_2}{2}\frac{\partial^2 A_X}{\partial t^2} + \frac{8}{9}i\gamma\left(|A_X|^2 + |A_Y|^2\right)A_X\\ \frac{dA_Y}{dz} &= -\frac{\alpha}{2}A_Y - i\frac{\beta_2}{2}\frac{\partial^2 A_Y}{\partial t^2} + \frac{8}{9}i\gamma\left(|A_Y|^2 + |A_X|^2\right)A_Y.\end{aligned} \tag{2.18}$$

It is worth noting that the coupled NLSE and the Manakov equation converge to the same results, as the spatial resolution used to solve them is increased (or as the step size used is decreased).

2.3.4.3 Split step Fourier method

Both the NLSE and the Manakov equations are nonlinear partial differential equations that generally do not have analytical solutions. In order to solve these equations, a numerical approach is required. One of the methods that is used to numerically solve these equations is the split-step Fourier method (SSFM) [82]. To explain the SSFM, the NLSE is used as an example. Eq. 2.16 can be conveniently rewritten as follows:

$$\frac{dA}{dz} = (\hat{D} + \hat{N})A, \tag{2.19}$$

where $\hat{D}$ is the differential operator that accounts for loss and dispersion (linear effects), and $\hat{N}$ is the operator that accounts for fibre nonlinearities. The operators are defined as:

$$\begin{aligned} \hat{D} &= -\frac{\alpha}{2} - i\frac{\beta_2}{2}\frac{\partial^2}{\partial t^2}, \\ \hat{N} &= i\gamma|A|^2. \end{aligned} \tag{2.20}$$

The SSFM obtains an approximate solution to Eq. (2.16) by assuming that in the propagation of the optical field over a small distance, both linear and nonlinear effects act independently. Therefore, the transmission from a distance z to $z+h$ is given by:

$$A(z+h,t) = \exp(h\hat{D})\exp(h\hat{N})A(z,t), \tag{2.21}$$

where the linear operator $\exp(h\hat{D})$ is evaluated in the frequency domain using the Fourier transform operator. As mentioned, the SSFM obtains an approximate solution to the propagation equation that is in general valid as long as the assumptions used for the derivation of the propagation equation hold.

2.3.5 Estimating system performance in the presence of nonlinearites

To evaluate the performance of an optical transmission system, numerical simulations are required to solve Eq. (2.16). This is the most accurate option to analyse the waveforms that are transmitted through a fibre channel; it is, however, also the most complex one. Due to the recursive nature of the SSFM and the necessity of a high spatial resolution to correctly approximate the solution of Eq. (2.16), alternative approaches were developed to evaluate the system performance. The introduction of the coherent receiver and the possibility of using DSP to compensate for fibre impairments, such as chromatic dispersion [83], lead to the possibility of deploying dispersion uncompensated transmission links. Together with greatly simplifying link design, dispersion uncompensated transmission links opened the possibility to assess system performance analysis using relatively simple analytical models [71, 90–92]. Among them, the Gaussian noise (GN) model [90] has gained popularity due to its simplicity and accuracy. The GN model treats nonlinear effects as a perturbation to the signal and it allows one to estimate a noise variance arising from nonlinear distortions. The system performance can be determined using:

$$SNR = \frac{P_{\text{ch}}}{P_{\text{ASE}} + P_{\text{NLI}}}, \tag{2.22}$$

where P_{ch} is the transmitted signal power, P_{ASE} and P_{NLI} are the noise powers from ASE and nonlinearity, respectively. Key assumptions from the GN model are that the

signal behaves statistically as a Gaussian process, an assumption partly achieved in an uncompensated transmission link due to the effect of dispersion on the transmitted signal, and that nonlinear distortions manifest themselves as additive Gaussian noise. This is justified due to the generation of new out-of-phase frequency components within the bandwidth of interest arising from nonlinear interactions. The new frequency components effectively *interfere* with the signal of interest and therefore, the noise variance arising from nonlinear distortions is usually termed nonlinear interference (NLI) noise in the GN model literature.

From [90], the power spectral density (PSD) of the NLI noise at the end of a transmission link can be expressed as:

$$\begin{aligned} G_{\mathrm{NLI}}(\omega) &= \frac{16}{27}\gamma^2 L_{\mathrm{eff}}^2 \\ &\cdot \int_{-\infty}^{\infty}\int_{-\infty}^{\infty} G_{\mathrm{WDM}}(\omega_1) G_{\mathrm{WDM}}(\omega_2) G_{\mathrm{WDM}}(\omega_1+\omega_2-\omega) \\ &\cdot \rho(\omega_1,\omega_2,\omega)\cdot\chi(\omega_1,\omega_2,\omega) d\omega_2 d\omega_1, \end{aligned} \tag{2.23}$$

where L_{eff} is the effective nonlinear length defined as $L_{\mathrm{eff}} = \frac{1-\exp(-\alpha L_s)}{\alpha}$ for a fibre span of length L_s, $G_{\mathrm{WDM}}(\omega)$ is the PSD of the transmitted signal, $\rho(\omega_1,\omega_2,\omega)$ is the normalised FWM efficiency and $\chi(\omega_1,\omega_2,\omega)$ is the phased-array factor responsible for the coherent accumulation of NLI noise with distance.

The PSD of an arbitrary signal $s(t)$ is defined as [93]:

$$S(\omega) = \lim_{T\to\infty} \mathbf{E}\left[|\hat{s}(\omega)|^2\right], \tag{2.24}$$

where $\hat{s}(\omega)$ is the Fourier transform of the signal $s(t)$ over the finite interval $[0,T]$ and $\mathbf{E}$ denotes the expected value.

Assuming lumped optical amplification in the link, the FWM efficiency and phased-array factor are defined as:

$$\rho(\omega_1,\omega_2,\omega) = \left|\frac{1-e^{-2\alpha L_s} e^{j\beta_2 L_s(\omega_1-\omega)(\omega_2-\omega)}}{2\alpha - j\beta_2(\omega_1-\omega)(\omega_2-\omega)}\right|^2 \tag{2.25}$$

$$\chi(\omega_1,\omega_2,\omega) = \frac{\sin^2(N_s\beta_2 L_s(\omega_1-\omega)(\omega_2-\omega)/2)}{\sin^2(\beta_2 L_s(\omega_1-\omega)(\omega_2-\omega)/2)}. \tag{2.26}$$

2.4 Stimulated Raman scattering

Stimulated Raman scattering (SRS) is an inelastic process where light is scattered from the molecules of a medium. It was originally observed in 1928 [94] in liquids and gases, and in the second half of the century this nonlinear phenomena was achieved in

optical fibres [95] and used to amplify optical signals. Since then, stimulated Raman scattering has been a potential alternative for optical amplification of signals in optical fibres. Raman amplifiers offer attractive properties, such as the potential to design broadband amplifiers and improved noise characteristic when used as a distributed amplifier, compared to lumped optical amplification solutions such as EDFAs [56].

2.4.1 Single pump amplification

Consider, for the sake of simplicity, the case where a monochromatic signal is amplified by a continuous monochromatic pump source. In this case, signal amplification in an optical fibre by stimulated Raman scattering is governed by the following set of coupled equations [96]:

$$\frac{dP_s}{dz} = -\alpha_s P_s + \left(\frac{g_R}{A_{\text{eff}}}\right) P_p P_s \tag{2.27}$$

$$\pm \frac{dP_p}{dz} = -\alpha_p P_p - \left(\frac{\omega_p}{\omega_s}\right)\left(\frac{g_R}{A_{\text{eff}}}\right) P_s P_p, \tag{2.28}$$

where P is optical power, α is previously defined, ω is the optical frequency of a wave and the subscripts p and s represent pump and signal frequencies, respectively. g_R is the Raman gain coefficient, which depends on the optical fibre properties. The $\pm$ sign represents a co- and counter-propagating pump wave, respectively. By neglecting depletion of the pump due to signal interactions (the second term of Eq. (2.28), Eq. (2.28) can easily be integrated for the copropagating case to obtain: $P_p(z) = P_p(0)\exp(-\alpha_p z)$; and by replacing this result in Eq. (2.27) the output power of a fibre of length L_s is given by:

$$P_s(L) = P_s(0)\exp\left(\frac{g_R P_p(0) L_{\text{eff,amp}}}{A_{eff}} - \alpha_s L_s\right), \tag{2.29}$$

where $L_{\text{eff,amp}}$ is the effective amplification length of the fibre given by $L_{\text{eff,amp}} = \frac{1-\exp(-\alpha_p z)}{\alpha_p}$. This represents the effective length where signal amplifications is obtained, which is reduced from the total fibre length due to pump attenuation.

Once the pump power reaches the Raman threshold, power is rapidly transferred from pump to the longer wavelength wave, called Stokes wave, almost in an exponential manner [96]. The Raman threshold is defined as the input pump power at which the power of the Stokes wave becomes equal to the pump power at the fibre output.

2.4.2 Noise performance of Raman amplifiers

There are three major noise sources when considering a Raman amplified signal propagating through an optical fibre. These are: (i) spontaneous Raman scattering, (ii) Rayleigh Backscattering and (iii) relative intensity noise (RIN) transfer from pump

to signal. The first source, and typically the most important, is also referred to as ASE noise. The spontaneous scattered photons, generated with random phase and direction, are added to the amplified signal as noise [56]. The amount of ASE generated depends on the phonon population in the vibrational state, which in turn depends on the amplifier temperature. Considering the signal evolution including the noise generated by spontaneous scattering using the NLSE and neglecting, for simplicity, the dispersive and nonlinear terms, Eq. (2.16) becomes:

$$\frac{dA}{dz} = \frac{1}{2} g_o(z) A - \frac{\alpha_s}{2} A + f_n(z,t), \tag{2.30}$$

where $g_o(z) = \frac{g_R P_p(z)}{a_p}$ is the gain coefficient across the fibre, and $f_n(z,t)$ is the ASE noise added. Since the Raman scattering events are time and space independent of each other, it is possible to model this process as a Gaussian stochastic process [82], with zero average and a second moment given by:

$$\langle f_n^*(z,t) f_n(z',t') \rangle = n_{sp} h \frac{\omega_0}{2\pi} \delta(z-z') \delta(t-t'), \tag{2.31}$$

where $h\frac{\omega_0}{2\pi}$ is the photon energy and n_{sp} is the spontaneous emission factor. The two delta functions in Eq. (2.31) mathematically represent the independent emissions of photons in time and space. Using Eq. (2.31), it is possible to define the PSD of the ASE noise as follows:

$$S_{\mathrm{ASE}}(\omega) = n_{sp} h \frac{\omega_0}{2\pi} G(L_s, \omega) \int_0^{L_s} \frac{P_p(z)}{G(z,\omega)} dz, \tag{2.32}$$

where $G(z,\omega)$ is the amplification factor defined as $G(z,\omega) = \exp\left(\int_0^z g_R(\omega) \frac{P_p(z')}{a_p} dz'\right)$ The noise is constant at all frequencies, as in the case of AWGN, but in practice it is limited to the amplifier bandwidth, and can be reduced by placing an optical filter at the amplifier output. From Eq. (2.32) it is possible to see that the ASE is generated along the fibre used to achieve amplification.

2.4.3 Types of Raman amplifiers

Depending on the medium chosen to achieve optical amplification through the Raman effect, there are two different amplifier configurations, namely *discrete* Raman amplifiers and *distributed* Raman amplifiers. Both configurations amplify the signal following the same physical process, and present the same properties regarding amplifier bandwidth and noise generation. They are shown in Fig. 2.3.

A *discrete* Raman amplifier, see Fig. 2.3 a), is the one that utilises a dedicated optical fibre as the amplification medium. A high power pump is injected into a dedicated

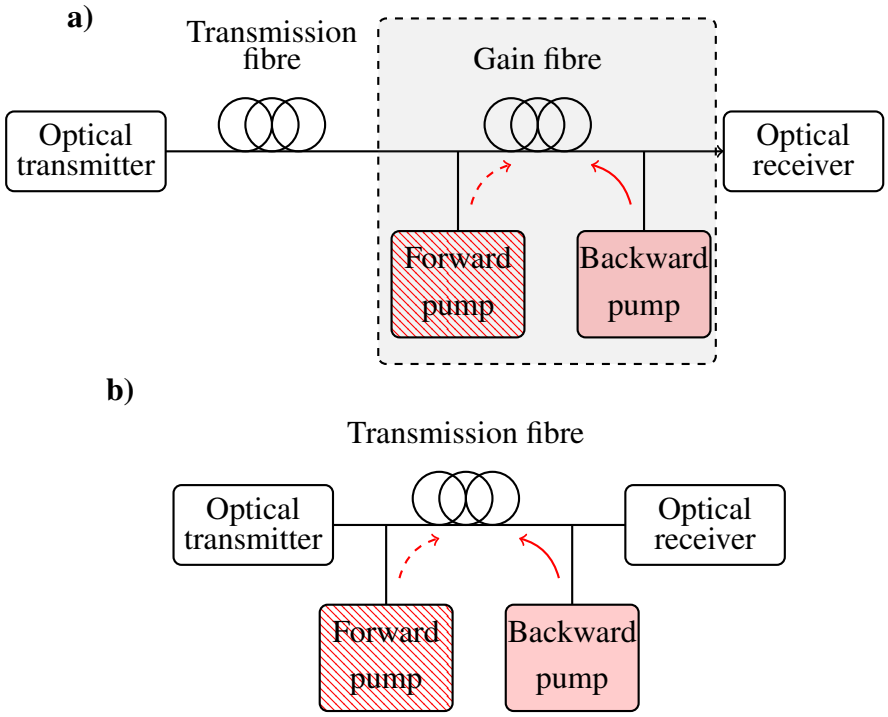

Figure 2.3: Possible configurations of a Raman amplifier, a) *discrete* Raman amplifier, b) *distributed* Raman amplifier.

fibre, separate from the transmission one, to achieve gain. The fibre selected as the gain medium usually has a high Raman gain coefficient, a property closely related to the nonlinear coefficient of the fibre. Early studies on the topic proposed the use of DCF as the gain medium for this type of amplifiers [96][Ch. 4] due to their small effective area and large Raman gain coefficient. Later research proposed the use of highly nonlinear photonic crystal fibres, highly nonlinear fibres (HNLF) and inverse dispersion fibres (IDF) [97–99], all of which offer the possibility of retaining the dispersion unmanaged properties of modern transmission links. Despite the reasearch performed in the early 2000s for discrete Raman amplifiers, the majority of the literature focuses on the amplifier gain properties and linear impairments. References on the nonlinear impairments introduced by *discrete* Raman amplifiers can be found in [100, 101], both using DCF as the gain medium, and only [101] focusing on the implications on transmission systems.

A *distributed* Raman amplifier is one that uses the transmission fibre as a gain medium. In this case, a high pump power is coupled directly into the transmission fibre. *Distributed* Raman amplifiers offer an improved noise performance compared to any discrete amplifier solution.

Depending on the direction the pump is launched into the fibre, different amplifier configurations are possible. If pump and optical signal propagate together in the same direction, the amplifier is said to be in a *forward-pumping* configuration. Alternatively, if signal and pump propagate in opposite directions, the amplifier is said to employ a

backward-pumping configuration. When a pump is used in both directions, the amplifier is said to be *bi-directionally* pumped. Each configuration presents different noise properties, in terms of ASE generation, nonlinear effects and other impairments such as relative intensity noise transfer.

Equation (2.32) describes the evolution of ASE noise in any Raman amplifier configuration, however, the value of the gain coefficient and the direction the pump is propagated will determine the total amount of ASE generated by the amplifier. In general, *discrete* Raman amplifiers present a higher noise figure than their *distributed* counterparts.

2.5 Nonlinearity compensation

The Kerr nonlinearity imposes a limit to the maximum throughput a single optical channel can achieve after transmission through a fibre channel, by introducing power dependant distortions that limit the received SNR. Luckily, the majority of the distortions are deterministic and, with knowledge of the optical field at the receiver, it is possible to compensate for their effects. However, the interactions between ASE noise and nonlinearties are a stochastic process due to the nature of ASE noise, and compensation of such effects remains an open research question. This section will address 3 different nonlinearity compensation schemes studied throughout this thesis, namely DBP, OPC, and the use of Volterra series frequency equaliser (VSFE).

2.5.1 Optical phase conjugation

The concept of OPC was introduced by Yariv, Fekete and Pepper in [67] as a way of compensating for chromatic dispersion effects in a transmission medium, and it was subsequently extended to include the effects from Kerr nonlinearity [68]. The use of OPC for dispersion compensation in optical communication systems was experimentally demonstrated in [102], and proposed for joint compensation of dispersion and Kerr nonlinearity later in [103, 104]. OPC remained as an alternative to dispersion compensating fibres during the early 2000s. Early demonstrations of OPC for optical communication systems employed SOA or periodically polled Lithium-Niobate waveguides as nonlinear media to conjugate the optical signals [105]

The principle of operation of a transmission system with an OPC is shown in Fig. 2.4 and works as follows. The link is comprised of Ns spans with attenuation coefficient, GVD parameter and nonlinear coefficient α, β_2 and γ, respectively. Considering that the propagation of pulses in an optical fibre is governed by the NLSE shown in Eq. (2.16), the complex conjugate of the NLSE is given by [104]:

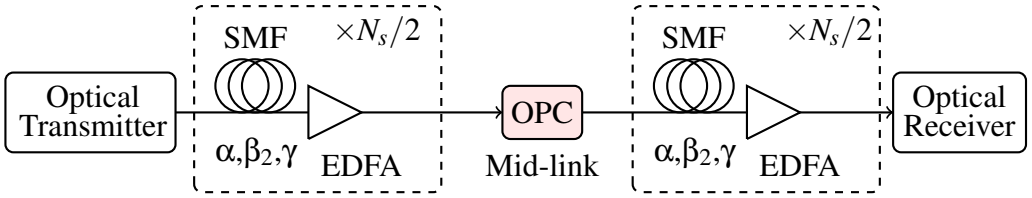

Figure 2.4: Schematic of a transmission using OPC for nonlinearity compensation.

$$\frac{dA^*}{dz} = -\frac{\alpha}{2}A^* + i\frac{\beta_2}{2}\frac{\partial^2 A^*}{\partial t^2} - i\gamma|A^*|^2A^*. \tag{2.33}$$

Comparing Eq. (2.16) with Eq. (2.33) we can observe that Eq. (2.33) is equivalent to the NLSE with with opposite signs for the dispersion and nonlinear terms. When OPC is placed in the middle of the link, this property allows one to undo the dispersion accumulated in the first $N_s/2$ spans in the second $N_s/2$ spans. Since nonlinearities depend on the instant power of the optical field, it is not always possible to perfectly compensate for nonlinear distortions. The nonlinear compensation achieved by OPC is limited by the asymmetric strength of the Kerr effect relative to the conjugation point. This is caused by the asymmetric light intensity changes along the link due to fibre loss. From Eq. (2.33) it can be noted that the conjugation of the field does not affect the effect of attenuation. Perfect compensation of nonliearities can only be achieved with symmetry in the signal power profile relative to the conjugation point, that is if $\alpha(z) = -\alpha(2L-z)$, where L is the conjugation point. The symmetry condition is hard to achieve in practice, and can only be approached using complex distributed amplification schemes.

Table 2.1 summarises the latest experiment results obtained using OPC as a nonlinear compensation scheme. Experimental demonstrations of OPC have relied on complex amplification schemes to improve the sigal power symmetry conditions in transmission links: in [70] the fibre spans were amplified using second order, bi-directionally pumped Raman amplification to obtain a 6 dB power excursion and spans with a symmetry of 82%. Furthermore, other experimental demonstrations have employed Raman amplification and obtained a superior performance from the systems with OPC as seen in [106, 107, 114, 115, 117, 118]. Although the above mentioned advanced amplification technologies offer improved performance when used jointly with OPC, the vast majority of optical links still employ EDFAs to amplify signals during transmission. A lack of signal power symmetry affects the performance of OPC as a NLC method. However, demonstrations of EDFA-based systems employing OPC have been shown to offer NLC gains up 2.5 dB in the system Q-factor [1, 105, 108, 109, 119]. The gains of 2.5 dB in Q-factor reported in [1, 2] using 64-QAM are extremely large for the used system configuration. However, they are not consistent with the results presented therein using

16-QAM, where a gain of 0.6 dB was found. Modern optical fibre transmission systems do not use in-line DCF, and therefore, if OPC is to become an attractive nonlinear compensation scheme for future systems it needs to efficiently work under practical conditions.

2.5.2 Digital back-propagation

The idea behind DBP is a very simple and elegant one: with the knowledge of the full optical field, digitally reverse the fibre propagation using an inverted fibre link with negative signs in the attenuation, dispersion and nonlinear coefficients. This can effectively undo the impairments generated during transmission. It relies on the use of coherent receivers to convert the optical field into an electrical one. A schematic diagram of the DBP concept is presented in Fig. 2.5. This scheme was proposed in 2005 in [61] and later studied in [62]. To digitally back-propagate the received signal, Eq. (2.16) needs to be solved using reversed signs for the fibre paramters. Computationally this is a very complex process as it requires the use of the SSFM, that is naturally recursive and requires high spatial resolution. Different approaches have been proposed in order to simplify DBP: for example, the use of finite impulse response (FIR) filters as shown in [62], or the use of reduced number of steps to solve the NLSE in the backwards direction [120]. Recently, the use of perturbation theory has also been proposed to

Table 2.1: Summary of OPC experimental demonstrations.

Ref	Throughput (Tb/s)	N° channels	Modulation format	Transmission distance (km)	Max Gain (dB)
[105]	1.8	44	QPSK	3402	0.5
[106]	1.024	8	QPSK	6000	0.8
[107]	0.912	8	QPSK	10400	1
[108]	0.64	22	16-QAM	800	0.8
[109]	1.12	5	16-QAM	800	0.9
[110]	0.38	3	QPSK	800	3.6
[111]	1.1	24	QPSK	144	1
[112]	2.048	8	16-QAM	900	1
[70]	4	60	16-QAM	2000	0.79
[2]	0.48	6	16-QAM	834	3
[113]	0.2	1	16-QAM	800	0.5
[114]	1.024	8	16-QAM	900	1.1
[1]	960	6	64-QAM	400	2.5
[115]	13.6	92	16-QAM	3840	0.7
[116]	3.6	30	QPSK	2400	2.3

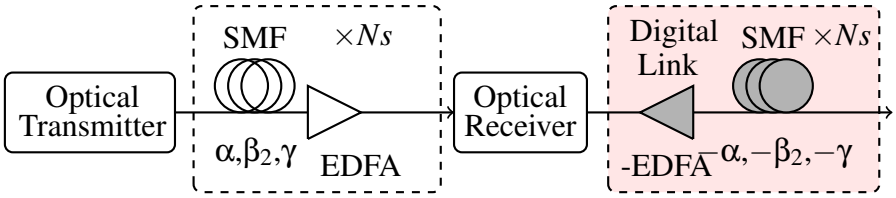

Figure 2.5: Schematic of a transmission using DBP for nonlinearity compensation.

reduce the number of steps in the DBP algorithm allowing an accurate estimation of the nonlinearity [121].

As the transmitted bandwidth and the number of channels is increased, the performance of DBP will be limited by 3 different factors, namely the back-propagation bandwidth, the algorithm complexity and stochastic effects. The receiver bandwidth determines the fraction of the optical bandwidth that can be back-propagated, and, if the optical bandwidth is larger than that of the receiver, DBP will perform incomplete nonlinearity mitigation. After DBP, the signal will have residual distortions generated from XPM from the uncompensated section of the transmitted spectrum. The possible gains from using single channel DBP, a technique where DBP is only applied over a single channel, has been studied in [122] showing a logarithmic reduction on the gains offered by DBP as the bandwidth increases. If the receiver bandwidth is large enough it can be used to back-propagate multiple channels at the same time, multichannel digital back-propagation (MC-DBP), allowing for larger improvements compared to single channel DBP. However, the complexity of the DBP algorithm rapidly increases as the back-propagated bandwidth grows [123], requiring a higher spatial resolution per span to correctly invert the NLSE and account for XPM effects. Finally, stochastic effects such as PMD can limit the performance of DBP when large bandwidths are transmitted and back-propagated. PMD causes different state of polarisations of light to travel at different speeds through the optical fibre, therefore DBP is not able to compensate for cross-polarisation nonlinear effects as it does not know exactly where in the fibre they occurred. However, improvements to the standard DBP scheme have been proposed recently in order to account for the effect of PMD [124, 125], allowing for an improvement on the gains obtained using the DBP algorithm.

2.5.3 Volterra series frequency equaliser

An alternative to evaluate the NLSE for signal propagation through optical fibre is to use Volterra series expansion. The use of the Volterra series transfer function (VSTF) to model the behaviour of optical transmission systems including dispersive and nonlinear effects was first proposed by Peddanarappagari and Brandt-Pearce [71]. As opposed to solving the NLSE, VSTF offers the possibility of analysing a transmission system in a non-recursive manner potentially decreasing the computation complexity compared to

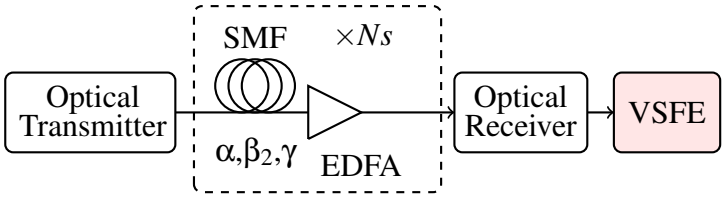

Figure 2.6: Schematic of a transmission using Volterra series frequency equaliser for nonlinearity compensation.

the SSFM. VSTF can be used to represent systems with any order or nonlinearities, and it was found in [71] that a third-order VSTF is comparable to using the SSF method for optical communication links. Additionally, the third-order term in the Volterra series was shown to be equivalent to the first-order regular perturbation solution of the NLSE [92].

The VSTF for the system presented in Fig. 2.6 is given by [71]

$$\begin{aligned}\tilde{A}(z,\omega) &= \tilde{A}(0,\omega)H_1(z,\omega) \\ &+ \iint \tilde{A}(0,\omega_2)\tilde{A}^*(0,\omega_1)\tilde{A}(0,\omega-\omega_2+\omega_1)H_3(z,\omega,\omega_1,\omega_2)d\omega_1 d\omega_2,\end{aligned} \tag{2.34}$$

where $\tilde{A}(z,\omega)$ is the Fourier transform of the optical field at a transmission distance z and angular frequency ω. The functions $H_1(z,\omega)$ and $H_3(z,\omega,\omega_1,\omega_2)$ are known as the Volterra kernels, and can be regarded as higher-order transfer functions of the system. In particular, the linear kernel $H_1(z,\omega)$ accounts for dispersion and attenuation and is defined in the frequency domain as follows:

$$H_1(z,\omega) = e^{(-\frac{\alpha}{2}+i\frac{\beta_2}{2}\omega^2)z}. \tag{2.35}$$

The third-order kernel $H_3(z,\omega,\omega_1,\omega_2)$, which accounts for nonlinear effects, is defined in the frequency domain as:

$$H_3(z,\omega,\omega_1,\omega_2) = i\frac{8}{9}\gamma H_1(z,\omega)F_1(\omega,\omega_1,\omega_2)\xi(\omega,\omega_1,\omega_2,N_s), \tag{2.36}$$

where the total transmitted distance is $z = L_s N_s$ with span of length L_s and total number of spans N_s. The FWM efficiency for one span $F_1(\omega,\omega_1,\omega_2)$ is defined as:

$$F_1(\omega,\omega_1,\omega_2) = \frac{1-e^{-\alpha L_s + i\beta_2(\omega-\omega_2)(\omega_1-\omega_2)L_s}}{-\alpha+i\beta_2(\omega-\omega_2)(\omega_1-\omega_2)} \tag{2.37}$$

and the phased array term $\xi(\omega,\omega_1,\omega_2,N_s)$, responsible for the coherent accumulation

of nonlinearities over the total number of spans N_s is defined as:

$$\xi(\omega,\omega_1,\omega_2,N_s)=\sum_{n=1}^{Ns} e^{i\beta_2(n-1)(\omega-\omega_2)(\omega_1-\omega_2)L_s}. \tag{2.38}$$

To use the VSTF to compensate for nonlinearities at the receiver, a Volterra series frequency equaliser (VSFE) can be used to reconstruct the original transmitted optical field using the received field. Both linear and third-order kernels need to be applied in the opposite direction, in a back-propagation manner, to the received signal. Finally, the approximation of the transmitted signal $A(\omega)$ is given by:

$$\begin{aligned}\tilde{A}(0,\omega) &= \tilde{A}(z,\omega)H_1(-z,\omega) \\ &+ \iint \tilde{A}_(z,\omega_2)\tilde{A}^*(z,\omega_1)\tilde{A}(z,\omega-\omega_2+\omega_1)H_3(-z,\omega,\omega_1,\omega_2)d\omega_1 d\omega_2,\end{aligned} \tag{2.39}$$

with $\tilde{A}(z,\omega)$ representing the received signal at frequency ω. Demonstrations, either experimental or numerical, of VSFE used as nonlinearity compensation method can be found in the literature. VSFE has been previously studied to compensate for nonlinearities in optical fibre communication systems mainly through numerical simulations in [126–130], showing performance gains similar to DBP with the potential of reducing the computational complexity, depending on the specific used VSFE implementation. Additionally, an experimental demonstration of VSFE was shown in [131]. In section 5.2, VSFE will be used for the first time in an OPC-based transmission link to improve the performance of both nonlinear compensation schemes.

2.6 Experimental testbed

The experiments performed whilst conducting the research described in this thesis were performed using the optical networks group's (ONG) experimental test bed. Throughout this thesis the transmission link used for the propagation of signals was varied depending on the purpose of the study. Section 4.1 used a recirculating loop configuration, allowing one to explore the nonlinear effects generated during fibre propagation for links with lengths in excess of 1000 km. Section 4.2 used a single fibre span with a maximum distance of 200 km to isolate the effects of SRS between the transmitted channels from the different components that introduce a wavelength dependent gain/loss, such as optical amplifiers and passive components. Section 5.1 used an installed optical network as the transmission link to investigate the performance of OPC in a practical transmission scenario. While different transmission links were used for the experiments described in this thesis, the optical transmitter and receiver remained the same for all experiments and are described in the following section. The optical transmitter and

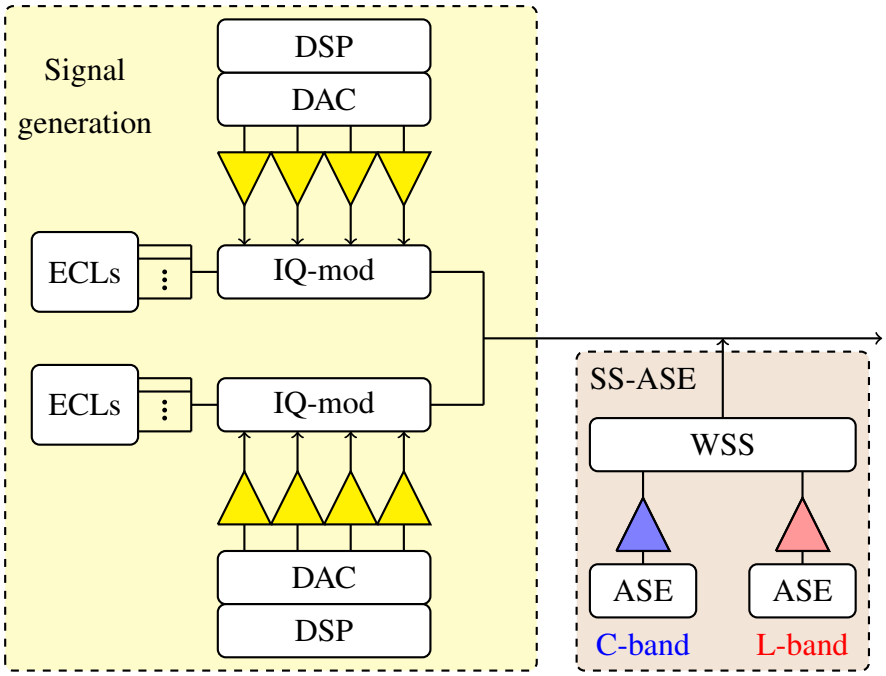

Figure 2.7: Schematic of the experimental setup of the optical networks group (ONG) transmitter.

receiver are among the most important assets from the ONG, and these have been in use for years. The current transmitter was put together by Drs. Kai Shi, Sezer ErkÄślÄśnç, Zhixin Liu and Lidia Galdino. The high-speed coherent receiver used in the experiments was build before I joined the group on 2014.

2.6.1 Optical transmitter

A general schematic of the optical transmitter is shown in Fig. 2.7. External cavity lasers (ECL) were used as optical carriers to modulate information. Depending on the experiment, a different number of ECLs was used, with a maximum of 14 laser sources used in section 5.1. The ECLs had a nominal linewidth of 100 kHz and maximum output power of 16 dBm. The ECLs were coupled together into separate signal paths using two 8x1 couplers, this was performed to ensure decorrelation between adjacent channels by forming odd and even channels. Each signal path was subsequently connected to an individual IQ-modulator driven by the electrically amplified outputs from a 92 GS/s digital-to-analogue converter (DAC). The drive signals were generated offline using MatLab. Sequencues of $2^{15} - 1$ pseudo-random bits were mapped into QAM formats with 4, 16, 64 and 256 symbols per constellation. A digital root raised cosine (RRC) filter was used to spectrally shape the signals and pre-emphasis was applied to overcome the electrical response of the transmitter components, including the limited bandwidth of electrical amplifiers and optical modulators. The experiments described in sections 3.2 and 4.1 were performed using single-polarisation modulators. In this case, dual

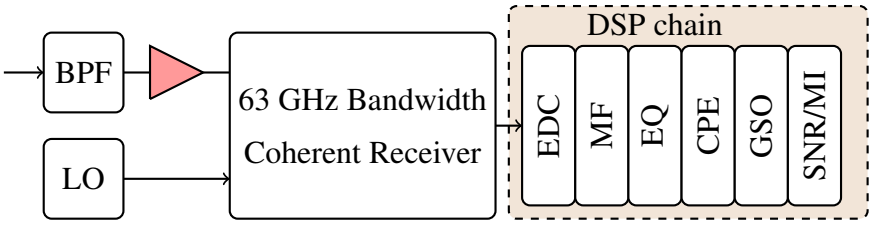

Figure 2.8: Schematic of the experimental setup of the ONG receiver.

polarisation (PM) signals were emulated by splitting the modulated carrier into two copies, delaying one relative to the other and rotating the polarisation state of one copy by 90°. Both polarisations were then re-combined by a polarisation beam combiner. The remaining experiments in sections 4.2 and 5.1 used a dual-polarisation IQ-modulators avoiding the need for the polarisation multiplexing emulation stage.

To emulate the transmission of bandwidths larger than the available number of sources, spectrally-shaped amplified spontaneous emission (SS-ASE) noise was used. SS-ASE was generated separately in each transmission band (C and L-bands) by a pair of EDFAs, and subsequently shaped by a wavelength selective switch (WSS). The WSS was also used to create a notch in the SS-ASE, with an extinction ratio of 35 dB, to couple the modulated signals without compromising their optical signal-to-noise ratio. The validity of this methodology was verified in [132, 133], showing that this technique provides a conservative measure of system performance.

2.6.2 Optical receiver

A general schematic of the optical receiver is shown in Fig. 2.8. At the receiver, the desired signal was filtered using a band-pass filter (BPF) with 120 GHz bandwidth, and subsequently amplified before entering the coherent receiver. A separate ECL, with the same parameters as the ones used in the transmitter, was used as the local oscillator (LO). Signal and LO were combined using a 90° hybrid and detection was carried out by balanced photodetectors with 70 GHz electrical bandwidth and sampled by a real-time digital oscilloscope with an analogue electrical bandwidth of 63 GHz at 160 GSa/s. The digitised signal samples were processed off-line to compensate for channel impairments and carrier phase was estimated. The DSP chain was comprised of: electronic dispersion compensation (EDC) performed in the frequency domain, matched filter (MF), channel equalisation (EQ) using a radius directed equaliser [134], with the constant modulus algorithm equaliser used for pre-convergence [135]. The carrier phase was estimated (CPE) per polarisation using a decision-directed phase estimation algorithm [136]. Gram-Schmidt orthogonalisation (GSO) [137] was performed in order to correct for any sub-optimal phase bias in the transmitter and receiver.

As performance metrics SNR and MI between the transmitted and received symbols

are used in this thesis.

For the experimental and simulation studies performed in this thesis, SNR was estimated using the received symbols after the DSP chain using:

$$\text{SNR} = \frac{P}{\sigma^2_{Noise}} \tag{2.40}$$

with the variance of the noise power was calculated as:

$$\sigma^2_{Noise} = \mathbb{E}\left(|y[n] - x[n]|^2\right), \tag{2.41}$$

where y_n and x_n are the received and transmitted symbols, respectively.

SNR was used as the performance metric when the amount of noise, either linear or nonlinear, in system was the studied variable.

Although SNR is a performance metric useful for understanding how much noise is generated in the transmission link, it does not translate directly to the rates at which the system can transmit information. As described in section 2.1, recent works have highlighted the importance on quantifying the performance for systems employing coded modulation schemes, or FEC codes. For this purpose, the MI is a more reliable indicator of the performance of coded optical fibre systems, regardless of the specific channel used for transmission [73].

In this thesis, MI was also used as a system performance metric and it was calculated from the transmitted and received symbol for each polarisation, using a mismatched decoder approach with a Gaussian auxiliary channel [138][Eq. (14)]. Further details on the MI calculations are found in appendix A.

2.7 Conclusion

This chapter reviewed the most important concepts to understand the research described in the following chapters. Chapter 3 will use the theory presented in sections 2.4 and 2.5, while chapters 4 and 5 will mainly use the theory from sections 2.3 and 2.5.

3

Raman amplification as an alternative for higher capacity systems

OPTICAL amplification was one of the enabling technologies that allowed for revolutionary capacity increases of optical communication systems during the early 90s. After the development of high-gain, broadband EDFAs in the late 80s [139], EDFAs became the number one choice for amplification in optical communication systems. It became evident later on however, that the bandwidth restrictions of the EDFA would impose a limit on the maximum throughput that optical communications are able to transmit. Alternative solutions to the EDFA are required to maximise the use of the bandwidth that is available for the transmission of signal in single mode optical fibres. In this context, all-Raman systems can extend the amplification bandwidth across the low-loss region of silica fibres allowing for distributed compensation of signal attenuation with improved noise performance, as described in section 2.4.

The work described in this chapter studies the benefits and challenges of Raman amplifiers to increase the throughput of optical communication systems. An experimental characterisation of the SRS effect was performed in section 3.1 to validate the numerical methods used to simulate Raman amplifiers.

Despite the improved noise performance offered by *distributed* Raman amplification, for some transmission scenarios such as network configurations with high losses due to routing components, or readily deployed links, a *discrete* optical amplification

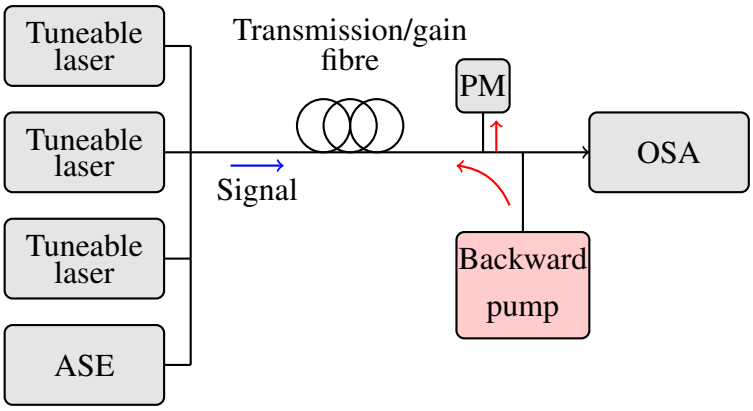

Figure 3.1: Experimental setup to characterise Raman amplifiers.

solution may be a more attractive solution. For this reason, section 3.2 describes the experimental characterisation of different gain fibres used to build *discrete* broadband Raman amplifiers, and their transmission performance.

Finally, section 3.3 details the study of *distributed* Raman amplifiers as an alternative for EDFAs in long-haul transmission systems. The linear and nonlinear regimes were studied, and for the first time, the benefits of using *distributed* Raman amplifiers in combination with DBP in long haul transmission systems occupying the full C-band were evaluated.

3.1 Raman gain and signal power profile

As described in chapter 2, Raman amplification is obtained through stimulated Raman scattering between a high power pump and an optical signal. During this process, energy is transferred from a pump wave to a signal wave by a factor proportional to the Raman gain coefficient. The Raman gain coefficient is, therefore, the main property that determines the amount of amplification that can be obtained using a pump wave. Due to the small values of the Raman coefficient in silica based fibres (approximately 0.3 $W^{-1}km^{-1}$ for SMF), long fibre lengths and high powers (compared to EDFAs) are required to observe amplification. This implies that the transmitted signal is amplified using fibres with lengths of several kilometres, which affects the signal power evolution along the fibre, and as a result modifies the nonlinear behaviour of the amplifier. The same phenomenon is observed for either configuration of Raman amplifiers, *discrete* or *distributed*, and for any pumping scheme. Therefore, an experimental characterisation was performed in order to, firstly, measure the Raman gain coefficient for a standard transmission fibre (SMF) and, subsequently, characterise the signal power profile to be able to emulate the Raman amplifier in numerical simulation.

The experimental setup used to characterise the optical fibre is shown in Fig. 3.1. A single tuneable laser was used as a signal together with SMF spans of different lengths

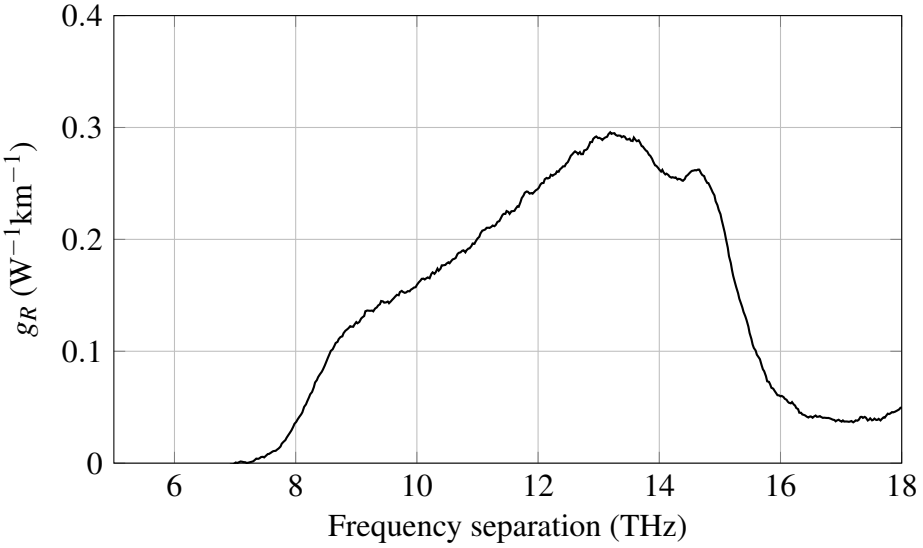

Figure 3.2: Raman gain coefficient measured for single mode fibre.

used as the transmission fibre. Two polarisation multiplexed high power laser diodes centred at 1445 nm were used as pump source emitting a total of 200 mW optical power. The pump power into the transmission fibre was monitored using a power meter and the output signal amplitude after the fibre span was measured using an optical spectrum analyser.

The *on-off* gain of a Raman amplifier ($G_{\text{on-off}}$) is defined as the ratio between the amplified signal power at the end of the fibre span and the signal power at the output of the fibre without Raman amplification. Mathematically, this is expressed as:

$$G_{\text{on-off}} = \frac{P_s(L)}{P_s(0)exp(-\alpha_s L)} = \exp(g_0 L), \tag{3.1}$$

where $g_0 = g_R\left(\frac{P_0 L}{A_{eff}L_{eff}}\right)$ and is known as the small signal gain, a condition that can be satisfied when no pump depletion is incurred. From Eq. (3.1), the Raman gain coefficient of an optical fibre can be estimated using:

$$g_R(\Omega) = \frac{A_{\text{eff}}}{L_{\text{eff}}P_p(0)}\left(\log\left(\frac{P_s(L)}{P_s(0)}\right) + \alpha_s L\right), \tag{3.2}$$

where Ω is the frequency separation between pump and signal. The small signal gain condition was satisfied in the characterisation by using a signal power into the fibre of 0 dBm.

The Raman gain coefficient, normalised by the fibre's effective area (A_{eff}), was characterised as a function of Ω by changing the wavelength of the tuneable laser, and the result is shown in Fig. 3.2. The gain coefficient shows a maximum value of approximately 0.3 W^{-1}km^{-1} at a frequency separation of approximately 13 THz.

Using the measured gain coefficient value, the theoretical on-off gain for different

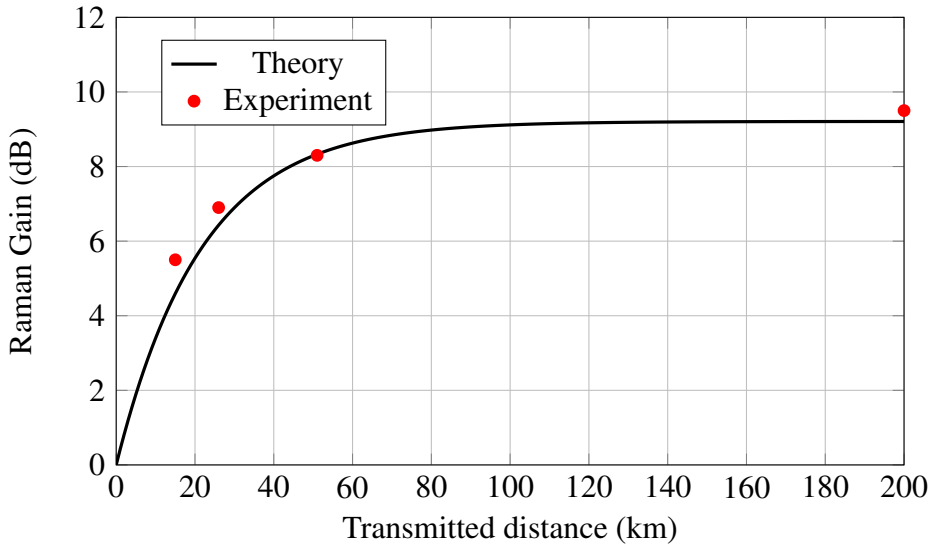

Figure 3.3: Theoretical and experimental on-off gain achieved using 200 mW of pump power for different span lengths.

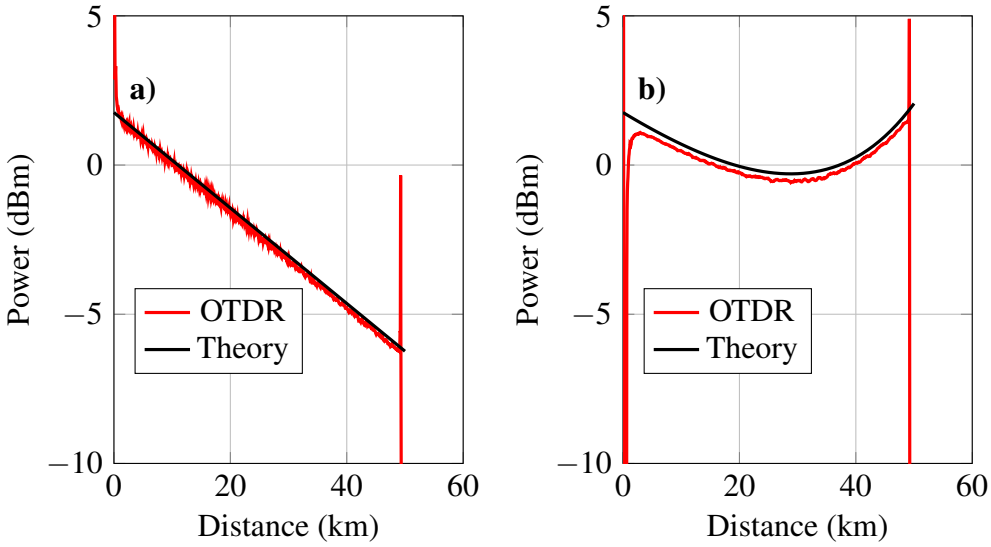

Figure 3.4: OTDR traces for a 50 km span of SMF a) Passive fibre , b) backward pumped Raman amplifier.

span lengths and a fixed pump power of 200 mW was calculated and compared to the experimental data. These results are shown in Fig. 3.3. A maximum difference between the experimental measurements and the theoretical prediction of 0.4 dB was found to be due to the changes in attenuation coefficient in the fibre spans tested. With knowledge of the Raman gain coefficient it is possible to use the propagation equations presented in the previous chapter to describe the characteristic signal evolution in a Raman amplified fibre span.

To characterise the signal power profile along the span, an optical time domain reflectometer (OTDR) was used, in place of the tuneable laser source in Fig. 3.1. The OTDR traces were compared to the power profile obtained using Eqs. (2.27) and (2.28).

Figure 3.4 shows the results for a 50 km span with and without Raman amplification. In Fig. 3.4 (a) the OTDR trace can be observed together with the theoretical prediction for a non-amplified span using Eq. (2.10). For the Raman-amplified span, the pump power was adjusted in order to compensate the attenuation present in the fibre span. The OTDR trace and the theoretical signal power profile can be seen in Fig. 3.4 (b). Again, good agreement can be seen between both curves. The knowledge of the signal power evolution across the optical fibre can be used to predict system performance by numerically solving any of the propagation equations, allowing for the analysis of nonlinear effects arising from the higher signal power across the fibre span.

3.2 Broadband discrete Raman amplifier

One of the main attractive features of SRS is that it can be generated at any wavelength in silica fibres, as long as a pump power higher than the SRS threshold is provided. Contrary to the EDFA, where the amplification window is determined by the properties of the doped fibre, Raman amplifiers can be designed to amplify large optical bandwidths by multiplexing pump sources at different wavelengths. During the late 1990s, when dispersion compensated transmission was widely used, the idea of introducing a Raman pump into the DCF modules to reduce their high loss was proposed. This lead to the development of *discrete* or *lumped* Raman amplifiers, where a dedicated fibre independent from the transmission link would be used to amplify a signal. This would, ideally, replace the mature EDFA offering the alternative of amplifying arbitrarily large bandwidths by employing multiple WDM pumps [8, 55]. Several configurations were proposed to achieve gains comparable to the ones obtained from EDFAs, such as *bi-directional* pumping and dual stage amplifiers. With the rediscovery of the coherent receiver, dispersion compensation was moved from the transmission line to the receiver, removing the need for in-line DCF modules. With this in mind, new fibre types were studied for the development of *discrete* Raman amplifiers such as highly nonlinear photonic crystal fibres, highly nonlinear fibres (HNLF) and inverse dispersion fibres (IDF) [97–99].

Although next-generation systems may be designed using *distributed* Raman amplification for higher capacity, *discrete* Raman amplifiers will remain important to upgrade existent systems that require increased bandwidth and in networking scenarios. In this context, it is necessary to identify which gain fibre exhibits the best linear and nonlinear performance.

3.2.1 Design of discrete Raman amplifier

There are 3 main properties of a *discrete* Raman amplifier, namely net gain, noise figure, and optical bandwidth. In analogy to an EDFA, the net gain is defined as the gain experienced by the signal at the output of the amplifier compared to the input as:

$$G_{\text{net}} = \frac{P_s(L)}{P_s(0)}, \tag{3.3}$$

where L is the length of the gain fibre. Similarly, the noise figure is defined by the ASE noise increase from input to output. Finally, the optical bandwidth is defined by the number of pump wavelengths used to pump the amplifier. Design guidance for amplifiers covering bandwidths of 100 nm were proposed in [8, 55], by incorporating every pump signal into the system of coupled equations described in Eqs. (2.27) and (2.28). By solving this system, the pump-pump interactions are considered, and an optical amplifier with a constant gain profile as a function of wavelength can be designed. As the number of pump wavelengths increases, the equalisation of the gain spectrum becomes easier with a greater control of the gain as a function of wavelength; however the power consumption of the amplifier module is increased.

In the design of *discrete* Raman amplifiers the pump power is optimised to maximise the gain and bandwidth. Neglecting pump depletion, the net amplifier gain is a function of the fibre length as in the following expression:

$$G_{\text{net}}(z) = \exp\left(g_R P_0 \frac{1-\exp(-\alpha_p z)}{\alpha_p A_{eff}} - \alpha_s z\right), \tag{3.4}$$

with the all parameters previously defined in chapter 2 section 2.4. From Eq. (3.4) it is evident that two main features determine the gain of the amplifier, namely, the *on-off* gain (G_A) experienced by the signal, and the signal attenuation. As the gain fibre increases in length, the signal loss becomes the most important contribution to Eq. (3.4), whilst for shorter fibre lengths the *on-off* gain dominates the net gain. Equation (3.4) experiences a maximum gain in terms of the fibre length when:

$$z = -\frac{1}{\alpha_p}\log\left(\frac{\alpha_s A_{eff}}{g_R P_0}\right), \tag{3.5}$$

leading to an optimum gain fibre length to minimise pump power consumption and maximise the net amplifier gain.

3.2.2 Experimental characterisation

Experimental characterisation of *discrete* Raman amplifiers was done to investigate the pump power consumption, net amplifier gain, amplifier noise figure and bandwidth

Table 3.1: Gain fibre parameters

Fibre type	α_s dB/km	α_p dB/km	peak g_R/A_{eff}	D ps/nm/km
DCF	0.7	0.9	2.9	90
HNLF	0.9	1.7	6	2

for different gain fibres. The experimental setup used for this purpose was shown in Fig. 3.1, however additional tuneable lasers were added together with an ASE noise source. Three unmodulated tuneable lasers spaced by 50 GHz were coupled together using 3 dB couplers. The laser outputs were coupled with a 70 nm flat ASE source generated using a separate *discrete* Raman unit. The amplifier module comprised of an isolator followed by the gain fibre. Backward pumps were coupled to the gain fibre by a WDM combiner. The pumping module was composed of eight laser diodes with four different wavelengths (1427, 1445, 1467 and 1490 nm) and a maximum output power of 250 mW per laser. Each frequency was polarisation multiplexed through a polarisation beam combiner. Drive currents for each laser were adjusted to obtain the same output power in both polarisations. Four different gain fibres were studied, three of them being DCF with different lengths, and a HNLF. The parameters of the fibres used are listed in Table 3.1.

3.2.2.1 Gain fibre length

The four *discrete* Raman amplifiers were set to have a net gain of 10 dB by adjusting the pump powers. The required pump power to achieve such gain was measured, with the results shown in Fig. 3.5 as a function of the DCF and HNLF gain fibre length. The measured pump powers were compared to the theoretical predictions using Eq. (3.4). From Eq. (3.4) the pump power is inversely proportional to the g_R and the L_{eff}; therefore, shorter gain fibres lead to a significantly higher pump power requirement, as shown in Fig. 3.5. To minimise the power consumption, an optimum gain fibre length can be obtained and for a specific fibre it depends exclusively on the effective amplification length. The optimum lengths for the evaluated DCF and HNLF gain fibres (highlighted with circles in Fig. 3.5) were found to be 8.4 and 5.2 km, respectively. The optimum HNLF fibre length is shorter compared to DCF due to the higher attenuation coefficient α_p, and therefore a shorter effective amplification length.

3.2.2.2 Noise figure and net gain

After the pump powers were adjusted, the amplifier net gain and noise figure was characterised as a function of the amplification bandwidth using an optical spectrum analyser (OSA) with 0.1 nm resolution. Both parameters were measured every 5 nm

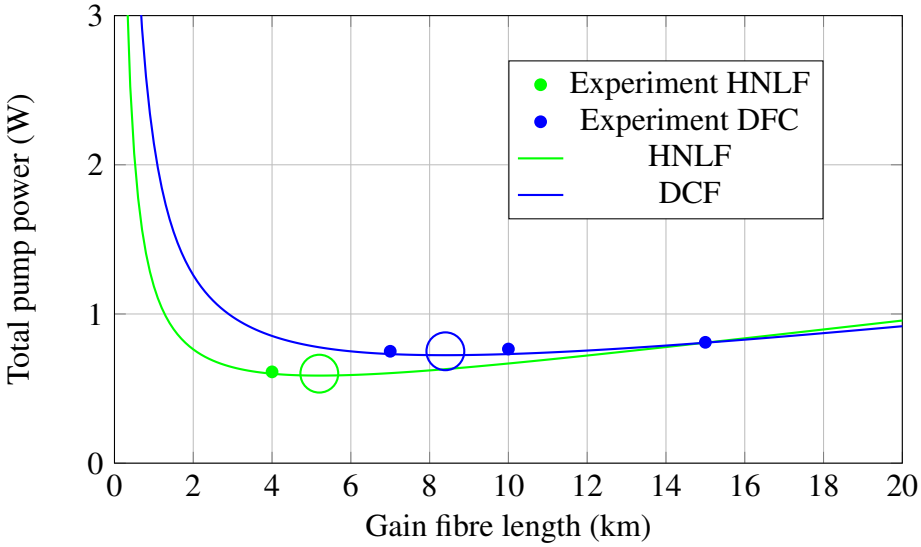

Figure 3.5: Pump power requirements for a *discrete* Raman amplifier. Solid lines represent theoretical values, and markers represent experimental data. Optimum length highlighted with circle.

with the tuneable laser signals. Due to the total pump power limitation of 1 W, the highest achieved net gain was 10.2 dB.

The net gain and noise figure from the amplifiers was characterised as a function of the signal wavelength and the results are shown in Fig. 3.6. A total gain bandwidth of 70 nm was obtained and the largest gain ripple of ± 1.01 dB was found for the HNLF-based amplifier. The large bandwidth of the discrete amplifier is the most attractive of its features, considering the simple pump configuration and pump wavelength allocation. This offers a good trade-off between amplifier complexity and bandwidth. For the DCF-based amplifiers, the highest gain was obtained using the shortest fibre (7 km), whilst for longer gain fibres this was reduced using the same pump power. As seen from Eq. (3.4) and the results of Fig. 3.5, for longer lengths of gain fibre the signal attenuation is increased while the *on-off* gain is maintained, leading to a smaller net gain.

The average measured noise figure across the 70 nm of amplification bandwidth was found to be 7.1, 7.5 and 8.1 dB for the 7, 10 and 15 km DCF-based amplifiers, respectively. For the HNLF-based amplifier an average noise figure of 6.5 dB was measured across the amplification bandwidth. The noise figure for all amplifiers was calculated by measuring the increase of the ASE noise level generated by the amplifier, using [140]:

$$NF = \frac{P_{ASE}}{h\nu\Delta\nu G_{\text{net}}} + \frac{1}{G_{\text{net}}}. \tag{3.6}$$

From Fig. 3.6 a) and b) it was concluded that a shorter fibre length leads to an improved net gain of the amplifier together with a smaller noise figure; however, the length of the gain fibre needs to be carefully chosen or the benefits obtained from a

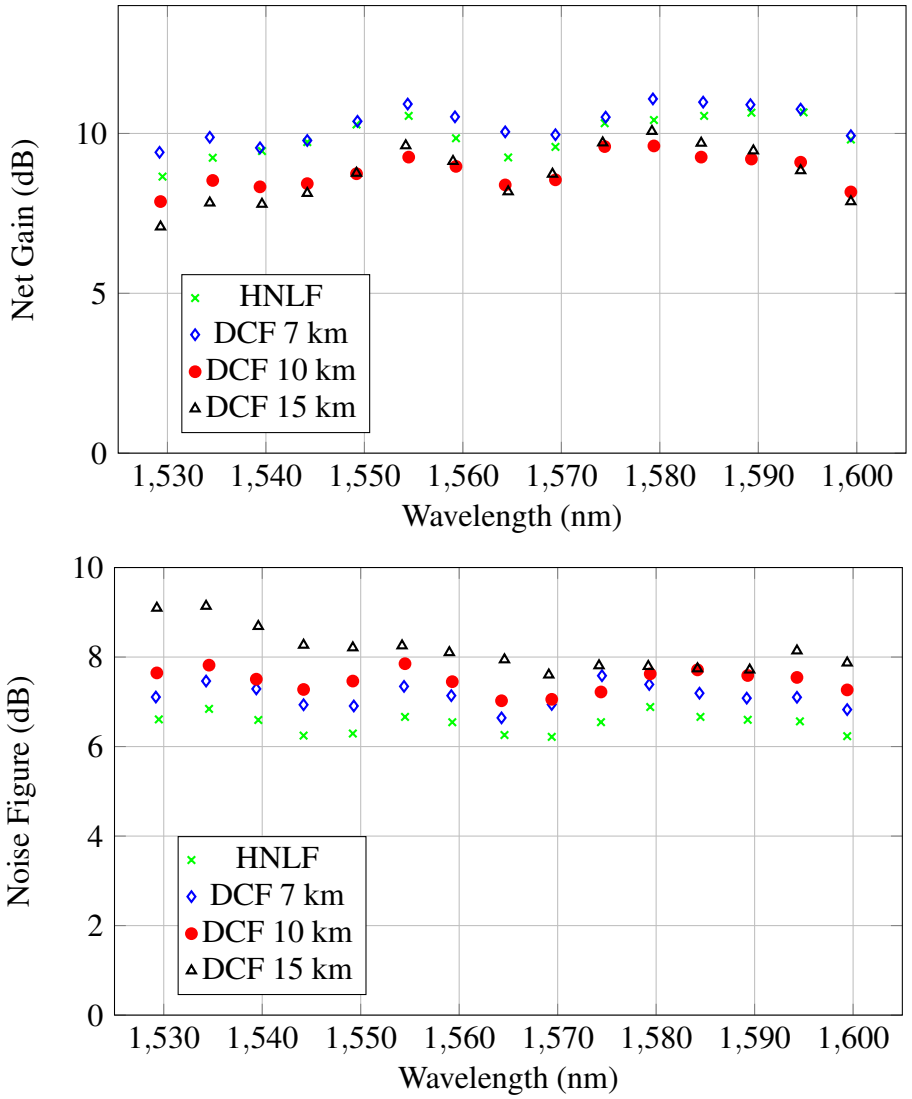

Figure 3.6: Characterisation of *discrete* Raman amplifiers, a) net gain as a function of wavelength, b) amplifier noise figure as a function of wavelength.

reduced noise figure can be outweighed completely by a dramatic increase in the pump requirements.

From the performed characterisation it was possible to conclude that among the studied gain fibres, the best solution was the HNLF. With a Raman gain coefficient of 6 $W^{-1}km^{-1}$ and a pump attenuation of 1.7 dB/km, a reduced noise figure with a lower pump consumption for a fixed net gain, compared to the DCFs, can be obtained if a fibre length close to the optimum is used. Although the aforementioned conclusion holds for a linear characterisation, the use of high powers in a transmission system modifies the way the amplifier behaves. Due to the long gain fibre lengths, compared to other discrete amplifier solutions (e.g. EDFA), the impact of other fibre impairments, namely chromatic dispersion and the nonlinear coefficient of the optical amplifier, need to be studied in a realistic transmission configuration.

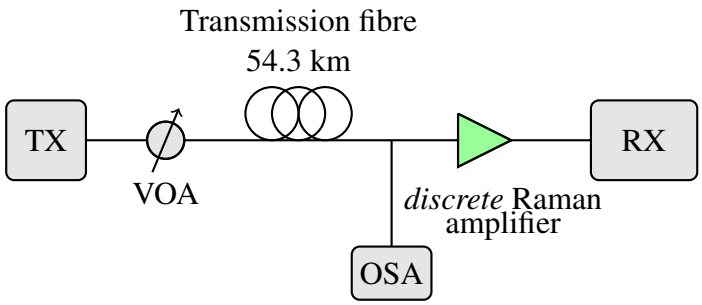

Figure 3.7: Schematic of the experimental setup to characterise the performance of *discrete* Raman amplifier in a transmission system.

3.2.3 Transmission performance using discrete amplifiers

A simple transmission experiment was performed to study the behaviour of *discrete* Raman amplifiers in a transmission system, and the implications the gain fibre properties have in this scenario. The transmission setup shown in Fig. 3.7 was used for the characterisation. The ONG transmitter (see section 2.6) was used to generate 11 channels, centered at 1550 nm, shaped with a RRC with 0.1% roll-off, and modulated using PM-QPSK or PM 256-QAM at a symbol rate of 8 GBd. The channel spacing was 8.1 GHz, to maximise the spectral efficiency of the transmitted channels. The generated signal was amplified and subsequently passed through a variable optical attenuator (VOA) to set the launch power. The first study was to measuring the receiver sensitivity using the Raman amplifiers. For this reason, QPSK was chosen as a modulation format due to its high noise tolerance, and the signal was connected directly from the transmitter to the receiver in a back-to-back configuration. Following the sensitivity measurements, a transmission fibre was used before the Raman amplifier. The fibre was a span of Corning®SMF-28®ULL fibre with a length of 54.3 km and a total attenuation of 9.2 dB in order to match the gain from the *discrete* Raman amplifier. The transmission fibre had a dispersion parameter (D) of 18 ps·km^{-1}·nm^{-1} and nonlinear coefficient of 1.1 W^{-1}km^{-1}.

At the receiver, an EDFA with 5.2 dB noise figure was used to maintain a constant received power into the coherent receiver. The use of the EDFA does not influence the noise figure of the the *discrete* Raman amplifier. In fact, the overall noise figure of a chain of amplifiers is given by [140]:

$$NF_{total} = NF_1 + \frac{NF_2 - 1}{G_1}, \tag{3.7}$$

where NF_i corresponds to the noise figure of the i-th amplifier in the chain, and G_i is the gain of the i-th amplifier. From Eq. (3.7), clearly the noise figure from the first amplifier, in this case the Raman amplifier, will dominate the noise contribution of the entire amplifier chain. Therefore, the use of the EDFA did not represent a significant

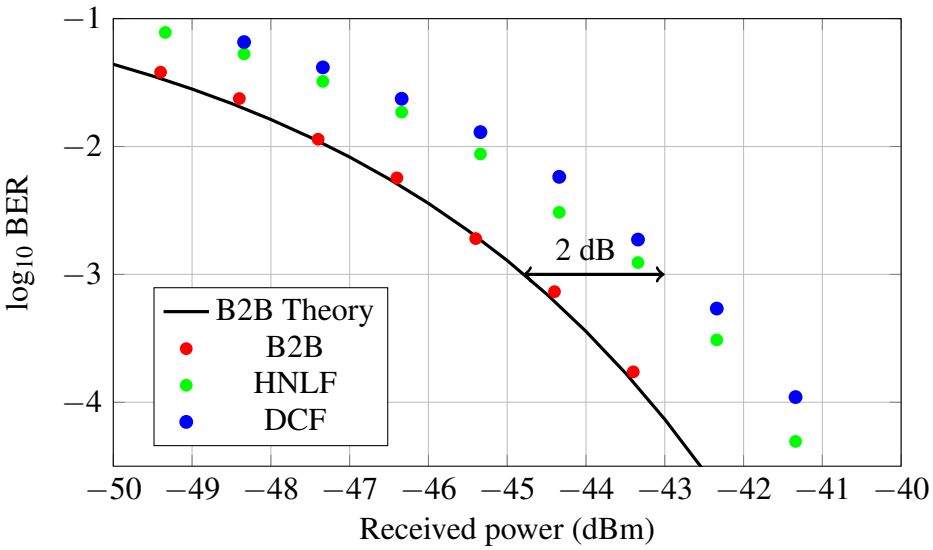

Figure 3.8: Receiver sensitivity for different *discrete* Raman amplifiers. Black solid line represents the theoretical back-to-back performance. Red, green and blue markers represent experimental data for back to back, HNLF and DCF based Raman amplifiers, respectively.

modification of the overall noise figure, and in this configuration, the EDFA only degraded the overall NF of the system by approximately 0.2 dB.

The signal was detected using the ONG receiver (see section 2.6). EDC was modified to take into account the additional dispersion incurred within the *discrete* Raman amplifier.

3.2.3.1 Receiver sensitivity

Evaluation of the *discrete* Raman amplifiers noise performance was done by measuring the sensitivity of the receiver. For this study, only the DCF module with 7 km length was used, due to the improved performance observed compared to longer lengths of DCF, as seen previously in Fig. 3.6. The bit error rate (BER) of the received signals was measured as a function of the received power and the results are shown in Fig. 3.8. The back-to-back performance of the system is illustrated by the red markers and solid black line, representing experimental data and theoretical predictions respectively. The performance for the different *discrete* Raman amplifiers is shown by the blue and green markers for DCF and HNLF-based Raman amplifiers, respectively. The back-to-back configuration corresponded to the use of an EDFA with 5 dB noise figure instead of the *discrete* Raman amplifier. These results show good agreement with the previous noise figure measurements of Fig. 3.6 b). The receiver sensitivity obtained for both Raman amplifiers shows a penalty of approximately 2 dB compared to the back-to-back configuration, corresponding, therefore, to amplifiers with a noise figure of approximately 7 dB. As in the previous section, the HNLF-based amplifier presents a sensitivity improved by 0.6 dB compared to the DCF amplifier. This indicates that

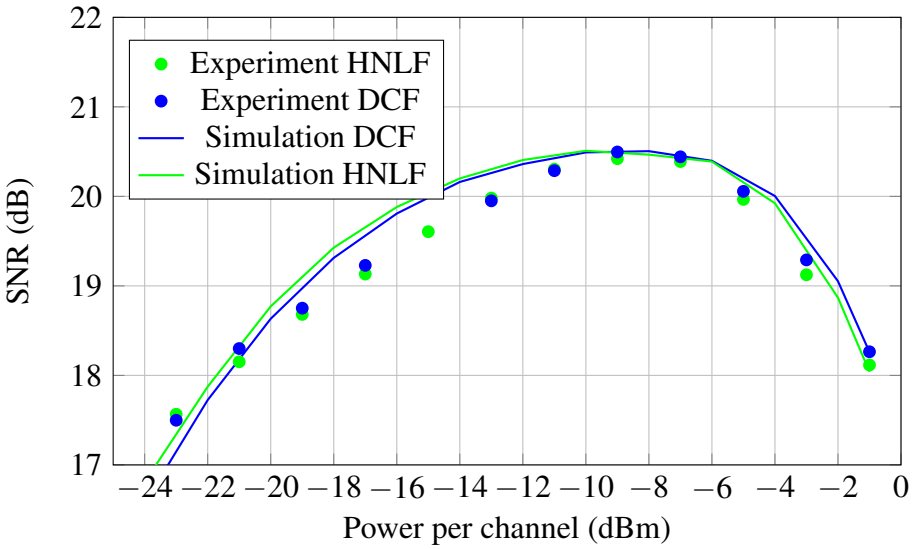

Figure 3.9: Received SNR as a function of signal launch power after the transmission of one span. Green and blue markers represent experimental data for HNLF and DCF based Raman amplifiers, respectively.

both studied Raman amplifiers perform similarly in the linear regime of an optical communication system.

3.2.3.2 Transmission performance

The performance of both *discrete* Raman amplifiers was subsequently evaluated in a transmission scenario. Additionally, the transmission system was numerically simulated and compared to the obtained experimental performance.

The received SNR of the central sub-channel was measured as a function of the signal launch power and the results are plotted in Fig. 3.9. In the linear regime, where the performance is dominated by amplifier ASE noise, the HNLF gain fibre shows an improved performance by 0.2 dB. This was expected due to the 0.6 dB different between the noise figures found in the previous section. As the signal power was increased, a maximum value for the received SNR of 20.7 dB was found for both amplifiers under test. In the nonlinear regime similar performance was observed for both amplifiers, despite the difference in the nonlinear coefficient of both gain fibres. Due to the lack of multiple amplifiers with 70 nm bandwidth, no recirculating loop could be built to study longer transmission distances, and this study could only be performed numerically. The Raman amplifiers were simulated after fibre propagation using the Manakov equation including Raman gain and an ASE noise term as detailed in appendix A. Nonlinear coefficients of 5.5 and 10.5 $\mathrm{W^{-1}km^{-1}}$ were used to simulate the DCF and HNLF gain fibres, respectively. Fig. 3.10 shows the received SNR for both amplifiers after a transmission distance of 1954.8 km, corresponding to 36 spans of 54.3 km. After long distance transmission the HNLF-based amplifier outperforms the DCF one in every

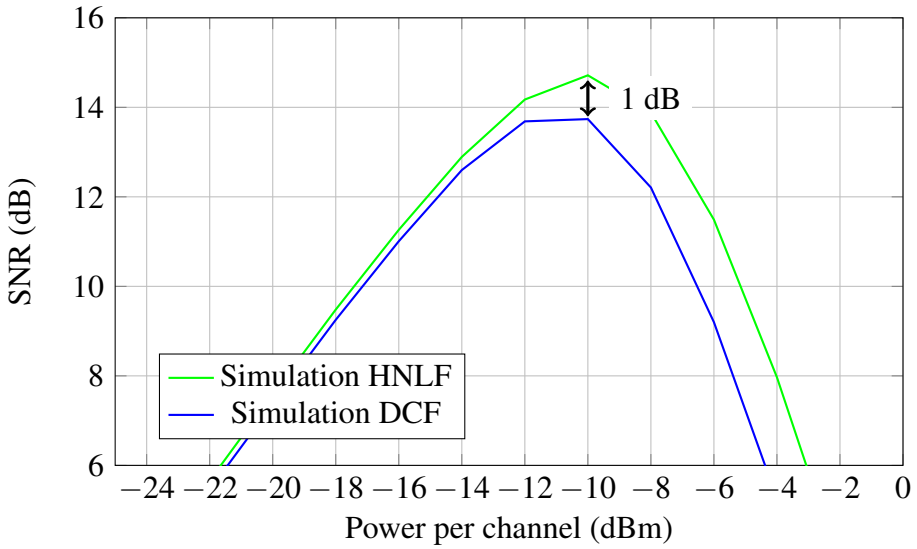

Figure 3.10: Received SNR as a function of signal launch power after the transmission of 36 spans. Green and blue solid lines represent simulation data for HNLF and DCF based Raman amplifiers, respectively.

power regime. Just as in the transmission over one span, the linear regime shows a received SNR 0.2 dB higher for this amplifier due to the reduced noise figure. The DCF amplifier, with a total dispersion of -650 ps·nm^{-1}, was partially compensating for the dispersion of the span, amounting to 918 ps·nm^{-1}. This effect lead to a temporal compression of the optical pulses, leading to a higher instantaneous power during transmission, which was translated in stronger degradation of the received SNR due to nonlinear effects. At optimum power, the HNLF-based amplifier presented a SNR higher by 1 dB, compared to the DCF-based one. Even with a higher nonlinear fibre coefficient (γ) from the HNLF-based amplifier, after transmission of 1954.8 km, HNLF outperforms the DCF-based amplifier in the nonlinear regime.

The characterisation performed for *discrete* Raman amplifiers provides some interesting design guidelines to optimise their performance in a transmission system. Firstly, the use of the optimum length, defined using Eq. 3.5, for the gain fibre minimises pump power consumption. To minimise the amplifier noise figure a gain fibre with a high Raman gain coefficient is required. Finally, for long distance transmission, a gain fibre with positive dispersion is recommended to avoid the enhancement of nonlinear effects during transmission due to dispersion compensation. Although a characteristion including more fibre types, such as IDF [99] and the nonlinear fibre from [97] remains to be performed, it can be concluded that among the evaluated gain fibres HNLF is the most convenient solution for the design of *discrete* Raman amplifiers, albeit only 1 dB in received SNR improvement was found using this fibre type.

3.3 Distributed Raman amplifiers

Besides the possibility of providing gain in any spectral region, Raman amplifiers can also provide an improved noise performance when used in a *distributed* configuration. The reduced ASE noise performance can be used either to extend the distance between repeaters (pumping stages) for a transmission system with a fixed distance, or alternatively, to extend the transmission distance for fixed target received SNR.

Current research on *distributed* Raman amplifiers is focused on the reduction of impairments generated by the amplifier during transmission, such as ASE noise or RIN transfer, by adopting novel pumping configurations [141–144]. *Distributed* Raman amplifiers have also been used jointly with OPC to improve the NLC efficacy of OPC, as described in section 2.5. Experimental demonstrations lead the state-of-the-art research in *distributed* Raman amplifiers, with little attention given to numerical studies, and therefore, to the generation of nonlinear impairments.

In this section the benefits obtained by adopting a *distributed* Raman amplifier configuration are studied.

3.3.1 Noise comparison

The simplest pumping configuration of a Raman amplifier uses a single first-order pump to overcome fibre attenuation. Although forward pumping configuration is usually discarded due to the high RIN transfer [145], compared to the backward pump configuration, it is interesting to understand the performance limits of both configurations due to nonlinear effects.

A study of the linear noise generated for different amplifier configurations was performed to quantify the improvement provided by the use of a *distributed* Raman amplifier. For this study, a multi-span transmission link was assumed based on ultra-low loss single mode fibre, with the fibre parameters are listed in Table 3.2. The transmission distance was varied from a single span up to 10,000 km.

To calculate the ASE noise powers for the *distributed* Raman amplifiers Eq. 2.32

Table 3.2: Transmission fibre parameters

Parameter	Value
L_s	80 (km)
α_s	0.165 (dB/km)
α_p	0.2 (dB/km)
Ω	13 (THz)
$g_R@\Omega$	0.3 ($W^{-1}\cdot km^{-1}$)
$\omega_0/2\pi$	193.5 (THz)

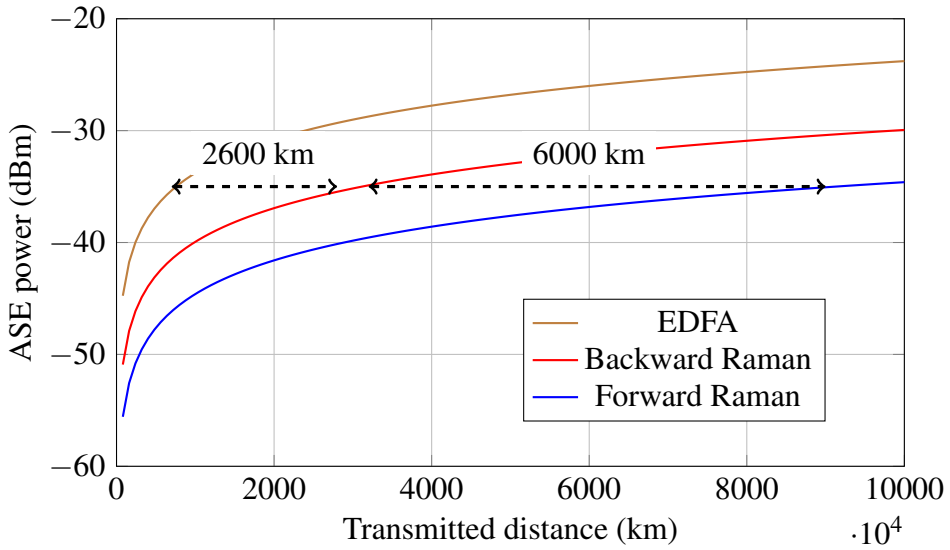

Figure 3.11: Total ASE noise power generated as a function of transmission distance. Brown, red and blue lines represent theoretical predictions for EDFA, backward and forward pumped *distributed* Raman, respectively.

was used. The calculated total ASE noise power generated for transmission over a 32 GHz bandwidth is shown in Fig. 3.11 as a function of the total transmission distance. The ASE noise generated using a backward and forward configuration was calculated, and it was compared to an ideal EDFA with a 3 dB noise figure. From the results it can be seen that both Raman configurations generate less ASE noise than an ideal EDFA for all studied distances. For a backward pumped configuration, an improvement of 6 dB was found in the ASE generation compared to the EDFA. This is translated to an increase of the transmission distance from 400 km to 3000 km for a target ASE noise level of -35 dB. The best performance was obtained by the use of a forward pump configuration. This configuration was shown to increase the transmission distance from 400 km to approximately 9000 km for an ASE level of -35 dBm. The use of forward pumping Raman presents a reduction of the ASE noise level of approximately 10 dB compared to an ideal EDFA.

Although the potential improvement in terms of ASE noise level offered by the use of *distributed* Raman amplification is extremely large, this is not necessarily directly translated into system performance. The increased average signal power over the transmission spans leads to an increase in the amount of NLI generated during transmission when employing *distributed* Raman amplifiers. Therefore, the received SNR of both pumping schemes is degraded, and the gains due to ASE noise generation are reduced. This effect has a greater influence in the forward pumping configuration. As the pump and signal propagate in the same direction along the transmission fibre, amplification is obtained in the first kilometres of the span. The higher average signal power along the span dramatically increases the NLI noise generated in transmission. Similarly,

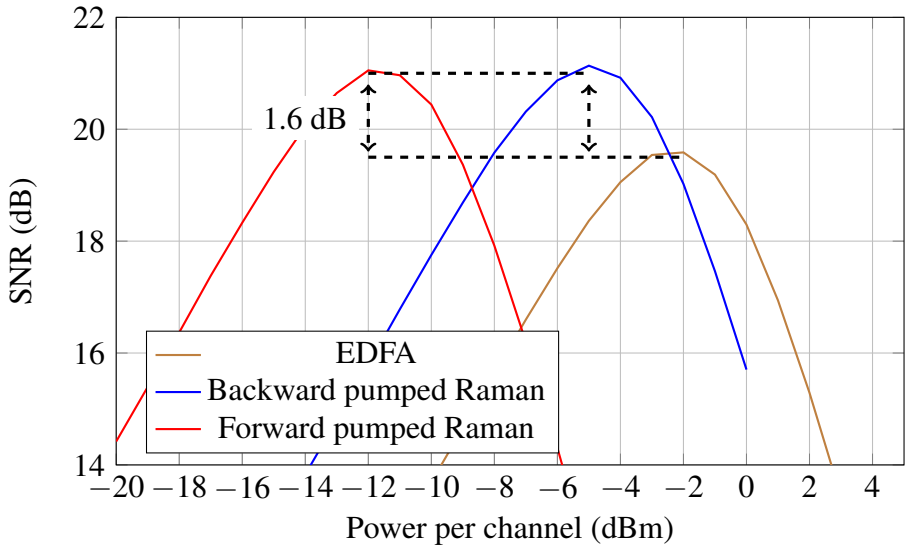

Figure 3.12: Received SNR as a function of signal launch power after the transmission of 2000 km. Brown, red and blue lines represent theoretical predictions for EDFA, backward and forward pumped *distributed* Raman, respectively.

the backward pump configuration also experiences an increased generation of NLI; however, as the signal is amplified towards the end of the fibre span the average signal power remains lower than in the forward pumping configuration. To quantify this effect, simulations were performed for the same fibre parameters presented in Table 3.2 and using a single PM-16-QAM channel. The results are presented in Fig. 3.12. The use of an ideal EDFA exhibits a maximum received SNR of 19.5 dB at a signal power of -2 dBm. The received SNR is increased to 21.1 dB using a *distributed* Raman amplifier. When RIN transfer is neglected, both forward and backward pumping configuration exhibited the same transmission performance due to a similar generation of nonlinear distortions.

3.3.2 Nonlinear distortions in distributed Raman amplifiers

As mentioned in the previous section, although *distributed* Raman amplifiers exhibit a large improvement in terms of the amount of ASE generated during transmission, the modified signal power profile leads to an increase in the NLI noise. To date, the use of NLC in Raman amplified systems has received limited attention, and few experimental demonstrations show gains of approximately 1 dB in the system Q-factor [63, 64], or an increase in transmission distance [65, 66] have been reported. While the benefits and challenges of DBP in EDFA-based optical systems are well known, a complete study of multi-span, *distributed* Raman systems has not been performed to date.

To study the performance of distributed Raman and EDFA-based systems, the GN-model [90] was used to estimate the NLI noise of both amplification schemes. The enhanced Gaussian noise (EGN) model requires an additional set of integrations to be

performed, which are usually computational time consuming, especially for non-ideal distributed Raman amplification and large optical bandwidths. For this reason and to ensure that the computational effort was manageable the modulation format dependence of NLI noise was neglected in this study.

Assuming that the NLI noise behaves as an additive noise source, SNR at the receiver is given by [146]

$$\mathrm{SNR} = \frac{P}{P_{\mathrm{ASE}} + P_{s-s} + P_{s-n}}, \tag{3.8}$$

with signal launch power P, ASE noise power P_{ASE}, NLI noise power resulting from signal-signal interactions P_{s-s} and NLI noise power resulting from signal-noise interactions P_{s-n}. This corresponds to an extension to Eq. (2.22) presented in section 2.3 including signal-noise interactions. When the system only compensates electronically for chromatic dispersion at the receiver, then the term P_{s-s} is much larger than P_{s-n} and so P_{s-n} can be neglected. When full-field DBP (FF-DBP) is performed the signal-signal interactions are fully compensated for at the receiver, and the term P_{s-s} is ideally reduced to 0. It is assumed that the NLI coefficients for signal-signal interactions are approximately equal to the ones of signal-noise interactions. The NLI terms are computed similarly to [146], where:

$$P_{s-s} = N_s^{1+\varepsilon} \eta P^3, \tag{3.9}$$

$$P_{s-n} \approx 3 P_{\mathrm{ASE}} \xi \eta P^2, \tag{3.10}$$

with

$$\xi \approx \sum_{k=1}^{N_s} k^{1+\varepsilon}, \tag{3.11}$$

with NLI coefficient η, number of spans N_s and coherence factor ε, responsible for coherent noise accumulation along the link. ε is calculated according to [90]. The NLI coefficient for the central channel is computed using:

$$\eta = \frac{16\gamma^2}{27 R_s^2} \int\int_{-\frac{B}{2}}^{\frac{B}{2}} \Pi\left(\frac{\omega_1 + \omega_2}{B}\right) \rho(\omega_1, \omega_2) d\omega_1 d\omega_2, \tag{3.12}$$

with total bandwidth $B = N_{ch} \cdot R_s$, where N_{ch} represents the number of channels, R_s the symbol rate, and $\Pi(x)$ denotes the rectangular function. The function $\rho(\omega_1, \omega_2)$ in Eq. (3.12) depends on the signal power profile along the span, and therefore, on the used amplifier scheme. The signal power profile of distributed Raman amplifiers is defined by the set of coupled differential equations defined in Eq. (2.27) and (2.28). For lumped-like amplification (e.g. EDFA) and non-ideal backward-pumped Raman amplification the functions $\rho(\omega_1, \omega_2)$ are given by (in the case of negligible pump

depletion)

$$\rho_{\text{EDFA}} = \left| \frac{1 - e^{\alpha_s L_s} e^{j\omega_1 \omega_2 \beta_2 L_s}}{\alpha_s - j\omega_1 \omega_2 \beta_2 L_s} \right|^2, \tag{3.13}$$

$$\rho_{\text{Raman}} = \left| e^{-\frac{g_R P_{p0}}{\alpha_p}} \int_0^{L_s} e^{-\alpha_s z} e^{\frac{C_R P_{p0}}{\alpha_p} e^{\alpha_p z}} e^{j\omega_1 \omega_2 \beta_2 z} dz \right|^2, \tag{3.14}$$

with the span length L_s, the group velocity dispersion parameter β_2 and the initial pump power P_{p0}.

Equations (3.8)–(3.14) were used to calculate the SNR at optimum signal launch power, the power at which the maximum SNR is found in the system. At optimum power, both the linear and nonlinear noise contribution are balanced to allow a maximum SNR. A relationship of 2:1 between the ASE and NLI noise powers is found at optimum power [57].

Expressions for the maximum SNR can be obtained from Eqs (3.8)–(3.14) for both amplification schemes, and for better theoretical understanding, the gain of FF-DBP relative to EDC only is expressed as the ratio between both SNRs to obtain:

$$\frac{SNR_{\text{FF-DBP}}}{SNR_{\text{EDC}}} = \frac{3^{\frac{1}{2}} N_s^{\frac{\varepsilon}{3}+\frac{1}{2}}}{2^{\frac{5}{3}} \xi^{\frac{1}{2}} \eta^{\frac{1}{6}} P_{\text{ASE}}^{\frac{1}{3}}} \tag{3.15}$$

For a fixed number of spans, the logarithmic scaling of Eq. (3.15) dependent on the NLI coefficient and the ASE noise is given approximately by:

$$\Delta \frac{SNR_{\text{FF-DBP}}}{SNR_{\text{EDC}}}[\text{dB}] \approx -\frac{1}{6}\eta[\text{dB}] - \frac{1}{3}P_{ASE}[\text{dB}]. \tag{3.16}$$

In addition to the possibility of studying the received SNR of the system either with EDC or FF-DBP, the GN-model offers the possibility to study different back-propagation bandwidths. To do this, Eq. (3.9) is redefined as:

$$P_{s-s} = (N_s^{1+\varepsilon_c} \eta_c - N_s^{1+\varepsilon_{DBP}} \eta_{DBP}) P^3, \tag{3.17}$$

where η_c and ε_c are the NLI coefficient and the coherence factor of the total transmitted optical bandwidth B in the transmission link. The back-propagated bandwidth is then defined as B_{DBP}, and η_{DBP} is the NLI coefficient of the back-propagated signals with coherence factor ε_{DBP}. Eq. (3.17) indicates the residual NLI noise over the central channel bandwidth after DBP is applied over a bandwidth B_{DBP}, and is an extremely useful tool in studying systems that employ optical bandwidths computationally hard to simulate.

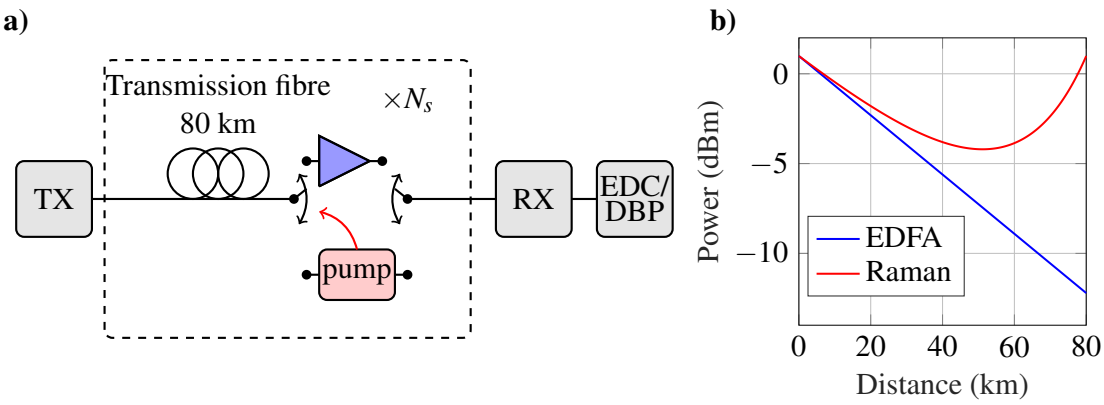

Figure 3.13: (a) Schematic of the simulation system. (b) Signal power profiles used for Raman (red) and EDFA systems (blue).

3.3.3 DBP in distributed Raman amplifiers

In the previous sections it was seen that the use of *distributed* Raman amplifiers increases the amount of NLI noise generated during transmission due to the modification of the signal power profile. However, they also offer a reduced ASE noise performance compared to any lumped amplification solution. The interaction, or balance, between both noise sources determines the system performance, with or without NLC schemes. This section focuses on the use of DBP as an NLC method for *distributed* Raman amplifiers, studying the gains and challenges presented by DBP in this configuration and comparing it to a typical EDFA amplified transmission link.

3.3.3.1 Simulation setup

Numerical simulations were carried out to analyse the transmission performance of a system using either EDFA or *distributed* Raman amplification, with the simulated system shown in Fig. 3.13(a). The transmitted signal consisted of 5 channels modulated at 32 GBd using PM 16-QAM and a RRC filter with a 0.1% roll-off factor. In both simulated cases the optical amplifiers were set to compensate exactly the loss of the span, and 480 mW was used as the Raman pump power for this purpose. The receiver performed either ideal EDC in the frequency domain or FF-DBP. DBP was implemented by solving the Manakov equation using the symmetrized SSFM (see appendix A) with negative signs on the fibre parameters, representing propagation in the opposite direction than the transmission fibre. A schematic diagram of the DBP implementation is shown in Fig. 3.14. Each *step* of the DBP algorithm evaluated the dispersion operator in the frequency domain, and the nonlinear operator in the time domain. The distributed gain, $g_0(z)$, was computed off-line for the Raman amplifier to match the signal power profile seen in Fig. 3.13 (b). When EDFA was used the distributed gain was set to zero. Each signal power profile generates different NLI noise during transmission, and in

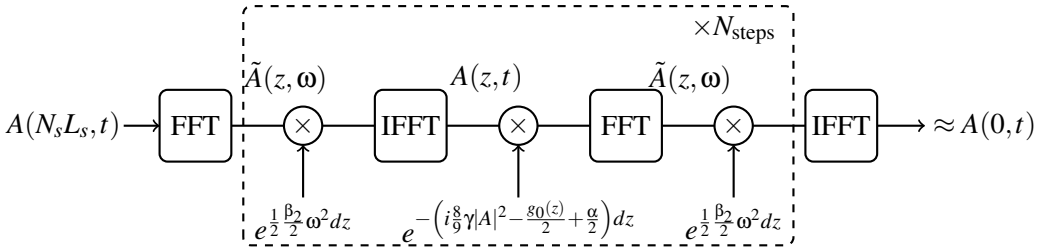

Figure 3.14: Schematic diagram of DBP implementation with distributed gain.

order to properly compensate signal-signal nonlinear interactions the power profile used for back-propagation needs to match that used in transmission. SNR was used as the performance metric of the numerical simulations. Additional fibre parameters can be found in Table 3.3.

Two different system scenarios were analysed in this work. The first corresponds to the transmission of a 5×PM-16-QAM channel, which will be called super-channel systems, and the performance of both amplification schemes was assessed at different distances through simulations and the GN-model. The second scenario extends the results to a fully loaded C-band system using the GN-model.

3.3.3.2 Super-channel system

The performance of the 2 systems was analysed for different distances, ranging from 2000 km up to 8000 km, and signal launch powers from -15 to 10 dBm per channel. SNR was measured for different signal powers and transmission distances and the results are shown in Fig. 3.15 and 3.16, respectively. In Fig. 3.15 it can be seen that the improved ASE noise performance from the distributed Raman amplifier offers a better performance in the linear regime, which is translated into a 2.9 dB higher SNR at optimum launch power compared to EDFA when only EDC is carried out at the receiver. Furthermore, a more severe degradation of the SNR in the nonlinear regime is clearly visible when Raman amplifiers are used, due to the higher signal power in the transmission fibre, as seen in Fig. 3.13(b). The use of FF-DBP at the receiver allows deterministic nonlinear distortions experienced during propagation to be compensated

Table 3.3: Fibre parameters

Parameter	Value
Attenuation coefficient @ 1550 nm (α_s)	0.160 (dB)
Attenuation coefficient @ 1450 nm (α_p)	0.20 (dB)
Dispersion parameter (D)	16.2 (ps·nm^{-1}·km^{-1})]
Nonlinear coefficient (γ)	1.2 (W^{-1}km^{-1})
PMD	0 (ps$\sqrt{km}$)
Span length (L_s)	80 (km)
Raman gain coefficient (g_R)	0.2 (W^{-1}km^{-1})

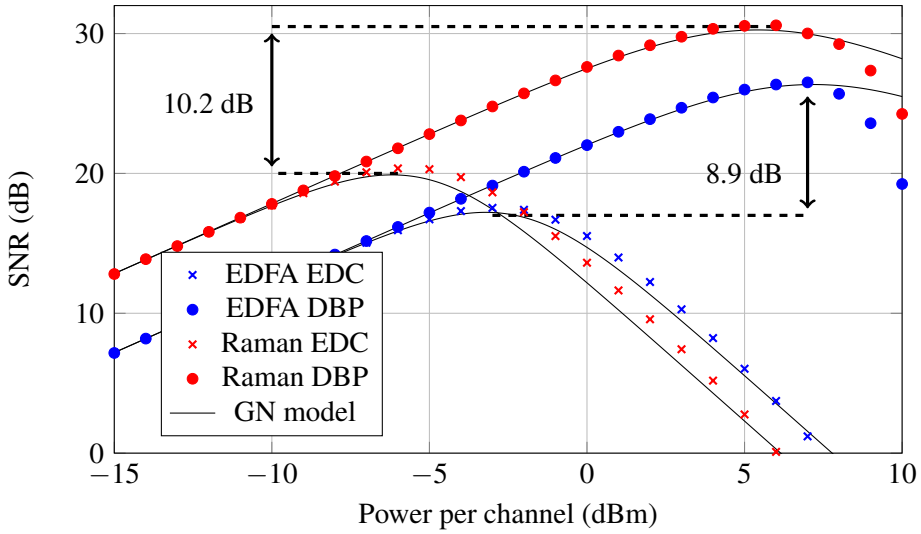

Figure 3.15: Received SNR as a function of signal launch power at 2000 km. Blue and red markers represent EDFA and Raman simulated systems, respectively. Crosses correspond to EDC only and circles correspond to the use of DBP. Solid lines represent GN model predictions.

for, thus enhancing the SNR. At 2000 km in the EDFA system, back-propagating all 5 transmitted channels resulted in an increase in the maximum SNR of 8.9 dB, compared to EDC only. However, when FF-DBP was applied in the Raman amplified system, an increase of 10.2 dB was found, compared to the EDC only case. Equation (3.16) offers insight into the parameters of the optical system that influence the achievable SNR gain when applying FF-DBP. A higher NLI coefficient leads to a decrease in the gain of FF-DBP. Likewise, a larger ASE noise contribution from the amplification process will have the same effect. Backward-pumped Raman amplification exhibits a higher nonlinear distortion coefficient due to a higher average power along a span; however, the improved ASE noise performance leads to a larger FF-DBP gain in Raman systems compared to the gain in EDFA systems. For the analysed system, the use of distributed Raman amplification together with FF-DBP exhibits a gain 1.3 dB higher, than in the EDFA case. Additionally, it is worth noting the good agreement between simulations and the GN-model for both amplification schemes, at least up to optimal launch power when EDC and DBP were applied at the receiver, as can be seen in Fig. 3.15. Using FF-DBP, beyond optimal power a first-order perturbation analysis is not accurate to discribe the performance of the system, and second-order signal-noise interactions need to be included in the used model[147, 148].

The SNR at optimal launch power was measured as a function of the transmission distance and the results are plotted in Fig. 3.16. In the absence of nonlinearity compensation, the use of distributed Raman amplification always offers a better performance than EDFA, with 2.9 dB higher SNR at optimal signal launch power. This benefit is enhanced by the use of FF-DBP, with an improvement in SNR (up to 4.2 dB) at all evaluated distances, consistent with the theory described by Eq. (3.16). The observed

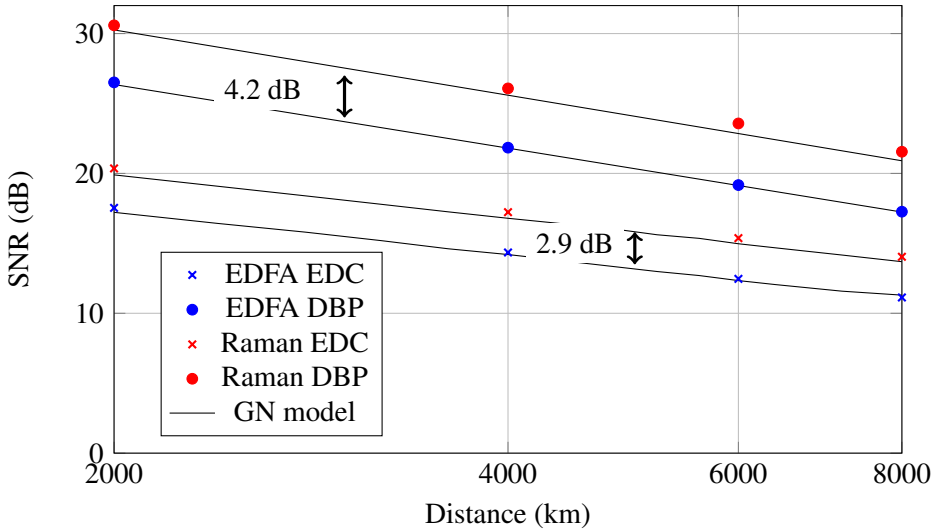

Figure 3.16: Received SNR as a function of distance at optimum launch power. Blue and red markers represent EDFA and Raman simulated systems, respectively. Crosses correspond to EDC only and circles correspond to the use of DBP. Solid lines represent GN model predictions.

FF-DBP gains for the EDFA system at 2000, 4000, 6000 and 8000 km were 8.9, 7.5, 6.7 and 6.1 dB respectively. The FF-DBP gains observed in the Raman systems were 10.2, 8.8, 8.2, and 7.5 dB for the same distances. This means that the 1.3 dB increase in NLC gain presented by the Raman based system is maintained even at longer distances, where DBP gains are decreased due to the interaction between ASE noise and nonlinear distortions.

The DBP algorithm needs to properly match the power profile from the signal in the forward propagation to compensate for deterministic nonlinear effects that take place during transmission, as a result the use of backward-pumped distributed Raman amplification, with a more complex signal power profile, leads to an increase in computational complexity, due to the increased number of steps required for the SSFM in the backward direction to obtain the maximum gain from the DBP algorithm. For the systems studied the algorithm complexity was evaluated at 2000 km by measuring the number of steps per span required to obtain the maximum gain when applying FF-DBP. The signal power profiles used are shown in Fig. 3.13 (b), and, in order to perform a fair comparison, no simplified variants of the SSFM (e.g. logarithmic step for EDFA) were used in the DBP algorithm to reduce the number of steps per span on either amplification schemes. To assess the DBP complexity, the number of steps per span was swept from 1 to 400 in increments of 40 for both amplifier schemes. Figure 3.17 shows the gain in SNR after DBP was performed as a function of the number of steps per span used in the algorithm. For the EDFA system a total number of 160 steps per span were required to achieve the maximum gain from DBP, showing good agreement with previous studies in this area [123]. For the Raman-amplified system however, 200 steps per span were required to obtain a larger gain than EDFA. This represents a 25% increase in the

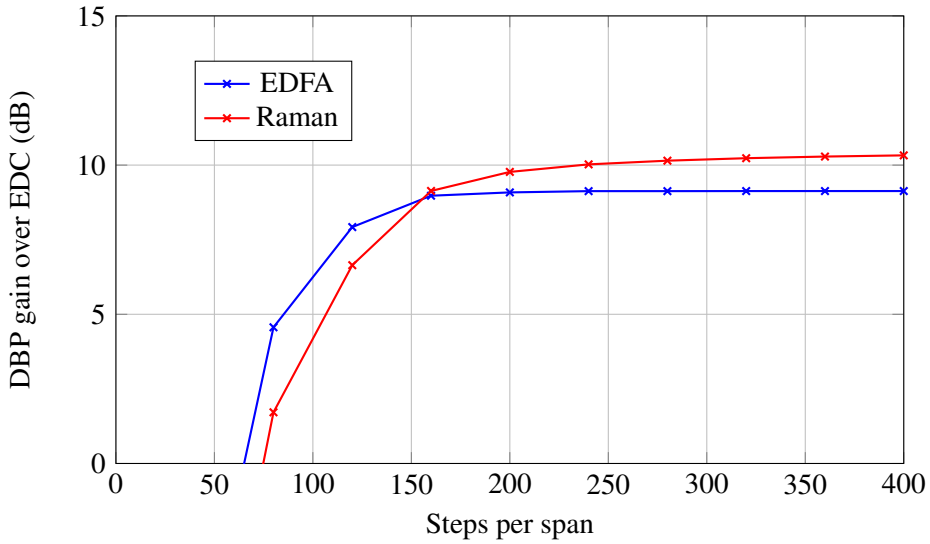

Figure 3.17: Gain obtained from performing FF-DBP using different steps per span. Blue and red markers represent EDFA and Raman simulated systems, respectively.

required number of steps to achieve the maximum gain from DBP. During transmission, the signal experiences power-dependent phase shifts from nonlinear interactions. In the presence of distributed amplification the nonlinear phase shifts are distributed along the fibre span as the signal power does not experience large losses during propagation. EDFA-based systems, on the other hand, experience the majority of the nonlinear effects in the first kilometres of the fibre span, where the signal power is highest. For this reason, the signal power profile from distributed Raman amplifiers is responsible for the complexity increase in the DBP algorithm and the larger number of steps required to fully compensate for the impairments experienced during transmission. Additionally, the use of an insufficient number of steps for back-propagation leads to an incomplete compensation of the nonlinear distortions, resulting in lower gains than expected, or even detrimental effects due to back-propagation inaccurately compensating for the nonlinear effects experienced during transmission effects. For the Raman-amplified case, the use of less than 80 DBP steps leads to detrimental effects.

3.3.3.3 Fully loaded C-band system

The study of large bandwidth systems requires complex computational simulations or experimental demonstrations. Each one of them come with limitations, such as the availability of computational resources for simulations or implementation penalties that limit the gains expected from nonlinearity compensation. Analytical models however, offer the possibility of studying a variety of systems, and good agreement with simulations and experimental demonstrations has been previously shown [90]. In order to study the benefits of DBP for both amplification schemes in a more practical transmission environment, a system with a total of 155 WDM channels, occupying the

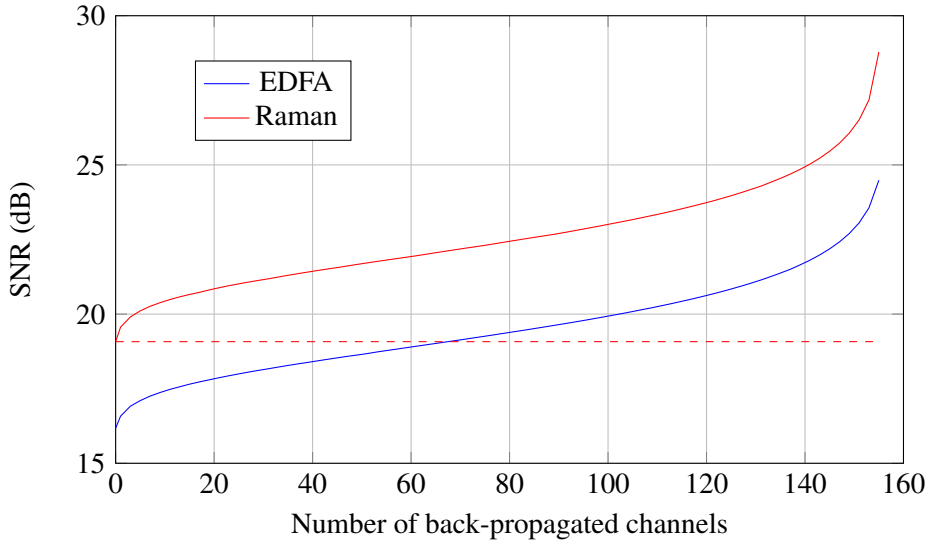

Figure 3.18: Received SNR as a function of back-propagated bandwidth for C-band loaded Raman and EDFA amplified systems. Solid lines represent the SNR after DBP, dashed line represents the EDC performance of the Raman amplified system. Blue and red lines represent EDFA and Raman simulated systems, respectively.

entire C-band (≈ 4.96 THz), was analysed using the GN-model. All the other system parameters remain the same as in the previous numerical studies in this chapter.

Equation (3.17) was used to explore the benefits of back-propagating a different number of channels over a distance of 2000 km. The number of back-propagated channels was varied from 0 (EDC-only) to 155 (FF-DBP) and the SNR values at the respective optimum signal launch power were calculated. The calculated SNR values for both systems as a function of the back-propagated bandwidth are shown in Fig. 3.18. The maximum SNR of the EDFA system using EDC was found to be 16.2 dB at a signal power of -6 dBm per channel, while in the Raman case, SNR was 19.1 dB at -9 dBm per channel.

In the absence of DBP, distributed Raman amplification exhibited 2.9 dB higher SNR compared to the EDFA, showing similar gain in performance as the super-channel system. As the number of back-propagated channels increases, the NLI arising from signal-signal interactions is mitigated, increasing the gain experienced in both amplification schemes. When approaching FF-DBP, the term P_{s-s} presented in Eq. (3.17) tends to zero, therefore the gain experienced by the system will be limited by the interaction between nonlinear effects and ASE noise, as shown in Eq. (3.16). The result of compensating all the deterministic nonlinear effects in the Raman amplified system yields a 4.4 dB improvement for the studied transmission system compared to the use of EDFA. In general, the use of DBP in Raman systems offers improved performance for all the back-propagated bandwidths studied with a maximum improvement obtained when FF-DBP is used. Moreover, the Raman amplified system using only EDC outperforms the EDFA system even with the use of DBP over a small number of back-propagated

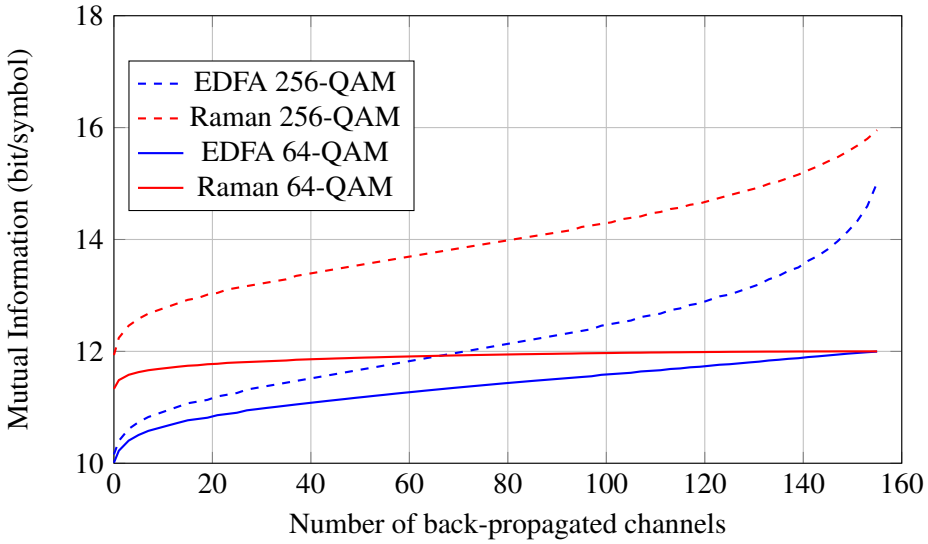

Figure 3.19: Received mutual Information as a function of back-propagated bandwidth for C-band loaded Raman and EDFA amplified systems. Solid lines represent the MI using 64-QAM, dashed line represents MI using 256-QAM. Blue and red lines represent EDFA and Raman simulated systems, respectively.

channels. In order to obtain the same SNR in an EDFA system, DBP needs to be applied over 70 channels, which corresponds roughly to 45% of the transmitted bandwidth.

The system throughput is directly related to the SNR and the modulation format used to transmit information, as described in chapter 2. Therefore, different gains in SNR after DBP will translate into different system throughputs. To quantify the benefits of DBP on the achievable rates in both studied amplification schemes, the MI for the modulation formats of PM 64- and PM 256-QAM was calculated. Both modulation formats were chosen due to the large SNR obtained for the systems under study, as seen in Fig. 3.18. The obtained SNR values from Fig. 3.18 were used to calculate MI using Monte-Carlo estimation under an AWGN channel assumption, as described in chapter 2, and is shown as a function of the number of back-propagated channels in Fig. 3.19. For example, if 64-QAM is used as the modulation format, the 16.2 dB SNR obtained for the EDFA with EDC system is translated into 10 bits per symbol. As expected, the highest achievable rates are given by the modulation format with the highest number of constellation points. The highest possible MI for 64-QAM, 12 bits per symbol (6 b/sym over both polarisations), is obtained when the back-propagated bandwidth is increased to 60 channels in the Raman system. In the EDFA system however, this value is only achieved by performing FF-DBP. The use of 256-QAM offers similar gains in MI for both amplification schemes. However, the Raman system exhibits higher MI for all the studied back-propagated bandwidths due to the higher SNR offered by this amplification scheme. In general, higher SNR and SNR gains obtained with the use of distributed Raman amplification, compared to EDFA-based systems, are translated into higher achievable information rates.

3.4 Summary

In this chapter, the physical properties of Raman amplifiers were studied together with the advatanges they offer when used in optical communication systems. *Discrete* Raman amplifiers were studied due to the possibility of extending the amplifier bandwidth compared to traditional EDFA amplifiers, and *distributed* Raman amplifiers were studied focusing on the reduced linear noise they generate. The key results from this chapter are the following:

- The performance of Raman amplifiers as a replacement for conventional EDFAs was experimentally and numerically studied. Highly nonlinear fibre (HNLF) and dispersion compensating fibre (DCF) were studied as gain mediums to build *discrete* Raman amplifiers with 70 nm of bandwidth. HNFL was shown to be the best medium presenting some performance improvement in transmission due to the generation fewer nonlinear distortions, compared to DCF.

- For the first time the benefits of using *distributed* Raman amplifiers together with full-field DBP in long haul transmission systems were quantified. The use of FF-DBP in *distributed* Raman amplifier-based systems presented an additional 1.3 dB gain in SNR with respect to EDFA, for all evaluated distances. However, due to the characteristic signal power profile of distributed Raman amplifiers, the complexity of the DBP algorithm is increased, requiring an increase of at least 25% in the number of steps per spans used.

- For a system utilising the entire C-band, distributed Raman amplification was found to outperform EDFAs for any back-propagated bandwidth. In fact, only compensating for chromatic dispersion in Raman systems exhibits better performance than the use of DBP with EDFA amplification when less than 45% of the bandwidth is back-propagated.

- Even in the presence of higher nonlinear distortions, *distributed* Raman amplifiers are an attractive solution to increase system capacity. This is due to their improved performance when DBP is used, leading to higher achievable information rates compared to EDFA solutions, in addition to the possibility of extending the bandwidth beyond the conventional EDFA limitations.

4

Extending the fibre transmission bandwidth

OPTICAL FIBRES are the fundamental transmission medium for modern communication systems. Among their most attractive features is that they present a low-loss region that spans tens of Terahertz. Alternative optical amplification solutions need to be considered to fully exploit this potential, such as Raman amplification discussed in the previous chapter. The nonlinear nature of silica fibres however, implies that as the signal bandwidth grows larger, nonlinear interactions also become stronger, increasingly degrading the performance of the communication system.

A solution to increase the capacity of optical communication system is the use of a larger optical bandwidth. Therefore, the work described in this chapter studies the growth and generation of nonlinear distortions in wideband transmission.

An experimental study on the generation of NLI noise arising from Kerr nonlinearity as a function the signal bandwidth is described in section 4.1, and evaluation of the accuracy of analytical models presented in the literature is performed in this ultra-wideband regime.

With the transmission of larger optical bandwidths the inter-channel stimulated Raman scattering (ISRS) effect becomes increasingly important. For this reason, section 4.2 reports the experimental study of the impact ISRS has on an ultra-wideband transmission system, namely, how it modifies the NLI noise, and the use of DBP as a way to mitigate this effect. Additionally, a proposed modification to the GN model in

[60] to account for ISRS was experimentally validated.

Finally, in section 4.3, the potential throughput increase that can be obtained by increasing transmission bandwidth is theoretically studied using the experimentally validated models.

4.1 Implications of increasing the transmission bandwidth on fibre nonlinearities

There are a number of physical effects, described in chapter 2, which limit the achievable rates and overall throughput of optical fibre communication systems. Significant efforts have focused on understanding and modelling the impact of NLI noise on optical fibre system performance and achievable information rates. The validity of these models, including the GN model described in section 2.3, has been assessed for several transmission fibre types and modulation formats via numerical simulations [57]. Due to the computational complexity required to simulate the propagation of large optical bandwidths using the SSFM, these validations have typically been limited to a small number of channels, e.g. 5 and 15 channels in [90, 149] respectively. Experimentally, several papers have shown good agreement with the model prediction [58, 59, 150] up to 3.5 THz, and results as a function of distance, at optimum signal power, for C-band systems have been reported [151]. However, a detailed experimental study analysing a variety of bandwidths and signal powers in the nonlinear regime has not been performed to date.

This section focuses on experimentally studying how NLI noise grows in an optical communication system as a function of the transmitted optical bandwidth and the results are compared to the predictions of the GN model. Moreover, the performance degradation of the transmission system is assessed, quantifying the achievable rates in the presence of nonlinear distortions.

4.1.1 Methodology

The study of any noise source in a transmission system requires a complete knowledge of the system parameters and the characteristics of the subsystems used. Subsystems, such as the transmitter and receiver, will introduce different amounts of noise at different stages of the system; however, if the amount of noise introduced by the transceiver subsystem is known, the study of the NLI noise generation remains feasible. This work assumes that the noise generated by the transceiver subsystem, ASE noise and NLI noise are independent and uncorrelated. Although interactions between different noise sources do exist during signal propagation, they remain relatively small compared to ASE, NLI and transceiver noise. Therefore, in the absence of nonlinearity compensation

they can be neglected. For example, as shown in the previous chapter in Eqs. (3.9) and (3.10), signal-signal interactions grow proportional to the signal power cubed, while signal-noise interactions grow proportional to the signal power squared. In this case, it is possible to use the methodology proposed in [152] to estimate the total noise variance after transmission. Here the different noise contributions are added in the form:

$$\sigma^2_{\text{total}} = \sigma^2_{\text{ASE}} + \sigma^2_{\text{NLI}} + \sigma^2_{\text{TRX}}, \tag{4.1}$$

where σ^2 represents the variance of a noise source, and the sub-index ASE, NLI and TRX represent ASE noise, NLI noise and transceiver noise, respectively. The quantity σ^2_{TRX} needs to be characterised in a back-to-back configuration with the same parameters used for the transmission system. Using this approach, the received SNR after transmission can be estimated using the following extension to Eq. (2.22):

$$SNR = \frac{P_{ch}}{P_{ASE} + P_{NLI} + P_{TRX}}, \tag{4.2}$$

where the noise from the transceiver subsystem $P_{TRX} = \sigma^2_{TRX}$. Using the experimentally measured SNR at the receiver and the measured values of ASE noise and transceiver characteristics, Eq. (4.2) was used to extract the NLI noise variance.

4.1.2 Transceiver characteristics

For this experimental work, the transmitter and receiver that comprise the ONG testbed, described in section 2.6, were used. For this experiment, seven ECLs were used as light sources and were modulated using 64-QAM with a 0.1% roll-off factor RCC shape at a rate of 40 GBd. Dual polarisation signals were obtained using a PM emulation stage described in section 2.6. The channels were spaced 41 GHz apart and were centred at 193.5 THz. SS-ASE noise was used to emulate the transmission of larger optical bandwidths. The propagated bandwidths used in this work were 40, 280, 600, 1200, 2500, 4100 and 7300 GHz. The C-band extended from 1535 to 1566 nm and the L-band was occupied from 1570 to 1591 nm. A gap of 4 nm between the C and L-bands was necessary to perform optical amplification in each band, due to the use of WDM combiners and the spectral roll-off they present. At the receiver, the optical BPF was set to 125 GHz to allow joint reception of 3 channels.

The transceiver performance was characterised as a function of the received optical signal to noise ratio (OSNR). This was performed by coupling the generated signal together with an ASE noise source before the coherent receiver, allowing the control of the OSNR by adjusting the amount of added ASE noise. The characterisation is shown in Fig. 4.1, where the received SNR is plotted as a function of the signal OSNR. The OSNR was measured using an optical spectrum analyser with a resolution of 0.1 nm

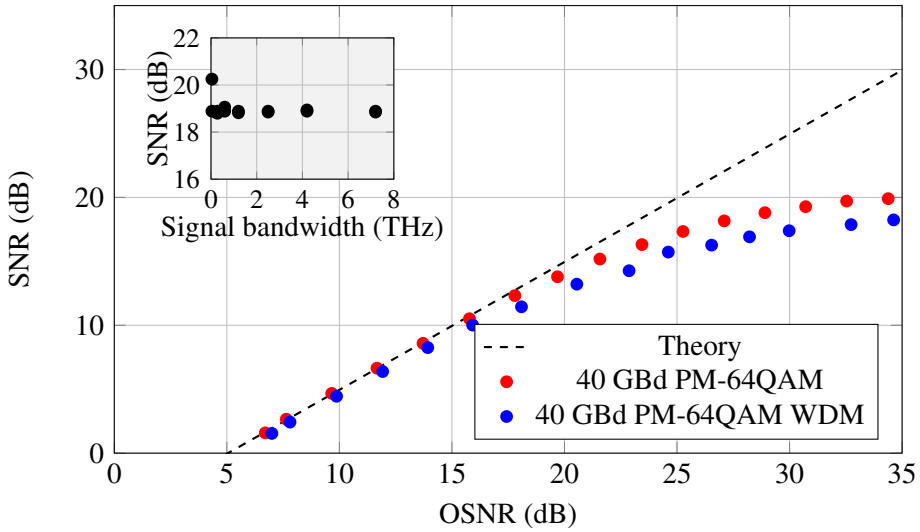

Figure 4.1: Back-to-back characterisation of the transceiver subsystem. Received SNR as a function of signal OSNR measured in 0.1 nm bandwidth. Red markers represent single channel system and blue markers WDM system. Inset shows the maximum SNR in back-to-back configuration, corresponding to SNR_{TR}, for all the signal bandwidths under investigation.

connected to one of the outputs of the coupler used to combine the signal with the ASE. A linear relationship between SNR and OSNR was observed for OSNR values below 16 dB. Higher OSNR resulted in a small increase in the SNR, which was eventually saturated after reaching 20 dB for a single channel and 19 dB in the WDM case. Beyond this point, increasing the OSNR does not increase the received SNR, mainly due to the noise introduced by the electrical components of the transceiver, such as the limited effective number of bits (ENOB) of the DAC and sampling scope, and the electrical amplifiers to drive the optical modulators. In this experiment, the ENOB of the DAC was of 5 bits at 15 GHz, and the electrical amplifiers had a noise figure of 6 dB at 15 GHz.

The inset of Fig. 4.1 shows the maximum SNR in the back-to-back configuration for all the signal bandwidths under investigation. A SNR of 20.1 dB was obtained when a single channel of 40 GBd was generated and detected, however, a penalty of approximately 1 dB was found when transmitting a larger bandwidth. This penalty arises from the use of digital oscilloscopes with interleaved analogue-to-digital converters (ADC) for the sampling of large bandwidth signals. This penalty is observed when the received signal occupies the entire oscilloscope bandwidth. The average received SNR for WDM signals is 18.9 dB, this value corresponds to σ^2_{TRX} in Eq. (4.2) and was used to calculate the theoretical SNR. The high extinction ratio of 35 dB from the WSS allowed for the OSNR of the transmitter, of 35 dB as seen in Fig. 4.1, to be maintained after combining the signal with the SS-ASE. Thus, the transmission of signals occupying bandwidths beyond 280 GHz was not affected by the introduction of additional penalties due to ASE accumulation.

4.1.3 Transmission setup

The experimental setup used to study the accumulation of NLI noise as a function of optical bandwidth is shown in Fig. 4.2. A single span recirculation loop was used to emulate long distance transmission. It is important to highlight that a single span recirculating loop only underestimates the transmission system performance in the linear regime compared to a straight-line system or a multi-span loop. This is because the ASE noise introduced by the EDFAs used to overcome the losses of the passive components. However, this does not change the nonlinear behaviour of the transmission system. The recirculating loop comprised a pair of acousto-optic modulators (AOM) acting as switches to determine when new light enters the loop and when the transmission is finished. A loop synchronous polarisation scrambler (PS) was used to ensure random polarisation rotations during transmission and a WSS was used as a dynamic gain flattening filter to compensate for any gain variation as a function of wavelength arising from operating the EDFAs using different input powers. The WSS in the loop was configured to filter the optical spectrum for maximum spectral flatness. The filter shapes were designed by measuring the optical spectrum at the output of every recirculation and applying the inverse profile to the WSS. This was done for every transmission distance at optimum launch power for the 7.3 THz signals. Subsequently, at 1010 km, the filters were updated, again using the received optical spectrum, for every signal launch power. Finally, the same filters were used for the transmission of smaller bandwidths. Optical amplification in the loop was carried out in separate bands by EDFAs. The maximum output power of the C- and L-band EDFAs was 33 and 23 dBm, respectively, hence the maximum signal power per channel for C+L-band transmission was limited to 4 dBm in order to maintain a constant PSD between both transmission bands. Since no optical power was inserted in the gap between the two transmission bands, that region of the spectrum did not contribute to the increase of NLI noise in the transmission system. Finally, the fibre span used was a 101 km of Corning® Vascade® EX2000 Fiber with an attenuation coefficient of 0.160 dB/km, dispersion parameter of 20.2 ps·nm^{-1}·km^{-1} and nonlinear coefficient of 0.85 W^{-1}km^{-1}. The signal power into the fibre span was controlled using a variable optical attenuator and monitored using a 2% tap and an optical spectrum analyser with a resolution of 0.1 nm. As an example, the transmitted spectrum of 7.3 THz is shown in Fig. 4.3.

4.1.4 NLI-induced impairments

The study of the accumulation of NLI noise over different bandwidths was first performed using a fixed transmision distance of 1010 km, corresponding to 10 fibre spans. From [57], a minimum accumulated dispersion needs to be reached in order for the signal to be statistically similar to a Gaussian process. Although this "Gaussianity"

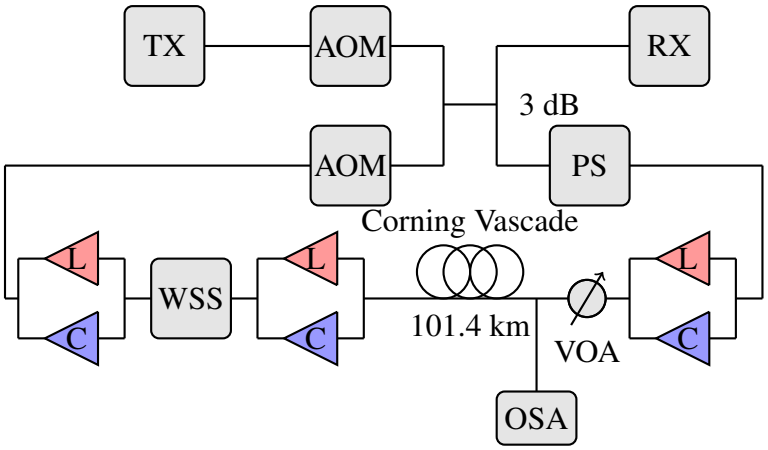

Figure 4.2: Schematic of experimental setup.

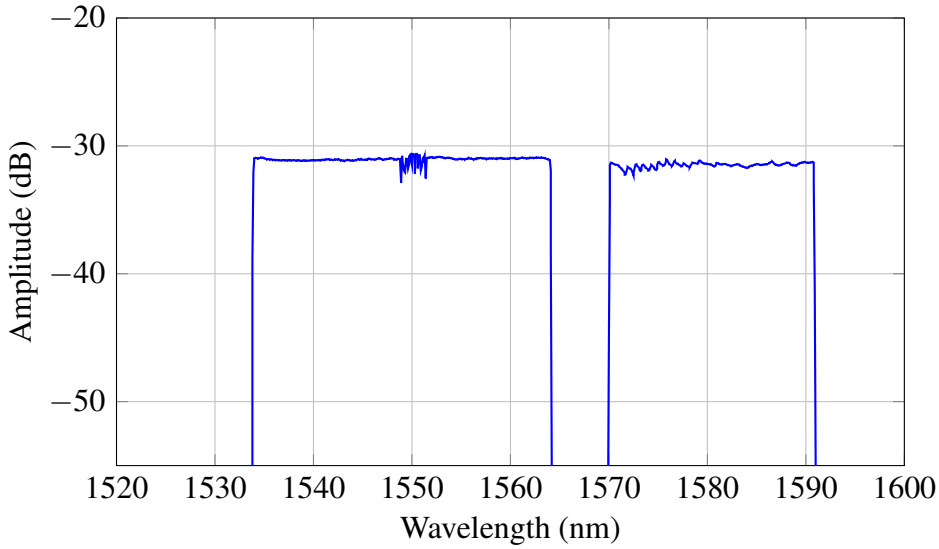

Figure 4.3: Optical spectrum of the transmitted signal measured using an optical spectrum analyser with 0.1 nm resolution.

assumption is never completely fulfilled using square QAM formats with a finite cardinality, after approximately 200 km of fibre this condition is sufficiently achieved to ensure accurate predictions using the GN model.

The first experiment consisted of a signal launch power sweep from -10 dBm per channel to the maximum output power allowed by the EDFAs. The received SNR as a function of the signal launch power is shown in Fig. 4.4. A difference of up to 0.8 dB was seen in the linear regime, highlighted in the figure, due to the different operation points of the EDFAs during transmission. Although the WSS was used to flatten the transmitted spectrum, this procedure failed to keep the noise performance of the EDFAs constant. Here, as the optical bandwidth is increased, a higher total power is transmitted for a fixed PSD, thereby changing the dynamics of the EDFAs and their noise figure. Another factor that influences the linear noise performance is the power equalisation process performed by the WSS within the recirculating loop. As

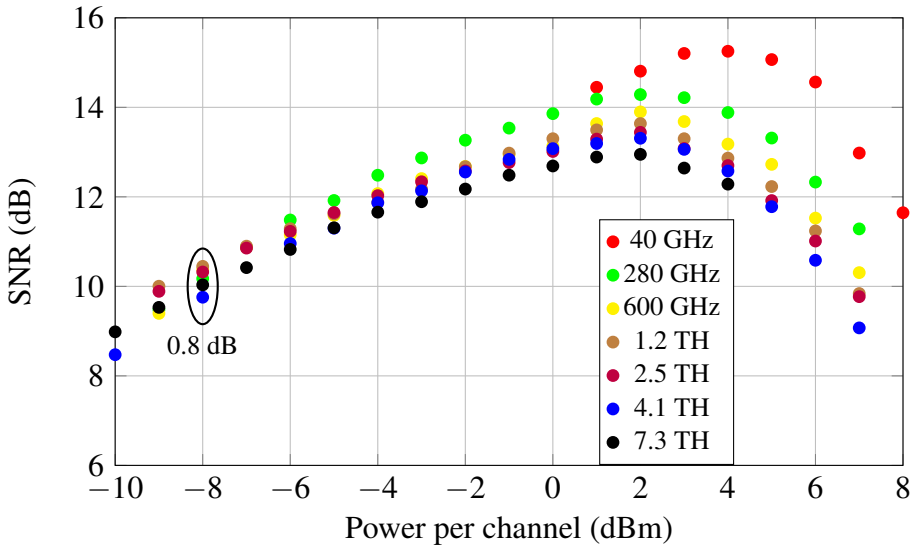

Figure 4.4: Experimental performance of the transmission system for all bandwidths under study after 1010 km transmission.

the propagated bandwidth is increased, the tilt from the EDFAs becomes larger and the WSS must be adjusted accordingly to correct the tilt, leading to different overall loop loss. From this figure, it is also possible to see that nonlinear effects continue to grow when the bandwidth is increased, with the highest SNR obtained for the transmission of a single channel of 15.25 dB, this is then reduced to 12.95 dB for 7.3 THz due to NLI noise.

Subsequently, the obtained results were compared to the predictions provided by the GN model using Eq (4.2). The NLI noise variance it is equal to:

$$P_{NLI} = \eta P_{ch}^3, \tag{4.3}$$

using η as defined in chapter 2 in Eq. (2.23). This was calculated using the transmission fibre parameters and the transmitted signal spectrum. Additionally, the ASE noise variance was measured from the experimental data for all the studied bandwidths at -8 dBm per channel. This power is low enough to guarantee that the generated NLI noise is negligible compared to the ASE level, allowing precise estimation of the ASE noise. Finally, the noise from the transceiver subsystem was obtained from the initial characterisation, and the results for all studied bandwidths can be seen in the inset of Fig. 4.1.

The SNR as a function of the signal launch power for different transmitted bandwidths is shown in Fig. 4.5. Towards the highly nonlinear regime, beyond 2 dBm per channel, for a fixed signal launch power, a penalty in SNR can be observed as the transmission bandwidth is increased. This behaviour is expected from the growth of the NLI noise power. For instance, at a launch power of 4 dBm per channel, the difference

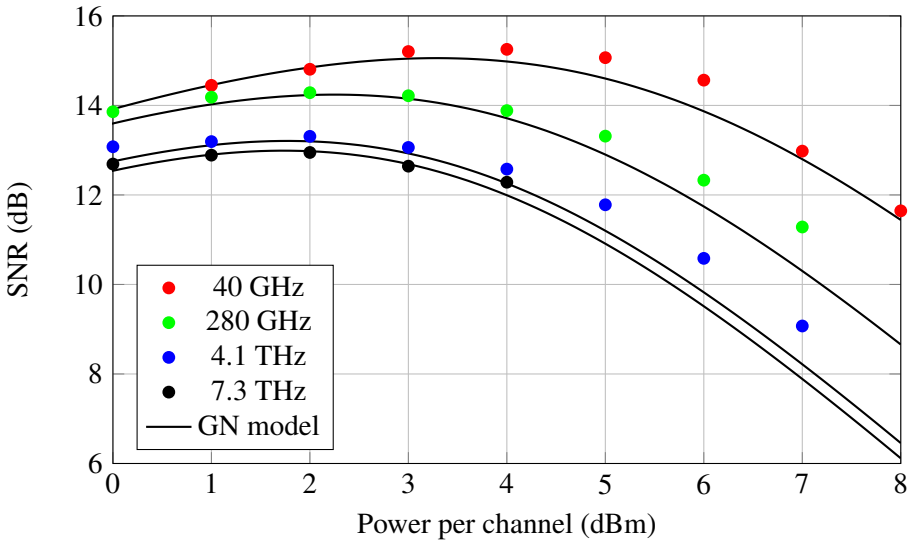

Figure 4.5: Performance of the transmission system for different transmitted bandwidths after 1010 km, solid lines represent the predictions obtained using GN model and markers correspond to experimental data.

observed in SNR between the transmission bandwidths of 40 GHz and 7.3 THz is approximately 2.7 dB. Figure 4.5 additionally depicts the performance of the system using solid lines for all the evaluated bandwidths obtained using the GN model. As discussed in chapter 2, one well-known limitation of the GN-model is the assumption that the transmitted signal behaves statistically like a Gaussian process, neglecting modulation format dependence of the NLI noise. The fact that modulated signals do not behave statistically as a Gaussian process even after a substantial amount of chromatic dispersion, is translated into an overestimation of the NLI noise by the GN model. This overestimation of the NLI noise variance leads to an underestimation of the system performance in the nonlinear regime when SNR or MI is used as a performance metric. Even though this issue has been addressed in the literature [153, 154], and alternative or improved models have been proposed, the use of the EGN model leads to additional complexity when computing the NLI noise power, especially for large bandwidth systems. Using the experimental data, the GN model was confirmed to give a slightly pessimistic prediction of performance in the nonlinear regime for the all evaluated bandwidths. For example, a penalty of 0.6 dB was found between the experiment and the predictions from the GN model at a signal power of 6 dBm per channel. The performance underestimation is reduced as the transmitted bandwidth increases for this experiment for one main reason: bandwidths greater than 280 GHz were transmitted using modulated signals together with SS-ASE. SS-ASE was generated from ASE noise that is usually modelled using Gaussian statistics. Therefore, NLI noise affecting the signal under test arising from wavelengths transmitting SS-ASE will agree with the GN model calculations.

The underestimation of the system SNR in the nonlinear regime, however, is reduced at optimum power and the experimental data is seen to be in closer agreement with the GN model. This effect is due to the balance between the linear and noise variances. At optimum signal power and in the absence of transceiver noise, a 2:1 ratio between the linear and nonlinear noise is found [57], which leads to a closer agreement in the difference between the predictions of the GN model and the experimental data according to the rule (as seen in [57, Eq. (32)]):

$$\Delta\mathrm{SNR}[\mathrm{dB}] \approx -\frac{1}{3}\Delta\eta[\mathrm{dB}], \tag{4.4}$$

where $\Delta\mathrm{SNR}[\mathrm{dB}]$ and $\Delta\eta[\mathrm{dB}]$ are the observed difference between the GN model and experimental data in SNR at optimum power and in NLI coefficient, respectively.

Once the overall performance of the system was studied using the received SNR as performance metric, the total amount of NLI noise generated during transmission was studied. In order to analyse the growth of the NLI noise as a function of transmitted bandwidth, the NLI noise power was obtained from the experimental results at a distance of 1010 km. To carry this out the following method was used: firstly, the received SNR was measured in the linear regime (at -8 dBm per channel as in the previous results), where NLI noise is negligible. This way it was possible to estimate the linear noise (P_{ASE}). Secondly, to estimate the nonlinear noise, the received SNR was measured at high signal launch power (+4 dBm per channel) and the NLI noise power was extracted using the following:

$$\frac{1}{\mathrm{SNR}_{\mathrm{NLI}}} = \frac{1}{\mathrm{SNR}} - \frac{1}{\mathrm{SNR}_{\mathrm{ASE}}} - \frac{1}{\mathrm{SNR}_{\mathrm{TRX}}} \tag{4.5}$$

Figure 4.6 shows the NLI noise power as a function of transmitted bandwidth. A closed-form expression was presented to calculate the NLI coefficient for a single span, defined as [57, Eq. (14)]):

$$G_{NLI}(0) \approx \frac{8}{27}\gamma^2 G_{WDM}^3 \frac{log_e(\pi^2 \beta_2 L_{eff,a} B_{WDM}^2)}{\pi\beta_2 L_{eff,a}}, \tag{4.6}$$

where B_{WDM} corresponds to the signal bandwidth. From Eq. (4.6) it is seen that the NLI coefficient is proportional to the logarithm of the total transmitted bandwidth. This same trend can be observed in Fig. 4.6, where the NLI noise power grows in a logarithmic way as the bandwidth is increased. The dashed line represents the predictions from the GN model using Eq. (4.3). An offset between the model and the experiment can be seen; this is again due to GN model NLI noise overestimation issue. For a bandwidth of 40 GHz, a difference of 1.5 dB was found between the model and experiment, and for a bandwidth of 7.3 THz this was reduced to 0.4 dB. The NLI noise growth observed in the

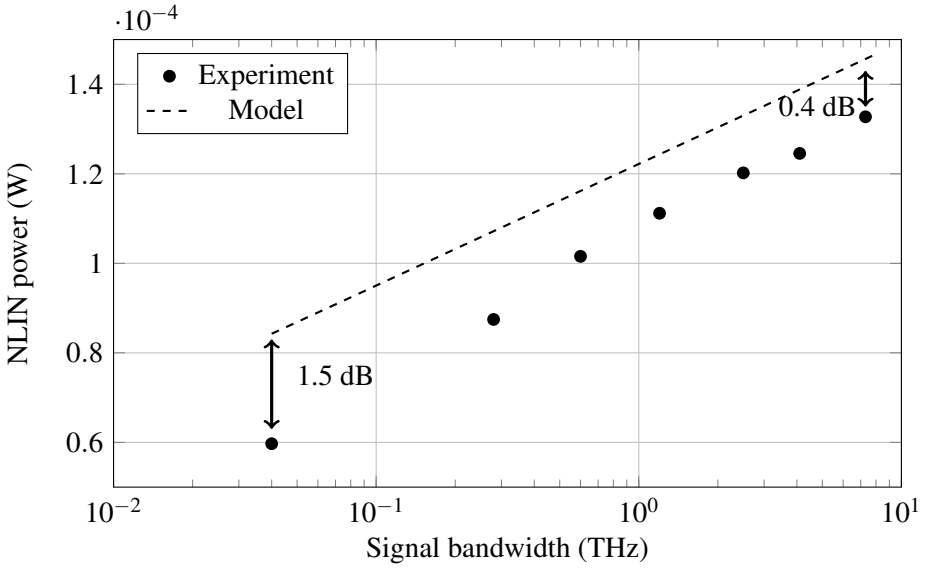

Figure 4.6: Growth of NLI noise power as the signal bandwidth is increased, evaluated after transmission of 1010 km. Markers show the experimentally obtained data and the dashed line the results predicted by the model.

experimental data follows the same logarithmic relationship with the signal bandwidth. Approximately 50% of the total NLI noise generated in the transmission of 7.3 THz occurs as the bandwidth is increased from a single channel of 40 GHz to 280 GHz. This is because as the signal bandwidth is increased, the outer channels with the largest frequency separation with respect to the evaluated channel contribute less to the total NLI noise power due to dispersion induced walk-off effects. Additionally, due to the use of SS-ASE to load the bandwidth beyond the 7 modulated channels, the accuracy of the model is improved in relationship to the experimental data as the larger fraction of the transmitted bandwidth corresponds to SS-ASE, as discussed previously.

4.1.5 The effect of NLI on the communication system performance

After analysing the impact NLI has on the SNR after transmission through an optical fibre, the next step was to investigate the effect of NLI on the optical communication system performance. The analysis of how the NLI decreases the information rates was performed using MI as a performance metric.

The previous subsection showed that NLI noise decreases the received SNR as the total transmitted bandwidth increases through an approximately logarithmic law. In an AWGN channel that uses square QAM constellations as modulation format, the received SNR determines the maximum achievable rate of a communication system (Eq. (1.1)), thus if the the SNR is decreased the achievable information rates will do so accordingly. To study this effect, the MI of the received channel was estimated as a function of the total transmitted bandwidth for a transmission distance of 1010 km, and

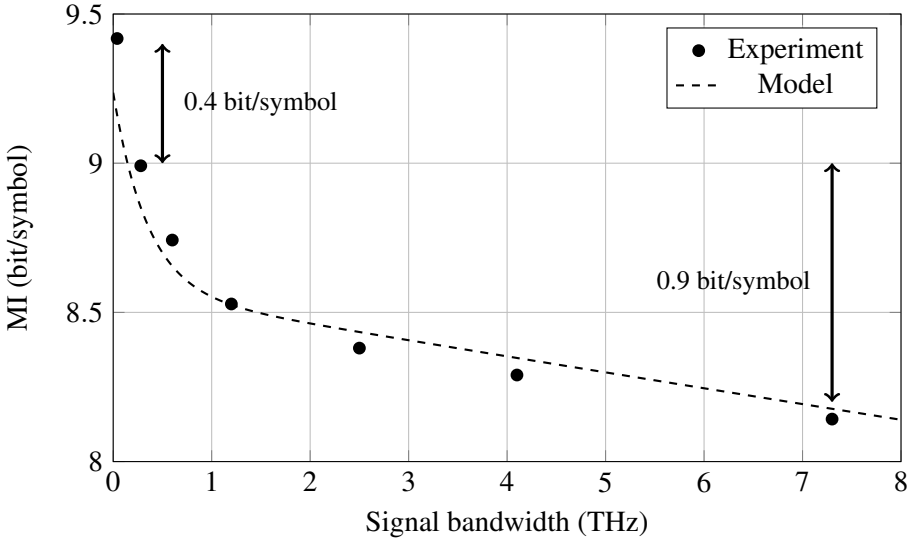

Figure 4.7: Impact of the NLI on the achievable rates at a transmission distance of 1010 km. Markers represent experimental data and solid line represents model predictions

the results are plotted in Fig. 4.7. It can be seen that when a single 64-QAM channel is transmitted, a MI of 9.4 bits/symbol can be achieved. Increasing the number of transmitted channels from 1 to 7 reduces the MI of the central channel to 9 bits/symbol due to the additional NLI noise generated during transmission. Finally, when the total transmitted bandwidth is increased up to 7.3 THz the MI is further decreased to 8.1 bits/symbol. This corresponds to a loss in the information rate of approximately 15% for the 64-QAM modulation format when the bandwidth is increased from a single channel to a full 7.3 THz optical bandwidth. Additionally, Fig. 4.7 shows the predictions from the GN-model converted to MI assuming a Gaussian channel.

The achievable rates in a communication system depend on the total transmission distance due to the accumulation of linear and nonlinear noise. To study the impact of NLI noise as a function of distance, MI values of a single 40 GBd channel and from a channel within a total bandwidth of 7.3 THz, were measured at different transmission distances, with the results plotted in Fig. 4.8. At short transmitted distances, below 300 km, there is only a small difference in the performance for both bandwidths (0.75 bit/symbol), since the system is largely dominated by the limited SNR from the transceiver. From the inset of Fig. 4.1, it is possible to note that back-to-back SNR for a single channel was approximately 1 dB higher than all the other evaluated bandwidths, as discussed previously. For both analysed bandwidths then, it can be seen that achievable rates converge to the back-to-back performance at short distances. At longer transmission distances, the MI of the central channel is reduced for wide bandwidth transmission due to the increased NLI noise and a difference of 1.1 bit/symbol after 2500 km transmission was observed, corresponding to a 15% decrease in the achievable information rate. It is expected that this difference will be maintained for

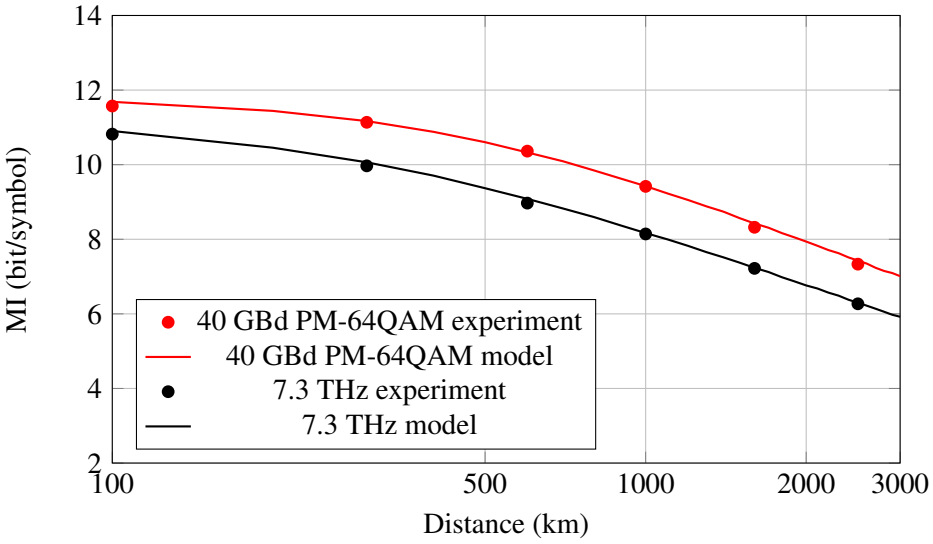

Figure 4.8: Achievable information rates as a function of transmitted distance for the transmission of a single channel (red) and 7.3 THz total bandwidth (black). Markers represent experimental data and solid line represents model predictions

transmission distances beyond those evaluated. Due to the relationship between SNR and MI, we find that the accuracy of the model improves when used to predict the achievable rates of the system, as can be seen from Fig. 4.8, with the largest observed difference between the model and the experiment of 0.2 bit/symbol for the transmission of a single channel. Therefore, as achievable throughput is ultimately the quantity of interest, it can be concluded that the GN model is particularly accurate at estimating central channel performance at optimum launch power, even in C+L-band transmission systems.

Finally, the trade-off between the use of large optical bandwidths and the accumulation of NLI noise was analysed using the measured MI. This analysis was carried out assuming that all the transmitted WDM channels are equally affected by NLI noise and ASE noise. Although this assumption is not valid in a realistic transmission scenario where the noise figure of the optical amplifiers can vary as a function of wavelength and the outer channels of the spectrum experience less NLI noise. However, this assumption provides sufficiently useful insight to study how the system throughput behaves in a transmission system impaired by NLI. It is well known that the capacity of an AWGN channel is given by Eq. 1.1, where W corresponds to the signal bandwidth. Ideally, the SNR is not reduced with the use of larger bandwidths if the channel is linear; therefore, increasing the transmission bandwidth would allow a linear growth in the system throughput. However, due to the accumulation of NLI noise as the bandwidth is extended, the MI of the transmitted channels is reduced resulting in a sublinear scaling of the system throughput. To address this nonlinear penalty on the system, Fig. 4.9 shows the system throughput as a function of the transmitted signal bandwidth after

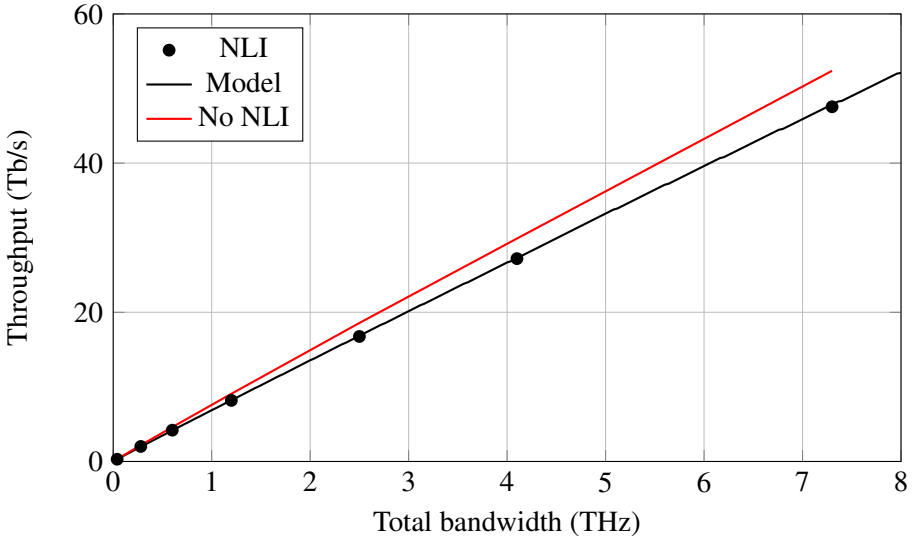

Figure 4.9: Total system throughput as a function of the transmitted bandwidth. Red line represents a system not impaired by NLI noise, obtained from the reiceved OSNR, and black line corresponds to the transmission system. Markers represent experimental data.

1010 km. The red line illustrates the throughput obtained from the measured received OSNR for each value of the transmitted bandwidth at optimum signal launch power; this represents a system not affected by nonlinear impairments. To calculate this, the received SNR was estimated from the OSNR using the back-to-back characterisation from Fig. 4.1, and subsequently, the MI was calculated from the estimated SNR. The degradation of the system throughput due to NLI noise was studied from the experimental data from Fig. 4.5 at optimum power, with the black line showing the total throughput as a function of bandwidth obtained using the GN model and the markers are the experimental data. For the transmission of a single channel, the throughput is reduced by 6% from 317 to 298 Gb/s due to the effect of nonlinearities. The increase of NLI noise is translated into a larger throughput penalty for the transmission of larger bandwidths. For a transmitted bandwidth of 7.3 THz the data throughput is decreased from 52 to 47.5 Tb/s due to nonlinear effects, corresponding to a reduction of approximately 10%. A number of digital and optical techniques have been explored to mitigate the impairments introduced by NLI noise, which would enable an increase in the received SNR. However, due to the logarithmic relationship between the system capacity and the SNR, the benefits of these techniques are limited for state-of-the-art nonlinearity compensation bandwidths. Increasing the transmission bandwidth, on the other hand, despite the sublinear scaling introduced by the accumulation of NLI noise, offers an attractive solution to increase the throughput in optical communication systems.

4.2 The inter-channel stimulated Raman scattering effect on large bandwidth transmission

Although an increase in the transmission bandwidth appears to be a promising solution for increasing the throughput of optical communication systems, it is important to be aware that additional nonlinear effects are likely to have a significant impact as the optical bandwidths are further increased. One major issue is SRS between the transmitted channels. When a signal is intentionally amplified by a high power pump, as seen in the previous chapter, the SRS effect can provide a variety of benefits allowing for distributed amplification. When the signal bandwidth is increased however, the low wavelength region of the signal spectrum acts as a Raman pump for the longer wavelengths. Due to the large frequency shift from the Raman gain spectrum in silica fibres, this effect does not influence the transmission using the C-band; however larger bandwidths will suffer from this effect. The nonlinear interaction between the channels propagating through an optical fibre through SRS will be termed *inter-channel stimulated Raman scattering* (ISRS) and is the focus of this section.

4.2.1 The ISRS effect

The simplest form of signal amplification from the SRS effect manifests itself when a monochromatic pump amplifies a monochromatic signal. The evolution of signal and pump in an optical fibre in this case is given by Eqs. (2.27) and (2.28). When a WDM signal with a large optical bandwidth is being propagated through a fibre, the interaction between the channels can be described using the following set of coupled differential equations [155]:

$$\frac{dP_i}{dz} = -\sum_{j=i+1}^{M} \frac{\omega_j}{2\omega_i} \frac{g_R(\Omega)}{A_{eff}} P_j P_i + \sum_{j=1}^{i-1} \frac{g_R(\Omega)}{2A_{eff}} P_j P_i - \alpha P_i, \tag{4.7}$$

where i is the channel index being evaluated from a total of M channels, P_i is the optical power of chanel i , Ω is the frequency separation between channel j and i, and the remaining symbols were defined in chapter 2. The channels are indexed such that the highest frequency channel has index $i = 1$.

The Raman gain coefficient of SMF was measured as a function of the frequency separation $g_R(\Omega)$ in chapter 3 and plotted in Fig. 3.2. From it, it is evident that if a WDM signal has a bandwidth smaller than 5 THz, almost no power transfer from ISRS will be experienced during transmission. However, signals with bandwidths larger than 7 THz will suffer from this effect, with almost a linear increase in the Raman gain coefficient for bandwidths up to 13 THz approximately. When a transmitted signal experiences ISRS, the power evolution through the optical fibre is affected with two

potential outcomes: if the signal is amplified from ISRS the increased average power can increase the generation of NLI; on the other hand, a depleted signal can experience lower NLI in the presence of ISRS.

4.2.2 Methodology of this study

The effects of ISRS on a transmission system were studied after signal propagation over an optical fibre. Firstly, the accuracy of the set of coupled differential equations from Eqs (4.7) was experimentally evaluated for different wavelengths as a function of signal power and wavelength. To correctly asses this, it is necessary to measure the Raman gain coefficient at the desired frequency shifts and wavelengths. This was performed using a high power tunable source in the C-band to amplify a signal in the L-band and measuring the gain experienced using the methodology described in chapter 3.

Secondly, as before, the received SNR was used as a performance metric to study how ISRS changes the NLI generated during transmission. To do this, different wavelengths were studied with and without the effect of ISRS.

Finally, the experimental results were compared to predictions based on the analytical model described in [60]. The model represents one of the first attempts to include the effects from ISRS in the GN model. It treats ISRS as a pure signal gain or loss component with no noise transfer between channels. This assumes that crosstalk, as a result of time-varying power fluctuations of the modulated channels, averages out due to the high number of uncorrelated interacting channels [156].

4.2.3 Transmission setup to characterise the effects of ISRS

The experimental setup to perform the study of ISRS on optical transmission systems is seen in Fig. 4.10. For this study the ONG testbed was used. The transceiver comprised the transmitter and receiver described in chapter 2. In this case, 14 C-band ECLs were placed between 1529 and 1540 nm, and spaced 100 GHz apart. The C-band sources were used for signal generation together with a tunable L-band ECL. The ECLs were modulated using 32 GBd 256QAM signals, shaped using a root raised cosine filter with a 1% roll-off factor. SS-ASE noise was used to emulate additional interfering channels and fill the remaining bandwidth. The SS-ASE was shaped as channels with a rectangular spectrum, 32 GHz bandwidth and 100 GHz spacing in the C-band. 1000 GHz spacing was used in the L-band, resulting in a total transmitted bandwidth of 9 THz. The number of channels in the L-band was determined by the maximum output power of the EDFAs of 23 dBm, and the channel spacing was chosen to maintain the power spectral density for all powers under study.

In this experiment transmission over a single fibre span was performed. The use of a single fibre span, as opposed to a recirculating loop, allowed us to completely isolate

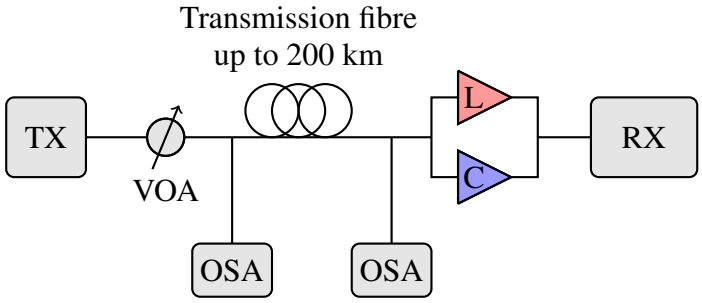

Figure 4.10: Schematic of experimental setup.

the ISRS from other optical components or devices that present a wavelength dependant gain or loss, e.g. the gain tilt from EDFAs. Because long distance transmission requires dynamic spectrum equalisation, performed by the WSS in the ONG testbed, the influence from ISRS on the system performance after transmission may have been affected. For transmission, ultra-loss fibre with standard core area was used, with attenuation coefficient of 0.18 dB/km, dispersion parameter of 16 ps·nm^{-1}·km^{-1} and nonlinear coefficient of 1.3 W^{-1}km^{-1}. The measured normalised Raman gain coefficient was 0.42 W^{-1}km^{-1} at a Stokes shift of 11.5 THz. The performance of single span transmission is directly determined by the length of the fibre. With nonlinear interaction being strongest in the first kilometres of transmission due to the higher signal power, the linear noise generated by the optical amplifiers dominates the system performance. The amount of ASE noise determines the optimum signal launch power, requiring higher signal powers to achieve the best performance when the transmission fibre is longer. For this reason, three different fibre lengths of 100, 160 and 200 km were used in this study. After the fibre span the optical signal was amplified by a set of C+L EDFAs. Finally, the receiver used in this experiment is described in chapter 2.

4.2.4 Signal gain/loss from ISRS

The affects of ISRS on the transmitted signals was evaluated by measuring the optical power transferred during propagation through the fibre for every channel. To do this, the optical spectra at the input and output of the fibre were measured using an OSA with 0.1 nm resolution. The power of the optical signal was varied using a VOA before being launched into the fibre. The input spectrum can be seen in Fig. 4.11 a) using an input power of 10.7 dBm per channel. When the optical spectrum is strongly affected by ISRS a large shift in power is observed. This effect is seen in the spectrum at the output of the fibre in Fig. 4.11 b). Comparing the input and output, the effect of ISRS is evident, and a tilt in the spectrum of approximately 15 dB is seen at the output of the fibre.

Two different wavelengths, located at opposite ends of the optical spectrum, were selected to measure the gain and loss experienced due to ISRS, as a function of the input

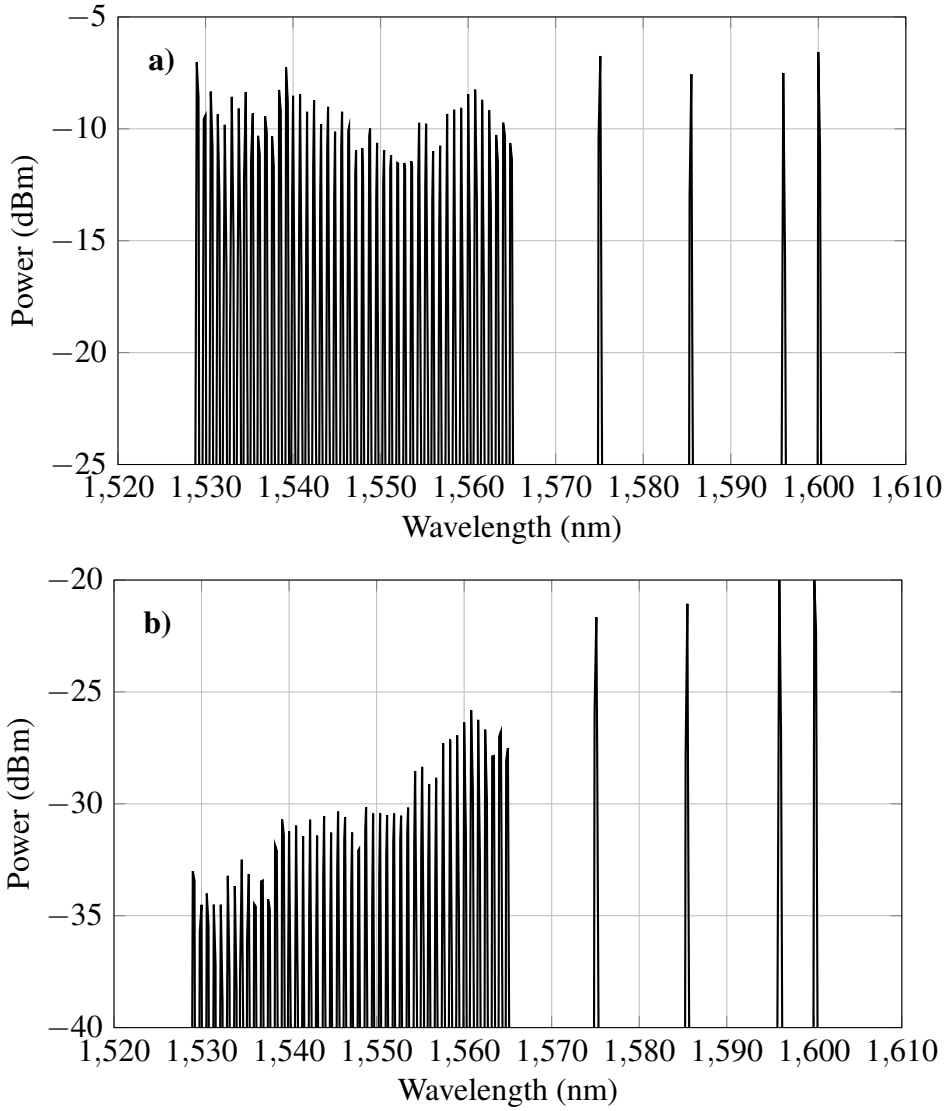

Figure 4.11: Optical spectra measured using 0.1 nm resolution at: a) fibre input, b) fibre output.

power. The chosen wavelengths were 1530 and 1600 nm, and the results are plotted in Fig 4.12. When the launched power was small, no power is transferred due to the ISRS effect; however as the power was increased ISRS started to become significant leading to a power transfer exceeding 0.2 dB for launch powers larger than -5 dBm. To place these values into context, they can be compared to the transmission experiment from Section 4.1. This power would be located in the linear regime of the transmission system and is still 7 dB below the optimal operation point of that system. Additionally, in a multi-span transmission system the effects of ISRS would accumulate in every span, making the influence of this effect increasingly important for long distance links. As the total launch power was increased, the channel placed at 1530 nm became depleted and its optical power was transferred to the longer wavelengths. The channel placed at 1600 nm however, was amplified as seen in Fig 4.12. Additionally, the model from Eq. (4.7) was compared to the measured power transfer, and showed a good agreement

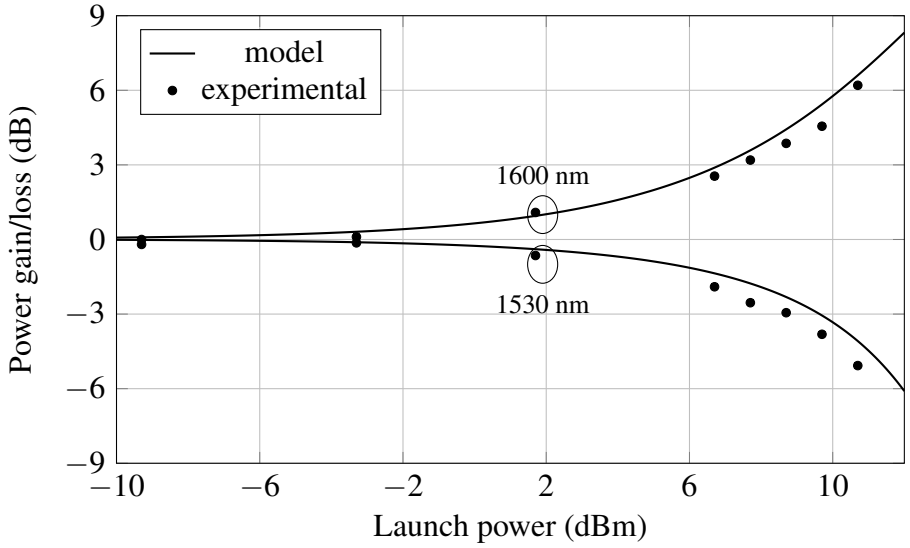

Figure 4.12: Power loss/gain from ISRS as a function of signal launch power for channels placed at 1530 and 1600 nm. Markers represent experimental results and solid lines the model.

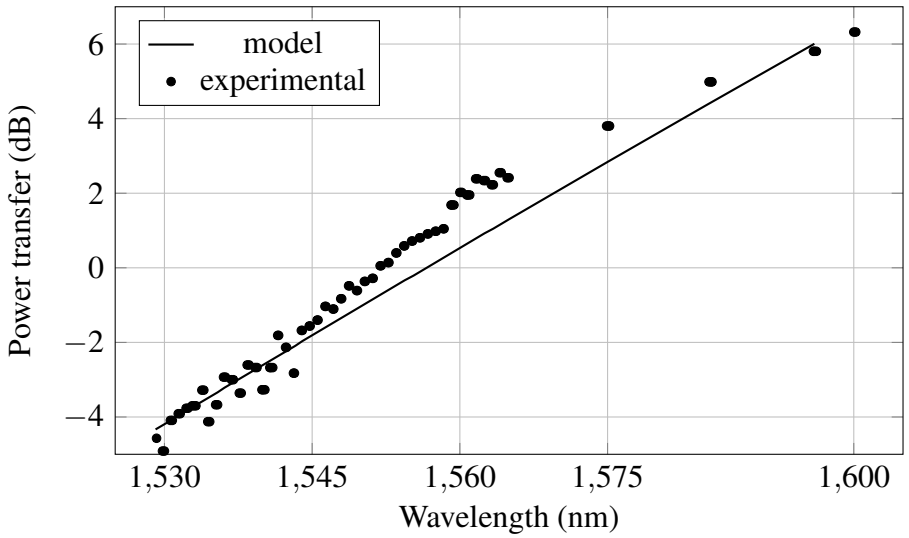

Figure 4.13: Power transfer due to ISRS as a function of signal wavelength for a input signal power of 10.7 dBm per channel. Markers represent experimental results and solid line the model.

with these experimental observations.

Finally, the power transfer at a fixed power was measured as a function of the signal spectrum, and is plotted in Fig 4.13. It can be seen that the power transfer follows the pattern from Fig. 4.11 b), with almost a linear tilt increasing from shorter to longer wavelengths. Because the model assumes that the Raman gain coefficient increases linearly with frequency, some experimental points show a deviation relative to the theoretical line in the figure. The maximum deviation is approximately 1 dB at 1560 nm.

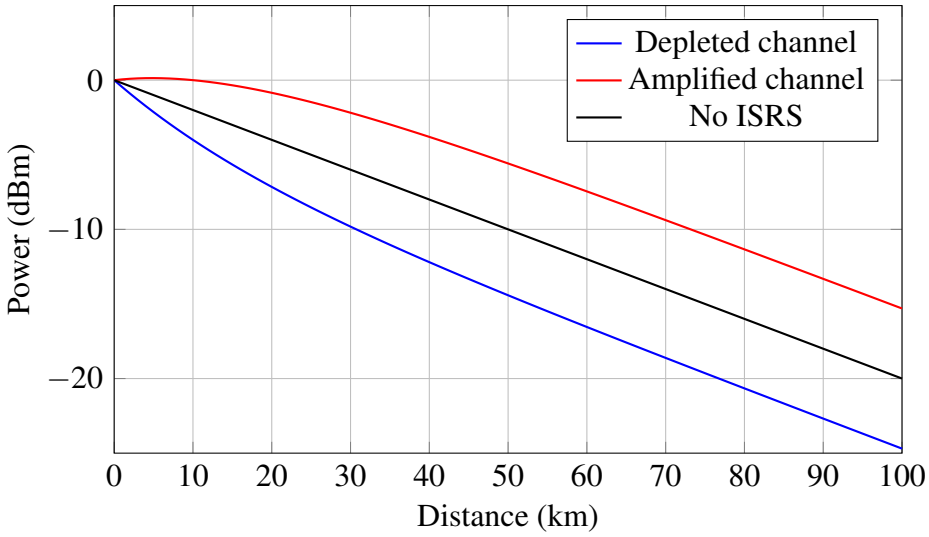

Figure 4.14: Three different signal power profiles obtained using Eq. (4.7).

4.2.5 Influence on NLI from ISRS

The power transfer experienced by the channels during transmission influences the signal power profile along the fibre, and therefore it changes the nonlinear interactions due to the Kerr effect act on the sigal. As an example, the signal power profiles along an optical fibre of two channels in the presence of ISRS and a channel experiencing pure loss is shown in Fig. 4.14. Here it is possible to see that the power transfer occurs in the first section of the fibre span, exactly the section where the majority of NLI is generated. This implies that in the presence of ISRS, NLI generated during transmission is also affected by the signal power. For modelling purposes, the previous assumptions of Eq. (4.3) are no longer valid, and the dependence on power of η becomes necessary. An initial attempt to include this effect in GN model was performed in [60]. Subsequently, several derivations for a GN model that includes the ISRS effect were published [157–159], however they all lacked experimental validation.

To investigate the impact of ISRS on a transmission system, two different channels were evaluated using SNR as a performance metric. Firstly, the transmission was performed using a single transmission band: only C-band for the 1530 nm channel and only L-band for the 1600 nm channel. This scenario represents a transmission system not impaired by ISRS due to the limited bandwidth used. Subsequently, the complete spectrum was transmitted and the performance of both channels was evaluated as a function of input power.

Figure 4.15 shows the results for both transmission scenarios for the channel placed at 1530 nm and the three different distances under study. It is possible to note that the optimum power was shifted towards the higher powers as the fibre span increases in length. As described before, this effect is due to the larger ASE noise generated to compensate for the loss of a longer fibre span. For the 100 km span it was not possible to

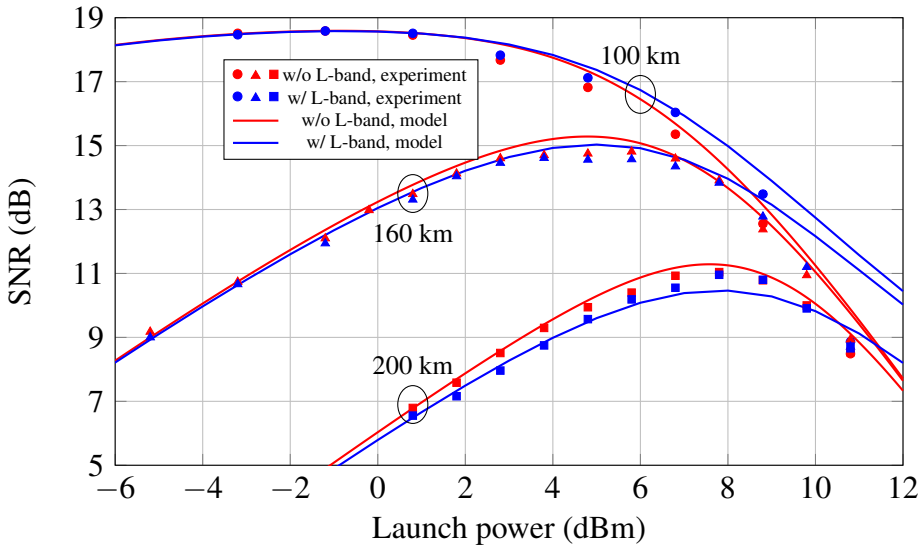

Figure 4.15: SNR as a function of launch power at 1530 nm. Markers show experimental data and solid lines represent the theoretical model. The transmission of the entire spectrum (9 THz) is shown in blue and the transmission of either only C-band or L-band channels are shown in red colour.

clearly distinguish the optimum power due to the effect of the noise from the transceiver subsystem. With a back-to-back SNR of 19 dB, this was the highest achievable SNR after transmission, and, therefore, saturation of the received SNR was found when the linear and nonlinear noise are smaller than this value. For the spans with lengths of 160 and 200 km the optimum power was found to be 6 and 8 dBm, respectively. Comparing this to Fig. 4.12, the channel located at 1530 nm experienced a power loss due to ISRS of 0.2, 1.5 and 2.6 dB for the 100, 160 and 200 km spans respectively. The depletion of the channel lead to a decrease in the NLI; however, due to the loss of power the optical amplifier after the fibre span needed to compensate a greater loss, introducing additional ASE in the process. For the spans of 160 and 200 km, the detrimental effect of the additional ASE noise can be seen before reaching the optimum power, with a reduction on the received SNR. As the signal power was increased, the channel experienced a stronger power depletion because of ISRS, the effect of NLI was reduced. This can be seen for all the evaluated distances, with the channels obtaining a higher received SNR after optimum power due to the ISRS effect.

At the other end of the spectrum the opposite effect was found. The measured SNR as a function of launch power is plotted in Fig. 4.16. The optimum powers for the three fibre spans when no ISRS was present were found to be 0, 7 and 9 dBm per channel. The difference, as compared to the 1530 nm channel, was due to the higher noise figures of the L-band EDFAs. As seen before, the 1600 nm channel experiences amplification due to ISRS. This amplification leads to a smaller gain required from the EDFAs after the fibre and, therefore, to a reduction of the ASE noise level at the receiver. For both spans of 200 km, an improvement in the received SNR before reaching optimum power

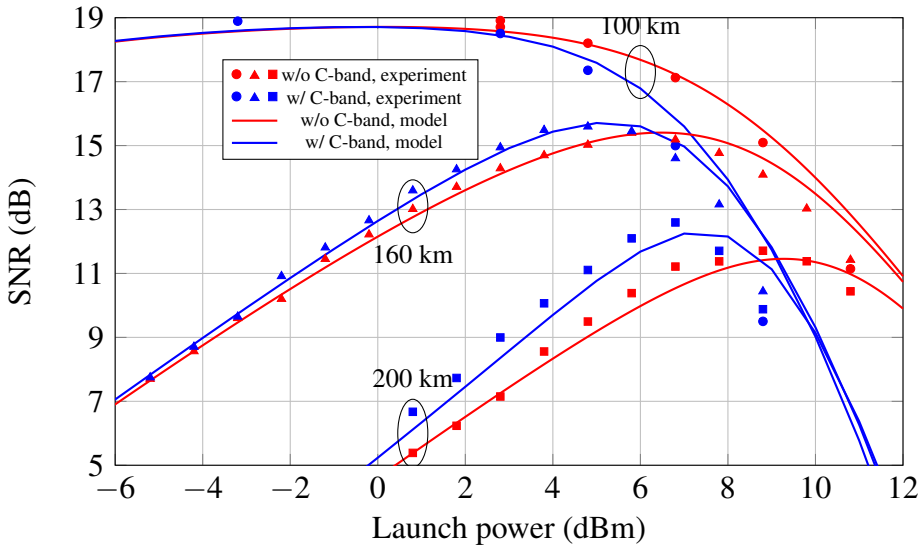

Figure 4.16: SNR as a function of launch power at 1600 nm. Markers show experimental data and solid lines represent the theoretical model. The transmission of the entire spectrum (9 THz) is shown in blue and the transmission of either only C-band or L-band channels are shown in red colour.

was found when the channel was amplified. The higher signal power also increased NLI noise, and for all three fibre spans a stronger degradation beyond the optimum power was observed. At 1600 nm, the overall performance of the channels was improved due to ISRS, with the reduction in the ASE level and the increase in NLI noise reducing the optimum signal power towards lower powers by approximately 1 dB. The received SNR was increased by 0.3 dB for the fibre with a length of 160 km, and by 0.9 dB for the 200 km long fibre.

As seen from the results ploted in Figs. 4.15 and 4.16, a system employing large optical bandwidths will be severly affected by nonlinear effects. ISRS and NLI are closely related, with ISRS influencing the generation of NLI. To design and plan the optical networks for the future, a precise channel model is required that includes all these nonlinear effects. In this work, the experimental results were compared to the modified GN model presented in [60]. The modified model uses the set of equations Eq (4.7) to calculate the power profile of a given channel i, and utilises an effective loss coefficient (α_{eff}) that matches the actual effective nonlinear length of the channel under test. The performance of the system is then given by a modified version of Eq. (1.1):

$$SNR_i = \frac{P_{ch}}{P_{\text{ASE},i} + P_{\text{NLI},i}}, \tag{4.8}$$

where $P_{\text{NLI},i} = \eta_i(P_{ch})P_{ch}^3$, with $\eta_i(P_{ch})$ described in [60]. The difference between Eq. (4.8) and Eq. (1.1) is that the ASE and NLI noise terms depend on the location of the evaluated channel i on the optical spectrum. The main assumption of this model is that no noise is transfered from one channel to another due to ISRS interactions.

From the experimental results in Figs. 4.15 and 4.16 it can be seen that the used model correctly predicts the performance of the system, both in terms of ASE and NLI noise generation. The crosstalk-free ISRS assumption is, therefore, confirmed by the experimental data following the predictions from the model for the ASE noise level ($P_{ASE,i}$), with no additional penalties observed. This assumption would later be independently verified in [160].

4.2.6 Improving system performance using DBP

As the transmitted bandwidth is increased and the ISRS effects starts to dominate the nonlinear impairments of the systems, solutions to cope with ISRS are required. It has been noted in the literature that to maximise the system throughput, ISRS needs to be harnessed without trying to suppress it by reducing the signal power [60]. A potential solution to maximise the system throughput is the use of power equalisation, as seen in [157], where the power of each transmitted channels was optimised to maximise the overall throughput in a system impaired by NLI noise and ISRS. In this section the use of nonlinearity compensation, namely DBP, is proposed to reduce the additional generation of NLI noise due to the ISRS effect.

In chapter 3, the use of DBP was introduced for distributed Raman amplifiers. Although it has a higher computational complexity due to the signal power profile, an improved performance was observed with the use of Raman amplification. Distributed Raman amplifiers are one of the possible applications of stimulated Raman scattering. The signal power evolution they present, especially in the forward pump configuration, can be similar to the one from a channel experiencing gain from ISRS. Then, if a channel is amplified by ISRS and the NLI noise grows for this reason, DBP can be used to mitigate this effect. Just as in the previous chapter, the signal power profile used in the backward propagation needs to match the one in the forward direction to maximise the nonlinearity mitigation.

In this section, Eq (4.7) was used to calculate the power evolution of the channel of interest at every power, which in turn was used in the back-propagation algorithm. DBP was implemented as described in chapter 3, in Fig. 3.14. The received SNR was calculated after using DBP in a channel impaired by ISRS as a function of the signal power and the results are plotted in Fig. 4.17. The studied channel was centred at 1600 nm, and two different distance of 160 and 200 km were evaluated. In both cases, the maximum SNR influenced by ISRS was improved by approximately 0.4 dB. In this wideband transmission regime, the gain is limited by the available received bandwidth, with DBP only compensating for nonlinear distortions within that bandwidth. Beyond the optimum power, it is evident that the nonlinear compensation obtained by DBP was not constant as a function of the input power, due to the extremely rapid growth of NLI

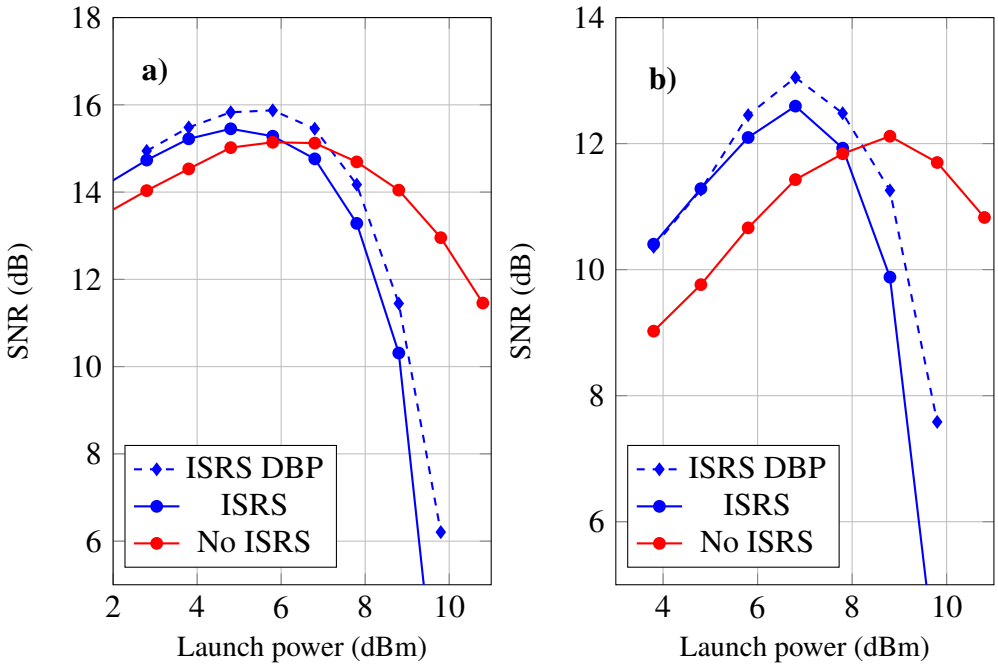

Figure 4.17: Received SNR as a function of launch power at 1600 nm. Triangular markers show the performance after DBP in the presence of ISRS. a) 160 km span, b) 200 km span.

noise as the power was increased.

DBP can be used to enhance the received SNR also in the presence of ISRS. Additionally, if used in the section of the spectrum where the channels are amplified due to ISRS, greater benefits can be observed due to the reduction of linear noise. Finally, it has been shown that the use of short fibre spans leads to an improved linear noise performance and therefore a higher received SNR can be obtained. An implication of this is that optimum signal power is found at lower powers, which in turn can help to reduce the effect of ISRS.

4.3 Benefits of increasing the fibre bandwidth

This chapter has focused on understanding the behaviour of nonlinear effects for the transmission of signals with bandwidth up to 9 THz. In this study, the validity of the GN model with the necessary modifications to include the ISRS effects have been experimentally confirmed for this transmission regime. The impairments introduced by fibre nonlinearity effectively limit the information rates at which an optical communication system can transmit information by setting a maximum SNR that can be obtained after transmission. As seen from Eq. (1.1), once the SNR is limited, the only way to increase the achievable rates in an AWGN communication channel is by increasing the signal bandwidth. Unfortunately, optical communication systems only support transmission in a small fraction of the low-loss region of silica fibres due to the scarce availability

of amplification solutions and components beyond the traditional transmission bands, making the use of larger optical bandwidths for signal transmission a difficult task. Additionally, as seen herein, as the transmitted optical bandwidth grows larger nonlinear effects continue to accumulate, further degrading the SNR of the transmitted channels.

To date, experimental demonstrations have achieved increases to the system throughput using techniques such as nonlinear compensation, coded modulation and constellation shaping schemes, either independently or in combination, for example in [49]. However, the benefits of all these techniques remain relatively limited, and even combined, they are unlikely to satisfy the capacity demands of future networks. Before the task of using a larger optical bandwidth by introducing new optical components to support said endeavour is undertaken, it is necessary to address the potential benefits of this approach. Numerical simulations for large optical bandwidths require enormous computational resources and, for this thesis, simulating beyond 10 THz was not feasible. Analytical models, on the other hand, offer a great trade off between complexity and bandwidth scalability. It was seen in this chapter that the GN model and its modified versions to include ISRS remain accurate up to 9 THz. The question to answer in this section is, then, how beneficial is the use of a larger optical bandwidth as a solution to increase the capacity of communication systems.

4.3.1 Methodology of this study

This section describes a purely theoretical and idealised study of ultra wideband transmission. Due to the nature of the large optical bandwidth, no experimental demonstrations can be carried out because of the lack of components across the entire bandwidth. To perform this study, the received SNR was used as a system performance metric and it was estimated using analytical models. This study first focused on analysing an optical fibre impaired only by ASE noise arising from optical amplifiers, and nonlinear effects were included later. The GN model, both in its original form from [90] and the ISRS modified version from [60] were used to calculate a NLI coefficient for every channel in the transmitted spectrum.

As a reference system a multi-span system was chosen, formed by 80 km spans and a total distance of 2000 km. The optical fibre had low loss and standard core area, with attenuation coefficient of 0.165 dB/km at 1550 nm and 80 μm core area. The optical signal was assumed to be formed by WDM channels shaped using an ideal root raised cosine filter, allowing for Nyquist channel spacing and a modulation rate of 32 GBd. The WDM signals had an uniform input power into the fibre spans. Optical amplification was assumed to be carried out in parallel bands for different spectral regions of 5 THz after every span and was performed by ideal optical amplifiers with a noise figure of 3 dB. The amplifiers had a maximum output power of 27 dBm. This

power level is already commercially available for C- and L-band solutions. A summary of the used system parameters is shown in Table 4.1. Finally, an ideal coherent receiver was assumed. This allowed us to neglect linear fibre impairments such as chromatic dispersion and polarisation mode dispersion due to the capability of DSP to compensate for them after transmission.

Parameter	**Value**
Fibre Length	80 (km)
Centre Wavelength (λ_c)	1480 (nm)
Dispersion (D_{λ_c})	13.15 (ps/nm/km)
Dispersion slope (S_0)	0.092 (ps/nm^2/km)
Nonlinear coefficient @ 1480 nm (γ)	1.2 (1/W/km)
Attenuation @ 1550 nm (α)	0.165 (dB/km)
Maximum Raman gain coefficient (g_R)	0.4 (1/W/km)
Mode field diameter @ 1310 nm	9.2 (μm)
Mode field diameter @ 1550 nm	10.5 (μm)
Symbol Rate	32 [GBd]
Number of spans (N)	25
Maximum amplifier power	5 [W]

Table 4.1: Transmission fibre parameters for ultra wideband transmission.

4.3.2 The linear channel

The performance of a linear fibre channel, with Rayleigh backscattering and infra-red absorption considered to be the only causes of fibre attenuation across the spectrum [84], was analysed first. In this scenario, the SNR at the receiver is limited by the ASE noise from the optical amplification process and the output power available from the amplifiers. Any lumped optical amplifier introduces a total amount of ASE noise power given by [82]:

$$P_{ASE}(\omega) = n_{sp} h \frac{\omega_0}{2\pi} (G-1) F_b, \tag{4.9}$$

where F_b is to the symbol rate of the channel centred at a frequency ω_0, n_{sp} is the spontaneous emission factor and G is the amplifier gain at ω. While in Eq. (4.9) the ASE noise generated within a channel is assumed to be spectrally flat, this assumption changes for greater bandwidths. With the use of large optical bandwidths two terms from Eq. (4.9) will significantly change between channels at different regions of the optical spectrum. Firstly, the central frequency (ω_0) of the channels can change over 20 THz operating in the low-loss region of SMF (1300-1700 nm), and secondly, the gain (G) required to amplify each channel is changed by the wavelength dependent attenuation coefficient, as see in Fig. 2.2. Using the attenuation coefficient from Fig. 2.2,

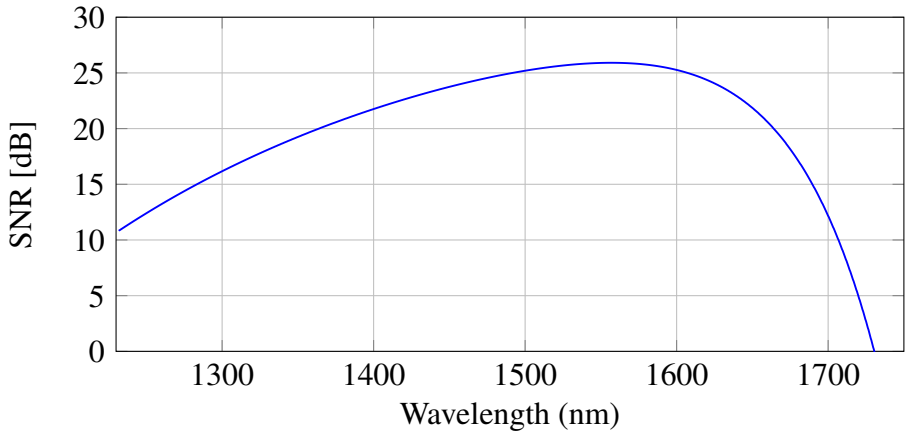

Figure 4.18: Received SNR as a function of channel wavelength for an ASE impaired system.

the loss for each of the channels within the spectrum was calculated, and subsequently used to compute the amount of ASE generated by an ideal optical amplifier. The SNR was then calculated as the ratio between received channel power and ASE noise in the channel bandwidth, where the received channel power was determined by the maximum amplifier output power. The SNR for every channel placed between 1230 and 1750 nm can be seen in Fig. 4.18. An increase in the received SNR is seen when moving from short wavelengths towards the longer ones, following the attenuation profile of Rayleigh backscattering. A maximum SNR can be seen within the L-band at approximately 1580 nm; beyond this point, SNR starts to decrease due to infra-red absorption. Due to the rapid increase of the infra-red absorption on silica fibres following a law proportional to $\exp(\lambda)$ the SNR was decreased accordingly, reaching a value of 0 dB at 1728 nm. Increasing the transmission bandwidth beyond 1700 nm offers diminishing returns due to the rapid increase in the attenuation coefficient. Extending the optical bandwidth towards the higher wavelength region of SMF is not a real solution for higher capacity communication systems. Altough some interest has emerged in researching optical amplifiers that operate in this spectral region [161], the properties of silica fibres will not take full advantage of it. However, this region can still remain useful for short or low data rate optical links. Towards the lower wavelengths a much slower decrease in the received SNR is seen and fibre attenuation does not impose a limit on the spectral region that can be used for transmission. However, towards the lower wavelengths, the condition of single mode guidance through optical fibres is no longer satisfied. In this region, power from the fundamental model will be lost to generate higher order modes: therefore, this study will remain confined to a minimum wavelength of 1260 nm, the cut-off wavelength of Corning SMF [162].

4.3.3 The nonlinear channel

The performance of a linear optical fibre system is limited by the attenuation experienced by light during propagation, but as described in section 2.3, optical fibre is a nonlinear medium, and it is of interest to include this behaviour in the study. To do so, the GN-model was used to calculate the NLI coefficient of the system under study using Eq. (2.23) for a variety of optical bandwidths. Two different types of nonlinear interactions were included: (i) signal-signal distortions generated by crosstalk induced between channels propagating together through the fibre, and, (ii) signal-noise distortions generated by the joint propagation of ASE noise with the optical signals. Therefore, the total NLI noise for the channel i was calculated using:

$$P_{NLI,i} = P_{s-s,i} + P_{s-n,i} \tag{4.10}$$

with $P_{s-s,i} = \eta_i P_i^3$ and $P_{s-n,i} = 3P_{ASE,i}\eta_i P_i^2 \sum_{k=1}^{N_s} k$.

Here η was calculated using Eq. (2.23) for one span, and bandwidths varying from 1 to 35 THz, using a central wavelength of 1480 nm and considering a uniform input power across the spectrum. To calculate η, a wavelength dependent nonlinear coefficient ($\gamma(\lambda)$) was used to include the variation of γ across the studied spectrum. This was carried out by using a linear scaling relative to the increase of the mode-field diameter (MFD) of the optical signal as a function of wavelength. The values used here were 9.2 and 10.5 μm at 1310 and 1550 nm from [162]. Finally, the NLI noise was assumed to add incoherently at every span, an assumption justified by the use of large optical bandwidths [57].

The calculated NLI coefficients for the reference system are shown in Fig. 4.19. The maximum bandwidth for the study of nonlinear effects was limited to avoid the zero dispersion wavelength of the optical fibre. In the spectral regions where dispersion has a value of 0, the assumption of the GN model are never obtained, and, therefore, the predictions of the model are not valid. For a fixed channel, as the signal bandwidth was increased, the NLI continues to accumulate. For the bandwidths under study, the channels on the outer edge of the spectrum experienced smaller nonlinear distortions compared to the central ones. The tilt observed for the NLI coefficients with a decrease from shorter to longer wavelengths is due to the dispersion slope that increases chromatic dispersion for longer wavelengths, along with the growth of the MFD towards this region. The received SNR obtained using Eq. (2.22) for the studied cases are shown in Fig. 4.20. Compared to the linear case, nonlinearity clearly imposes a limit on the performance of the system by restricting the power into the fibre spans. The maximum SNR is reduced by approximately 10 dB compared to the linear case due to nonlinear effects. As in the linear channel, the received SNR is increased towards the longer wavelengths due to the reduced ASE noise and smaller NLI coefficient. The optimum signal power was

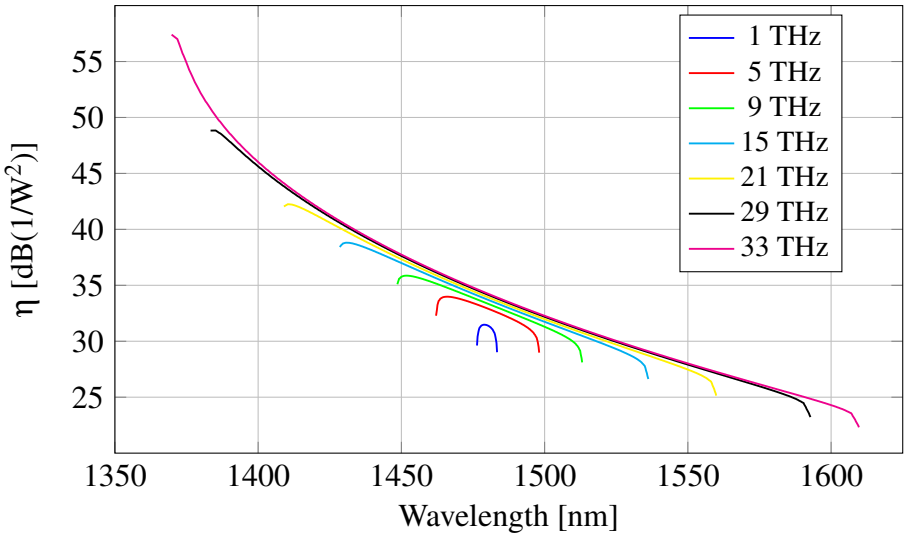

Figure 4.19: NLI coefficient as a function of chanel wavelength.

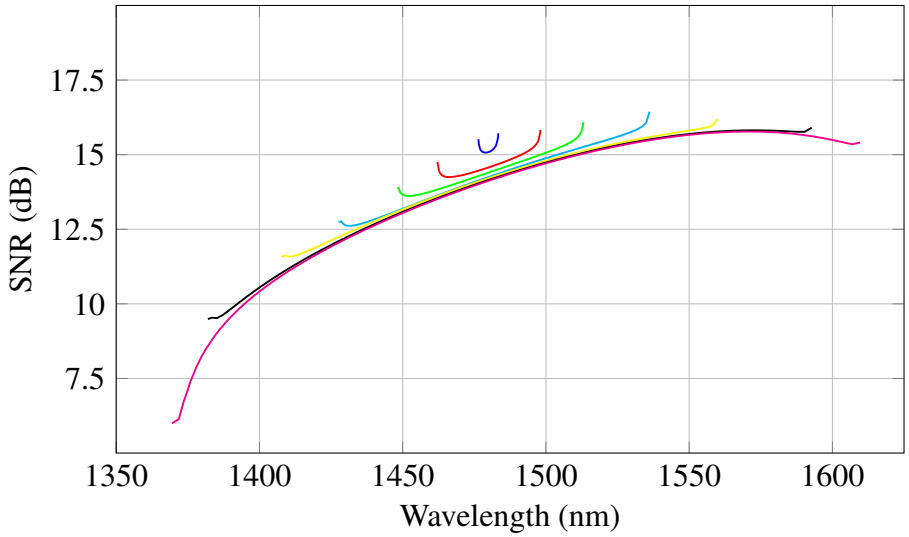

Figure 4.20: Received SNR as a function of channel wavelength for NLI impaired system.

defined as the power that maximises the sum of SNR over all channels, and it was found to be -3 and -4 dBm for the studied bandwidths. As the bandwidth was increased, nonlinear effects continued to grow, and for the largest studied bandwidth of 35 THz, the received SNR ranged from approximately 6 dB for the lower wavelengths up to 16 dB at 1580 nm.

As seen in section 4.2, ISRS becomes increasingly important as the transmission bandwidth grows: therefore, its inclusion for all studied bandwidths was necessary. The signal power profiles for the channels within the bandwidth of interest were calculated using Eq. (4.7). The power profiles were used to obtain new NLI coefficients in the presence of ISRS using the model from [60]. Finally, the received SNR was calculated for signal launch powers from -20 to 0 dBm. The nonlinear interactions included for this calculation were the same as Eq. (4.10), namely signal-signal and signal-noise

interactions, however the linear noise was modified to include the signal depletion or amplification experienced due to ISRS. The overall ASE noise introduced by an optical amplifier after a fibre span including the ISRS effects is given by:

$$P_{ASE,i} = n_{sp} h \frac{\omega_i}{2\pi} \left(\frac{G_{\alpha,i}}{G_{ISRS,i}} - 1 \right) F_b, \tag{4.11}$$

where $G_{\alpha,i}$ is the gain to compensate for the loss due to fibre attenuation, and $G_{ISRS,i}$ is the gain to overcome the effect of ISRS. The term $G_{ISRS,i}$ is greater than 1 if the channel is amplified, thus an overall gain smaller than the one from fibre attenuation is required after a span. Conversely, the term $G_{ISRS,i}$ is smaller than 1 when the channel is depleted and an overall higher gain needs to be compensated for after the span. The power transfer effect from ISRS modifies the signal power profile of every channel along the optical fibre, either reducing NLI if the channel is being depleted or increasing it if the channel is being amplified with other crosstalk effects being negligible. This effect becomes stronger as the optical bandwidth grows, reaching a maximum at approximately 13 THz. Beyond this point, the Raman gain coefficient is rapidly reduced as seen in Fig. 3.2, therefore in this study a channel is assumed to scatter photons due to ISRS only up to a frequency shift of 13 THz.

The received SNR was calculated as a function of the channel wavelength and launch power for three different transmitted bandwidths, and the results are plotted in Fig. 4.21. For the transmission of 1 THz the effect of ISRS is negligible, with little reduction of the received SNR compared to Fig. 4.20. Again, a reduced amount of NLI noise is experienced by the channel in the outer region of the transmitted spectrum and almost equal performance for the channels in the centre was found. Optimum signal power in this case was found to be -3 dBm as in the previous analysis. For 9 THz, the power shift from ISRS dramatically reduces the SNR for longer wavelengths as the signal power is increased. It can be seen in Fig. 4.21 b), that for input powers above optimum, the contour of the surface plot was changed due to ISRS, with longer wavelengths experiencing increased NLI noise, and shorter wavelengths presenting improved nonlinear tolerance due to power depletion. For the central part of the optical spectrum ISRS has little influence, this is because channels in the central section of the spectrum experience depletion and gain, losing power to higher wavelengths and amplified by the shorter wavelengths. For this bandwidth of 9 THz, optimum launch power was found to be -4 dBm.

For bandwidths greater than 9 THz, ISRS had a strong influence on the transmission system, and a reduction of 1 dB in the optimum signal power, compared to the previous case where ISRS was neglected, was found for the transmission of 33 THz. Figure 4.21 (c) shows the received SNR for the transmission of 33 THz. Again a contour change was found in the surface plot due to ISRS. To quantify the effect ISRS has on

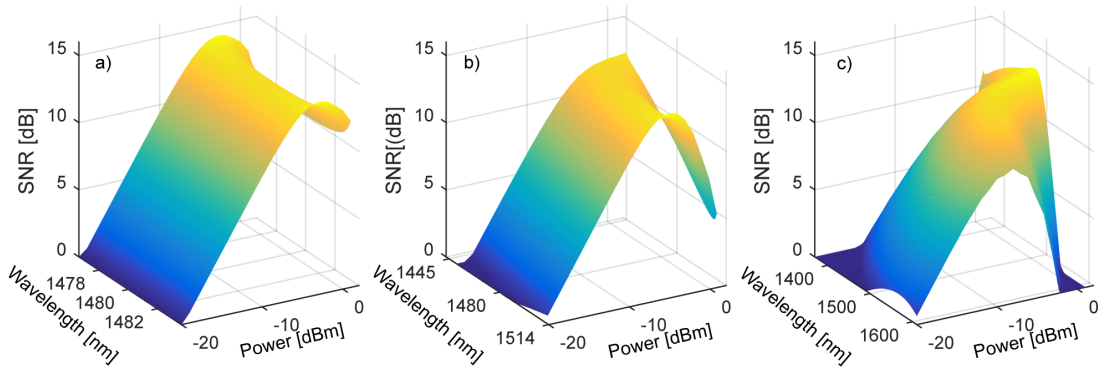

Figure 4.21: Received SNR as a function of signal power and channel wavelength for different optical bandwidths in the presence of ISRS. a), b) and c) correspond to 1, 9 and 33 THz, respectively.

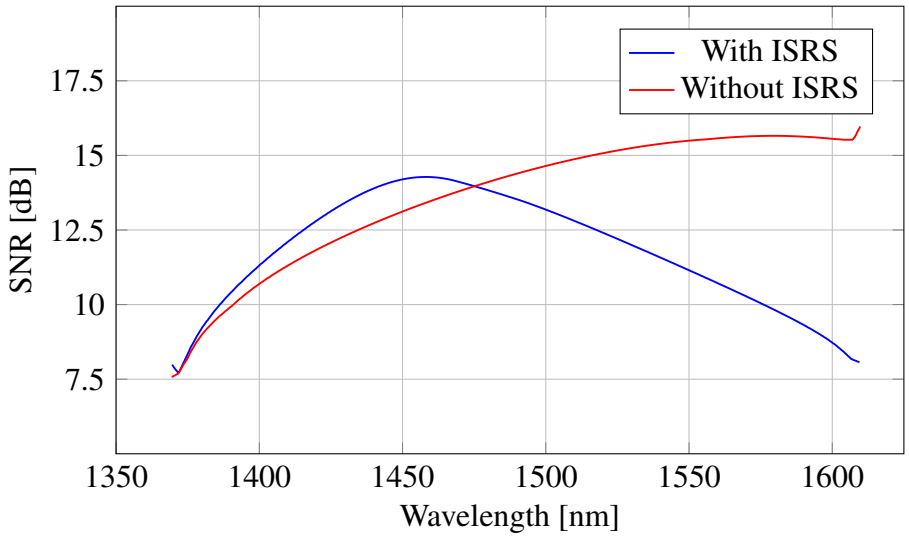

Figure 4.22: Received SNR at optimum signal power as a function of channel wavelength with and without the effect of ISRS.

the received SNR as a function of channel wavelength, the received SNR at optimum power for all the evaluated channels occupying a bandwidth of 33 THz is plotted in Fig. 4.22 neglecting ISRS and considering it. In the lower wavelength region (between 1370 and 1450 nm), an increase in the received SNR was observed, compared to the scenario when ISRS was neglected. A maximum increase of 0.9 dB was found at 1450 nm. This is due to the smaller generation of NLI noise when the channel experiences depletion due to ISRS. Wavelengths longer than 1450 nm experienced a decrease in the received SNR due to ISRS. This detrimental effect was increased for channels at longer wavelengths, and a maximum difference of 8 dB was found for the longest wavelength of 1610 nm. On average it was found that the received SNR, across the entire 33 THz spectrum, was reduced by 2.5 dB due to ISRS, compared to the study when ISRS was neglected.

Fig. 4.22 also offers insight into the physical processes responsible for the reduction

of the SNR across the transmitted spectrum. Firstly, the dispersion slope, that reflects the reduction of chromatic dispersion for shorter wavelengths, is the main reason for the increase in NLI noise in this spectral region. To reduce this effect, the fabrication of new optical fibres is required, with an increased dispersion over the bandwidth of interest. Secondly, ISRS further increases the generation of NLI on the opposite side of the spectrum. In order to overcome this limitation a new material would be required. Due to the stimulated Raman scattering response of silica this effect will always be present in silica based optical fibres.

4.3.4 Benefits of increasing the transmission bandwidth

Extending the usable optical bandwidth will increase the generation and strength of nonlinear effects. However, as a solution to increase the capacity of modern optical communication systems, using an extended optical bandwidth can still be an attractive option. It was seen in this chapter that NLI noise has an approximately logarithmic relationship with the bandwidth of the transmitted signals. In any logarithmic function, the fastest growing stage is found close to zero, implying that the closest frequency components contribute the most to the generation of nonlinear distortions in a channel of interest, while channels with a large frequency separation present only a small contribution to it. However, ISRS modifies the generation of NLI along the transmission fibres making the answer of how much the throughput is increased by using a larger optical bandwidth not simple.

The potential achievable throughput as a function of optical bandwidth is plotted in Fig. 4.23. Due to the way the linear and NLI noise are treated in the used models, the throughput was estimated assuming an additive white Gaussian noise channel, using $\log_2(1+\text{SNR})$. For the linear channel, where the fibre attenuation determines the received SNR, increasing the transmission bandwidth always results in an increase in the transmitted throughput. An exception is found when the region beyond 1750 nm is used, where the attenuation exceeds usable values yielding a SNR of 0 dB. In this linear case, transmitting a total bandwidth of 35 THz would result in throughputs of 558 Tb/s: corresponds to a throughput higher by a factor of 3.7 compared to a linear system occupying the state-of-the-art available bandwidth of 9 THz.

NLI noise generation in the transmission system reduced the achievable throughput considerably by changing the optimum optical power into each fibre span. In this scenario, a throughput of 306.5 Tb/s was found using an optical bandwidth of 35 THz. This corresponds to a reduction by a factor of 1.8 compared to the ideal linear case. Employing this large optical bandwidth, however, is still beneficial compared to the current available fibre bandwidth. In the presence of NLI, a throughput of 86.5 Tb/s was found using 9 THz.

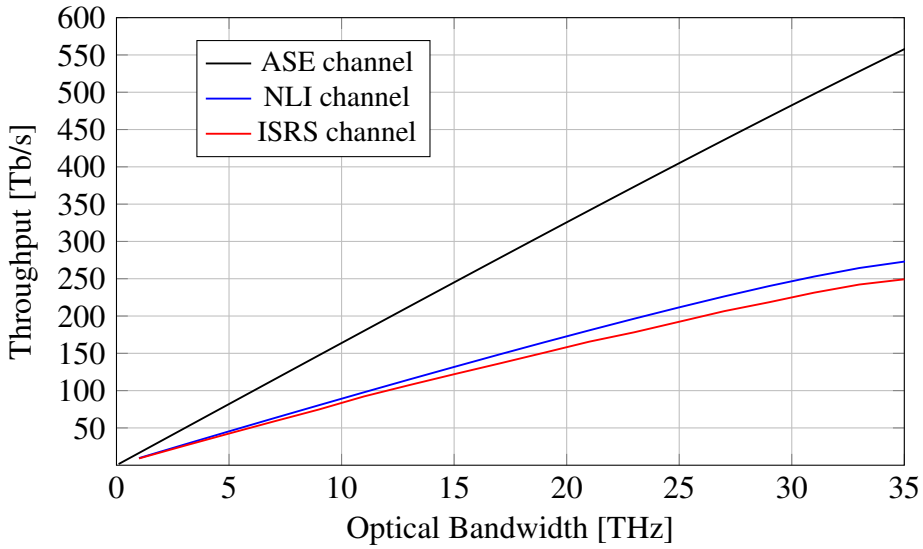

Figure 4.23: Estimation of system throughput as a function of the transmitted optical bandwidth.

Finally, including impairments introduced by the ISRS effect, the system throughput is further reduced. It accounts for a further 10% reduction compared to the NLI scenario. Including ISRS, a throughput of 279.3 Tb/s was found using the available 35 THz, corresponding to a 3.2 times increase in the throughput of a system employing state-of-the-art bandwidth of 9 THz. Overall, increasing the transmitted bandwidth was found beneficial for all the 3 studied scenarios. Considering all the modelled channel impairments to date, namely ASE, NLI and ISRS, an average increase of 7 Tb/s was found for every additional THz of bandwidth occupied at this particular studied distance. This represents however an upper bound on the potential benefits of extending the transmission bandwidth, due to the idealised nature of the study (ideal optical amplification and capacity achieving modulation formats).

Even with the dramatic change in the power profiles of the transmitted channels, and the implications on the generation of NLI noise, using all the available bandwidth results in an increased throughput, and remains the most attractive solution in increasing the transmission capacity of single-mode silica based optical fibres.

Summary

Increasing the usable optical fibre bandwidth continues to be a promising solution to increase the capacity of state-of-the-art communication systems. In this chapter, the impact of nonlinear effects as the transmitted bandwidth is increased was experimentally studied. The growth of nonlinear interactions as the occupied bandwidth is increased does not prevent the throughput being increased. The capacity of single mode silica based fibre is still fundamentally limited by linear and nonlinear impairments; however, current communication systems are far from utilising the full potential of the

transmission channel. The key results from this chapter are summarised as follows:

- For the first time, an experiment was designed and performed to study the growth of nonlinear effects up to bandwidths of 7.3 THz, confirming a logarithmic law for all the studied bandwidths. It was found that the predictions of the GN model remain accurate as the transmitted bandwidth was increased, highlighting its capability to design and study transmission systems.
- ISRS was confirmed to modify the amount of NLI noise experienced by every transmitted channel depending of the signal power. Additionally, no linear crosstalk was found in channels experiencing ISRS. The high speed changes of the transmitted waveforms, and large amount of modulated channels used create an averaging effect that allows modelling of ISRS as a pure gain/loss effect. The proposed modification to the GN model presented in [60] was experimentally validated in a system employing a bandwidth of 9 THz, allowing accurate estimation of the NLI noise generated by a channel experiencing ISRS.
- The potential benefits of increasing transmission bandwidths were studied using both models validated for large bandwidth transmission within this chapter. For bandwidths larger than 9 THz, it was found that, on average, every additional THz used theoretically allows an increase in the transmitted throughput of 7 Tb/s. For all the studied cases, increasing the transmission bandwidth was beneficial, allowing a larger throughput to be transmitted.

5

Optical phase conjugation

As shown in chapters 3 and 4, digital NLC schemes offer promising enhancement to the performance of optical communication systems by mitigating nonlinear distortions generated during fibre transmission. However, all digital NLC schemes are fundamentally constrained to only compensate for nonlinear effects within a reduced bandwidth, limited either by the transmitter, receiver or a combination of both subsystems. As an alternative, optical NLC schemes are implemented in the optical domain without the need to convert the optical signal into an electrical one. Making use of the large bandwidth provided by optical fibres, optical NLC can potentially compensate for nonlinear effects in multiple channels at the same time, offering the possibility of operating at a much larger bandwidth that its digital counterpart. Among the optical NLC schemes, optical phase conjugation (OPC) can notionally provide nonlinearity compensation without any loss in the available transmission degrees of freedom. With several experimental demonstrations, and offering transparency on the used signal (symbol rate and modulation format), OPC is one of the most studied optical NLC method for current optical communication systems.

This chapter describes, in section 5.1, a study on the performance of OPC on an installed network employing standard amplification solutions, namely EDFA, and evaluates how important the power symmetry is to achieve nonlinearity compensation. Finally, due to the limited gains found obtained using OPC, section 5.2 presents a new NLC method that brings together the benefits of optical and digital NLC. The method jointly used OPC and Volterra series frequency equaliser, and shows improved

performance compared to either of the schemes is used in isolation.

5.1 OPC benefits in EDFA based networks

The use of OPC to compensate for linear and nonlinear impairments was already introduced in chapter 2 together with a review on the experimental demonstrations of this NLC method. Perfect symmetry relative to the conjugation point in terms of signal power and chromatic dispersion is required for ideal nonlinearity compensation. To obtain the desired power symmetry, advanced amplification schemes are needed. Noticeably, due to the small slope of chromatic dispersion across the C-band, OPC can be used as a simple method to jointly compensate for dispersion effects of multiple channels, allowing a reduction the complexity of the DSP at the receiver.

In this section, the study of the performance of OPC as a NLC method in a 440 km EDFA-based non-dispersion-compensated field-installed transmission experiment is described.

5.1.1 Methodology

An experimental study of a transmission system employing EDFAs as the optical amplification solution and a mid-link OPC module was carried out to evaluate the potential of OPC as a NLC method. For this purpose, an installed optical network was utilised, allowing to carry out an investigation moving away from the controlled laboratory environments where OPC has been shown to work effectively.

The main challenge of such an experiment is the remote optimisation of different devices and components to obtain the best possible performance. The National Dark Fibre Infrastructure Service (NDFIS) [163] was chosen as the optical network in which the experiment was performed. NDFIS offers a dedicated fibre network linking four universities, UCL, Bristol, Cambridge and Southampton. Remote operation of the optical network was carried out from UCL, and OPC was performed remotely in the University of Southampton. Real-time optimisation of the OPC module was carried out with the help of Yujia Sun at the Optoelectronics Research Centre.

5.1.2 Transmission setup to characterise the performance of OPC

The transmission setup to investigate the performance of OPC as a NLC method in an installed optical network is shown in Fig. 5.1. For this experiment, the ONG transmitter and receiver were used. The transmitter comprised of 14 ECLs. The allocation of the signal wavelengths was varied depending on the transmitted bandwidth to maximise the conversion efficiency for small bandwidths, and to avoid crosstalk from higher order

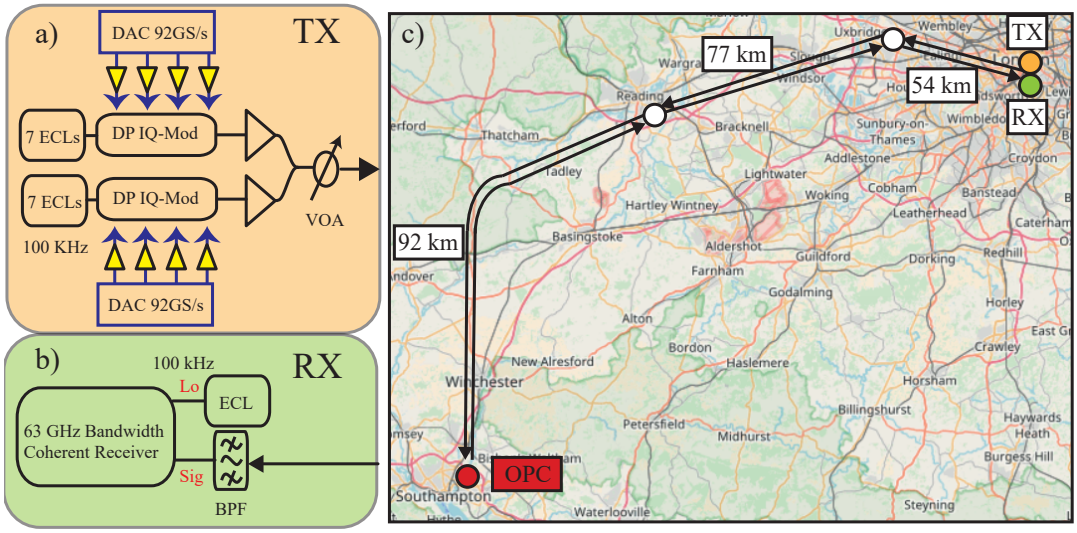

Figure 5.1: Schematic of the experimental transmission setup.

idlers for the transmission of all 14 channels. To perform the transmission of different bandwidths the following configuration was used: for the transmission of three channels a single sub-band was used, centred at 1555.2 nm; for the transmission of six channels another sub-band was added centred at 1557.2 nm. Finally, for the transmission of 14 channels the wavelengths used were divided into two sub-bands with 7 channels each: a short wavelength sub-band between 1552.12 and 1554.13 nm, and a long wavelength sub-band between 1558.29 and 1560.20 nm. For all three cases, and in both wavelength sub-bands, the spacing between the lasers was 41 GHz. The ECLs were modulated using 40 GBd 256-QAM signals shaped using a root raised cosine filter with a 1% roll-off factor.

Transmission was performed over the NDFIS connecting UCL and the University of Southampton via two intermediate sites. The first fibre link had a length of 54 km, the second connecting London and Reading had a length of 77 km, and the third link connecting Reading and Southampton had a length of 92 km. The total distance of the optical path was 446 km. Optical amplification was carried out by EDFAs at every node of the network. Despite the option of using DCF modules at every node, this option was not chosen due to the tendency of modern transmission systems to compensate for chromatic dispersion using DSP. Additionally, a similar experiment was performed using in-line dispersion compensation in [1]. OPC was then performed at the University of Southampton, corresponding to the middle of the link, and the conjugated signal was redirected to UCL using a different fibre from the network.

At the output of the transmission link, the signals were amplified and a band-pass filter was used to select the channel to be detected. At the receiver, the signal was conjugated back after detection when OPC was in place. This was performed off-line using the conjugation function from MatLab. The conjugation was performed in the

time domain for both polarisations. If no OPC was used, the standard DSP chain from the ONG receiver, described in section 2.6, was used.

5.1.2.1 OPC module

OPC is a process where an optical signal is propagated through a nonlinear medium in the presence of a pump beam to create a *phase conjugated* copy (or idler) of the original signal. Usually, the conjugating medium is a nonlinear optical waveguide which can support FWM [164], such as HNLF [165]. During the propagation in the nonlinear medium, when the phase matching condition is met for all the photons participating in the nonlinear process, the FWM phenomenon creates an idler wave at frequency $\omega_i = 2\omega_p - \omega_S$, where ω_p and ω_S correspond to the pump and signal frequencies respectively.

Neglecting pump to signal depletion, and assuming that the pump power is much higher than the signal, the FWM process is governed by the coupled linear differential equations [82]:

$$\begin{aligned} \frac{dA_s}{dz} &= 2i\gamma A_p^2 e^{-i\kappa z} A_i^*, \\ \frac{dA_i}{dz} &= 2i\gamma A_p^2 e^{-i\kappa z} A_s^*, \end{aligned} \tag{5.1}$$

with signal and idler optical fields defined as A_s and A_i, input pump field A_p, and total phase mismatch κ given by:

$$\kappa = \beta(\omega_s) + \beta(\omega_i) - 2\beta(\omega_p) + 2\gamma P_0, \tag{5.2}$$

where $\beta(\omega)$ is the propagation constant of the fibre at frequency ω, γ is the nonlinear coefficient of the medium, and $P_0 = |A_p|^2$. From Eq. (5.1) it is seen that the amplitude of the idler field is directly related to the complex conjugate of the signal field.

The conversion efficiency of an OPC module is defined as the ratio between the output idler power at the end of the nonlinear medium of length L to the input signal power, is given by:

$$\eta_c = \frac{P_i(L)}{P_s(0)} = \left(\frac{\gamma P_0}{g}\right)^2 \sinh^2(gL), \tag{5.3}$$

where g is the parametric gain of the nonlinear process.

The setup used to perform OPC is shown in Fig. 5.2. It was developed and built in the Univerisity of Southampton by the students of Prof. Periklis Petropoulos and Dr. Francesca Parmigiani. This setup corresponds to the one used in the experiments of [1, 2]. The main features of the OPC module include efficient bandwidth utilisation in a single nonlinear medium and insensitivity to the polarisation of the incoming signal due to the use of a dual pump configuration. Firstly, to maximise the bandwidth utilisation,

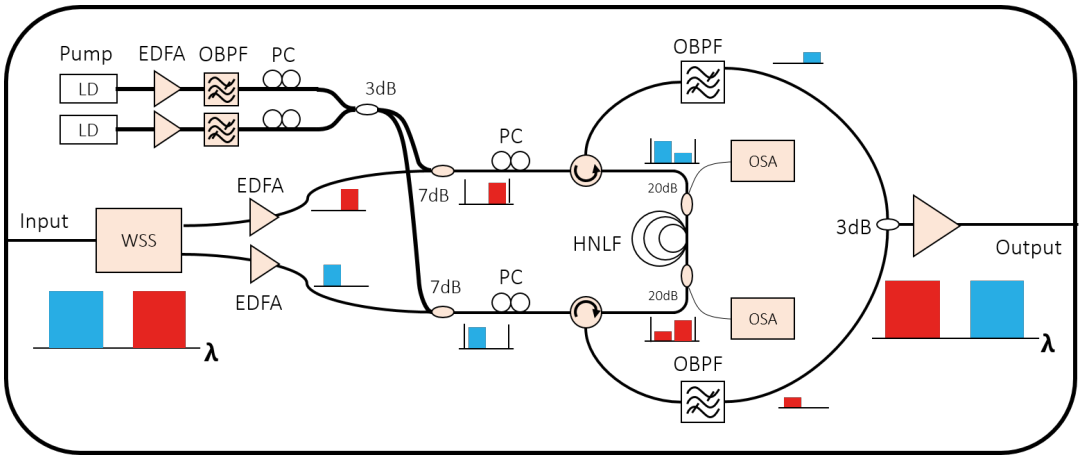

Figure 5.2: OPC module setup from [1, 2].

the entire bandwidth was divided into two sub-bands and each sub-band was processed by an independent OPC device. Here, each OPC device is formed of the same nonlinear medium, exploiting the possibility of bi-directional transmission of optical fibres and each sub-band is defined by the position of one pump and the average frequency of the two pumps.

The operation principle of the OPC module was as follows: the incoming signal was separated into two different sub-bands by a WSS, and each band was launched into one end of the nonlinear medium where conjugation would be performed. Two continuous-wave pumps were used, separated by 12 nm (1.5 THz), and located at 1550.12 and 1562.23 nm. They were amplified separately by EDFAs and filtered to suppress out-of-band amplified spontaneous emission noise. A pair of polarisation controllers ensured the orthogonality of their states of polarisation. After the two pumps were combined in the same fibre, they were split into two copies, directed to the two opposite ends of the nonlinear medium combined this way with each one of the signal sub-bands. The power per pump per direction was 22 dBm.

The nonlinear medium chosen to perform the FWM was HNLF. The HNLF was a 101 m span of strained germanium-doped silica fibre with a zero-dispersion wavelength of 1531 nm, a dispersion slope of 0.018 ps $\cdot$ km$^{-1}\cdot$ nm^{-2}, a polarisation mode dispersion of 0.31 ps $\cdot$ km$^{-1/2}$, and a nonlinear coefficient of 11.6 W^{-1}km^{-1}. The conversion efficiency of the OPC module was measured, using the output and input signal powers, to be approximately -10dB.

At the output, the original signals were filtered out by optical band-pass filters, therefore, leaving the phase-conjugated idlers occupying the wavelengths of the opposite band.

The optical spectrum of the transmission of 3 channels is shown in Fig. 5.3 for the transmission employing both EDC and OPC. The received spectrum for the OPC transmission is shifted towards the long wavelength sub-band. For OPC transmission

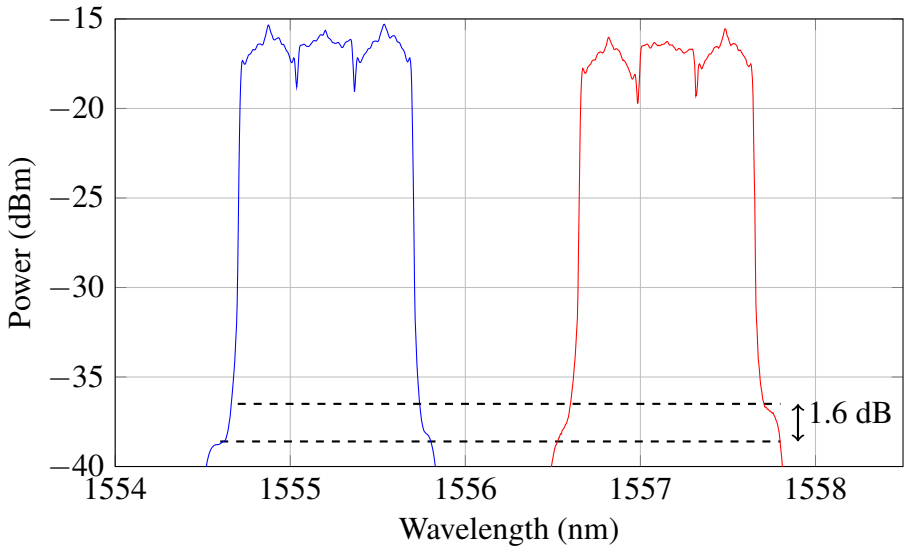

Figure 5.3: Spectra of the received signals after transmission of 3 channels. Blue and red correspond to a system without and with an OPC module, respectively.

it is also possible to see an increase of 1.6 dB in the ASE noise level. This is due to the negative conversion efficiency of the OPC module, and the noise generated by the EDFA used to overcome the conversion efficiency and losses in the module.

5.1.3 Transmission results using OPC

The performance of the transmission system was evaluated for 3, 6 and 14 channels. Overall, the maximum bandwidth occupied by the signals was of 560 GHz. Additionally, SSFM simulations were performed to obtain a greater theoretical insight into the system and the obtained results.

A launch power sweep was performed for all the bandwidths under study. The system performance as a function of launch power for the transmission of 3 channels is plotted in Fig. 5.4. In the linear regime both transmission configurations show a similar performance; however, as noted from the ASE level in the received spectrum, the OPC configuration introduces a higher amount of linear noise and a reduction of 0.4 dB in the linear regime was found. As the signal power was increased, the EDC configuration reached a maximum SNR of 17.7 dB at a power of 2.6 dBm, beyond which the received SNR decreased due to nonlinear effects. The configuration employing OPC reached a maximum SNR of 17.4 dB at the same launch power. The nonlinear regime of the OPC configuration shows however an improved nonlinear tolerance compared to its EDC counterpart. For all the evaluated power points in the nonlinear regime, the OPC configuration presented 1.4 dB higher SNR than the EDC configuration. The higher SNR in the nonlinear regime indicates that the OPC module used in this transmission does offer nonlinearity compensation, albeit very limited. Although NLC is achieved,

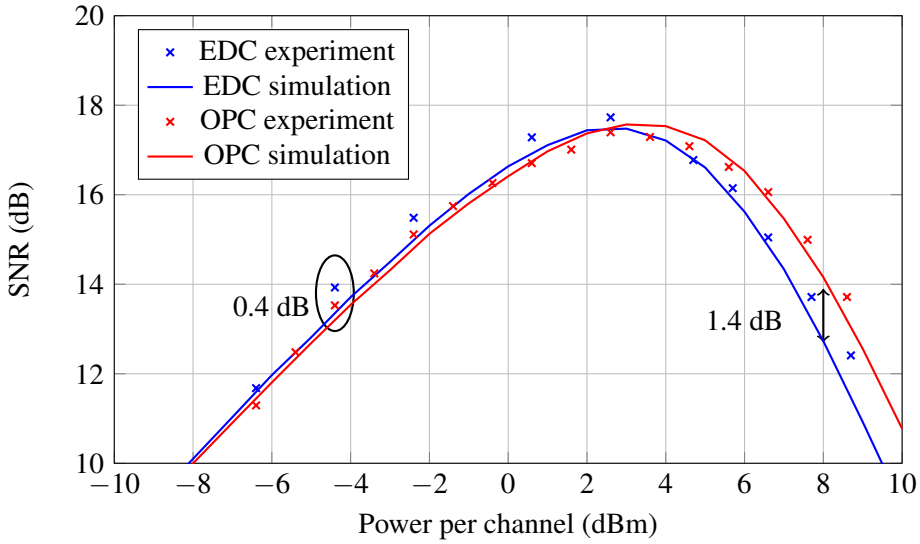

Figure 5.4: Received SNR as a function of the signal launch power for a system using 3 channels. Blue and red denote EDC and OPC scenarios; markers and lines represent experimental data and simulations.

in this transmission configuration OPC does not offer any performance gain compared to EDC only.

The system performance as a function of launch power for the transmission of 14 channels is shown in Fig. 5.5. The same trend from the transmission of 3 channels is observed for all powers. The linear regime presented a reduction of 0.2 dB when the OPC device was used, in this scenario the penalty seems to be reduced due to optimisation on the power of the pumps used in the OPC module. For this reason, the same performance was observed for both configurations with a maximum SNR of 16.9 dB. In the nonlinear regime the NLC gain from OPC is further reduced to 1.1 dB. This reduction in performance is due to the increased optical bandwidth of the transmitted signal.

The simulation results are shown jointly with the experimental ones in both Figs. 5.4 and 5.5. Good agreement was seen for all cases between the simulations and the experimental data. The simulations for the transmission of 3 channels show that a slightly better performance could have been achieved with the OPC device at 3.6 and 4.6 dBm. This is attributed to implementation penalties due to the non-ideal properties of the OPC module, such as component losses and negative conversion efficiency. The increase in bandwidth from 3 to 14 channels results in a reduction of the NLC efficiency of OPC of 0.3 dB, in good agreement with the experimental results. The observed gain was limited by the properties of the transmission link, e.g., the signal power profile from the use of EDFA and power asymmetry relative to the conjugation point. Optical networks often employ different span lengths to connect different nodes, further reducing the power symmetry, and thus the gain from the compensation of nonlinear

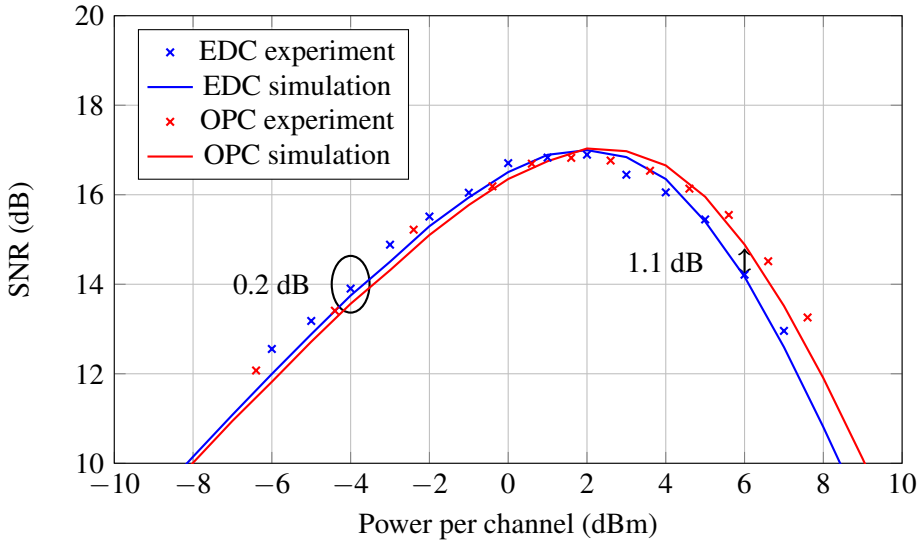

Figure 5.5: Received SNR as a function of the signal launch power a system using 14 channels. Blue and red denote EDC and OPC scenarios; markers and lines represent experimental data and simulations.

effects. The following subsection will describe the study of the degradation caused by the power asymmetry and different network configurations. The experiment suggests that the OPC configuration used allows for the processing of an increased number of transmitted channels without introducing signal degradation by the generation of parasitic higher-order idlers during the conjugation process. Additional benefits offered by OPC relate to the simultaneous compensation of chromatic dispersion for all the transmitted WDM channels within the transmission link, and as the number of channels is increased this benefit can be exploited to reduce the power consumption of the receivers and reduce transmission latency.

5.1.4 Gain reduction in OPC systems

The performance of the experimentally studied system employing OPC to compensate for nonlinear effects was shown to present limited benefits, by only extending the operation power range by 1 dB and with no overall improvement in the received SNR, compared to the use of an EDC configuration. Due to the good agreement found between the numerical simulations and the performed experiment, a variety of transmission configurations were simulated in order to explore the reason for the reduced gain obtained by employing OPC. The studied scenarios were the following: (i) a reduced noise figure from the optical amplifiers, (ii) an ideal transceiver without noise, (iii) using the same system but with a longer transmission distance, (iv) and a network with the same average span length connecting every node. The same experimental conditions were used for all simulations, and the negative conversion efficiency of -10 dB from the OPC module was used. The overall gains at optimum power observed

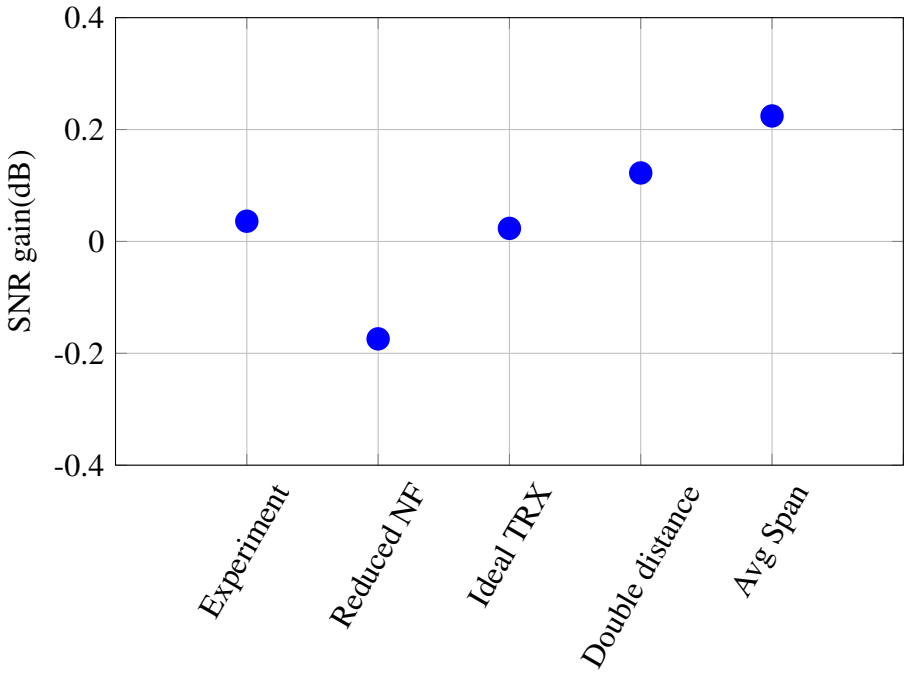

Figure 5.6: SNR gain over EDC using OPC in different system configurations

for all the studied configurations are shown in Fig. 5.6.

The first scenario analysed was the use of optical amplifiers with a reduced noise figure. The experimental conditions, with only 14 transmitted channels and EDFAs placed within the installed optical network, significantly influenced the total linear noise in the transmission link. With only a fraction of the amplifier bandwidth used by the transmitted channels, out-of-band ASE noise build up without the possibility of filtering it at each node. To model this effect during the simulation, a noise figure of 8 dB was used from the optical amplifiers. A reduced noise figure was expected to reduce the signal-noise interactions in the system and, therefore, allow a higher gain from the use of OPC; however, as seen in Fig. 5.6, the overall gain was reduced. This was the result of negative conversion efficiency of the OPC module. Due to the reduced generation of ASE noise in transmission, the linear noise from the OPC module (fixed due to the conversion efficiency) represents a larger percentage of the total ASE level at the receiver, which was translated into a decrease of SNR in the linear regime of 0.5 dB when OPC was used compared to the EDC transmission. On the other hand, the nonlinear transmission regime presented the same improvement as the experimental results with an increase in the received SNR of 1.1 dB for signal power values higher than optimum power. As the optimum power for the system is determined by the balance between linear and nonlinear noise contributions, the use of OPC resulted in a SNR penalty of 0.2 dB compared to the EDC link.

The second case studied was that of an ideal transceiver subsystem with no noise generation. The noise generated by the transceiver limits the back-to-back performance

of the system independent of the OSNR, and can also limit the performance after transmission for short distances as seen in the previous chapter in Fig. 4.8. The use of an ideal transceiver translated into an improvement in the received SNR at optimum power of 1.7 dB for the EDC and OPC configurations. For this simulation scenario the linear and NLI noise contributions were the same as in the experimental configuration leading to the same gain using the OPC configuration, and experiencing a 1.1 dB increase in the received SNR in the nonlinear regime.

The third test consisted of simulating the transmission of the signals passing twice through the optical network. The transmission link was comprised by a connection from UCL to Southampton and back, subsequently OPC was performed at UCL and the same loop-back link was simulated for a second time. This lead to a total transmission distance of 892 km. For this configuration the gain from OPC was improved compared to that experimentally observed, however the increase was only of 0.1 dB. Transmission links employing OPC modules benefit from the effect of dispersion accumulation, and therefore present larger gains at longer distances.

Finally, the total distance of 446 km was divided into 6 spans of 74.3 km. This was performed to improve the symmetry properties in the signal power profile. This configuration, with spans of equal length, did improve the power profile conditions, increasing the gain in the nonlinear regime from 1.1 dB to 1.4 dB which was translated into an overall gain over the EDC configuration of 0.2 dB. This result confirms that the use of different span lengths in a network environment reduces the power symmetry even further, and that the gains from nonlinearity compensation are highly dependent on the power symmetry. The gains reported in this analysis remain limited, and the effectiveness of OPC as a NLC method in EDFA based links needs to be reconsidered. These results by no means subtracts from the importance of using the optical domain to reduce the load on the DSP processing stage at the optical receivers.

As the signal power profile was identified to be the dominant factor to reduce the effectiveness of OPC as an NLC method, a final set of simulations was performed to assess the gain of OPC for different power profiles. Three different amplification solutions were simulated using the parameters from the NDFIS link. A single channel was simulated and an ideal transceiver was assumed. Finally, all amplification methods were assumed to generate the same ASE level per span. All mentioned assumptions were used to study purely the effect of the signal power profile on the OPC performance. The selected amplification solutions were EDFA, backward pumped distributed Raman amplifier and an ideal distributed amplifier. The asymmetry of the different amplification solutions was evaluated using the link asymmetry percentage (AS) as defined in [111]:

$$AS = \frac{\int_0^{L/2} |P_1(z) - P_2(L_s N_s/2 - z)| dz}{\int_0^{L/2} P_1(z) dz} \times 100, \tag{5.4}$$

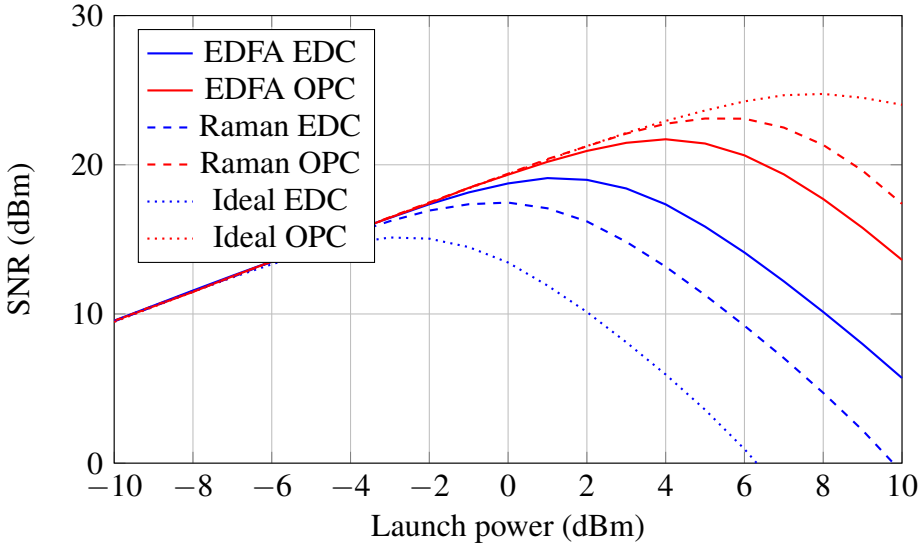

Figure 5.7: Received SNR as a function of signal for EDC (blue) and OPC (red) based transmission links. Line styles represent different amplification technologies with EDFA shown using a solid line, backward pumped distributed Raman amplification using dashed line and ideal distributed amplification using dotted line.

where $P_1(z)$ and $P_2(z)$ are the signal power profiles before and after the conjugation point, and L is the total length of the transmission link. Due to the discontinuities in the power profile when EDFAs are used, and the different lengths of spans used in the studied link, the integrations need to be performed in a *per span* manner as:

$$AS = \frac{\sum_{i=1}^{N_s/2+1} \int_{L_i}^{L_{i+1}} |P_1(z) - P_2(L_s N_s/2 - z)| dz}{\sum_{i=0}^{N_s/2} \int_{L_i}^{L_{i+1}} P_1(z) dz} \times 100, \tag{5.5}$$

with total number of spans N_s and the length of the n-th span defined as $L_{n+1} - L_n$. Using Eq. (5.5), the asymmetry percentages of the three amplifier solutions studied are 106%, 80% and 0% for EDFA, Raman and ideal distributed amplification respectively.

Figure 5.7 shows the received SNR as a function of the signal launch power for all three amplification solutions. With the lowest symmetry, the EDFA system presented a 2.6 dB gain using an OPC module, compared to EDC only. The use a Raman amplified link, with a higher symmetry, presented 5.6 dB gain with the use of the OPC, compared to EDC only. Finally, perfect symmetry lead to 9.4 dB gain using OPC, compared to EDC only. In this case, perfect compensation of the deterministic nonlinear effects is achieved, and it is the only configuration where ASE noise limits the gain obtained due to the signal-ASE interactions.

5.2 The Volterra-assisted OPC method for nonlinearity compensation

In the previous section, a low NLC effectiveness was observed in practical transmission links using OPC. The signal power profile and, therefore, the lack of power symmetry, was identified as the main reason for the limited NLC performance. Even with this limited performance, OPC remains an attractive way to reduce the DSP load at the receiver. This section describes a scheme capable of improving the NLC properties of OPC. The proposed NLC scheme was named *Volterra-assisted OPC* (VAO), and uses a digital VSFE tailored to an OPC-based link at the receiver to compensate the residual NLI noise present after transmission due to the lack of symmetry. It is the first joint optical and digital NLC method, where the optical and digital processing complement each other to obtain improved NLC.

5.2.1 Volterra series transfer function for OPC-base systems

As described in chapter 2, the use of Volterra series to obtain an approximate solution to the NLSE was introduced in [71]. Using VSTF the received signal can be constructed using Eq. (2.34). For standard EDFA-based links, the first and third-order Volterra kernels are given by Eqs. (2.35) and (2.36). The use of an OPC module changes the way dispersion, nonlinearities, and the interaction between the two evolve along the link. For this reason, systems using OPC are not represented by the Volterra kernels from [71]. Rewriting Eq. (2.34) to model the effects from an OPC, we obtain that the received signal in polarisation X after a transmission distance of N_sL_s is given by (see Apendix B for derivation):

$$\begin{aligned}\tilde{A}_X(N_sL_s,\omega) &= \tilde{A}_X^*(0,\omega) \\ &+ i\gamma\frac{8}{9}\iint [\mathcal{S}_{XXX}^*(-\omega,-\omega_1,-\omega_2)+\mathcal{S}_{YYX}^*(-\omega,-\omega_1,-\omega_2)] \\ &\times H_3(N_sL_s,\omega,\omega_1,\omega_2)d\omega_2 d\omega_1.\end{aligned} \tag{5.6}$$

Equation (5.6) was derived directly from the Manakov equation (Eq. (2.18)) to account for the transmission of dual polarisation signals and the fibre birefringence effects. In Eq. (5.6), the signal kernels $\mathcal{S}_{XXX}(\omega,\omega_1,\omega_2)$ and $\mathcal{S}_{YYX}(\omega,\omega_1,\omega_2)$ are defined as:

$$\begin{aligned}\mathcal{S}_{XXX}(\omega,\omega_1,\omega_2) &\triangleq A_X(0,\omega_1)A_X^*(0,\omega_2)A_X(0,\omega+\omega_1-\omega_2), \\ \mathcal{S}_{YYX}(\omega,\omega_1,\omega_2) &\triangleq A_X(0,\omega_1)A_Y^*(0,\omega_2)A_X(0,\omega+\omega_1-\omega_2).\end{aligned} \tag{5.7}$$

Finally, $H_3(N_sL_s,\omega,\omega_1,\omega_2)$ is defined as:

$$H_3(N_sL_s,\omega,\omega_1,\omega_2)=\xi^*\left(\frac{N_s}{2},\omega,\omega_1,\omega_2\right)\times K(L_s,\omega,\omega_1,\omega_2). \tag{5.8}$$

For EDFA-based transmission links, the FWM efficiency $(K(L_s,\omega,\omega_1,\omega_2))$ is given by:

$$\begin{aligned}&K(L_s,\omega,\omega_1,\omega_2)\triangleq\\&\frac{(e^{-i\beta_2\Delta\Omega L_s}e^{-\alpha L_s}-1)(\alpha-i\beta_2\Delta\Omega)}{\alpha^2+\beta_2^2\Delta\Omega^2}\\&+\frac{(e^{-i\beta_2\Delta\Omega L_s}-e^{-\alpha L_s})(\alpha+i\beta_2\Delta\Omega)}{\alpha^2+\beta_2^2\Delta\Omega^2},\end{aligned} \tag{5.9}$$

with $\Delta\Omega\triangleq(\omega-\omega_1)(\omega_1-\omega_2)$. As seen here, the FWM efficiency has changed compared to the one defined in chapter 2 due to the presence of the OPC module, and the phased array only accounts for half of the total transmission distance.

5.2.1.1 Improved symmetry conditions for OPC

Using the third-order Volterra kernel it is possible to study the effect that different fibre parameters have on the performance of OPC as an NLC method. To assess the different configurations, the NLI noise power generated by the third-order kernel (H_3) was calculated for system configurations with and without OPC, and the ratio between both was used as performance metric indicating the suppression of NLI noise. The calculation of the PSD of NLI noise requires several assumptions on the signal, such as the ones used in the GN model [57]. However, the ratio between third-order kernel powers provides enough insight on the physical parameters of a transmission link that can improve the performance of a system using OPC.

The ratio between the third-order kernels for a system with and without OPC at a fixed frequency ω is given in dB by:

$$\psi(\omega)=10\log_{10}\left(\frac{\iint|H_{3,OPC}|^2d\omega_1d\omega_2}{\iint|H_{3,EDFA}|^2d\omega_1d\omega_2}\right), \tag{5.10}$$

where $H_{3,EDFA}$ is the third-order kernel for a system without OPC based on EDFA presented in [71] and shown in Eqs. (2.36)–(2.38).

The systems under investigation were the following: (i) 10x100 km SMF, (ii) 10x100 km record-low attenuation fibre with $\alpha=0.1419$ dB/km from [86], (iii) 20x50 km SMF and (iv) 20x50 km record-low attenuation fibre. All systems have the same transmission distance, however the fibre attenuation coefficient and the span length were varied. Both parameters directly affect the signal power profile and, there-

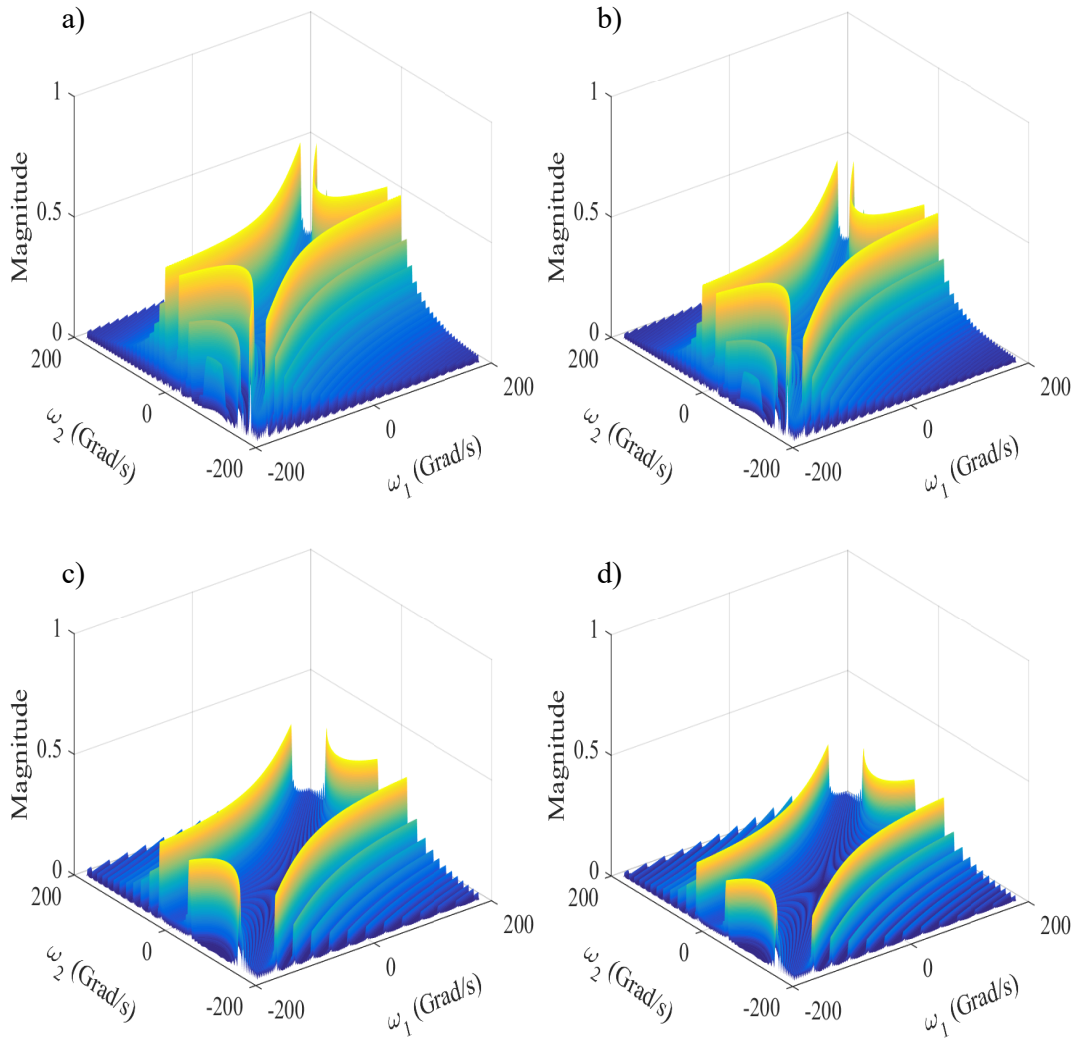

Figure 5.8: Normalised third order Volterra kernel for $\omega = 0$ and transmission of 1000 km using a) 100 km spans SSMF, b) 100 km spans with $\alpha = 0.1419$ dB/km, c) 50 km spans SSMF, d) 50 km spans with $\alpha = 0.1419$ dB/km

fore, the symmetry conditions of the transmission link. For all four systems studied the asymmetry percentages were 163, 134, 104, and 77 %.

Figure 5.8 shows the magnitude of the third-order Volterra kernels for the systems under investigation using a mid-link OPC, normalised relative to the respective kernel without OPC. All kernels show some degree of nonlinear compensation. Noticeably, the centre of the kernel together with the combination $\omega_1 = \omega_2$ always has a value of 0, implying complete removal of nonlinearites for the mentioned combinations. Other frequency combinations, however, present different degrees of NLC that depend of the parameters of the transmission fibre. With the highest asymmetry percentage, both links comprised of 100 km spans present a smaller compensation of NLI. The use of a fibre with a lower attenuation coefficient increases slightly the symmetry conditions of the link and, therefore, the third-order kernel presents a smaller magnitude compared

to SMF. The ratios between the third-order kernels with and without OPC ($\psi(\omega)$) at $\omega = 0$, obtained using 100 km spans were -6.6 and -8.1 dB for $\alpha = 0.2$ dB/km and $\alpha = 0.1419$ dB/km, respectively. The use of shorter spans resulted in an improved power symmetry, due to the smaller power excursion experienced by the transmitted signal. Compared to the use of longer spans, the third order Volterra kernel shows a greater reduction in the generation of new frequency components. The centre region of both kernels in Fig. 5.8 c) and d), where complete suppression of NLI noise is found, presented a larger area, compared to the system with 100 km spans. Moreover, the use of a lower attenuation coefficient in this configuration further improves the performance of OPC as a NLC method. For both systems using 50 km spans ξ ratios at $\omega = 0$, were -13.1 and -15.6 dB for $\alpha = 0.2$ dB/km and $\alpha = 0.1419$ dB/km, respectively.

As seen in section 5.1, the signal power profile has a strong influence on the performance of OPC as a NLC method. However, even when using EDFAs it is possible to improve the link symmetry conditions and thus, the efficacy of an OPC module used as a NLC method. The use of fibres with lower attenuation than SMF or, more interestingly, the use of shorter fibre spans lead to a greater NLC using OPC. For the particular studied transmission distance of 1000 km, decreasing the span length from 100 to 50 km yields a reduction of 6.6 dB in NLI noise using OPC.

5.2.2 Volterra-assisted OPC

As described in chapter 2, using the VSTF it is possible to implement a nonlinear equaliser tailored to the the nonlinear response of a system. When an OPC is used in an EDFA link, a fraction of the nonlinear effects is left uncompensated due to the lack of power symmetry, and a VSFE derived from Eq. (5.6) can be used to compensate the residual NLI noise the receiver.

Point-to-point links are formed by an optical fibre followed by an EDFA, repeating this structure a total of N_s times until the destination is reached. The normalised third order Volterra kernel for a transmission link comprised of 10 fibre spans of 100 km of SMF is shown in Fig. 5.9 a). The kernel presents a maximum when the frequencies $\omega_1 = \omega_2$. Frequencies further away from this combination show a decrease in the strength of nonlinear interactions due to the walk-off effect induced by fibre dispersion. The oscillations observed in the kernel arise from the coherent accumulation of nonlinearites in every span.

The nonlinear kernel for the same link using OPC is shown in Fig. 5.9 b) normalised relative to the kernel from Fig. 5.9 a). The use of OPC effectively reduces the magnitude of the nonlinear kernel approximately by half, an effect that can be understood from the phased-array seen in Eq (5.8) only accumulating nonlinearites over $N_s/2$ spans. Furthermore, complete suppression of nonlinearities was achieved by the OPC when

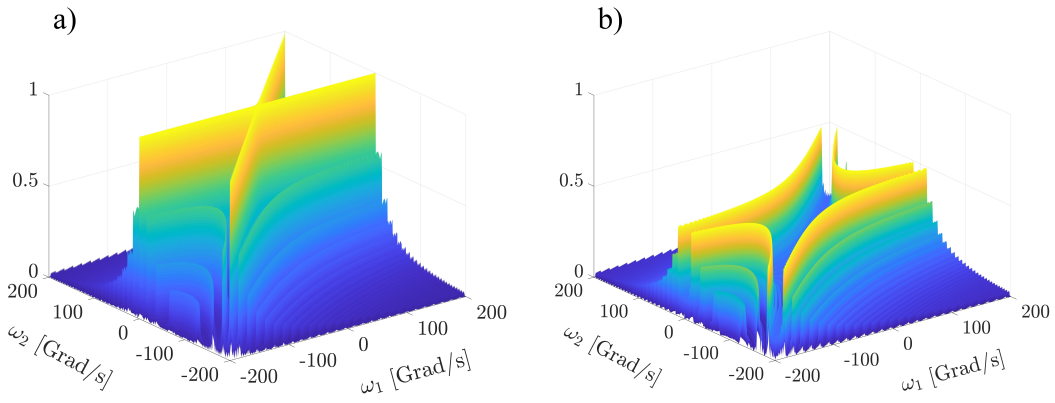

Figure 5.9: Third-order nonlinearity kernels for a 10x100 km SSMF, EDFA-amplified link a) without OPC, and b) with OPC.

$\omega_1 = \omega_2$, however for different combinations of frequencies the residual nonlinearites are still present at the receiver. Using the VSTF described in Eq. (5.6), a nonlinear equaliser can be developed to compensate for the residual NLI noise at the receiver, seen in Fig. 5.9 b), forming the VAO method. The following section details the simulation system used to investigate the performance, and how the nonlinear equalisers were numerical implemented for this study.

5.2.2.1 Simulation system

To characterise the performance of the proposed NLC method numerical simulations were performed. All the investigated system scenarios are shown in Fig. 5.10, with different colours representing the different NLC schemes. An ideal optical transmitter was used to generate 5×PM-16QAM channels at a symbol rate of 32 GBaud with a sequence length of 2^{16} symbols. The signal pulses were shaped using a root raised cosine filter with 0.1% roll-off factor. The fibre spans were based on SMF, with an attenuation coefficient of 0.2 dB/km, dispersion parameter of 17 $\text{ps} \cdot \text{nm}^{-1} \cdot \text{km}^{-1}$ and nonlinear coefficient of 1.2 $\text{W}^{-1}\text{km}^{-1}$. Within the transmission link the optical signal was amplified using an EDFA after each span. At the middle point of the link the signal could either continue to the following span (blue path) or undergo phase conjugation (red path). Ideal optical phase conjugation was performed by taking the complex conjugate of the optical signal in the time domain.

In this work two transmission scenarios were studied. Firstly, ASE noise free transmission was simulated to characterise the suppression of nonlinearites using different NLC methods. In this scenario the ASE noise from the EDFAs was set to zero, leaving the interactions between dispersion and nonlinearites as the only cause of signal distortions. Secondly, the complete transmission system was simulated to evaluate performance using the studied NLC schemes in a practical scenario. In this case, the noise figure from the EDFAs was set to 5 dB.

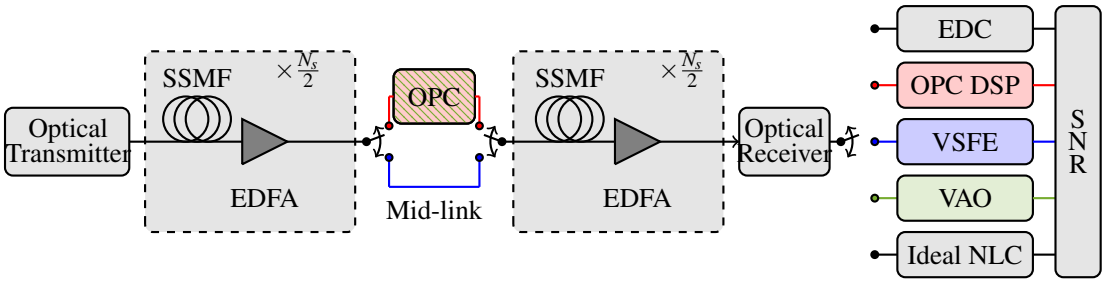

Figure 5.10: Simulation setup

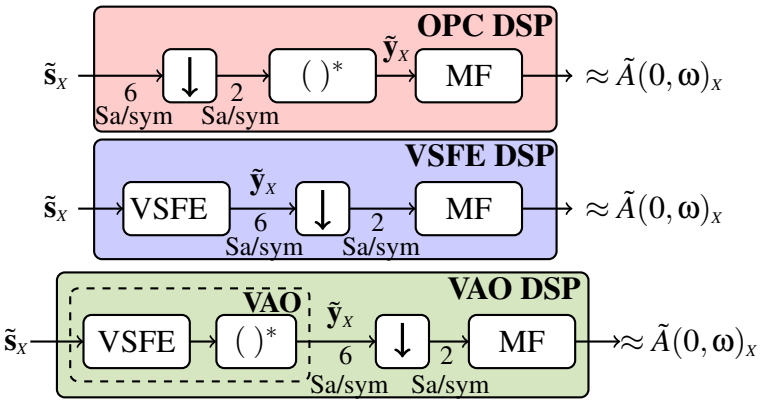

Figure 5.11: DSP chain for the different NLC methods under study

At the receiver, one of the following methods was applied: (i) electronic dispersion compensation if the link did not use OPC (to give a base line to compare all the NLC schemes under study); (ii) conjugation of the received signal when OPC was in place; (iii) single-step per link VSFE as described in [166, Eq. (13)] if the link did not use OPC; (iv) VSFE using a recursive (span per span) implementation; (v) VSFE using Eq. (5.6) in the opposite propagation direction when OPC was in place; (vi) ideal NLC performed by solving the Manakov equation in the opposite propagation direction. Finally, a matched filter was applied to the signal and SNR was used as the performance metric. The DSP chain for the methods under study is shown in Fig. 5.11.

5.2.2.2 VSFE and VAO implementation

A VSFE aims to reconstruct the transmitted signal field using the Volterra series expansion through a frequency-domain processing. In the equaliser, the received signal is multiplied by the Volterra kernels in a back-propagation direction, that is with inverted signs in the fibre parameters (α, β_2 and γ), as described in section 2.5. Depending on the type of VSFE and system configuration, different nonlinear Volterra kernels were used to compensate for nonlinearities, however, the implementation of the nonlinear equalisers remained the same in all cases.

In VSFE, the equaliser processes N samples of the received time-domain signal at a

time. The nonlinearly equalised signal, for the X polarisation, is then obtained as:

$$y_{X,n} = (s_{X,n} + p_{X,n})\, e^{-j(n\Delta\omega)^2 \beta_2 N_s L_s} \text{ for } n = 0, 1, ..., N-1 \tag{5.11}$$

where $s_{X,n}$ is the discrete Fourier transform of the received sampled time-domain signal over a N-sample window of duration T, and $\Delta\omega = 1/T$. The sequence $p_{X,n}$ corresponds to the third-order Volterra term, and the exponential term corresponds to the linear kernel of the VSFE.

For a single-step VSFE with no OPC module in the transmission link, the third-order Volterra term, $p_{X,n}$, is given by:

$$p_{X,n} = \sum_{i=0}^{N-1} \sum_{j=0}^{N-1} \Xi_{ijk} \mathbf{F}_{ijk} \left[s_{X,i} s_{X,j} s_{X,k+i-j} + s_{X,i} s_{Y,j} s_{Y,k+i-j} \right] \tag{5.12}$$

where $\mathbf{F}_{ijk} \triangleq F(i\Delta\omega, j\Delta\omega, k\Delta\omega)$, and $\Xi_{ijk} \triangleq \xi(N_s, i\Delta\omega, j\Delta\omega, k\Delta\omega)$ for $i = 0, 1, ..., N-1$ are the discrete frequency-domain representations of the four-wave mixing efficiency factor and *phased-array* in a backward direction defined in [71], respectively. As the frequency-domain signals in (5.8) are replaced by the discrete Fourier transforms, the integral effectively reduces to the double-summation

The same numerical implementation was used to study an iterative VSFE for the link without OPC, however the recursive nature of this method requires the equalisation to be performed one span at a time in a backward direction, hence no *phased-array* was used to calculate $p_{n,X}$. With this in mind, the equalised output of one span is given by:

$$y_{X,n} = (s_{X,n} + p_{X,n})\, e^{-j(n\Delta\omega)^2 \beta_2 L_s} \text{ for } n = 0, 1, ..., N-1 \tag{5.13}$$

and the third-order Volterra term:

$$p_{X,n} = \sum_{i=0}^{N-1} \sum_{j=0}^{N-1} \mathbf{F}_{ijk} \left[s_{X,i} s_{X,j} s_{X,k+i-j} + s_{X,i} s_{Y,j} s_{Y,k+i-j} \right] \tag{5.14}$$

Finally, due to the compensation of the chromatic dispersion during the link, the equaliser used in the VAO method did not require compensation of linear impairments, and hence the nonlinearly equalised signal is given by:

$$y_{X,n} = s_{X,n} + p_{X,n} \text{ for } n = 0, 1, ..., N-1. \tag{5.15}$$

with third-order Volterra term:

$$p_{X,n} = \sum_{i=0}^{N-1} \sum_{j=0}^{N-1} \Xi_{ijk} \mathbf{K}_{ijk} \left[s_{X,i} s_{X,j} s_{X,k+i-j} + s_{X,i} s_{Y,j} s_{Y,k+i-j} \right] \tag{5.16}$$

with $\mathbf{K}_{ijk} \triangleq K(i\Delta\omega, j\Delta\omega, k\Delta\omega)$, and $\Xi_{ijk} \triangleq \xi^*(N_s/2, i\Delta\omega, j\Delta\omega, k\Delta\omega)$ For the VAO equaliser, the third-order Volterra term is implemented using Eq. (5.16), however, the FWM efficiency and *phased-array* were redefined accordingly using Eq. 5.8. Additionally, the signal kernels for the VAO equaliser are defined in Eq. (5.7).

In this work, VSFE was applied sequentially over subsequent sequences of samples, whose size was varied (between 128 and 1024 symbol periods) depending on the transmission distance. For each processed sequence, a certain number of symbols were discarded from each side of the window, to account for the cyclic effects. Although this increases the complexity per sample of the VSFE [130], it benefits the equaliser performance. As discussed in the following sections, the performance metrics analysed in this work (NLI suppression and SNR) are closely related to the reduction of NLI distortion. To always guarantee the best performance, the VSFE window size was set to 4 times (up to a maximum of 1024 symbols) the estimated channel memory. A rough estimate can be obtained using $M \approx |\beta_2| \cdot R_s \cdot B \cdot L$ where R_s is the channel symbol rate, B is the entire transmitted bandwidth, and L is the total transmitted distance. Each sub-sequence was sequentially processed by the VSFE, and then detected. The boundary symbols of the detected sub-sequence were then increasingly discarded until the *performance metric* of choice converged within a tolerance of 0.05 dB. Multiple sub-sequences were then processed to accumulate sufficient received symbols and to guarantee the accuracy of the *performance metric* calculation.

5.2.2.3 Nonlinearity suppression

To assess the NLC effectiveness of the proposed scheme, the NLI suppression factor η_{NLC} was studied through numerical simulations. This NLC suppression factor can be defined as:

$$\zeta_{\text{NLC}} = \frac{\sigma^2_{\text{EDC}}}{\sigma^2_{\text{NLC}}}, \tag{5.17}$$

where σ^2_{EDC} and σ^2_{NLC} represent the NLI power when either EDC or NLC was applied in the absence of any other noise source. The η_{NLC} factor is crucial to understand, in the absence of any other noise sources, what is the efficacy of a NLC scheme to reduce the NLI noise. For an ideal NLC scheme η_{NLC} tends to infinity as σ^2_{NLC} is suppressed to 0. On the other hand, this value tends to 1 if the NLI is left uncompensated (EDC-only schemes), or goes below zero when additional nonlinear distortions are added (NLC schemes with limited accuracy or that introduce numerical errors). To fully characterise the proposed VAO scheme, the η_{NLC} parameter was studied as a function of the signal power for a transmission distance of 1000 km.

The NLI suppression was calculated for the NLC methods under study, namely OPC, single-step VSFE, recursive VSFE and the VAO scheme, as a function of signal power and the results are plotted in Fig. 5.12. The use of a mid-link OPC showed a

constant suppression of NLI as a function of signal power. Due to the nature of OPC, where NLI is compensated throughout the link, the compensation is independent of the signal properties, and is only determined by the parameters of the fibre that form the link. For this particular link, a NLI suppression of 1.2 dB was found.

On the other hand, both implementations of VSFE were shown to be dependent on the transmitted signal power. From the equaliser structure, with the received symbols used to calculate the third order Volterra term, this power dependence becomes evident. Interestingly, both equaliser implementations studied show different trends as a function of the signal power. The single-step VSFE implementation shows a decreasing NLI suppression as the signal power is increased. For the powers of interest for a 100 km span (around 0 dBm per channel), the same performance as OPC was found with approximately 1.2 dB NLI suppression. The improved performance for lower power, and also reduced performance for higher power, can be understood from the strength of NLI noise and reconstruction of the received signal from the VSFE. When VSFE was implemented, the transmitted signal was reconstructed using Eq. (5.6) in the backward direction. As the signal power is increased, the third-order truncation of the VSTF becomes insufficient to approximate the stronger nonlinear distortions experienced by the signal and, therefore, the equaliser is unable to compensate all the distortions. The opposite behaviour is found as the signal power is reduced, where a better approximation of the transmitted signal can be reconstructed using only the third order. This degradation is partly mitigated using a recursive VSFE scheme. The recursive VSFE scheme performs better beyond 1 dBm/channel and achieves up to 5 dB NLI suppression at 2 dBm/channel, albeit at the expense of a significantly higher computational complexity than a single-step VSFE scheme. Due to the improved performance of the recursive VSFE at higher powers, it becomes more attractive as NLC method. However, at least one equaliser must be performed once per span in order to achieve the shown performance, which in terms of complexity per compensated symbol requires increasingly more calculations as the transmission distance is increased. Further discussion on the complexity of VSFE is included in the following subsections.

VAO significantly outperforms both OPC and conventional Volterra equalisation over the entire range of powers of interest. This can be attributed to the reduction of the NLI noise and its memory when OPC is applied. Both these effects are beneficial to the performance of the Volterra equaliser. It is interesting to notice that, the VAO ζ factor is significantly higher than the sum of the singular ζ contributions arising from OPC and conventional Volterra equalisation. This demonstrates the particular effectiveness of matching OPC with a Volterra equaliser. At a launch power of -5 dB an improvement of 25 dB was found in the NLI suppression factor compared to a single-step VSFE, and 15 dB improvement at 2 dB per channel was observed compared to the recursive VSFE.

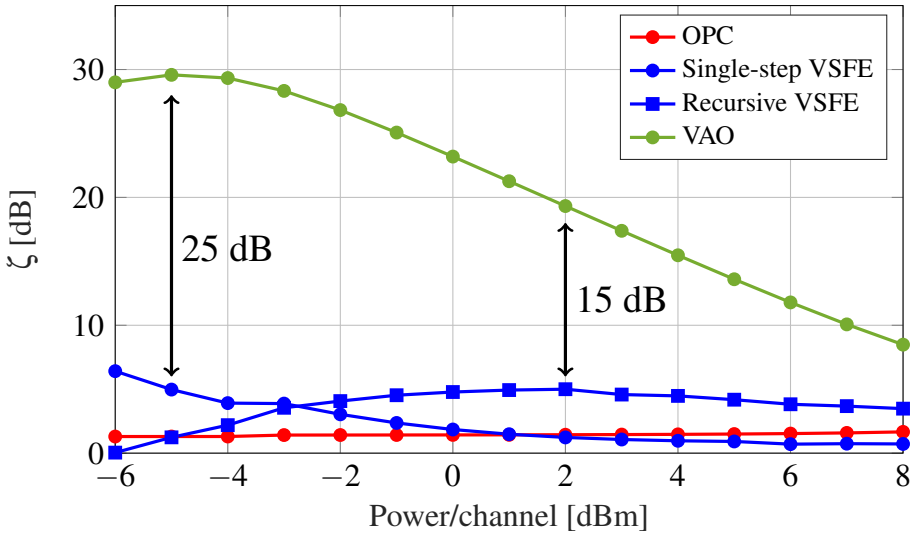

Figure 5.12: Nonlinearity suppression factor (ζ) as a function of transmitted power for the NLC schemes studied in this work.

However, as the transmission power increases the NLI suppression of the VAO method is reduced, and a ζ factor of 8.5 dB was found at 8 dB/channel, due to the VSFE used.

5.2.2.4 Performance enhancement of transmission links

Numerical simulations were carried out to assess the performance of different NLC methods and compare them to the one presented herein. Two different scenarios were studied: first the performance was evaluated for a fixed transmission distance of 1000 km as a function of the signal launch power, and secondly, the transmission distance was varied at optimum power from 400 to 3200 km.

The received SNR was calculated as a function of launch power per channel after transmission of 1000 km and is plotted in Fig. 5.13 for the different NLC techniques studied. EDC presented the worst performance of all the methods, with no nonlinear effects compensated by this scheme, it served as a baseline to evaluate the effectiveness of the NLC methods under study. EDC exhibited a maximum SNR of 17.3 dB at 0 dBm per channel. At this distance, OPC presented a gain over EDC limited to 0.4 dB, with a maximum SNR of 17.7 dB, indicating that only a small portion of the nonlinear effects were compensated. The spectral region where complete cancellation of nonlinearites was observed in Fig. 5.9 was not sufficiently large to account for the effects of all 5 transmitted channels. In the highly nonlinear regime, e.g. using a power of 4 dBm, an increase of 1.2 dB in the SNR was observed with the use of OPC, in good agreement with the nonlinear suppression factor observer for OPC in the previous section. Similar performance was observed for the use of single-step VSFE at maximum SNR. In this case, the single-step VSFE was implemented using a window size of 512 symbols. A maximum SNR of 17.7 dB was found using this method at a signal power of 1 dBm. As the power was increased the efficiency of this method was decreased as a result of

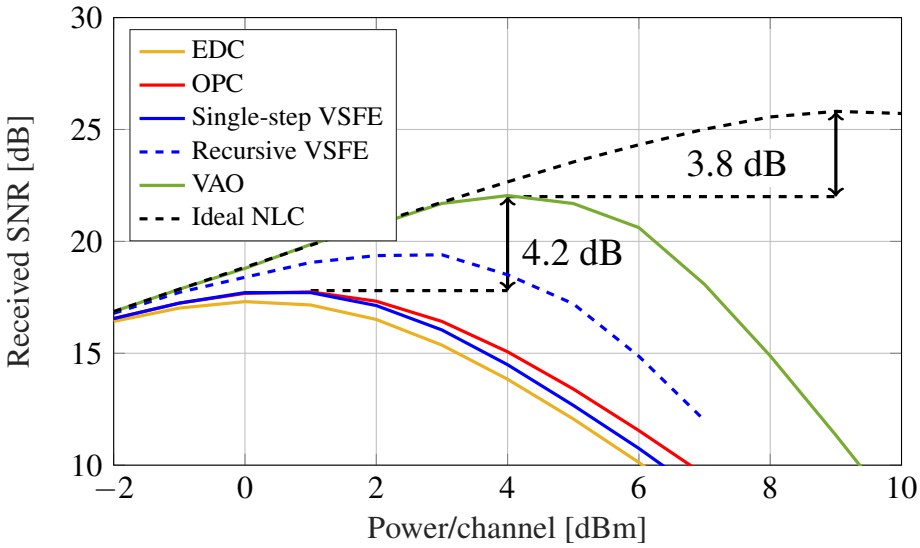

Figure 5.13: Received SNR for different NLC schemes as a function of signal power at 1000 km

the truncation of the Volterra series used for the VSFE, presenting a gain of 0.6 dB at 6 dB/channel. For the recursive VSFE, a window size of 256 symbols was used. This method presented an improved performance relative to the single-step implementation with a maximum SNR of 19.4 dB at 2 dBm signal power. Using VAO presented a significant improvement compared to the previously mentioned NLC techniques, with a gain of 4.6 dB compared to EDC, 4.2 dB relative to either standard single-step VSFE or OPC, and 2.6 dB compared to recursive VSFE. The VAO was implemented using a window size of 512 symbols in the VSFE section, to allow a direct comparison with the single-step VSFE method. Whilst the VSTF truncation is one of the factors that limits the performance of standard VSFE implementations, the reduction of nonlinear effects due to the mid-link OPC is translated in a better reconstruction of the transmitted signal using the VAO scheme. Finally, as a comparison tool, the performance of ideal NLC is shown, obtained by propagating the received signal through a perfectly inverted transmission link. This represents the maximum performance that can be obtained using any receiver based NLC scheme. Although the VAO scheme presented improved performance relative to the aforementioned NLC schemes, a 3.8 dB gap was still observed compared to an ideal NLC method. The maximum received SNR was calculated for all the NLC methods under study as a function of transmission distance, and the results are plotted in Fig. 5.14. The same trend from Fig. 5.13 in terms of nonlinear effects was observed, with EDC exhibiting the worst performance among the studied methods. OPC presented a reduced gain of 0.2 dB relative to EDC after 200 km, however greater nonlinear compensation was obtained for longer distances and 0.6 dB gain was observed after 3200 km. The opposite behaviour was found for the use of single-step VSFE, where a superior performance at short distances was found. The gain over EDC was slowly reduced for longer distances, up to the point where no

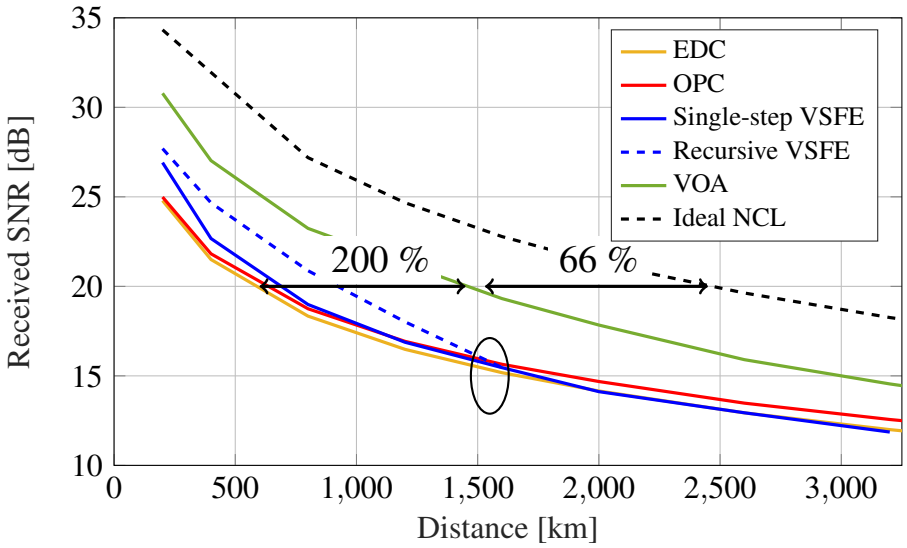

Figure 5.14: Received SNR for different NLC schemes as a function of transmission distance at optimum power.

improvement was observed. The reduction of gain from VSFE can be understood from the memory effects introduced by chromatic dispersion. When the temporal spreading of the propagated signal exceeded the VSFE window size, the performance of both implementations, single-step and recursive, was dramatically reduced. For the studied system no gain from NLC was observed for transmission distances longer than 1600 km using single-step and recursive VSFE implementations.

The VAO scheme was shown to outperform both standard implementations of VSFE, and OPC at all evaluated distances. For a received SNR of 20 dB, VAO was shown to attain a 200% increase in transmission distance compared to EDC, going from 500 to 1500 km. The VAO method however, did not offer full NLI compensation experienced during transmission and reduced performance was found compared to ideal NLC. Additionally, VAO presented an increased reduction of the gain from NLC compared to ideal NLC as the transmission distance was increased. We attribute this behaviour to the nonlinear equaliser in the VAO scheme, that presented the same limitations from the standard VSFE implementation. Although the system memory was greatly reduced in the VAO case, a limited window size still leads to an incomplete compensation of nonlinearities. The use of ideal NLC achieved an extra 66% increase of transmission distance compared to VAO.

5.2.2.5 On the computational complexity of VAO

Real-time implementation of any NLC method for future optical transmission systems is determined by the performance, and the complexity required to achieve said performance. State-of-the-art transceivers need to be able to process large waveforms considering all the concerns from the DSP processing unit within them, such as chip

area for NLC and power dissipation. In this subsection a comparison on the computational complexity of different NLC methods is reported. First, the performance of VAO and single-step VSFE was compared using different window sizes in the equaliser, using the NLI suppression factor as a performance metric, and subsequently, a discussion on the complexity of DBP and VAO is performed.

The computational complexity of a VSFE, in its conventional implementation, scales as $O(N_{\mathrm{FFT}}^2)$ per sample [126] due to the double integral in the third-order Volterra kernel shown in Eq. (5.8). For continuous data transmission, this limits the window size over which the VSFE can be sequentially applied. Conversely, a minimum window size must be guaranteed to allow for an absorbing window for the fibre channel memory effects to be factored out.

The NLI suppression factor at 0 dBm was calculated as a function of distance using a range of window sizes from 128 up to 1024 processed symbols, and the results for single-step VSFE are plotted in Fig. 5.15. A high NLI suppression of 15 dB was observed after one span for window sizes larger than 256, with a rapid decrease in performance as a function of distance for all evaluated time windows, however, for a window size of 128 symbols, a poor performance was already found after a single span, where a NLI suppression of approximately 5 dB was present. As the distance was increased, a larger time window was required to account for the spreading of the symbols in time. For distances longer than 500 km a sequence length of 128 symbols did not offer any NLC benefits, in fact the NLI suppression becomes negative due to the numerical errors in the calculation of the third-order Volterra kernel arising from the limited number of symbols. The same effect was found for longer sequences at different distances, with 1000 and 3000 km the maximum distances where gain was found using sequences of 256 and 512 symbols respectively.

VAO achieves a complete compensation of chromatic dispersion along the transmission link due to the OPC, reducing the memory effects after transmission. Although residual memory effects were still present due to the interaction between nonlinearites and dispersion along the link, this technique presented a significant performance improvement compared to VSFE for the same window sizes. The NLI suppression factor as a function of distance for transmission using VAO are shown in Fig. 5.16. For all evaluated window sizes the VAO was shown to present a higher NLC suppression factor compared to single-step VSFE. Additionally, VAO was shown to be more robust as a function of the transmission distance, with a slower reduction of the obtained gain as the transmission distance increases. For sequences of 512 and 1024 symbols, the NLI suppression factor of VAO was shown to be 20 dB higher than VSFE at 1000 km, and remained approximately 10 dB higher after 4000 km.

Although a performance benefit was observed when comparing VAO to either of the two NLC methods that comprise this technique, separately shown in Figs. 5.13 and 5.14,

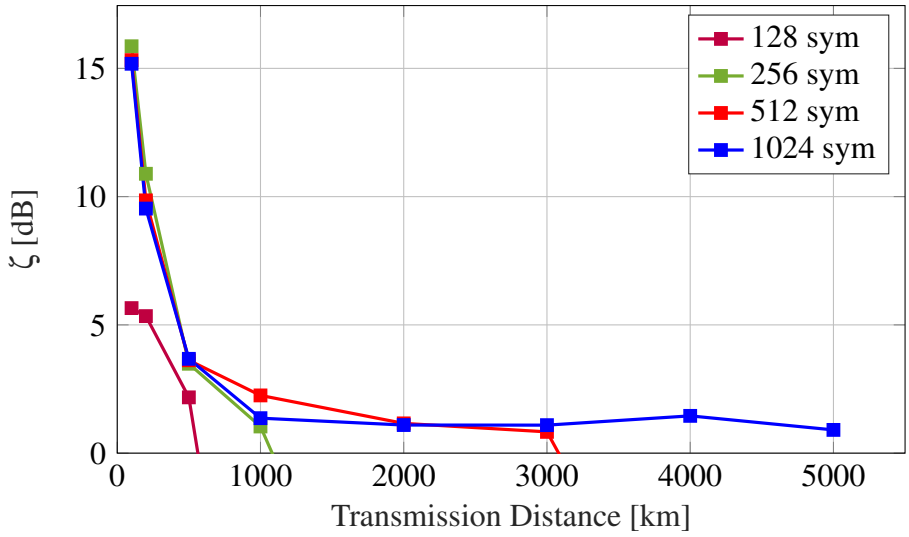

Figure 5.15: Nonlinearity suppression factor (ζ) as a function of transmission distance and different equaliser window sizes for VSFE.

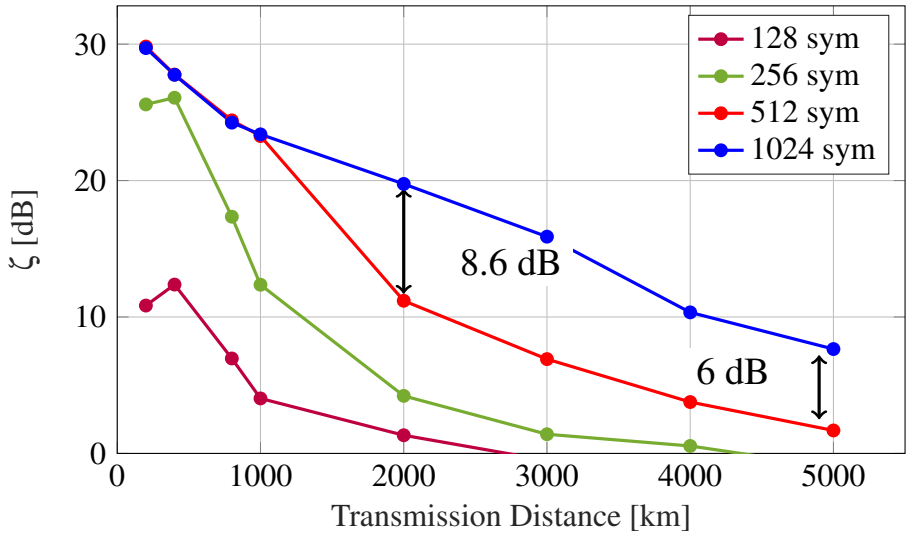

Figure 5.16: Nonlinearity suppression factor (ζ) as a function of transmission distance and different equaliser window sizes for VAO.

a substantial performance penalty (e.g. 3.8 dB at 1000 km transmission distance) was still observed with respect to the use of an ideal full NLC scheme capable of removing all signal-signal nonlinear distortions experienced during transmission (as seen in Fig. 5.13). Such an ideal NLC performance could be theoretically achieved through a *full-complexity* implementation of the DBP algorithm over the entire transmitted bandwidth (FF-DBP). Considering this, an interesting question to answer is which NLC method, VAO or DBP, represents a better trade-off between performance and complexity.

Comprehensive studies on the complexity of VSFE and different simplified variants thereof can be found in the literature [126, 166], where the main challenge of VSFE was described to be the $O(N^2)$ number of complex multiplications required to process

a symbol within a sub-sequence of length N. These highlight the fact that, despite a complexity per symbol scaling asymptotically as $C_{\mathrm{VSFE}} \propto N^2$ for a standard VSFE implementation, complexity can be reduced down to $O(\log(N)$ at the cost of a controlled performance penalty. In [129, 167] two different VSFE implementations have been proposed that allow the aforementioned complexity reduction. In [129] parallel equalisation branches are proposed similar to the SSFM, however this method was shown to underperform compared to DBP. Alternatively, in [167] a factorisation method was applied to the third-order Volterra kernel to reduce the complexity of the algorithm, but it was also shown to underperform compared to a full VSFE implementation. In an effort to retain the performance of VSFE, other implementation methods were proposed in [128, 130] using symmetry conditions from the third order Volterra kernel or parallel structures for the equaliser that allow the use of shorter sequences. The mentioned modifications to the VSFE implementation were not applied in this work however, and the potential complexity reduction they can offer for the computation of the VAO third-order kernel remains an interesting research problem.

On the other hand, for a large number of processed samples N DBP complexity per processed symbol scales as $N_{\mathrm{steps}} \log N$ where N_{steps} is the number of DBP steps performed. As in the VSFE/VAO case the minimum value of N for DBP is dictated by the target NLC performance and the channel memory. The impact of the channel memory on the required complexity was discussed in, e.g., [130, 168]. Due the logarithmic scaling, matching increasing channel memory by increasing N only results in a minor complexity increase for DBP. The main issue in extending DBP to larger NLC bandwidths is instead in the minimum N_{steps} required to preserve a fixed NLC suppression. The latter is determined by the accuracy of the SSFM, whose relationship with N_{steps} and the system bandwidth depends on the specific SSFM variant adopted. For the logarithmic step-size SSFM, for instance, N_{steps} scales quadratically with the NLC bandwidth (at fixed power spectral density) [169]. Conversely, the complexity per symbol of VSFE scales asymptotically (for large N) as N^2. As the memory of the channel M scales as $M \propto LB^2$ (in number of samples), the VSFE sequence length rapidly becomes prohibitively large for an increasing B. However, asymptotic regimes are often not of interest for real systems. For intermediate NLC bandwidth regimes ($M < 1000$), VSFE could still be a viable option when approximated values of the double summation in the third order kernel are considered [168].

In conclusion, a comprehensive study of the performance/complexity trade-off between VAO and DBP requires a detailed description of the implementation of both algorithms, which is outside the scope of this work. However, VAO was shown to be a valid alternative to DBP, with the same complexity as a standard VSFE or less, when the NLC bandwidth extends beyond 5 channels, as shown in this section.

5.3 Summary

The compensation of nonlinear effects is key to increasing the capacity of future optical communication systems. In this chapter the performance of optical phase conjugation (OPC) in an installed network was experimentally investigated, with reasons for its limited performance identified. Additionally, a novel hybrid optical-digital NLC method, called Volterra-assisted OPC (VAO), was presented, where a Volterra series frequency equaliser (VSFE) was used to improve the performance of an OPC module in the absence of symmetry conditions. The key results from this chapter are summarised as follows:

- Transmission over an installed network using PM 14×256QAM channels was performed and OPC as NLC methods, achieving a throughput of 5.7 Tb/s. An increase in the nonlinear tolerance of the system of approximately 1 dB was observed using OPC. However, practically no improvement on the maximum received SNR was observed for all bandwidths evaluated.

- The OPC module effectively performed chromatic dispersion compensation during propagation, even in the presence of a dispersion slope.

- The transmission distance and the different lengths of fibre in each span were found to affect the observed gains after transmission. However, EDFA's noise figure and transceiver limitations do no improve the performance of the OPC system.

- The signal power profile along the link was found to be the key limitation on the NLC performance of OPC. Alternative amplification solutions, such as distributed Raman amplifiers and ideal distributed amplification were shown to present gains higher by 3 and 6.8 dB compared to EDFA for the same system configuration.

- A VSTF for systems using a mid-link OPC was derived and used to study how different system parameters affect the NLC performance of the OPC. It was shown that shorter span lengths and lower attenuation coefficients improve the performance of the OPC system. For the particular studied transmission distance of 1000 km, decreasing the span length from 100 to 50 km yields a reduction of 6.6 dB in NLI noise using OPC.

- A VSFE was implemented to mitigate the residual NLI in asymmetric links using OPC. The VAO method presented improved performance compared to either OPC or standard VSFE implementations. A twofold advantage was found for the VAO method: overcoming OPC limitations in asymmetric links and substantially enhancing the performance of Volterra equalisers. The proposed scheme was

shown to outperform both OPC and Volterra equalisation used independently by 4.2 dB in a 1000 km EDFA-amplified fibre link.

6

Conclusions and future work

THE RESEARCH described in this thesis studied different solutions to increase the capacity of optical communication systems. Two actions of research were identified to achieve this goal, which are: (i) improving the received signal-to-noise ratio (SNR), and/or (ii) increasing the bandwidth of the transmitted signal. To achieve this, the use of alternative amplification solutions to reduce noise generation and increase optical bandwidth was investigated, and, a the study on the generation and mitigation of fibre nonlinearities in the optical channel was performed.

The benefits of using Raman amplification, as an alternative to the erbium-doped fibre amplifier (EDFA), were studied in chapter 3. Section 3.2 analysed the potential of using *discrete* Raman amplifiers, due to their extended bandwidth, in transmission systems. Average noise figures of 6.5 and 7.1 dB were measured for highly nonlinear fibre (HNLF) and dispersion compensating fibre (DCF) based amplifiers. An improvement in transmission performance of 1 dB was achieved using HNLF-based *discrete* Raman amplification, compared to DCF, due to the reduction in the generation of nonlinear interference (NLI) noise during transmission. Moreover, section 3.3 presented results on the use of *distributed* Raman amplifiers in transmission systems. With reduced generation of amplified spontaneous emission (ASE) noise , *distributed* Raman amplifiers allow approximately a 100% increase in transmission distance compared to an EDFA-based link. Furthermore, the use of *full-field* digital back-propagation (FF-DBP) in combination with *distributed* Raman amplification resulted in higher gains from nonlinearity compensation (NLC) compared to the use of EDFAs. NLC gains higher

by up to 1.3 dB were found using backward pumped *distributed* Raman amplification. From the results described in chapter 3, it can be concluded that Raman amplifiers are an attractive solution to increase the capacity of optical communication systems, either by increasing the optical amplification bandwidth, or by reducing noise and achieving higher gains using NLC.

Chapter 4 studied the accumulation of NLI noise in a wideband transmission regime. Section 4.1 presented experiments performed to quantify the growth of nonlinear distortions as a function of the transmitted optical bandwidth, up to 7.3 THz. A logarithmic increase in nonlinearities as a function of the optical bandwidth was observed with no signs of saturation. This work was the first to validate the Gaussian noise model, ubiquitous in the design of transmission links, in this wideband regime. The trade-off between an increase in the transmission bandwidth and the growth of nonlinear effects was studied. Increasing the transmission bandwidth was found to, due to the logarithmic relationship between the system capacity and SNR, outweigh the benefits of nonlinearity compensation. Therefore, the use of larger optical bandwidths has the potential to provide revolutionary increases in transmission capacity for future optical communication systems and networks.

As the transmitted bandwidth is increased, inter-channel stimulated Raman scattering (ISRS) becomes an important nonlinear effect that dominates the performance of optical communication systems. In section 4.2, the effects of ISRS were investigated in a transmission system employing 9 THz of optical bandwidth. For this bandwidth, due to the strength of the Raman gain coefficient, ISRS becomes a major challenge transferring power between channels co-propagating in an optical fibre. For the first time, the change in the signal power profile due to ISRS, and its effect on the generation of NLI noise was experimentally studied. It was found that ISRS can be modelled as a pure loss-amplification process modifying the signal power profile, with no significant noise transfer between signals. Further, the validity of an analytical model capable of predicting system performance of a system impaired by ISRS [60] was confirmed.

The experiments from sections 4.1 and 4.2 led to a greater understanding of nonlinear interactions for wideband signals, which is the first step in increasing the usable fibre bandwidth to maximise optical communications system capacity. In section 4.3, both the GN model and its modified ISRS version, were used to study the merit of increasing the transmission bandwidth as a potential solution to boost the capacity of optical fibres. It was shown that the capacity of a state-of-the-art system using a bandwidth of 9 THz could be increased by a factor of 3.3 extending the optical bandwidth to 35 THz. For the studied system it was found that, for bandwidths larger than 9 THz, every additional THz of bandwidth allows an average increase in the transmitted throughput of 7 Tb/s. For all the studied cases, increasing the transmission bandwidth was beneficial, with the potential to transmit a larger throughput regardless of the increase in NLI noise.

An alternative to cope with the larger NLI noise as the transmitted bandwidth is increased is optical NLC. In chapter 5 the benefits and limitations of using optical phase conjugation (OPC) as a nonlinearity compensation method in transmission links using EDFA were studied. In section 5.1, an experiment performed using the *National Dark Fibre Infrastructure Service* (NDFIS) installed optical network was described showing only 1 dB improvement on the nonlinear tolerance of the system, however no gain in the received SNR at optimum signal power was observed. The limited performance was confirmed to be the result of a lack of power symmetry relative to the conjugation point, and of the use of different span lengths in the transmission links. As a solution to the limited gain of OPC in EDFA-based transmission links, in section 5.2 a novel NLC scheme was proposed and developed to overcome the symmetry limitations. The proposed Volterra-assisted OPC (VAO) scheme was designed to overcome the limitations of both OPC and Volterra series frequency equalisation (VSFE) in practical transmission scenarios, whilst preserving the complexity of a conventional VSFE. VAO was demonstrated to effectively recover the NLC capabilities of OPC over a large optical bandwidth, in EDFA-amplified links. The addition of mid-link OPC was shown to significantly enhance the NLC performance of a conventional VSFE. For example, up to 10 dB higher NLC suppression was demonstrated for VAO and 4.2 dB enhancement in the received SNR in a 1000 km link compared to either OPC or VSFE.

Overall, from the research work presented in this thesis two overarching conclusions can be drawn. Firstly, even with the monotonic increase of NLI noise as a function of the signal bandwidth, increasing the signal bandwidth still appears to be among the most promising solutions for continuing the development of high capacity systems. Potentially, a 3-fold capacity increase could be achieved by using a total of 35 THz of optical bandwidth, compared to state-of-the-art system employing 9 THz. Secondly, to achieve higher transmission rates in future optical communication systems *distributed* amplification solutions are required to reduce the generation of noise, and NLC schemes will be crucial to mitigate the effect of NLI noise, potentially leading to up to 200% increases in the transmission distance for a fixed throughput.

6.1 Future work

The research described in this thesis has given rise to a number of additional interesting research questions, described below:

- Building on the work from chapter 3, several physical phenomena impair the performance of Raman amplifiers. In this thesis it was assumed that the main impairment is ASE noise for any configuration studied. In addition to ASE noise, two other main impairments remain to be studied for Raman amplifiers, namely

double Rayleigh backscattering and RIN transfer from pump to signal. Although from [96][Chap. 2], such impairments could be neglected in a backward pump configuration, which presents double Rayleigh backscattering levels 40 dB lower than the signal power and a RIN transfer limited in frequency to a few kilohertz. However, different configurations will suffer considerably more from both effects. Additionally, the RIN transfer and double Rayleigh backscattering accumulate linearly in a multi span system, potentially limiting the performance of long-haul transmission systems. As future work, the inclusion of both impairments in the Raman amplifier simulator is proposed together with an experimental characterisation of the amplifiers. Moreover, the limitations arising from both impairments for transmission systems in different Raman amplifier configurations can be studied.

- RIN transfer in Raman amplifiers is an impairment that affects mainly low frequency components of the signal being transmitted. In future work, the development of digital techniques to mitigate this effect is proposed. For example, line coding schemes that were developed to achieve DC balance in transmission lines [170], in addition, different modulation formats or pulse shapes might show an improved tolerance to low frequency noise.

- Results presented in chapter 3 showed an increase in the generation of NLI noise in *discrete* Raman amplifiers based on either HNLF or DCF. A reduction of the aforementioned nonlinear effects can increase the potential of *discrete* Raman amplifiers. Digital NLC methods, such as DBP or VSFE, could fully enable the use of *discrete* amplifiers in high-capacity links, however the gain fibre needs to be considered in the back-propagation algorithm or in the third order kernel of the VSFE.

- The work presented in chapter 3 also showed increased benefits for NLC when *distributed* Raman amplifiers were used due to their lower ASE generation. Additionally, in chapter 5, it was shown that *distributed* Raman amplification greatly enhances the performance of transmission link employing OPC as a NLC method. It would be useful to study the performance of Raman amplified links using either a reduced complexity VSFE or the VAO method, and compare the system performance to a traditional DBP scheme. Appendix B presents a generalised VSTF for any arbitrary power profile, making the extension to Raman amplifiers straightforward, and the improved performance of OPC is expected to further increase the benefits from VAO.

- Regarding the VAO method presented in chapter 5, a comprehensive complexity study is required. Moreover, the use of simplified VSFE implementations can

yield further complexity benefits from VAO compared to DBP.

- Finally, a possible solution to mitigate the impact of ISRS in optical communication systems, studied in chapter 4, is proposed. The solution is based on the property of frequency conversion through four-wave mixing produced by OPC modules. This could be done by placing one or several OPC modules in a system impaired by ISRS, thus inverting the spectrum of the optical signal. This way, after an OPC module, the following section of link will experience power transfer due to ISRS in the opposite direction, a phenomenon that could potentially equalise the effects of ISRS.

Bibliography

[1] S. Yoshima, Y. Sun, Z. Liu, K. R. H. Bottrill, F. Parmigiani, D. J. Richardson, and P. Petropoulos, "Mitigation of Nonlinear Effects on WDM QAM Signals Enabled by Optical Phase Conjugation with Efficient Bandwidth Utilization," *Journal of Lightwave Technology*, vol. 35, pp. 971–978, Feb 2017.

[2] Y. Sun, K. R. Bottrill, F. Parmigiani, D. J. Richardson, and P. Petropoulos, "Optical phase conjugation for simultaneous dispersion and nonlinearity compensation performed over an 800-km long field-installed transmission link," in *ECOC 2017; 43rd European Conference on Optical Communication*, pp. 1–3, IEEE, 2017.

[3] Cisco, *The Zettabyte Era: Trends and Analysis*, 2017 (accessed March 20, 2018). `https://www.cisco.com/c/en/us/solutions/collateral/service-provider/visual-networking-index-vni/vni-hyperconnectivity-wp.pdf`.

[4] K. C. Kao and G. A. Hockham, "Dielectric-fibre surface waveguides for optical frequencies," *Proceedings of the Institution of Electrical Engineers*, vol. 113, no. 7, pp. 1151–1158, 1966.

[5] T. Miya, Y. Terunuma, T. Hosaka, and T. Miyashita, "Ultimate low-loss single-mode fibre at 1.55 μm," *Electronics Letters*, vol. 15, no. 4, pp. 106–108, 1979.

[6] M. Yamada, H. Ono, T. Kanamori, S. Sudo, and Y. Ohishi, "Broadband and gain-flattened amplifier composed of a 1.55 μm-band and a 1.58 μm-band Er3+-doped fibre amplifier in a parallel configuration," *Electronics Letters*, vol. 33, no. 8, pp. 710–711, 1997.

[7] T. N. Nielsen, A. J. Stentz, K. Rottwitt, D. S. Vengsarkar, Z. J. Chen, P. B. Hansen, J. H. Park, K. S. Feder, S. Cabot, S. Stulz, D. W. Peckham, L. Hsu, C. K. Kan, A. F. Judy, S. Y. Park, L. E. Nelson, and L. Gruner-Nielsen, "3.28-Tb/s transmission over 3 x 100 km of nonzero-dispersion fiber using dual C- and L-band distributed Raman amplification," *IEEE Photonics Technology Letters*, vol. 12, pp. 1079–1081, Aug 2000.

[8] H. Kidorf, K. Rottwitt, M. Nissov, M. Ma, and E. Rabarijaona, "Pump interactions in a 100-nm bandwidth Raman amplifier," *IEEE Photonics Technology Letters*, vol. 11, no. 5, pp. 530–532, 1999.

[9] T. Okoshi, "Feasibility study of frequency-division multiplexing optical fiber communication systems using optical heterodyne or homodyne schemes," in *Pap. Tech. Group IECE Japan*, pp. no. OQE 78–139, Feb 1979.

[10] T. Okoshi, "Heterodyne and Coherent Optical Fiber Communications: Recent Progress," *IEEE Transactions on Microwave Theory and Techniques*, vol. 30, pp. 1138–1149, Aug 1982.

[11] S. J. Savory, "Digital Coherent Optical Receivers: Algorithms and Subsystems," *IEEE Journal of Selected Topics in Quantum Electronics*, vol. 16, pp. 1164–1179, Sept 2010.

[12] R. Maher, K. Croussore, M. Lauermann, R. Going, and J. Xu, X. Rahn, "Constellation Shaped 66 GBd DP-1024QAM Transceiver with 400 km Transmission over Standard SMF," in *ECOC 2017; 43rd European Conference on Optical Communication*, pp. 1–3, Sept 2017.

[13] S. L. I. Olsson, J. Cho, S. Chandrasekhar, X. Chen, E. C. Burrows, and P. J. Winzer, "Record-High 17.3-bit/s/Hz Spectral Efficiency Transmission over 50 km Using Probabilistically Shaped PDM 4096-QAM," in *2018 Optical Fiber Communications Conference and Exposition (OFC)*, pp. 1–3, Mar 2018.

[14] C. R. Davidson, C. J. Chen, M. Nissov, A. Pilipetskii, N. Ramanujam, H. D. Kidorf, B. Pedersen, M. A. Mills, C. Lin, M. I. Hayee, J. X. Cai, a. B. Puc, P. C. Corbett, R. Menges, H. Li, A. Elyamani, C. Rivers, and N. S. Bergano, "1800 Gb/s transmission of one hundred and eighty 10 Gb/s WDM channels over 7000 km using the full EDFA C-band," *2000 Optical Fiber Communications Conference and Exposition (OFC)*, vol. 4, pp. 242–244, 2000.

[15] G. Vareille, B. Julien, F. Pitel, and J. F. Marcerou, "3.65 Tbit/s (365 x 11.6 Gbit/s) transmission experiment over 6850 km using 22.2 GHz channel spacing in NRZ format," in *ECOC 2001; 27nd European Conference on Optical Communication*, vol. 6, pp. 14–15, IEEE, 2001.

[16] J. X. Cai, M. Nissov, A. N. Pilipetskii, A. J. Lucero, C. R. Davidson, D. Foursa, H. Kidorf, M. A. Mills, R. Menges, P. C. Corbett, D. Sutton, and N. S. Bergano, "2.4 Tb/s (120 x 20 Gb/s) Transmission over Transoceanic Distance using Optimum FEC Overhead and 48% Spectral Efficiency," in *2001 Optical Fiber Communications Conference and Exposition (OFC)*, (Washington, D.C.), p. PD20, OSA, Mar 2001.

[17] J. X. Cai, M. Nissov, A. N. Pilipetskii, C. R. Davidson, R. . Mu, M. A. Mills, L. Xu, D. Foursa, R. Menges, P. C. Corbett, D. Sutton, and N. S. Bergano, "1.28 Tb/s (32 x 40 Gb/s) transmission over 4,500 km," in *ECOC 2001; 27nd European Conference on Optical Communication*, vol. 6, pp. 4–5, IEEE, 2001.

[18] A. H. Gnauck, G. Raybon, S. Chandrasekhar, J. Leuthold, C. Doerr, and L. Stulz, "2.5 Tb/s (64ÃŮ42.7 Gb/s) Transmission Over 40ÃŮ100 km NZDSF using RZ-DPSK Format and All-Raman-Amplified Spans," in *2002 Optical Fiber Communications Conference and Exposition (OFC)*, pp. 21–23, Opt Soc. America, 2002.

[19] D. G. Foursa, C. R. Davidson, M. Nissov, M. A. Mills, L. Xu, J. X. Cai, A. N. Pilipetskii, Y. Cai, C. Breverman, R. R. Cordell, T. J. Carvelli, P. C. Corbett, H. D. Kidorf, and N. S. Bergano, "2.56 Tb/s (256 x 10 Gb/s) transmission over

11,000 km using hybrid Raman/EDFAs with80 nm of continuous bandwidth," in *2002 Optical Fiber Communications Conference and Exposition (OFC)*, p. FC3, Opt Soc. America, 2002.

[20] M. Nissov, Jin-Xing Cai, and C. Davidson, "Ultra-long haul WDM transmission at data rates exceeding 10 Gb/s," in *2002 Optical Fiber Communications Conference and Exposition (OFC)*, pp. 290–292, Opt Soc. America, 2002.

[21] A. Hugbart, R. Uhel, F. Pitel, G. Vareille, G. Grandpierre, O. Gautheron, and J. Marcerou, "32ÃŮ40 Gbit/s WDM transmission over 1704 km," in *ECOC 2001; 27nd European Conference on Optical Communication*, vol. 3, pp. 240–241, IEEE, 2001.

[22] G. Charlet, J.-P. Thiery, P. Tran, H. Mardoyan, J.-C. Antona, C. Martinelli, and S. Bigo, "80x10.7Gbit/s with NRZ, RZ-DPSK formats over sixty 100-km long terrestrial (non dispersion managed) fiber spans with all-Raman amplification," in *Optical Amplifiers and Their Applications*, (Washington, D.C.), p. PD1, OSA, Jul 2003.

[23] J. X. Cai, D. G. Foursa, C. R. Davidson, Y. Cai, G. Domagala, H. Li, L. Liu, W. W. Patterson, A. N. Pilipetskii, M. Nissov, and N. S. Bergano, "A DWDM demonstration of 3.73 Tb/s over 11,000 km using 373 RZ-DPSK channels at 10 Gb/s," in *Conference on Optical Fiber Communication, Technical Digest Series*, vol. 2003-Janua, pp. PD22.1–PD22.3, Optical Society of America, 2003.

[24] L. Becouarn, G. Vareille, S. Dupont, P. Plantady, J. Marcerou, A. Klekamp, R. Dischler, W. Idler, and G. Charlet, "42/spl times/42.7 Gb/s RZ-DPSK transmission over a 4820 km long NZDSF deployed line using C-band-only EDFAs," *Optical Fiber Communication Conference, 2004. OFC 2004*, vol. 2, pp. 14–16, 2004.

[25] G. Charlet, E. Corbel, J. Lazaro, A. Klekamp, R. Dischler, P. Tran, W. Idler, H. Mardoyan, A. Konczykowska, F. Jorge, and S. Bigo, "WDM transmission at 6-Tbits/s capacity over transatlantic distance, using 42.7-Gb/s differential phase-shift keying without pulse carver," *Journal of Lightwave Technology*, vol. 23, pp. 104–107, Jan 2005.

[26] G. Charlet, P. Tran, H. Mardoyan, M. Lefrancois, T. Fauconnier, F. Jorge, and S. Bigo, "151x43 Gb/s transmission over 4080 km based on return-to-zero-differential quadrature phase-shift keying," in *31st European Conference on Optical Communication (ECOC)*, vol. 2005, pp. v6–5–v6–5, IEE, 2005.

[27] D. van den Borne, E. Gottwald, G. D. Khoe, H. de Waardt, P. M. Krummrich, and S. L. Jansen, "1.6-b/s/Hz Spectrally Efficient Transmission Over 1700 km of SSMF Using 40 x 85.6-Gb/s POLMUX-RZ-DQPSK," *Journal of Lightwave Technology, Vol. 25, Issue 1, pp. 222-232*, vol. 25, pp. 222–232, Jan 2007.

[28] J. Renaudier, G. Charlet, O. Bertran Pardo, H. Mardoyan, P. Tran, M. Salsi, and S. Bigo, "Experimental analysis of 100Gb/s coherent PDM-QPSK long-haul transmission under constraints of typical terrestrial networks," in *2008 34th European Conference on Optical Communication*, pp. 1–2, IEEE, 2008.

[29] M. Salsi, H. Mardoyan, P. Tran, C. Koebele, E. Dutisseuil, G. Charlet, and S. Bigo, "155x100Gbit/s coherent PDM-QPSK transmission over 7,200km," *Ecoc*, vol. 2009-Suppl, p. PD2.5, 2009.

[30] G. Charlet, M. Salsi, P. Tran, M. Bertolini, H. Mardoyan, J. Renaudier, O. Bertran-Pardo, and S. Bigo, "72x100Gb/s Transmission over Transoceanic Distance, Using Large Effective Area Fiber, Hybrid Raman-Erbium Amplification and Coherent Detection," in *Optical Fiber Communication Conference and National Fiber Optic Engineers Conference*, (Washington, D.C.), p. PDPB6, OSA, Mar 2009.

[31] J.-X. Cai, Y. Cai, Y. Sun, C. R. Davidson, D. G. Foursa, A. Lucero, O. Sinkin, W. Patterson, A. Pilipetskii, G. Mohs, and N. S. Bergano, "112ÃŮ112 Gb/s transmission over 9,360 km with channel spacing set to the baud rate (360% spectral efficiency)," in *36th European Conference and Exhibition on Optical Communication*, pp. 1–3, IEEE, Sept 2010.

[32] M. Salsi, C. Koebele, P. Tran, H. Mardoyan, E. Dutisseuil, J. Renaudier, M. Bigot-Astruc, L. Provost, S. Richard, P. Sillard, S. Bigo, and G. Charlet, "Transmission of 96ÃŮ100Gb/s with 23% Super-FEC Overhead over 11,680km, using Optical Spectral Engineering," in *Optical Fiber Communication Conference/National Fiber Optic Engineers Conference 2011*, (Washington, D.C.), p. OMR2, OSA, Mar 2011.

[33] Jin-Xing Cai, Yi Cai, C. R. Davidson, D. G. Foursa, A. Lucero, O. Sinkin, W. Patterson, A. Pilipetskii, G. Mohs, and N. S. Bergano, "Transmission of 96 x 100-Gb/s Bandwidth-Constrained PDM-RZ-QPSK Channels With 300% Spectral Efficiency Over 10610 km and 400% Spectral Efficiency Over 4370 km," *Journal of Lightwave Technology*, vol. 29, pp. 491–498, Feb 2011.

[34] M. Salsi, O. Bertran Pardo, J. Renaudier, W. Idler, H. Mardoyan, P. Tran, G. Charlet, S. Bigo, and S. Bigo, "WDM 200Gb/s single-carrier PDM-QPSK transmission over 12,000km," in *37th European Conference and Exposition on Optical Communications*, (Washington, D.C.), p. Th.13.C.5, OSA, Sept 2011.

[35] A. H. Gnauck, P. J. Winzer, C. R. Doerr, and L. L. Buhl, "10 x 112-Gb / s PDM 16-QAM Transmission Over 630 km of Fiber with 6 . 2-b / s / Hz Spectral Efficiency," *Optical Fiber Communication Conference and National Fiber Optic Engineers Conference*, pp. 6–8, Mar 2009.

[36] A. H. Gnauck, P. J. Winzer, G. Raybon, M. Schnecker, and P. J. Pupalaikis, "10*224-Gb/s WDM transmission of 56-Gbaud PDM-QPSK signals over 1890 km of fiber," *IEEE Photonics Technology Letters*, vol. 22, pp. 954–956, Jul 2010.

[37] M. V. Mazurczyk, D. Foursa, H. G. Batshon, H. Zhang, C. Davidson, J.-X. Cai, A. Pilipetskii, G. Mohs, and N. Bergano, "30 Tb/s Transmission over 6,630 km Using 16QAM Signals at 6.1 bits/s/Hz Spectral Efficiency," in *European Conference and Exhibition on Optical Communication*, (Washington, D.C.), p. Th.3.C.2, OSA, Sept 2012.

[38] S. Zhang, M.-F. Huang, F. Yaman, E. Mateo, D. Qian, Y. Zhang, Y. Shao, I. B. Djordjevic, T. Wang, Y. Inada, T. Inoue, T. Ogata, and Y. Aoki, "40x117.6 Gb/s PDM-16QAM OFDM Transmission over 10,181 km with Soft-Decision LDPC Coding and Nonlinearity Compensation," in *Optical Fiber Communication Conference (OFC)*, (Washington, D.C.), p. PDP5C4, OSA, Mar 2012.

[39] J. Renaudier, O. Bertran-Pardo, H. Mardoyan, P. Tran, G. Charlet, S. Bigo, A. Konczykowska, J.-I. Dupuy, F. Jorge, M. Riet, and J. Godin, "Spectrally Efficient Long-Haul Transmission of 22-Tb/s using 40-Gbaud PDM-16QAM with Coherent Detection," in *Optical Fiber Communication Conference*, (Washington, D.C.), p. OW4C.2, OSA, Mar 2012.

[40] M. Salsi, R. Rios-Muller, J. Renaudier, P. Tran, L. Schmalen, and A.-l. B. Labs, "38 . 75 Tb / s Transmission Experiment over Transoceanic Distance," *39th European Conf. on Opt. Commun. (ECOC)*, no. 1, p. PD3.E.2, 2013.

[41] J.-X. Cai, H. G. Batshon, H. Zhang, C. R. Davidson, Y. Sun, M. Mazurczyk, D. G. Foursa, O. Sinkin, A. Pilipetskii, G. Mohs, and N. S. Bergano, "25 Tb / s transmission over 5 , 530 km using 16QAM at 5 . 2 b / s / Hz spectral efficiency," *Optics Express*, vol. 21, pp. 1555–1560, Jan 2013.

[42] D. Foursa, H. Batshon, and H. Zhang, "44.1 Tb/s transmission over 9,100 km using coded modulation based on 16QAM signals at 4.9 bits/s/Hz spectral efficiency," *39th European Conf. on Opt. Commun. (ECOC)*, pp. 8–10, 2013.

[43] J. X. Cai, Y. Sun, H. G. Batshon, M. Mazurczyk, H. Zhang, D. G. Foursa, and A. N. Pilipetskii, "54 Tb/s transmission over 9,150 km with optimized hybrid Raman-EDFA amplification and coded modulation," in *European Conference on Optical Communication, ECOC*, pp. 1–3, IEEE, Sep 2014.

[44] J.-X. Cai, H. Zhang, H. G. Batshon, M. Mazurczyk, O. V. Sinkin, Y. Sun, A. Pilipetskii, and D. G. Foursa, "Transmission over 9 , 100 km with a Capacity of 49 . 3 Tb / s Using Variable Spectral Efficiency 16 QAM Based Coded Modulation," *Optical Fiber Communication Conference*, pp. 8–10, Mar 2014.

[45] J. X. Cai, H. Zhang, H. G. Batshon, M. Mazurczyk, O. V. Sinkin, D. G. Foursa, A. N. Pilipetskii, G. Mohs, and N. S. Bergano, "200 Gb/s and dual wavelength 400 Gb/s transmission over transpacific distance at 6.0 b/s/Hz spectral efficiency," *Journal of Lightwave Technology*, vol. 32, pp. 832–839, Feb 2014.

[46] A. Sano, T. Kobayashi, A. Matsuura, S. Yamamoto, S. Yamanaka, E. Yoshida, Y. Miyamoto, M. Matsui, M. Mizoguchi, and T. Mizuno, "100 x 120-Gb/s PDM 64-QAM Transmission over 160 km using linewidth-tolerant pilotless digital coherent detection," in *European Conference on Optical Communication, ECOC*, vol. 1-2, pp. 1–3, IEEE, Sept 2010.

[47] J.-X. Cai, H. G. Batshon, M. Mazurczyk, H. Zhang, Y. Sun, O. V. Sinkin, D. Foursa, and A. N. Pilipetskii, "64QAM Based Coded Modulation Transmission over Transoceanic Distance with > 60 Tb/s Capacity," *Optical Fiber Communication Conference Post Deadline Papers*, p. Th5C.8, Mar 2015.

[48] A. Ghazisaeidi, I. Fernandez, R. Rios-Muller, L. Schmalen, P. Tran, P. Brindel, A. Carbo Meseguer, Q. Hu, F. Buchali, G. Charlet, and J. Renaudier, "Advanced C+L-Band Transoceanic Transmission Systems Based on Probabilistically-Shaped PDM-64QAM," *Journal of Lightwave Technology*, vol. 35, pp. 1–1, Apr 2017.

[49] J.-X. Cai, H. G. Batshon, M. V. Mazurczyk, O. V. Sinkin, D. Wang, M. Paskov, W. W. Patterson, C. R. Davidson, P. C. Corbett, and G. M. Wolter, "70.46 Tb/s Over 7,600 km and 71.65 Tb/s Over 6,970 km Transmission in C+ L Band Using Coded Modulation With Hybrid Constellation Shaping and Nonlinearity Compensation," *Journal of Lightwave Technology*, vol. 36, no. 1, pp. 114–121, 2018.

[50] J. Renaudier, A. C. Meseguer, A. Ghazisaeidi, P. Tran, R. R. Muller, R. Brenot, A. Verdier, F. Blache, K. Mekhazni, B. Duval, H. Debregeas, M. Achouche, A. Boutin, F. Morin, L. Letteron, N. Fontaine, Y. Frignac, and G. Charlet, "First 100-nm Continuous-Band WDM Transmission System with 115Tb/s Transport over 100km Using Novel Ultra-Wideband Semiconductor Optical Amplifiers," in *ECOC 2017; 43rd European Conference on Optical Communication*, pp. 1–3, Sept 2017.

[51] M. Ionescu, L. Galdino, A. Edwards, J. James, W. Pelouch, E. Sillekens, D. Semrau, D. Lavery, R. I. Killey, S. Barnes, P. Bayvel, and S. Desbruslais, "91 nm C+L Hybrid Distributed Raman/Erbium-Doped Fibre Amplifier for High Capacity Subsea Transmission," *ECOC 2018; 44th European Conference on Optical Communication*, pp. 1–3, 2018.

[52] C. E. Shannon, "A Mathematical Theory of Communication," *Bell System Technical Journal*, vol. 27, pp. 379–423, Jul 1948.

[53] C. M. Caves, "Quantum limits on noise in linear amplifiers," *Physical Review D*, vol. 26, pp. 1817–1839, Oct 1982.

[54] T. Naito, T. Tanaka, K. Torii, N. Shimojoh, H. Nakamoto, and M. Suyama, "A broadband distributed Raman amplifier for bandwidths beyond 100 nm," *Optical Fiber Communication Conference and Exhibit*, pp. 6–7, 2002.

[55] S. Namiki and Y. Emori, "Ultrabroad-band Raman amplifiers pumped and gain-equalized by wavelength-division-multiplexed high-power laser diodes," *IEEE Journal of Selected Topics in Quantum Electronics*, vol. 7, no. 1, pp. 3–16, 2001.

[56] J. Bromage, "Raman Amplification for Fiber Communications Systems," *Journal of Lightwave Techonology*, vol. 22, no. 1, pp. 79–93, 2004.

[57] P. Poggiolini, "The GN model of non-linear propagation in uncompensated coherent optical systems," 2012.

[58] A. Nespola, S. Straullu, A. Carena, G. Bosco, R. Cigliutti, V. Curri, P. Poggiolini, M. Hirano, Y. Yamamoto, T. Sasaki, J. Bauwelinck, K. Verheyen, and F. Forghieri, "GN-model validation over seven fiber types in uncompensated PM-16QAM Nyquist-WDM Links," *IEEE Photonics Technology Letters*, vol. 26, no. 2, pp. 206–209, 2014.

[59] R. Pastorelli, G. Bosco, A. Carena, P. Poggiolini, V. Curri, S. Piciaccia, and F. Forghieri, "Investigation of the Dependence of Non-Linear Interference on the Number of WDM Channels in Coherent Optical Networks," *ECOC 2012; 38th European Conference on Optical Communication*, p. We.2.C.2, 2012.

[60] D. Semrau, R. Killey, and P. Bayvel, "Achievable rate degradation of ultra-wideband coherent fiber communication systems due to stimulated Raman scattering," *Optics Express*, vol. 25, p. 13024, Jun 2017.

[61] R.-J. Essiambre and P. J. Winzer, "Fibre nonlinearities in electronically predistorted transmission," in *ECOC 2005; 31st European Conference on Optical Communication*, vol. 2, pp. 191–192 vol.2, Sept 2005.

[62] X. Li, X. Chen, G. Goldfarb, E. Mateo, I. Kim, F. Yaman, and G. Li, "Electronic post-compensation of WDM transmission impairments using coherent detection and digital signal processing," *Optics Express*, vol. 16, p. 880, Jan 2008.

[63] E. Yamazaki, A. Sano, T. Kobayashi, E. Yoshida, and Y. Miyamoto, "Mitigation of nonlinearities in optical transmission systems," in *2011 Optical Fiber Communications Conference and Exposition (OFC)*, pp. 1–3, Mar 2011.

[64] A. Sano, H. Takara, T. Kobayashi, and Y. Miyamoto, "Crosstalk-managed high capacity long haul multicore fiber transmission with propagation-direction interleaving," *Journal of Lightwave Technology*, vol. 32, pp. 2771–2779, Aug 2014.

[65] K. Toyoda, Y. Koizumi, T. Omiya, M. Yoshida, T. Hirooka, and M. Nakazawa, "Marked performance improvement of 256 QAM transmission using a digital back-propagation method," *Optics Express*, vol. 20, pp. 19815–19821, Aug 2012.

[66] L. Galdino, M. Tan, A. Alvarado, D. Lavery, P. Rosa, R. Maher, J. D. Ania-Castanon, P. Harper, S. Makovejs, B. C. Thomsen, and P. Bayvel, "Amplification Schemes and Multi-Channel DBP for Unrepeatered Transmission," *Journal of Lightwave Technology*, vol. 34, pp. 2221–2227, May 2016.

[67] A. Yariv, D. Fekete, and D. M. Pepper, "Compensation for channel dispersion by nonlinear optical phase conjugation.," *Optics Letters*, vol. 4, no. 2, p. 52, 1979.

[68] D. M. Pepper and A. Yariv, "Compensation for phase distortions in nonlinear media by phase conjugation," *Optics Letters*, vol. 5, p. 59, Feb 1980.

[69] S. Watanabe and M. Shirasaki, "Exact compensation for both chromatic dispersion and Kerr effect in a transmission fiber using optical phase conjugation," *Journal of Lightwave Technology*, vol. 14, pp. 243–248, Mar 1996.

[70] A. D. Ellis, M. Tan, M. A. Iqbal, M. A. Z. Al-Khateeb, V. Gordienko, G. Saavedra Mondaca, S. Fabbri, M. F. C. Stephens, M. E. McCarthy, A. Perentos, I. D. Phillips, D. Lavery, G. Liga, R. Maher, P. Harper, N. Doran, S. K. Turitsyn, S. Sygletos, and P. Bayvel, "4 Tb/s Transmission Reach Enhancement Using 10×400 Gb/s Super-Channels and Polarization Insensitive Dual Band Optical Phase Conjugation," *Journal of Lightwave Technology*, vol. 34, pp. 1717–1723, Apr 2016.

[71] K. V. Peddanarappagari and M. Brandt-Pearce, "Volterra series transfer function of single-mode fibers," *Journal of Lightwave Technology*, vol. 15, no. 12, pp. 2232–2241, 1997.

[72] R. J. Essiambre, G. Kramer, P. J. Winzer, G. J. Foschini, and B. Goebel, "Capacity Limits of Optical Fiber Networks," *Journal of Lightwave Technology*, vol. 28, pp. 662–701, Feb 2010.

[73] A. Alvarado, E. Agrell, D. Lavery, R. Maher, and P. Bayvel, "Replacing the Soft-Decision FEC Limit Paradigm in the Design of Optical Communication Systems," *Journal of Lightwave Technology*, vol. 33, pp. 4338–4352, Oct 2015.

[74] R. Maher, A. Alvarado, D. Lavery, and P. Bayvel, "Increasing the information rates of optical communications via coded modulation: a study of transceiver performance," *Scientific Reports*, vol. 6, no. 1, p. 21278, 2016.

[75] Y. Ogiso, H. Wakita, M. Nagatani, H. Yamazaki, M. Nakamura, T. Kobayashi, J. Ozaki, Y. Ueda, S. Nakano, S. Kanazawa, T. Fujii, Y. Hashizume, H. Tanobe, N. Nunoya, M. Ida, Y. Miyamoto, and N. Kikuchi, "Ultra-High Bandwidth InP IQ Modulator co-assembled with Driver IC for Beyond 100-GBd CDM," in *2018 Optical Fiber Communications Conference and Exposition (OFC)*, p. Th4A.2, Optical Society of America, 2018.

[76] M. Zhang, C. Wang, X. Chen, M. Bertrand, A. Shams-Ansari, S. Chandrasekhar, P. Winzer, and M. Lončar, "Ultra-High Bandwidth Integrated Lithium Niobate Modulators with Record-Low Vπ," in *2018 Optical Fiber Communications Conference and Exposition (OFC)*, p. Th4A.5, Optical Society of America, 2018.

[77] X. Chen, S. Chandrasekhar, G. R. S. Olsson, J. Cho, A. Adamiecki, and P. Winzer, "Generation and intradyne detection of single-wavelength 1.61-Tb/s using an all-electronic digital band interleaved transmitter," in *2018 Optical Fiber Communications Conference and Exposition (OFC)*, pp. 1–3, Mar 2018.

[78] G. Raybon, A. Adamiecki, J. Cho, F. Jorge, A. Konczykowska, M. Riet, B. Duval, J.-Y. Dupuy, N. Fontaine, P. J. Winzer, S. Chandrasekhar, and X. Chen, "180-GBaud All-ETDM single-carrier polarization multiplexed QPSK transmission over 4480 km," in *2018 Optical Fiber Communications Conference and Exposition (OFC)*, p. Th4C.3, Optical Society of America, 2018.

[79] I. T. U. (ITU), *G.694.1 : Spectral grids for WDM applications: DWDM frequency grid*, 2012 (accessed March 3, 2016). `https://www.itu.int/rec/T-REC-G.694.1-201202-I/en`.

[80] R. Schmogrow, S. Ben-Ezra, P. C. Schindler, B. Nebendahl, C. Koos, W. Freude, and J. Leuthold, "Pulse-Shaping With Digital, Electrical, and Optical Filters: A Comparison," *Journal of Lightwave Technology*, vol. 31, no. 15, pp. 2570–2577, 2013.

[81] P. J. Winzer and R.-J. Essiambre, "Advanced optical modulation formats," *Proceedings of the IEEE*, vol. 94, no. 5, pp. 952–985, 2006.

[82] G. P. Agrawal, *Optical fiber communication systems*. Wiley, 2010.

[83] S. J. Savory, "Digital filters for coherent optical receivers," *Optics Express*, vol. 16, no. 2, pp. 804–817, 2008.

[84] M. Ohashi, K. Shiraki, and K. Tajima, "Optical Loss Property of Silica-Based Single-Mode Fibers," *Journal of Lightwave Technology*, vol. 10, no. 5, pp. 539–543, 1992.

[85] M. C. Fugihara and A. Nolasco Pinto, "Fiber attenuation Fitting Function," *Microwave and Optical Technology Letters*, vol. 51, no. 10, pp. 2294–2296, 2009.

[86] Y. Tamura, H. Sakuma, K. Morita, M. Suzuki, Y. Yamamoto, K. Shimada, Y. Honma, K. Sohma, T. Fujii, and T. Hasegawa, "The First 0.14-dB/km Loss Optical Fiber and its Impact on Submarine Transmission," *Journal of Lightwave Technology*, vol. 36, pp. 44–49, Jan 2018.

[87] C. R. Menyuk, "Nonlinear pulse propagation in birefringent optical fibers," *IEEE Journal of Quantum Electronics*, vol. 23, no. 2, pp. 174–176, 1987.

[88] D. Marcuse, C. R. Menyuk, and P. K. Wai, "Application of the Manakov-PMD equation to studies of signal propagation in optical fibers with randomly varying birefringence," *Journal of Lightwave Technology*, vol. 15, no. 9, pp. 1735–1745, 1997.

[89] P. K. A. Wai, C. R. Menyuk, and H. H. Chen, "Stability of solitons in randomly varying birefringent fibers," *Optics Letters*, vol. 16, no. 16, p. 1231, 1991.

[90] P. Poggiolini, G. Bosco, A. Carena, V. Curri, Y. Jiang, and F. Forghieri, "The GN-model of fiber non-linear propagation and its applications," *Journal of Lightwave Technology*, vol. 32, no. 4, pp. 694–721, 2014.

[91] A. Mecozzi and R.-J. Essiambre, "Nonlinear Shannon Limit in Pseudolinear Coherent Systems," *Journal of Lightwave Technology*, vol. 30, pp. 2011–2024, Jun 2012.

[92] A. Vannucci, P. Serena, and A. Bononi, "The RP Method : A New Tool for the Iterative Solution of the Nonlinear Schrödinger Equation," *Journal of Lightwave Technology*, vol. 20, no. 7, pp. 1102–1112, 2002.

[93] S. Miller and D. Childers, *Probability and random processes: With applications to signal processing and communications*. Academic Press, 2012.

[94] C. V. Raman and K. S. Krishnan, "A New Type of Secondary Radiation," *Nature*, vol. 121, no. 3048, pp. 501–502, 1928.

[95] R. H. Stolen and E. P. Ippen, "Raman gain in glass optical waveguides," *Applied Physics Letters*, vol. 22, no. 6, pp. 276–278, 1973.

[96] C. Headley and G. P. Agrawal, *Raman amplification in fiber optical communication systems*. Academic press, 2005.

[97] D. Mongardien and S. Borne, "10Gb/s WDM Operation of a Lumped Raman Fiber Amplifier Using Highly Non-Linear Ge-Doped Photonic Crystal Fiber," *ECOC 2006; 32nd European Conference on Optical Communication*, vol. 2, no. October 2015, pp. 10–11, 2006.

[98] T. Miyamoto, M. Tanaka, J. Kobayashi, T. Tsuzaki, M. Hirano, T. Okuno, M. Kakui, and M. Shigematsu, "Highly nonlinear fiber-based lumped fiber Raman amplifier for CWDM transmission systems," *Journal of Lightwave Technology*, vol. 23, no. 11, pp. 3475–3483, 2005.

[99] A. El-Taher, M. Tan, M. A. Iqbal, L. Krzczanowicz, I. D. Phillips, W. Forysiak, and P. Harper, "High gain, flattened, discrete raman fiber amplifier and its transmission performance," in *2017 Conference on Lasers and Electro-Optics Europe European Quantum Electronics Conference (CLEO/Europe-EQEC)*, pp. 1–1, Jun 2017.

[100] Y. Akasaka, I. Morita, M. Marhic, M.-C. Ho, and L. Kazovsky, "Cross phase modulation in discrete Raman amplifiers and its reduction," in *2000 Optical Fiber Communications Conference and Exposition (OFC)*, vol. 3, pp. 197–199, 2000.

[101] J. Thiele, J. Bromage, and L. Nelson, "Impact of Discrete Raman Amplifier Architecture on Nonlinear Impairments," *ECOC 2002; 28th European Conference on Optical Communication*, pp. 9–10, 2002.

[102] S. Watanabe and T. Naito, "Compensation of Chromatic Dispersion in a Single-Mode Fiber by Optical Phase Conjugation," *IEEE Photonics Technology Letters*, vol. 5, pp. 92–95, Jan 1993.

[103] K. Kikuchi and C. Lorattanasane, "Compensation for pulse waveform distortion in ultra-long distance optical communication systems by using midway optical phase conjugator," *IEEE Photonics Technology Letters*, vol. 6, pp. 104–105, Jan 1994.

[104] C. Lorattanasane and K. Kikuchi, "Design Theory of Long-Distance Optical Transmission Systems using Midway Optical Phase Conjugation," *Journal of Lightwave Technology*, vol. 15, no. 6, pp. 948–955, 1997.

[105] S. L. Jansen, D. van den Borne, P. Krummrich, S. Spalter, G.-D. Khoe, and H. de Waardt, "Long-haul DWDM transmission systems employing optical phase conjugation," *IEEE Journal of Selected Topics in Quantum Electronics*, vol. 12, pp. 505–520, Jul 2006.

[106] H. Hu, R. M. Jopson, A. H. Gnauck, M. Dinu, S. Chandrasekhar, X. Liu, C. Xie, M. Montoliu, S. Randel, and C. J. McKinstrie, "Fiber nonlinearity compensation of an 8-channel WDM PDM-QPSK signal using multiple phase conjugations," in *2014 Optical Fiber Communications Conference and Exposition (OFC)*, (Washington, D.C.), p. M3C.2, OSA, 2014.

[107] I. D. Phillips, M. Tan, M. F. C. Stephens, M. E. McCarthy, E. Giacoumidis, S. Sygletos, P. Rosa, S. Fabbri, S. T. Le, T. Kanesan, S. K. Turitsyn, N. J. Doran, P. Harper, and A. D. Ellis, "Exceeding the nonlinear-Shannon limit using

Raman laser based amplification and optical phase conjugation," in *2014 Optical Fiber Communications Conference and Exposition (OFC)*, (Washington, D.C.), p. M3C.1, OSA, 2014.

[108] L. B. Du, M. M. Morshed, and A. J. Lowery, "Fiber nonlinearity compensation for OFDM super-channels using optical phase conjugation.," *Optics express*, vol. 20, no. 18, pp. 19921–19927, 2012.

[109] F. Da Ros, I. Sackey, R. Elschner, T. Richter, C. Meuer, M. Nolle, M. Jazayerifar, K. Petermann, C. Peucheret, and C. Schubert, "Kerr nonlinearity compensation in a 5x28-GBd PDM 16-QAM WDM system using fiber-based optical phase conjugation," in *ECOC 2014; 40th European Conference on Optical Communication*, pp. 1–3, IEEE, Sep 2014.

[110] D. Vukovic, J. Schröder, F. D. Ros, L. B. Du, C. J. Chae, D.-Y. Choi, M. D. Pelusi, and C. Peucheret, "Multichannel nonlinear distortion compensation using optical phase conjugation in a silicon nanowire," *Optics Express*, vol. 23, pp. 3640–3646, Feb 2015.

[111] K. Solis-Trapala, T. Inoue, and S. Namiki, "Signal Power Asymmetry Tolerance of an Optical Phase Conjugation-Based Nonlinear Compensation System," *ECOC 2014; 40th European Conference on Optical Communication*, pp. 1–3, 2014.

[112] H. Hu, R. M. Jopson, A. H. Gnauck, D. Pilori, S. Randel, and S. Chandrasekhar, "Fiber Nonlinearity Compensation by Repeated Phase Conjugation in 2.048-Tbit/s WDM transmission of PDM 16-QAM Channels," in *2017 Optical Fiber Communications Conference and Exposition (OFC)*, p. Th4F.3, Optical Society of America, 2016.

[113] I. Sackey, R. Elschner, C. Schmidt-Langhorst, T. Kato, T. Tanimura, S. Watanabe, T. Hoshida, and C. Schubert, "Novel Wavelength-Shift-Free Optical Phase Conjugator Used For Fiber Nonlinearity Mitigation in 200-Gb/s PDM-16QAM Transmission," in *2017 Optical Fiber Communications Conference and Exposition (OFC)*, p. Th3J.1, Optical Society of America, 2017.

[114] H. Hu, R. M. Jopson, A. H. Gnauck, S. Randel, and S. Chandrasekhar, "Fiber nonlinearity mitigation of WDM-PDM QPSK/16-QAM signals using fiber-optic parametric amplifiers based multiple optical phase conjugations," *Optics Express*, vol. 25, p. 1618, Feb 2017.

[115] T. Umeki, T. Kazama, A. Sano, K. Shibahara, K. Suzuki, M. Abe, H. Takenouchi, and Y. Miyamoto, "Simultaneous nonlinearity mitigation in 92 $\times$ 180-Gbit/s PDM-16QAM transmission over 3840 km using PPLN-based guard-band-less optical phase conjugation," *Optics Express*, vol. 24, p. 16945, Jul 2016.

[116] M. A. Z. Al-Khateeb, M. Tan, M. A. Iqbal, A. Ali, M. E. McCarthy, P. Harper, and A. D. Ellis, "Experimental demonstration of 72% reach enhancement of 36Tbps optical transmission system using mid-link optical phase conjugation," *Optics Express*, vol. 26, p. 23960, Sept 2018.

[117] I. Brener, B. Mikkelsen, K. Rottwitt, W. Burkett, G. Raybon, J. Stark, K. Parameswaran, M. Chou, M. Fejer, E. Chaban, R. Harel, D. Philen, and A. Kosinski, "Cancellation of all Kerr nonlinearities in long fiber spans using a LiNbO3 phase conjugator and Raman amplification," *2000 Optical Fiber Communications Conference and Exposition (OFC)*, vol. 4, no. l, pp. 266–268, 2000.

[118] M. A. Z. Al-Khateeb, M. A. Iqbal, M. Tan, A. Ali, M. McCarthy, P. Harper, and A. D. Ellis, "Analysis of the nonlinear Kerr effects in optical transmission systems that deploy optical phase conjugation," *Optics Express*, vol. 26, pp. 3145–3160, Feb 2018.

[119] M. A. Z. Al-Khateeb, M. E. McCarthy, and A. D. Ellis, "Performance enhancement prediction for optical phase conjugation in systems with 100km amplifier spacing," in *ECOC 2017; 43rd European Conference on Optical Communication*, pp. 1–3, Sept 2017.

[120] E. Ip and J. M. Kahn, "Compensation of dispersion and nonlinear impairments using digital backpropagation," *Journal of Lightwave Technology*, vol. 26, no. 20, pp. 3416–3425, 2008.

[121] X. Liang, J. D. Downie, and J. E. Hurley, "Perturbation-Assisted DBP for Nonlinear Compensation in Polarization Multiplexed Systems," *IEEE Photonics Technology Letters*, vol. 29, pp. 1812–1815, Nov 2017.

[122] R. Dar and P. J. Winzer, "On the Limits of Digital Back-Propagation in Fully Loaded WDM Systems," *IEEE Photonics Technology Letters*, vol. 28, no. 11, pp. 1253–1256, 2016.

[123] G. Liga, T. Xu, A. Alvarado, R. I. Killey, and P. Bayvel, "On the performance of multichannel digital backpropagation in high-capacity long-haul optical transmission," *Optics Express*, vol. 22, no. 24, p. 30053, 2014.

[124] C. B. Czegledi, G. Liga, D. Lavery, M. Karlsson, E. Agrell, S. J. Savory, and P. Bayvel, "Digital backpropagation accounting for polarization-mode dispersion," *Optics Express*, vol. 25, pp. 1903–1915, Feb 2017.

[125] G. Liga, C. B. Czegledi, and P. Bayvel, "A PMD-adaptive DBP Receiver Based on SNR Optimization," in *2018 Optical Fiber Communications Conference and Exposition (OFC)*, pp. 1–3, Mar 2018.

[126] F. P. Guiomar, J. D. Reis, A. L. Teixeira, and A. N. Pinto, "Digital Postcompensation Using Volterra Series Transfer Function," *IEEE Photonics Technology Letters*, vol. 23, pp. 1412–1414, Oct 2011.

[127] F. P. Guiomar, J. D. Reis, A. L. Teixeira, and A. N. Pinto, "Mitigation of intrachannel nonlinearities using a frequency-domain Volterra series equalizer," *Optics Express*, vol. 20, pp. 1360–1369, Jan 2012.

[128] F. P. Guiomar and A. N. Pinto, "Simplified Volterra Series Nonlinear Equalizer for Polarization-Multiplexed Coherent Optical Systems," *Journal of Lightwave Technology*, vol. 31, pp. 3879–3891, Dec 2013.

[129] L. Liu, L. Li, Y. Huang, K. Cui, Q. Xiong, F. N. Hauske, C. Xie, and Y. Cai, "Intrachannel Nonlinearity Compensation by Inverse Volterra Series Transfer Function," *Journal of Lightwave Technology*, vol. 30, pp. 310–316, Feb 2012.

[130] A. Bakhshali, W. Y. Chan, J. C. Cartledge, M. O Sullivan, C. Laperle, A. Borowiec, and K. Roberts, "Frequency-Domain Volterra-Based Equalization Structures for Efficient Mitigation of Intrachannel Kerr Nonlinearities," *Journal of Lightwave Technology*, vol. 34, pp. 1770–1777, Apr 2016.

[131] F. P. Guiomar, J. D. Reis, A. Carena, G. Bosco, A. L. Teixeira, and A. N. Pinto, "Experimental demonstration of a frequency-domain Volterra series nonlinear equalizer in polarization-multiplexed transmission.," *Optics Express*, vol. 21, no. 1, pp. 276–88, 2013.

[132] D. J. Elson, L. Galdino, R. Maher, R. I. Killey, B. C. Thomsen, and P. Bayvel, "High spectral density transmission emulation using amplified spontaneous emission noise," *Optics Letters*, vol. 41, pp. 68–71, Jan 2016.

[133] D. J. Elson, G. Saavedra, K. Shi, D. Semrau, L. Galdino, R. I. Killey, B. C. Thomsen, and P. Bayvel, "Investigation of bandwidth loading in optical fibre transmission using amplified spontaneous emission noise," *Optics Express*, vol. 25, pp. 19529–19537, Aug 2017.

[134] M. J. Ready and R. P. Gooch, "Blind equalization based on radius directed adaptation," in *International Conference on Acoustics, Speech, and Signal Processing*, pp. 1699–1702 vol.3, Apr 1990.

[135] D. Godard, "Self-recovering equalization and carrier tracking in two-dimensional data communication systems," *IEEE Transactions on Communications*, vol. 28, pp. 1867–1875, Nov 1980.

[136] T. Pfau, S. Hoffmann, and R. Noé, "Hardware-efficient coherent digital receiver concept with feedforward carrier recovery for M-QAM constellations," *Journal of Lightwave Technology*, vol. 27, pp. 989–999, Apr 2009.

[137] I. Fatadin, S. J. Savory, and D. Ives, "Compensation of Quadrature Imbalance in an Optical QPSK Coherent Receiver," *IEEE Photonics Technology Letters*, vol. 20, pp. 1733–1735, Oct 2008.

[138] G. Liga, A. Alvarado, E. Agrell, and P. Bayvel, "Information Rates of Next-Generation Long-Haul Optical Fiber Systems Using Coded Modulation," *Journal of Lightwave Technology*, vol. 35, pp. 113–123, Jan 2017.

[139] R. J. Mears, L. Reekie, I. M. Jauncey, and D. N. Payne, "Low-noise erbium-doped fibre amplifier operating at 1.54 nm," *Electronics Letters*, vol. 23, pp. 1026–1028, Sept 1987.

[140] E. Desurvire, D. Bayart, B. Desthieux, and S. Bigo, *Erbium-doped fiber amplifiers: Device and System Developments*. J. Wiley, 2002.

[141] M. A. Iqbal, M. Tan, and P. Harper, "Enhanced long-haul transmission using forward propagated broadband first order raman pump," in *ECOC 2017; 43rd European Conference on Optical Communication*, pp. 1–3, Sept 2017.

[142] M. A. Iqbal, M. Tan, and P. Harper, "On the Mitigation of RIN Transfer and Transmission Performance Improvement in Bidirectional Distributed Raman Amplifiers," *Journal of Lightwave Technology*, vol. 36, pp. 2611–2618, Jul 2018.

[143] M. A. Iqbal, M. Tan, and P. Harper, "Enhanced Transmission Performance Using Backward-Propagated Broadband ASE Pump," *IEEE Photonics Technology Letters*, vol. 30, pp. 865–868, May 2018.

[144] M. Tan, P. Rosa, S. T. Le, V. V. Dvoyrin, M. A. Iqbal, S. Sugavanam, S. K. Turitsyn, and P. Harper, "RIN Mitigation and Transmission Performance Enhancement With Forward Broadband Pump," *IEEE Photonics Technology Letters*, vol. 30, pp. 254–257, Feb 2018.

[145] C. R. S. Fludger, V. Handerek, and R. J. Mears, "Pump to signal RIN transfer in Raman fiber amplifiers," *Journal of Lightwave Technology*, vol. 19, no. 8, pp. 1140–1148, 2001.

[146] A. D. Ellis, S. T. Le, M. A. Z. Al-Khateeb, S. K. Turitsyn, G. Liga, D. Lavery, T. Xu, and P. Bayvel, "The impact of phase conjugation on the nonlinear-Shannon limit: The difference between optical and electrical phase conjugation," in *2015 IEEE Summer Topicals Meeting Series (SUM)*, pp. 209–210, Jul 2015.

[147] M. A. Z. Al-Khateeb, M. McCarthy, C. Sánchez, and A. Ellis, "Effect of second order signal–noise interactions in nonlinearity compensated optical transmission systems," *Opt. Lett.*, vol. 41, pp. 1849–1852, Apr 2016.

[148] N. A. Shevchenko, T. Xu, D. Lavery, G. Liga, D. J. Ives, R. I. Killey, and P. Bayvel, "Modeling of nonlinearity-compensated optical communication systems considering second-order signal-noise interactions," *Opt. Lett.*, vol. 42, pp. 3351–3354, Sept 2017.

[149] R. Dar, M. Feder, A. Mecozzi, and M. Shtaif, "Properties of nonlinear noise in long, dispersion-uncompensated fiber links," *Optics Express*, vol. 21, pp. 25685–25699, Nov 2013.

[150] L. Galdino, G. Liga, G. Saavedra, D. Ives, R. Maher, A. Alvarado, S. Savory, R. Killey, and P. Bayvel, "Experimental Demonstration of Modulation-Dependent Nonlinear Interference in Optical Fibre Communication," *ECOC 2016; 42nd European Conference on Optical Communication*, pp. 1–3, 2016.

[151] J. X. Cai, H. G. Batshon, H. Zhang, M. Mazurczyk, O. V. Sinkin, D. G. Foursa, and A. N. Pilipetskii, "Transmission performance of coded modulation formats in a wide range of spectral efficiencies," in *2014 Optical Fiber Communications Conference and Exposition (OFC)*, pp. 1–3, Mar 2014.

[152] L. Galdino, D. Semrau, D. Lavery, G. Saavedra, C. B. Czegledi, E. Agrell, R. I. Killey, and P. Bayvel, "On the limits of digital back-propagation in the presence of transceiver noise," *Optics Express*, vol. 25, no. 4, p. 4564, 2017.

[153] A. Carena, G. Bosco, V. Curri, Y. Jiang, P. Poggiolini, and F. Forghieri, "EGN model of non-linear fiber propagation," *Optics Express*, vol. 22, pp. 16335–16362, Jun 2014.

[154] R. Dar, M. Feder, A. Mecozzi, and M. Shtaif, "Accumulation of nonlinear interference noise in fiber-optic systems," *Optics Express*, vol. 22, pp. 14199–14211, Jun 2014.

[155] S. Tariq and J. C. Palais, "A computer model of non-dispersion-limited stimulated Raman scattering in optical fiber multiple-channel communications," *Journal of Lightwave Technology*, vol. 11, pp. 1914–1924, Dec 1993.

[156] K.-P. Ho, "Statistical properties of stimulated Raman crosstalk in WDM systems," *Journal of Lightwave Technology*, vol. 18, pp. 915–921, Jul 2000.

[157] I. Roberts, J. M. Kahn, J. Harley, and D. W. Boertjes, "Channel Power Optimization of WDM Systems Following Gaussian Noise Nonlinearity Model in Presence of Stimulated Raman Scattering," *Journal of Lightwave Technology.*, vol. 35, pp. 5237–5249, Dec 2017.

[158] M. Cantono, D. Pilori, A. Ferrari, and V. Curri, "Introducing the Generalized GN-model for Nonlinear Interference Generation including space/frequency variations of loss/gain," *arXiv preprint arXiv:1710.02225*, 2017.

[159] D. Semrau, R. I. Killey, and P. Bayvel, "The Gaussian Noise Model in the Presence of Inter-channel Stimulated Raman Scattering," *Journal of Lightwave Technology*, pp. 1–1, 2018.

[160] K. Minoguchi, S. Okamoto, F. Hamaoka, A. Matsushita, M. Nakamura, E. Yamazaki, and Y. Kisaka, "Experiments on Stimulated Raman Scattering in S- and L-bands 16-QAM Signals for Ultra-Wideband Coherent WDM Systems," in *2018 Optical Fiber Communications Conference and Exposition (OFC)*, p. Th1C.4, Optical Society of America, 2018.

[161] S. V. Firstov, S. V. Alyshev, K. E. Riumkin, V. F. Khopin, A. N. Guryanov, M. A. Melkumov, and E. M. Dianov, "A 23-dB bismuth-doped optical fiber amplifier for a 1700-nm band," *Scientific reports*, vol. 6, p. 28939, 2016.

[162] Corning, *Corning SMF-28 Ultra Optical Fiber: Product information*, 2018 (accessed June 12, 2018). `https://www.corning.com/media/worldwide/coc/documents/Fiber/PI1424_11-14.pdf`.

[163] EPSRC, *NDFIS: National Dark Fibre Infrastructure Service*, 2017 (accessed June 19, 2018). `http://www.ndfis.org/`.

[164] R. Stolen, "Phase-matched-stimulated four-photon mixing in silica-fiber waveguides," *IEEE Journal of Quantum Electronics*, vol. 11, pp. 100–103, Mar 1975.

[165] S. Watanabe, S. Takeda, and T. Chikama, "Interband wavelength conversion of 320 Gb/s (32 $\times$10 Gb/s) WDM signal using a polarization-insensitive fiber four-wave mixer," in *ECOC 1998; 24th European Conference on Optical Communication*, vol. 3, pp. 83–87 vol.3, Sep 1998.

[166] J. C. Cartledge, F. P. Guiomar, F. R. Kschischang, G. Liga, and M. P. Yankov, "Digital signal processing for fiber nonlinearities," *Optics Express*, vol. 25, pp. 1916–1936, Feb 2017.

[167] G. Shulkind and M. Nazarathy, "Nonlinear Digital Back Propagation compensator for coherent optical OFDM based on factorizing the Volterra Series Transfer Function," *Optics Express*, vol. 21, pp. 13145–13161, Jun 2013.

[168] M. Secondini, S. Rommel, G. Meloni, F. Fresi, E. Forestieri, and L. Poti, "Single-step digital backpropagation for nonlinearity mitigation," *Photonic Network Communications*, vol. 31, no. 3, pp. 493–502, 2016.

[169] G. Bosco, A. Carena, V. Curri, R. Gaudino, P. Poggiolini, and S. Benedetto, "Suppression of Spurious Tones Induced by the Split-Step Method in Fiber Systems Simulation," *IEEE Photonics Technology Letters*, vol. 12, no. 5, pp. 489–491, 2000.

[170] J. Griffiths, "Binary code suitable for line transmission," *Electronics Letters*, vol. 5, no. 4, pp. 79–81, 1969.

A Simulation tools

Numerical simulations were carried out throughout this thesis to study the performance of different system configurations, optical amplification schemes and nonlinear compensation methods. This appendix describes the general numerical tools used to performed the simulations.

A.1 Transmitter

The simulation setup starts with a generation of the signals to be propagated through optical fibres. A pseudo-random bit sequence of length 2^n is generated independently for every channel to be simulated. The length of the sequence n depends on the transmitted system, and it should provide enough symbols to represent the system memory, and enough frequency resolution to perform the FFT and IFFT in the SSFM. Typical values of n used in this thesis range between $n = 16$ and $n = 18$. The bits are then subsequently mapped into the selected modulation format, and labelled using Gray labelling. The modulation formats include quadrature amplitude modulation (QAM) with constellation size of M, where M is chosen from the set 4, 16, 64, 256. The QAM waveforms are subsequently upsampled to satisfy Nyquist criteria and include any spectral broadening effects due to nonlinearites. The upsample factor corresponds to at least twice the largest frequency component of the total signal to be generated. A root raised cosine (RRC) is applied with a $R\%$ roll-off to shape the optical pulses. The roll-off factor (R) is determined by the desired spectrum shape of the signal. Typical values range from $R = 0.1$ to $R = 1$. These values allow for a maximum spectral efficiency, due to the small required channel spacing. Once all the channels are generated, a frequency shift (FS), determined by the channel spacing of the system, is applied to each channel separately. The channels are subsequently added in time domain to form a single waveform, creating in this way the entire optical signal to be transmitted.

In order to simulate systems employing both available polarisation states the second polarisation is generated independently using the same procedure detailed above, and both polarisation are stored in a matrix to allow for joint evaluation of the chosen propagation equation.

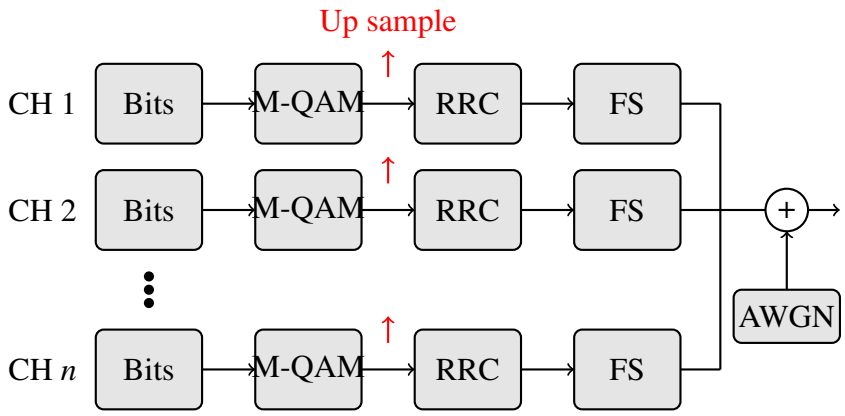

Figure A.1: Schematic of the transmitter for numerical simulations

The final stage of the signal generation corresponds to the addition of additive white Gaussian noise (AWGN) to the generated optical signal. This is done to account for different noise sources contributing to a degradation of the signal quality in experimental cases, such as quantization noise from digital-to-analogue converters (DAC), the use of electrical amplifiers to drive the optical modulators and limited bandwidth of components. This is done using a characterisation of the transceiver subsystem in a back-to-back configuration, where the received signal to noise ratio (SNR) is measured as a function of the optical signal to noise ratio (OSNR), and AWGN is added to the generated signal to match the SNR from the transceiver with the highest possible OSNR. Alternatively, an ideal transmitter can be used and no noise is added for this option. This is the most convenient way of studying fundamental impairments generated during transmission. A schematic of the transmitter used for numerical simulations is shown in Fig. A.1 for illustrative purposes.

A.2 Fibre propagation

The simulation of the signal propagation through the optical fibres that comprise the transmission link is carried out by numerically solving either the NLSE or the Manakov equation. Advantages of using the Manakov equation are the inclusion of polarisation rotation effects due to fibre birefringence, and the possibility of using a longer step size in the SMF with the same accuracy than a version of the CNLSE with the inclusion of the rotation of the polarisation state.

The numerical simulation is performed by solving the propagation equation using the SSFM as detailed in chapter 2. For the work presented in this thesis every simulation was performed using the Manakov equation due to the use of dual polarization signals. Section 2.3 presented the general implementation of the SSFM, however, for the numerical simulations performed in this thesis the symmetrized SSFM was used, that improves the accuracy of the solution by including the nonlinear step in the middle section of the step h. The symmetrized SSFM was used as follows:

$$A(z+h,T) = \exp(\frac{h}{2}\hat{D}) \exp\left(\int_z^{z+h} \hat{N}(z')dz'\right) \exp(\frac{h}{2}\hat{D})A(z,T) \tag{A.1}$$

Two different amplification solutions were used in the fibre propagation simulations: EDFA and distributed Raman amplifiers.

A.2.1 EDFA

EDFA-based links are characterised for possessing passive fibre spans with an optical amplifier following the span to compensate the fibre loss. To simulate passive fibre links, Eq. 2.18 is used and is numerically solved using the SSFM. The attenuation coefficient (α) corresponds to that of the fibre, with typical values of 0.2 dB/km for standard single mode fibre. The EDFA used to amplify the signal after the span was modelled as a device with a small signal gain of $G = \alpha L_s$, and a fixed noise figure. Typical values of noise figure for EDFA amplifiers vary between 4.5 and 5 dB.

The ASE PSD generated by an EDFA is given by:

$$S_{ASE} = 2n_{sp}h\frac{\omega_0}{2\pi}(G-1) \tag{A.2}$$

The factor of two accounts for the generation of ASE noise in both polarisations. The term n_{sp} is called the spontaneous emission factor, and it is physically related to the atomic population levels of the ground and excited energy states, from which spontaneous emission is generated. On a more practical level, n_{sp} is related to the noise figure from the optical amplifier by:

$$F_n = 2n_{sp}\left(1-\frac{1}{G})\right)+\frac{1}{G}. \tag{A.3}$$

A.2.2 Raman

Stimulated Raman scattering is a nonlinear process where energy from a high frequency wave is transferred to a short frequency wave via the medium used for their propagation. In silica fibres, the frequency separation (or Stokes shift) between the pump wave and the idler required to obtain maximum gain is approximately 13 THz. In this thesis the majority of the theory of Raman amplifiers was covered in chapters 2 and 3, including experimental characterisation of the Raman gain coefficient and signal power profiles. To simulate the propagation of signals through optical fibre using distributed amplification, the loss component in the Manakov equation needs to be modified to account for the gain experienced during transmission. The linear loss component is, therefore, modified to $\frac{-\alpha+g_0(z)}{2}A$, where $g_0(z)$ is the gain experienced by the optical signal due to Raman amplification at a transmission distance z.

Independent of the Raman amplifier used, either *discrete* or *distributed*, the Raman gain as a function of distance $g_0(z)$ was calculated off-line before performing the SSFM. For this purpose Eqs. (2.27) and (2.28) were used. Pump depletion was neglected in the majority of the simulations performed due to the use of a backward pumped Raman configuration. As detailed in section 6.1, the inclusion of other impairments, such as RIN transfer and double Rayleigh backscattering, in the Raman amplifier simulation tools is still necessary together with an experimental comparison to validate the numerical methods.

A.2.3 Step size of SSFM

The step size used in a SSFM-based simulation depends on a number of factors, including the amplification scheme, the fibre parameters/type, the signal input power, and the signal bandwidth. In general, it is not possible to state a priori what the ideal

step size should be, however there are several techniques which can be used to simultaneously estimate the maximum step size for modelling transmission and accelerate the simulation. The simplest method for SSFM is to use a constant step size, with an equal split ratio for the dispersive step. Contrary to some early theoretical studies of this approach, the constant step size method is extremely flexible in terms of modelling, e.g. differential group delay (DGD) or non-uniform signal power profiles. However, it requires the step to be equal to the step required to model the largest nonlinear phase shift in the transmission link, and is, therefore, computationally expensive to execute. Logarithmic step size algorithms, originally developed for modelling systems with periodic, lumped amplification, offer an excellent trade-off between the complexity of implementation and the ease of modelling the transmission system. Logarithmic step size simulations can, in fact, be applied to transmission simulations using any amplification scheme, provided that the minimum step is still large enough to capture the nonlinear phase shift at the highest signal power point of the simulation. Finally, the adaptive step size algorithm will estimate the step size required at each step, and adapt the length of the dispersive step, as appropriate. For example, in the low power regime, the step size could be of the order of several kilometres, whereas in the high power regime, the step size could be of the order of a few centimetres. This method is extremely valuable for modelling systems with a high range of signal powers, but offers the least flexibility when modelling DGD and non-uniform signal power profiles. For all of the above methods, the Fourier transform required to change between the time- and frequency-domains of the SSFM can be accelerated using a general purpose graphics processing unit (GPGPU). The ONG toolbox typically uses the MATLAB interface to the GPU (GPUArray), which implements the nvidia CUDA algorithm: cuFFT, although cuFFT can be implemented outside of the MATLAB environment, if required. For wide-bandwidth simulations or, more generally, simulations involving a large number of samples, we tailor the number of samples, the precision and the SSFM algorithm to the target hardware, in order to minimise both the simulation time, and the memory (i.e., RAM) required on each GPGPU. Before every set of simulations an optimization procedure is carried out in order to ensure a minimum step size required to obtain an accurate representation of the signal propagation using the SSFM. The use of Raman amplification does not employ the logarithmic step size method. This is because of the distinct signal power profile from distributed Raman amplifiers that, as opposed to to EDFA systems, does not follow an exponential loss of power along the fibre span. To ensure an adequate step size is used for the simulations, preliminary simulations are performed reducing the step size until convergence is reached in the received SNR after transmission. An example of this is shown in Fig. A.2, where different step sizes were used to simulate a transmission span for EDFA and distributed Raman amplifiers at different power levels. It can be observed that an increase in the signal power requires a smaller step size, analogous to the use of distributed Raman amplification. For all the signal powers shown in Fig. A.2, a minimum step size of 100 m was found enough to accurately represent the transmission fibre. It is noted however, that an increase in the transmitted number of channels will lead to a further reduction of the step size.

A.3 Receiver and DSP

After transmission, an ideal coherent receiver is simulated impaired only by shot noise. An ideal DSP chain is performed after the signal is detected. Firstly, the signal undergoes

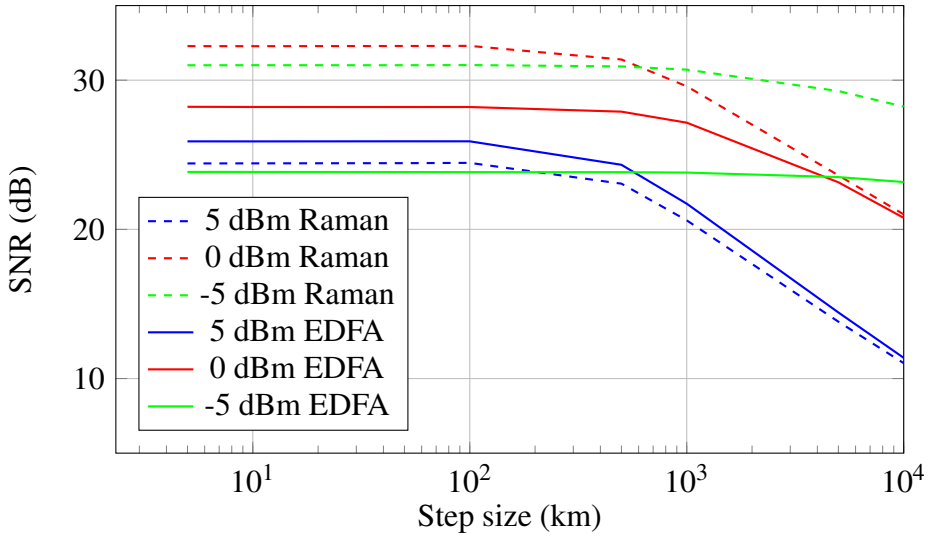

Figure A.2: Step size optimisation for different signal launch powers for EDFA system (solid lines) and distributed backward pump Raman (dashed)

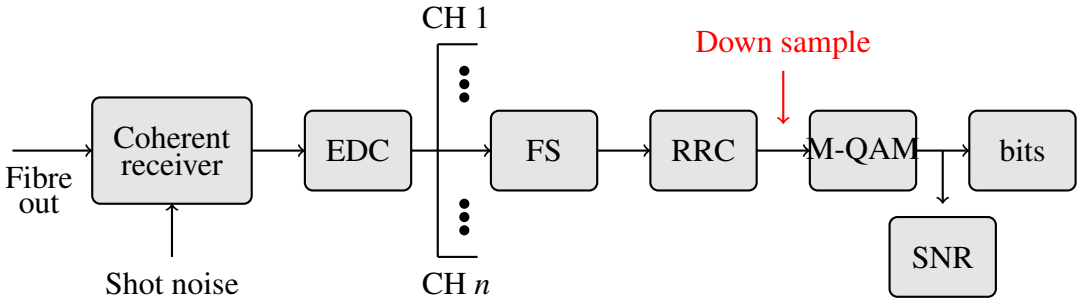

Figure A.3: Schematic of the receiver for numerical simulations

ideal electronic chromatic dispersion (EDC) in the frequency domain. Alternatively, NLC methods can be applied such as DBP and VSFE. To performed DBP, firstly a band-pass filter is used on the received signal to determine the back-propagation bandwidth. Once the signal bandwidth is determined, the SSFM is used to solve the Manakov equation in the backward direction. VFSE was implemented as described in chapter 5. Subsequently, the channel of interested is frequency shifted to baseband where a filter matched to the signal shape (RRC) is applied. Following the matched filter, the signal is down-sampled to be represented using 1 sample per symbol, which is later used to calculate the performance metrics of interest. A schematic of the transmitter used for numerical simulations is shown in Fig. A.3 for illustrative purposes.

After the receiver and the DSP chain, different performance metrics are calculated. Firstly, using the received symbols, the signal to noise ratio (SNR) is calculated.

To compensate the phase rotations experienced during propagation by the signal, the genie phase noise removal (GPNR) technique, that uses the transmitted symbol to estimate the phase difference, was used. For each transmitted symbol within a constellation, the GPNR algorithm estimates the phase rotation relative to the ideal transmitted constellation point using $\theta = \angle y[n] * x[n]$, and then rotates the received symbol by $y[n] * e^{-i\theta}$.

As mentioned in chapter 2, MI was also used as a performance metric. To calculate it the transmitted and received symbols were used, and the integration was performed

using the Monte Carlo approximation as follows:

$$\mathrm{MI} = \log_2 m - \frac{1}{mN_s}\sum_{i=1}^{m}\sum_{n=1}^{N_s} \log_2 \sum_{j=1}^{m} \exp\left[-\frac{|x_i - x_j|^2 + 2\,\mathrm{Re}\left\{(x_i - x_j)^*(y_i[n] - x_i)\right\}}{\sigma^2}\right], \tag{A.4}$$

where m is the constellation cardinality, N_s is the number of received samples, $y_i[n]$ is the n-th sample of the random variable Y corresponding to the transmitted symbol x_i.

After the DSP chain, the symbols are de-mapped to obtain the received bits as a result of this process. The received bits are then compared to the transmitted ones in order to obtain the amount of incorrectly detected bits, from which the BER is calculated. Finally, the quality (Q) factor can be calculated from the received BER using:

$$Q(dB) = 20\log_{10}\left(\sqrt{2}\mathrm{erfcinv}(2BER)\right), \tag{A.5}$$

where erfcinv corresponds to the inverse complementary error function. For the QAM modulation format, the Q-factor is related to (but not equal to) the SNR. As both the order of the modulation and/or the BER increases, the relationship between Q and SNR is increasingly nonlinear. As is conventional for experimental BER measurements, simulations should also target the 95% confidence interval. Therefore, to report this level of confidence for any given simulation, sufficient symbols should be transmitted such that approximately 100 errors are measured on average.

B

Derivation of VSTF for OPC-based transmission systems

This appendix explains in detail the derivation of the Volterra based filter used for nonlinearity compensation for links that employ optical phase conjugation.

We begin the derivation of the third-order Volterra kernel from the Manakov equation in the frequency domain for a dual polarization signal. Here only the X polarization solution will be derived, noting that the solution for the Y polarization is obtained interchanging the sub-indexes X and Y. Considering the signal on the X polarization we have:

$$\frac{\partial \tilde{A}_X}{\partial z} = j\frac{\beta_2}{2}\omega^2\tilde{A}_X - \frac{\alpha(z)}{2}\tilde{A}_X + j\frac{8}{9}\gamma\mathcal{F}\{(A_X A_X^* + A_Y A_Y^*)A_X\}, \tag{B.1}$$

where $\mathcal{F}\{(A_X A_X^* + A_Y A_Y^*)A_X\}$ is the Fourier transform of the signal product in the nonlinear term. The zero-th order solution in the frequency domain for a propagation distance of $N_s L_s$, where N_s is the number of span and L_s is the span length, is given by:

$$\tilde{A}_{0X}(\omega, N_s L_s) = \tilde{A}_X(\omega, 0)e^{\left(-\frac{\alpha(z)}{2} + i\frac{\beta_2}{2}\omega^2\right)N_s L_s}, \tag{B.2}$$

where the optical field at the input of the fibre at frequency ω is $\tilde{A}_X(\omega, 0)$. The zero-th order solution is subsequently used to solve Eq. (B.1) to the first order with solution:

$$\begin{aligned}\tilde{A}_{1X}(\omega, N_s L_s) =& i\frac{8}{9}\gamma e^{\left(i\frac{\beta_2}{2}\omega^2 - \frac{\alpha(z)}{2}\right)N_s L_s} \\ & \int_0^{N_s L_s} e^{\int_0^{z'}(-i\frac{\beta_2}{2}\omega^2 + \frac{\alpha}{2})dz''} D(z')dz',\end{aligned} \tag{B.3}$$

where the term $D(z)$ comes from substituting Eq. (B.2) into the nonlinear term of

Eq. (B.1), and is defined as:

$$\begin{aligned} D(z) = -\iint \big(&\tilde{A}_{0X}(\omega_2,z)\tilde{A}^*_{0X}(\omega_1,z)\tilde{A}_{0X}(\omega-\omega_2+\omega_1,z) \\ &+\tilde{A}_{0Y}(\omega_2,z)\tilde{A}^*_{0Y}(\omega_1,z)\tilde{A}_{0X}(\omega-\omega_2+\omega_1,z)\big)\, d\omega_2 d\omega_1, \end{aligned} \tag{B.4}$$

where the operator * represents complex conjugation. Substituting Eq. (B.4) into Eq. (B.3) we obtain the first order solution at N_sL_s:

$$\begin{aligned} \tilde{A}_{1X}(\omega,N_sL_s) =& i\frac{8}{9}\gamma e^{\left(i\frac{\beta_2}{2}\omega^2-\frac{\alpha(z)}{2}\right)N_sL_s} \\ &\times\iint \left[\mathcal{S}_{XXX}(\omega,\omega_1,\omega_2)+\mathcal{S}_{YYX}(\omega,\omega_1,\omega_2)\right] \\ &F\left(\omega,\omega_1,\omega_2\right)\zeta\left(N_s,\omega,\omega_1,\omega_2\right)d\omega_2 d\omega_1. \end{aligned} \tag{B.5}$$

As seen in [71], for a transmission that does not employ an OPC module, the four-wave mixing efficiency $F\left(\omega,\omega_1,\omega_2\right)$ and the *phased array* factor $\zeta\left(N_s,\omega,\omega_1,\omega_2\right)$ are defined as follows:

$$F(\omega,\omega_1,\omega_2) = \frac{1-e^{-\alpha L_s}e^{i\beta_2\Delta\Omega L_s}}{i\beta_2\Delta\Omega-\alpha} \tag{B.6}$$

$$\zeta\left(N_s,\omega,\omega_1,\omega_2\right) = \sum_{n=1}^{Ns} e^{i\beta_2(n-1)\Delta\Omega L_s}. \tag{B.7}$$

The signal kernels, $\mathcal{S}_{XXX}(\omega,\omega_1,\omega_2)$ and $\mathcal{S}_{YYX}(\omega,\omega_1,\omega_2)$, were previously defined in (5.7), and $\Delta\Omega$ was defined in chapter 5 section 5.2 as $\Delta\Omega \triangleq (\omega-\omega_1)(\omega_1-\omega_2)$.

To study the effect of an OPC module placed in the middle point, that is after $\frac{N_s}{2}$ spans, the solution from (B.3) is conveniently rewritten into two sections, one before and one after the OPC module. Here the attenuation coefficient of the fibre $\alpha(z)$ is replaced with the function $P(z)$ to represent any arbitrary power profile. It is noted that in the case of constant loss this becomes $P(z) = e^{-\alpha z}$. Rewriting Eq. (B.3) we have:

$$\begin{aligned} \tilde{A}_{1X}(\omega,N_sL_s) =& i\frac{8}{9}\gamma e^{\left(i\frac{\beta_2}{2}\omega^2\right)N_sL_s}P(N_sL_s) \\ &\left[\int_0^{\frac{N_s}{2}L_s} P(-z')e^{\int_0^{z'}-i\frac{\beta_2}{2}\omega^2 dz''}D(z')dz'\right. \\ &\left.+\int_{\frac{N_s}{2}L_s}^{N_sL_s} P(-z')e^{\int_0^{z'}-i\frac{\beta_2}{2}\omega^2 dz''}D(z')dz'.\right] \end{aligned} \tag{B.8}$$

Both integrals in Eq. (B.8) represent propagation up to specific part of the transmission link. The first one correspond to propagation from the transmitted up the mid-link point, and the second one corresponds to propagation from the mid-link point to the end the last fibre span. Using the first order solution for the first half of the link $\left(\tilde{A}_{1X}\left(\omega,\frac{N_sL_s}{2}\right)\right)$, Eq. (B.8) is rewritten as follows:

$$\begin{aligned} \tilde{A}_{1X}(\omega,N_sL_s) &= \tilde{A}_{1X}\left(\omega,\frac{N_sL_s}{2}\right)P\left(\frac{N_sL_s}{2}\right)e^{i\frac{\beta_2}{2}\omega^2\frac{N_sL_s}{2}} \\ +i\frac{8}{9}\gamma P(N_sL_s)e^{i\frac{\beta_2}{2}\omega^2 N_sL_s}&\int_{\frac{N_s}{2}L_s}^{N_sL_s} e^{\int_0^{z'}\left(-i\frac{\beta_2}{2}\omega^2+\frac{\alpha}{2}\right)dz''}D(z')dz'. \end{aligned} \tag{B.9}$$

When an OPC module is used both zero-th and first-order solution undergo conjugation in time-domain at $z = \frac{N_s L_s}{2}$, leading to:

$$\begin{aligned}\tilde{A}_{1X}(\omega, N_s L_s) =& \hat{A}_{1X}\left(\omega, \frac{N_s L_s}{2}\right) P\left(\frac{N_s L_s}{2}\right) e^{i\frac{\beta_2}{2}\omega^2 \frac{N_s L_s}{2}} \\ &+ i\frac{8}{9}\gamma P(N_s L_s) e^{i\frac{\beta_2}{2}\omega^2 N_s L_s} \\ &\times \int_{\frac{N_s}{2}L_s}^{N_s L_s} e^{\int_0^{z'}\left(-i\frac{\beta_2}{2}\omega^2+\frac{\alpha}{2}\right)dz''} D(z')dz'.\end{aligned} \tag{B.10}$$

where the conjugation of the first order term is given by:

$$\begin{aligned}\hat{A}_{1X}\left(\omega, \frac{N_s L_s}{2}\right) &\triangleq \mathcal{F}\left\{A^*_{1X}\left(t, \frac{N_s L_s}{2}\right)\right\} \\ &= \tilde{A}^*_{1X}\left(-\omega, \frac{N_s L_s}{2}\right)\end{aligned} \tag{B.11}$$

The term corresponding to the first half of the transmission link then becomes:

$$\begin{aligned}&\hat{A}_{1X}\left(\omega, \frac{N_s L_s}{2}\right) P\left(\frac{N_s L_s}{2}\right) e^{i\frac{\beta_2}{2}\omega^2 \frac{N_s L_s}{2}} \\ &= -i\gamma\frac{8}{9}P(N_s L_s)\iint S^*(\omega, \omega_1, \omega_2)\zeta^*\left(\frac{N_s}{2}, \omega, \omega_1, \omega_2\right)d\omega_2 d\omega_1,\end{aligned} \tag{B.12}$$

where

$$\begin{aligned}\zeta(\frac{N_s}{2}, \omega, \omega_1, \omega_2) \triangleq \sum_{n=1}^{\frac{N_s}{2}} \Bigg[&\frac{P(nL_s)e^{i\beta_2\Delta\Omega nL_s}}{\alpha(nL_s)+i\beta_2\Delta\Omega} \\ &-\frac{P((n-1)L_s)e^{i\beta_2\Delta\Omega(n-1)L_s}}{\alpha((n-1)L_s)+i\beta_2\Delta\Omega}\Bigg],\end{aligned} \tag{B.13}$$

and

$$S^*(\omega, \omega_1, \omega_2) = \mathcal{S}^*_{XXX}(-\omega, -\omega_1, -\omega_2) + \mathcal{S}^*_{YYX}(-\omega, -\omega_1, -\omega_2). \tag{B.14}$$

For transmission beyond the conjugation point, the zero-th order solution needs to undergo conjugation after a distance of $\frac{N_s L_s}{2}$. Therefore, the linear solution for $z \geq \frac{N_s L_s}{2}$ is given by:

$$\tilde{A}_{0X}(\omega, z) = A^*_X(-\omega, 0)P(z)e^{i\frac{\beta_2}{2}\omega^2(z-N_s L_s)}. \tag{B.15}$$

Substituting (B.15) into $D(z)$ we obtain:

$$\begin{aligned}D(z) =& -P^3(z)e^{i\frac{\beta_2}{2}\omega^2(z-N_s L_s)} \\ &\iint A^*_X(-\omega_2, 0)A_X(-\omega_1, 0)A^*_X(\omega_2-\omega_1-\omega, 0) \\ &e^{i\beta_2\Delta\Omega(z-N_s L_s)}d\omega_2 d\omega_1\end{aligned} \tag{B.16}$$

Now the second term in Eq. (B.9) becomes:

$$\begin{aligned} &P(N_sL_s)e^{i\frac{\beta_2}{2}\omega^2N_sL_s}\int_{\frac{N_s}{2}L_s}^{N_sL_s}P^{-1}(z')e^{-i\frac{\beta_2}{2}\omega^2z'}i\frac{8}{9}\gamma D(z')dz' \\ &=i\gamma\frac{8}{9}P(N_sL_s)\iint S^*(\omega,\omega_1,\omega_2)\psi\left(\frac{N_s}{2},\omega,\omega_1,\omega_2\right)d\omega_2 d\omega_1 \end{aligned} \tag{B.17}$$

where

$$\begin{aligned} &\psi\left(\frac{N_s}{2},\omega,\omega_1,\omega_2\right)\triangleq e^{-i\beta_2\Delta\Omega N_sL_s} \\ &\times\sum_{n=\frac{N_s}{2}+1}^{N_s}\left[\frac{P(nL_s)e^{i\beta_2\Delta\Omega nL_s}}{\alpha(nL_s)+i\beta_2\Delta\Omega}-\frac{P((n-1)L_s)e^{i\beta_2\Delta\Omega(n-1)L_s}}{\alpha((n-1)L_s)+i\beta_2\Delta\Omega}\right] \end{aligned} \tag{B.18}$$

Finally, we obtain:

$$\begin{aligned} A_{1X}(\omega)=&i\gamma\frac{8}{9}P(N_sL_s)\iint S^*(\omega,\omega_1,\omega_2) \\ &\left[\psi\left(\frac{N_s}{2},\omega,\omega_1,\omega_2\right)-\zeta^*\left(\frac{N_s}{2},\omega,\omega_1,\omega_2\right)\right]d\omega_2 d\omega_1 \end{aligned} \tag{B.19}$$

where the nonlinear kernel in the presence of OPC is given by:

$$\Gamma(N_s,\omega,\omega_1,\omega_2)\triangleq\psi\left(\frac{N_s}{2},\omega,\omega_1,\omega_2\right)-\zeta^*\left(\frac{N_s}{2},\omega,\omega_1,\omega_2\right) \tag{B.20}$$

In order to suppress the first-order solution for all ω one condition is having $\Gamma(N_s,\omega,\omega_1,\omega_2)=0\ \forall\ \omega,\omega_1,\omega_2$. This is verified if

$$P((N_s-n)L_s^-)=P((n-1)L_s^+) \tag{B.21}$$
$$P((N_s-n-1)L_s^+)=P(nL_s^-) \tag{B.22}$$
$$\alpha((N_s-n)L_s^-)=-\alpha((n-1)L_s^+) \tag{B.23}$$
$$\alpha((N_s-n-1)L_s^+)=-\alpha(nL_s^-). \tag{B.24}$$

In the case where $\alpha=0$ (lossless fibre), all the terms in the sum in (B.20) are the same and, thus, $\Gamma(N_s,\omega,\omega_1,\omega_2)=0$. If $\alpha(z)=\alpha$ everywhere except in $z=nL_s$ for $n=0,1,2,...$ where $\alpha(z)=\delta(z-nL_s)$ (EDFA amplification) we have

$$P((N_s-n)L_s^-)=P(nL_s^-), \tag{B.25}$$
$$P((N_s-n-1)L_s^+)=P((n-1)L_s^+), \tag{B.26}$$
$$\begin{aligned} &\alpha((N_s-n)L_s^-)=\alpha((n-1)L_s^+) \\ &=\alpha((N_s-n-1)L_s^+)=\alpha(nL_s^-),\ \text{for}\ n=1,2,...,\frac{N_s}{2} \end{aligned} \tag{B.27}$$

and the OPC kernel becomes:

$$\begin{aligned}\Gamma(N_s,\omega,\omega_1,\omega_2) =&\zeta^*\left(\frac{N_s}{2},\omega,\omega_1,\omega_2\right)\\ &\frac{(e^{-i\beta_2\Delta\Omega L_s}e^{-\alpha L_s}-1)(\alpha-i\beta_2\Delta\Omega)}{\alpha^2+\beta_2^2\Delta\Omega^2}\\ &+\frac{(e^{-i\beta_2\Delta\Omega L_s}-e^{-\alpha L_s})(\alpha+i\beta_2\Delta\Omega)}{\alpha^2+\beta_2^2\Delta\Omega^2}.\end{aligned} \tag{B.28}$$

C Acronyms

ADC analogue-to-digital converters

AOM acousto-optic modulators

ASE amplified spontaneous emission

AWGN additive white Gaussian noise

BER bit error rate

BPF band-pass filter

CMA constant modulus algorithm

DAC digital-to-analogue converter

DBP digital back-propagation

DCF dispersion compensating fibre

DSF dispersion shifted fibre

DSP digital signal processing

ECL External cavity lasers

EDC electronic dispersion compensation

EDFA erbium-doped fibre amplifier

EGN enhanced Gaussian noise

ENOB effective number of bits

FEC forward error correction

FF-DBP full-field DBP

FFT fast Fourier transform

FIR finite impulse response

FWM four wave mixing

GN Gaussian noise

GVD group velocity dispersion

HNLF highly nonlinear fibres

IFFT inverse fast Fourier transform

ISRS inter-channel stimulated Raman scattering

LO local oscillator

MC-DBP multichannel digital back-propagation

MFD mode-field diameter

MI Mutual information

MZM Mach-Zehnder modulator

NDFIS National Dark Fibre Infrastructure Service

NLC nonlinearity compensation

NLI nonlinear interference

NLSE nonlinear Schrödinger equation

OPC optical phase conjugation

OSA optical spectrum analyser

OSNR optical signal to noise ratio

OTDR optical time domain reflectometer

PM polarisation multiplexing

PMD polarisation mode dispersion

PS polarisation scrambler

PSD power spectral density

QAM quadrature amplitude modulation

SMF Single Mode Fibre

RIN relative intensity noise

RRC root raised cosine

SNR signal-to-noise ratio

SPM self phase modulation

SRS Stimulated Raman scattering

SSFM split-step Fourier method

SS-ASE spectrally-shaped amplified spontaneous emission

SOA semiconductor optical amplifier

VOA variable optical attenuator

VSFE Volterra series frequency equaliser

VSTF Volterra series transfer function

WDM wavelength division multiplexing

WSS wavelength selective switch

XPM cross-phase modulation